The star formation history of Virgo spiral galaxies. Combined spectral and photometric inversion.

Cirino Pappalardo, Bernd Vollmer, Ariane Lancon

Observatoire astronomique de Strasbourg

Thèse pour l'obtention du grade de
Docteur
de l'Université de Strasbourg

Spécialité Astrophysique

par Cirino Pappalardo

The Star Formation History of Virgo spiral galaxies Combined spectral and photometric inversion

Soutenue publiquement en janvier 2010

Membres du jury

Directeur de thèse :	Mme. Ariane Lançon, Professeur, Université de Strasbourg
Directeur de thèse :	M. Bernd Vollmer, Astronome Adjoint, Université de Strasbourg
Rapporteur Interne :	M. Rodrigo Ibata, Dir. de recherche CNRS, Université de Strasbourg
Rapporteur Externe :	Mme. Florence Durret, Astronome, IAP
Rapporteur Externe :	Mme. Pascale Jablonka, Maitre-assistante, Observatoire de Genève
Examinateur :	M. Pierre-Alain Duc, Chargé de recherche CNRS, CEA Saclay

Contents

.

Chapter 1

Introduction

A galaxy is a physical system gravitationally bound, formed by stars, gas in different phases, embedded in a dark matter halo. Following the Hubble classification (Hubble 1936, Hubble 1927, Hubble 1926a, Hubble 1926b) we divide galaxies in three different 'Hubble types', according to their morphology.

Elliptical galaxies (early type) have an ellipsoidal shape that can have different eccentricities. They are formed of old stars with no current star formation and a small amount of gas. Spiral galaxies (late type) are composed of a central bulge with a high concentration of stars, and a rotating flat disk containing stars, gas and dust. Finally there are lenticular galaxies, intermediate between spiral and elliptical galaxies, with a central bulge similar to the spiral galaxies, but ill-defined spiral arms. Beyond these 'Hubble types' there is a broad class of galaxies with lack of regular structure, they form the group of Irregular galaxies.

1.1 Spiral galaxies

A proper description of spiral galaxies is more complex than defined above. The bulge hosts at its center a supermassive black holes and the disk can have different shapes. In approximatively half of the cases the disk presents a central bar composed of stars (Mihalas & Routly, 1968). In the Hubble sequence of spiral, galaxies fork in two sub-samples according to the presence or not of a central bar (see Fig. 1.1).

In spiral disks gas can be present in different phases that depend on density and temperature (Bakos et al. 2002). We can divide the interstellar medium into 5 phases (Dahlem 1997) : hot ionized medium, warm ionized medium, warm neutral medium, cold neutral medium and the molecular component. The hot and warm component consist of hot ionized gas and neutral HI medium that we can assume homogeneously distributed all along the gas disk. The cold and the molecular

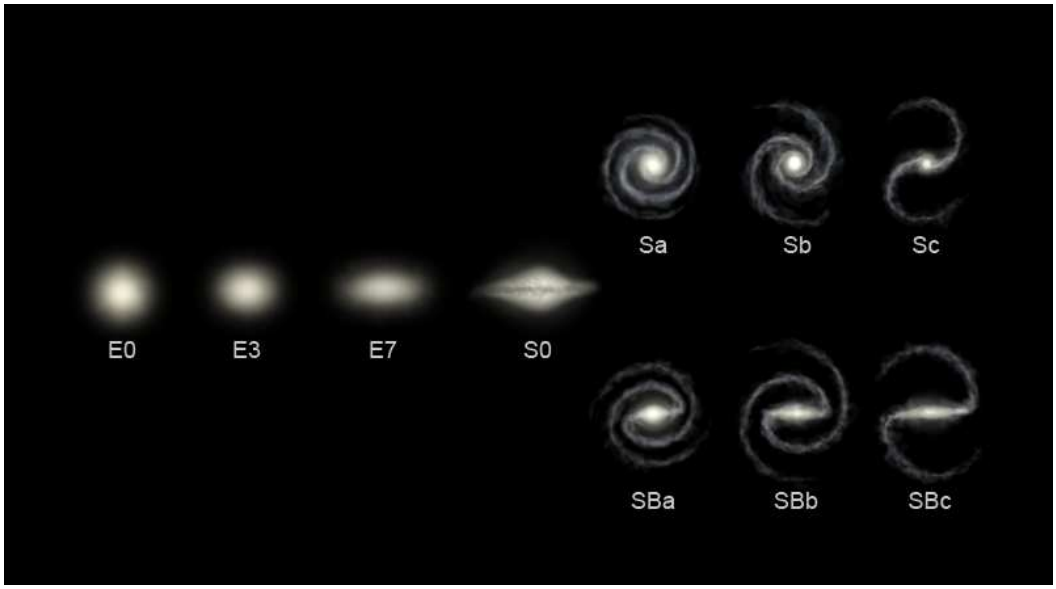

Figure 1.1: Hubble sequence (courtesy Ville Koistinen).

component have instead a clumpy structure not uniformly distributed. The disks of spirals are riches of gas in which there is a high star formation rate.

Spirals are rotation supported systems that can undergo different perturbations due to the environment in which they evolve. In reality this is the usual case, since galaxies are not isolated system. At larger scales the Universe is structured in cluster of galaxies, that can collect thousands of galaxies of any Hubble type (Stevens et al. 1999).

Studying 55 nearby clusters Dressler (1980) observed the so-called 'morphology-density relation': the early type galaxies are more frequently found in high density environments. This relation spans a range of 6 order of magnitude in density and has been verified in galaxy groups (Postman & Geller, 1984) and in higher redshift clusters (Capak et al., 2007).

Spiral galaxies are most frequently found in the outskirts of clusters, in low density regions, but during their orbit in the potential well of the cluster they can pass the center of cluster, a much denser environment.

Different observations of nearby clusters (Schindler et al. 1999, Binggeli et al. 1985, Giovanelli & Haynes 1983) showed that in dense environments spiral galaxies can evolve in a strongly different way with respect to their isolated counterparts.

We can identify three main categories of physical effects that modify the structure of a spiral galaxy:

- gravitational effects (e.g. tidal interactions in galaxy-galaxy encounters),

- hydrodynamical effects (e.g. ram pressure stripping or thermal evaporation),
- hybrid processes, i.e. those involving both type of effects, such as preprocessing and starvation (see Boselli & Gavazzi 2006 and references therein).

The property of spiral galaxies are related to the environment in which they formed, because they are strongly affected both from the density of the medium in which they move, and the interaction with other galaxies during their lifetime. The detailed study of the relationship between spiral galaxies and their environment is based primarily on nearby Universe observations, because the resolving power of current telescopes provide insufficient details of more distant objects.

The closest spirals rich cluster of galaxies is Virgo ($d \approx 16.7$ Mpc), that is also massive ($M = 1.2 \times 10^{15} M_{\odot}$) and still dynamically active. Virgo is in reality an aggregate of three sub-clumps centered on the galaxies M87, M86, M49 and has a total extension of $\approx$ 2.2 Mpc, with $\approx$ 1800 galaxies. This number could be an underestimation, because of the unknown fraction of dwarf galaxies (Sabatini et al., 2003).

One of the most interesting characteristics of Virgo spiral galaxies is their lack of gas (Giovanelli & Haynes 1983, Chamaraux et al. 1980). The amount of atomic gas in Virgo spirals is less than that of galaxies in the field, in particular they show truncated HI disks (Giovanelli & Haynes 1983, Cayatte et al. 1990). The galaxies on radial orbits are on average more HI deficient[1] that the ones on circular orbits (Dressler 1986). In some case Chung et al. (2007) found long HI tails associated to the spiral disks (VIVA : VLA Imaging of Virgo galaxies in Atomic gas survey, Fig. 1.2).

The physical processes able to remove gas from a spiral disk are essentially tidal interaction and ram pressure stripping. Both processes have been studied theoretically (e.g. Vollmer et al. 2001, Schulz & Struck 2001, Quilis et al. 2000, Abadi et al. 1999, Roediger & Hensler 2005, Acreman et al. 2003) and observationally (e.g. Kenney et al. 2004, Solanes et al. 2001, Cayatte et al. 1990, Warmels 1988). Disentangling the two effects is still a delicate problem.

1.2 Star Formation in cluster spirals

Using the Hα emission line as a tracer of the star formation rate of a galaxy and observing a great number of spirals, has been possible to study star formation as

[1]The HI deficient parameter is the logarithmic difference between the observed HI mass and the expected value in isolated object of the same Hubble type, and comparable in size and mass (Giovanelli & Haynes, 1983).

Figure 1.2: Image of Virgo cluster taken with VLA telescope (Chung et al. 2007). Distribution of HI disks of 47 spiral galaxies with overplotted in yellow X-ray emission of the hot ICM, from ROSAT observations. The color of galaxies depends on their radial velocities (right-bottom corner). The size of galaxies is been increased by a factor of ten.

a function of environment. Gavazzi et al. (2002) studying a sample of galaxies in Virgo cluster showed that spirals in cluster have, on average, a low star formation activity, and redder colors. SDSS observations of Gómez et al. (2003) found that star formation in cluster spirals begins to decrease with respect to their isolated field counterparts, out to 3-4 virial radii. This results are in agreement with Solanes et al. (2001), who studied the HI content of about 1900 spirals in nearby clusters and detected in some cases spiral galaxies that are HI deficient out to 2 virial radii. Dynamical models give us a different scenario, in which ram pressure becomes efficient only when the galaxy is near the cluster center, less than one virial radius.

The maximum distance from the cluster center at which a galaxy is bound to the Virgo cluster is between 1.7 and 4.1 Mpc (Mamon et al., 2004). However Solanes et al. (2001) observed galaxies that are HI deficient out to 25-30 Mpc. Moreover the galaxy crosses the central regions of the cluster in a very-short time-scale, compared to the orbital time.

Where and when cluster spirals begin to lose their ISM is still an open question. In the core of the cluster, where strong stripping ablates most of the spiral gas in few Myr, or in a more 'soft' way, with ICM that slowly but constantly removes gas since 3-4 virial radii?

In any case once the gas has left the galactic disk, star formation, that is ultimately fueled by the neutral hydrogen, stops. The stellar populations evolve then passively and this evidence should be detectable both in optical spectra and photometry.

The determination of the underlying star formation history since spectral energy distribution of galaxies and photometry is complex. In the next section we review some methods developed in order to recover the star formation history of a spiral galaxy.

1.3 Fitting SEDs

The spectral energy distribution of a galaxy can be considered as the integrated light produced by different stellar populations, with different ages and metallicity. In this sense the emission of a galaxy collects informations that includes its whole life, such as passive evolution, merging, metal recycling and so on.

The physical problem is characterized by a star formation history, a metallicity evolution, a global velocity dispersion and a parameter that takes into account the dust extinction. All these informations must be recovered from the spectral energy distribution of the galaxy. For this reason in a more precise way we must

talk of luminosity weighted stellar age distribution and luminosity weighted age-metallicity relation.

For low and medium resolution spectra a method that is widely used to detect these information is the 'Lick indices' method (Worthey 1994, Faber 1973).

Using this method we measure the strength of a small region of the spectrum, in which there is an age or metal sensitive feature. After continuum subtraction, we associate to the measured feature a spectral index. The recovered index is then compared with the model predictions. The Lick indices are very robust but use only small windows of the spectrum. In addition they are highly sensitive to the continuum estimation.

After Worthey (1994) other methods have been introduced, which face the problem of a fit that involves the whole spectrum (Cid Fernandes et al. 2005, Mateu et al. 2001, Reichardt et al. 2001). With the improvement of more and more refined methods and, at the same time, with the development of a more rigorous mathematical formalism, (Cid Fernandes et al. 2005), the inverse problem associated to the spectral fits has been deeply investigated. These analysis showed that the problem of star formation history determination by fitting a spectrum is strongly ill-posed (Ocvirk et al. 2006a, Morrissey et al. 2007, Moultaka et al. 2004).

In the present work the problem of ill-conditioning of the problem is solved via maximum a posteriori likelihood method, or equivalently maximum penalized likelihood. This method overcomes the problem of ill-conditioning introducing in the minimization of the χ^2 associated to the inverse problem a penalty function, whose goal is to regularize the solution, when it becomes too irregular. The main advantage of such an approach is that the constraints to the solution are minimal, and the ill conditioning of the problem can be managed and quantified. The maximum a posteriori likelihood methods are used in a wide variety of problems, from seismology to the image reconstruction of medical tomography. In astrophysics, it has been used for light deprojection (Kochanek & Rybicki 1996), determination of star formation histories and extinction parameter (Vergely et al. 2002), multiband photometric inversion (Dye, 2008) and many other domains (e.g. Thiebaut 2002, Thiébaut 2005, Saha & Williams 1994, Pichon & Thiebaut 1998 and Merritt 1997).

1.4 Galaxy evolution in cluster of galaxies

We consider the Virgo spiral NGC 4388. It is an edge on Seyfert 2 galaxy (Sab type) with $m_B = 12.2$ and radial velocity $V_{\rm rad} \sim 1400$ km s^{-1} with respect to the

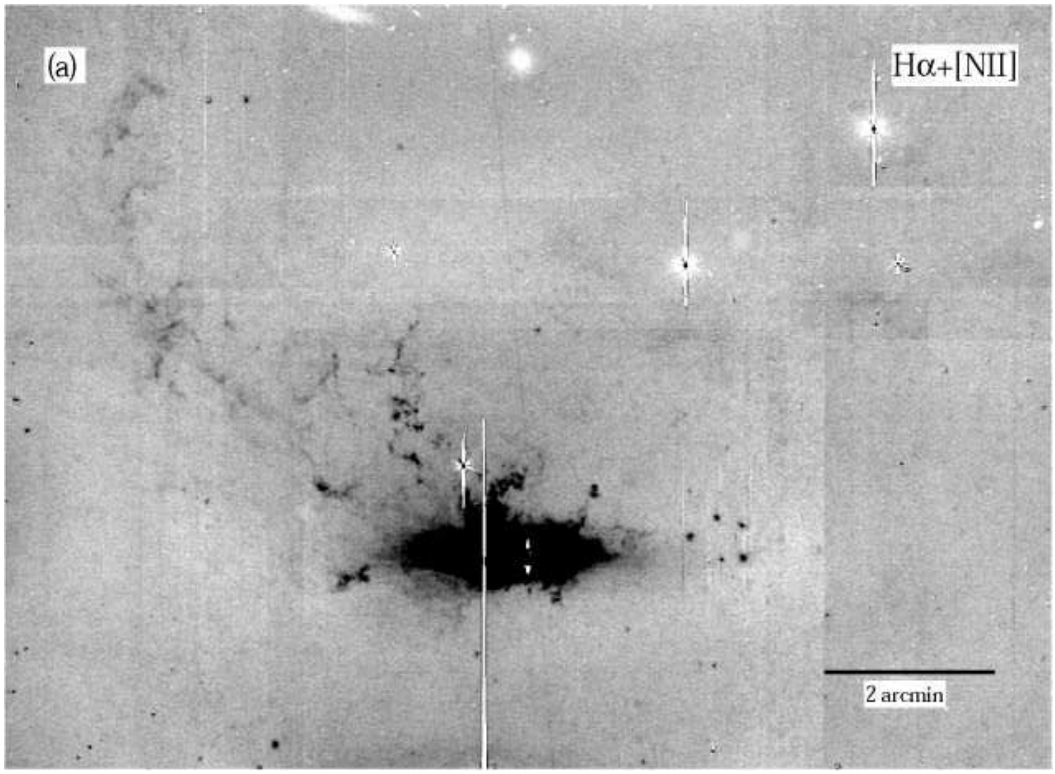

Figure 1.3: Extended plume of Hα in NGC 4388 detected by Yoshida et al. (2002) with SUBARU telescope.

cluster mean. NGC 4388 is located at a projected distance[2]) of 1.3° (≈ 400 kpc) from the Virgo cluster center (M87) and, using the Tully-Fisher method, Yasuda et al. (1997) realized a three dimensional de-projection, placing NGC 4388 very close to M87. The disk of NGC 4388 has lost 85% of its HI (Cayatte et al. 1990), that is truncated within the optical disk ($R \sim 4.5$ kpc). Observing the galaxy in Hα Veilleux et al. (1999) found a large plume of ionized gas of 4 kpc above the plane, that in subsequent SUBARU observations (Yoshida et al. 2002) has been detected up to 35 kpc off the galactic plane in NE direction (Fig. 1.3). In soft X-ray Iwasawa et al. (2003) found an emission in the same region of the ionized gas.

At radio wavelength Vollmer & Huchtmeier (2003) performing 21-cm line observations at Effelsberg 100-m radio telescope discovered neutral gas out at least 20 kpc NE of NGC 4388 disk, with a HI mass of 6×10^7 $M_\odot$. Further observations with the Westerbrok Synthesis Radio Telescope (WSRT) showed that this gas extends further than it has been detected before. Oosterloo & van Gorkom (2005) discovered an HI plume of 110×25 kpc^2 in size and a mass of 3.4×10^8 $M_\odot$ (Fig. 1.4).

The origin of the extraplanar gas of NGC 4388 was highly debated. For the 4

[2]We assume a distance from Virgo of 16.7 Mpc.

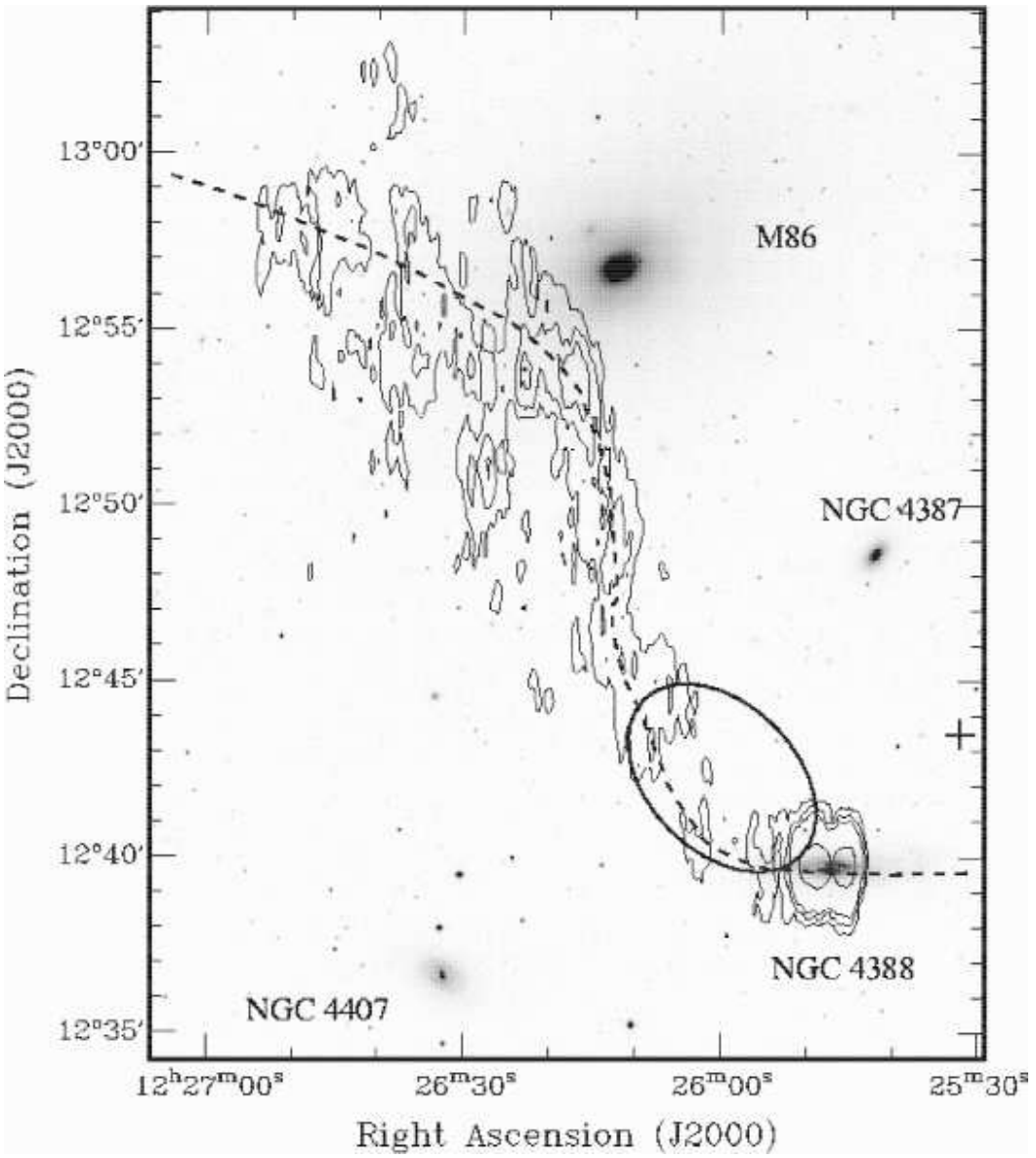

Figure 1.4: Integrated HI emission line from Oosterloo & van Gorkom (2005) observations with Westerbork Synthesis Radio Telescope (WSRT). The ellipse indicates the region where Yoshida et al. (2002) detected ionized gas.

kpc plume Veilleux et al. (1999) discussed 4 different origins:

1. minor mergers,
2. galactic wind,
3. nuclear outflow,
4. ram pressure stripping.

In the region closer to the center of the galaxy the gas ionization is probably due to the AGN jet, and Veilleux et al. (1999) suggested both 1. and 4. as possible origin of the 4 kpc plume. But this cannot explain the extended plume of 35 kpc. For this reason Yoshida et al. (2002) preferred a combination of 3. and 4. to explain this elongated structure.

For the 110 kpc HI cloud Oosterloo & van Gorkom (2005) favor ram pressure stripping. Vollmer & Huchtmeier (2003), assuming ram pressure stripping as principal effect, showed results from dynamical modeling that are able to reproduce the HI deficiency, the truncated HI disk, and the extraplanar emission of NGC 4388. The extended plume of gas of NGC 4388 is then due to ram pressure stripping.

1.4.1 Ram Pressure Stripping scenario

The interstellar medium (ISM) of a spiral galaxy that is moving inside the potential well of a cluster, undergoes a pressure due to the intracluster medium (ICM), that is hot ($T_{\rm ICM} \approx 10^7 - 10^8$ K) and dense ($\rho_{\rm ICM} \approx 10^{-3} - 10^{-4}$ atoms cm^{-3}). If this pressure is larger than the restoring force due to the galactic potential, the galaxy loses gas form the outer disk. Quantitatively ram pressure is expressed by the Gunn & Gott (1972) criterion:

$$\rho_{\rm ICM} V_{\rm gal}^2 \geq 2\pi G \Sigma_{\rm star} \Sigma_{\rm gas}, \tag{1.1}$$

where $\rho_{\rm ICM}$ is the density of the ICM, $V_{\rm gal}$ is the peculiar velocity of the galaxy inside the cluster, $\Sigma_{\rm star}$ and $\Sigma_{\rm gas}$ are the surface density of stars and gas, respectively.

To create an exhaustive model of ram pressure stripping we must take into account the pressure force expressed in Eq. 1.1, but also hydrodynamical processes acting on the gas, such as turbulent stripping or thermal evaporation (Nulsen, 1982). Since a fully analytical solution of the problem is not possible, the numerical approach has been extensively used to investigate the ram pressure stripping scenario. The interstellar medium can be modeled using a continuous approach, i.e. using Eulerian hydrodynamic codes (e.g. Roediger & Hensler 2005, Roediger & Brüggen 2006, Quilis et al. 2000, Acreman et al. 2003), an hybrid approach mixing

continuous and discrete description, such as smoothed particles hydrodynamics (e.g. Abadi et al. 1999, Schulz & Struck 2001), and a discrete approach, such as sticky particles codes (e.g. Vollmer et al. 2001). The stripping can have two different origins: a classical momentum transfer, described by Gunn & Gott (1972), in which we have a strong stripping in the central region of the cluster with a timescale of $\sim$ 10 - 100 Myr. Another origin is the turbulent/viscous stripping (Nulsen, 1982), that remove slowly the gas with a timescale of $\sim$ 1 Gyr. To take into account for turbulent/viscous stripping a continuous approach is necessary, i.e. Eulerian hydrodynamic codes.

Using a discrete approach Vollmer et al. (2001) are able to quantify the importance of this effect in the Virgo cluster. The results showed that ram pressure is sufficient to remove a considerable part of the ISM in cluster spirals that are on radial orbits in the cluster potential. The timescale of viscous/turbulent stripping in spirals is comparable to their crossing time, i.e. few Gyr (Bekki et al. 2002). For the momentum transfer stripping, the time scale is $\sim$ 10 - 100 Myr, i.e. the time at which the galaxies transit in cluster-cores.

In the case of NGC 4388 Vollmer & Huchtmeier (2003) estimated that ram pressure stripping is able to remove more than 80 % of the ISM (Fig. 1.5), consistent with the observations of Cayatte et al. (1990). They also estimated that the galaxy passed the cluster center $\sim$ 120 Myr ago.

In this thesis I investigate the effect of ram pressure stripping on the star formation history of cluster spiral galaxies.

We study as a first case NGC 4388, for which, as shown in Sect. 1.4 there are clear observational evidences of undergoing ram pressure stripping. The goal is to recover the 'stripping age', i.e. the time elapsed since the halt of star formation, using only observational constraints independent from the dynamical models.

Starting with the purely spectroscopic approach of Ocvirk et al. (2006a), we develop a new non parametric inversion tool that allows us to analyze spectra and photometric fluxes jointly.

As a side project we present the CO(1-0) observations of NGC 4522, that represents a further example of spiral with truncated HI disk.

The thesis is structured as follows: in Chapt. 2 we introduce the new approach used in this thesis that combines spectral and photometric analysis. In Chapt. 3 we perform also an extensive test campaign in order to verify the robustness of the method. In Chapt. 4 we describe the observations and we explain how we extract the photometry used as input data. Moreover, we investigate, using different

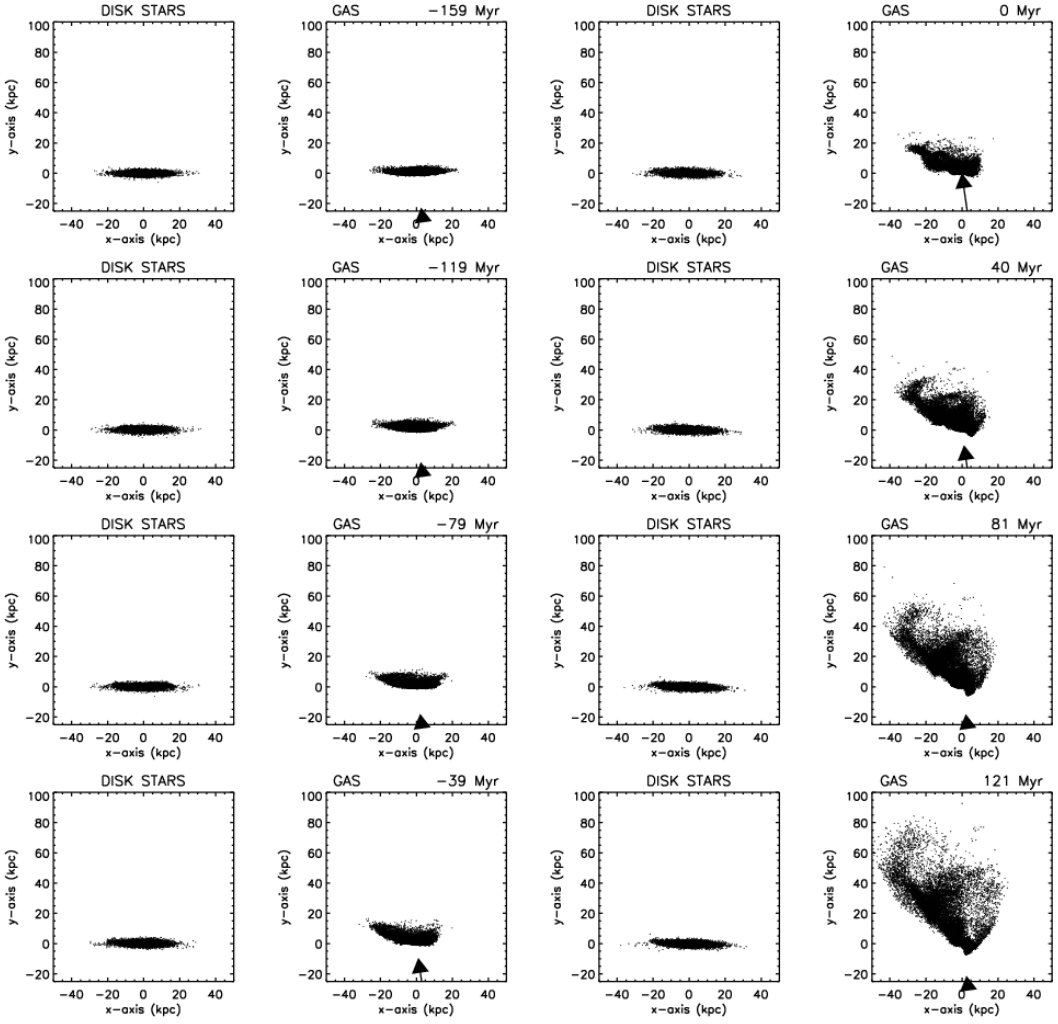

Figure 1.5: Evolution of the stellar model and disk of NGC 4388. Time 0 corresponds to the passage in the cluster center. The arrow represents the pressure of the ICM, and its length is proportional to $\rho_{\rm ICM} V_{\rm gal}^2$, i.e. the ram pressure (Vollmer & Huchtmeier, 2003).

configurations, the consistency of the results in comparison to the campaign performed with artificial data. In Chapt. 5 we present the results obtained for the CO radio observations of NGC 4522. Finally in Chapt. 6 we summarize the main results of the thesis.

Chapter 2

Method

The spectral energy distribution (hereafter SED) and the photometry of a galaxy can be considered as the integrated light produced by different simple stellar populations (SSP) with different ages and metallicities. The light and mass contributions of each population depends on the star formation history of the observed region during the galaxy's life. In this chapter we explain the mathematical tools necessary to recover the star formation history of a galaxy from a combined analysis of spectrum and photometry. The formalism is adapted from Ocvirk et al. (2006a) and Ocvirk et al. (2006b), who did not discuss broad-band photometry.

2.1 Starting equations

2.1.1 The construction of synthetic spectra and fluxes

Assuming that the physics of stars and their spectra are understood, we can calculate the SED $S(\lambda, m, t, Z)$ of a set of stars having initial mass m, age t, and metallicity Z. We assume that a simple population of stars fulfills these hypothesis:

1. The stars are formed at the same time (single age population) with a unique metallicity.
2. The distribution of the mass when $t = 0$ follows a specified Initial Mass Function IMF.

Under these conditions, by integrating between the mass cut-offs of the adopted initial mass function $IMF(m)$, we obtain the spectrum of a simple stellar population (SSP) of age t, metallicity Z and unit mass:

$$B^0(\lambda, t, Z) = \int_{M_{\min}}^{M_{\max}} IMF(m)\, S(\lambda, m, t, Z)\, \mathrm{d}m. \tag{2.1}$$

In the hypothesis of an unobscured galaxy, assuming a single-valued age-metallicity

relation $Z(t)$ and integrating over the Hubble time we can calculate the SED as:

$$F_{\rm rest}(\lambda) = \int_{t_{\rm min}}^{t_{\rm max}} {\rm SFR}(t)\ B^0(\lambda, t, Z(t))\ {\rm d}t, \tag{2.2}$$

in which $F_{\rm rest}(\lambda)$ is the SED of a galaxy at rest and SFR(t) is the star formation rate, i.e. the mass of stars created per unit time at lookback time t.

Since what we observe in a galaxy is the light and not the mass, it is more convenient to convert the mass weighted spectral basis $B^0(\lambda, t, Z(t))$ into a luminosity weighted basis $B(\lambda, t, Z(t))$. The mass weighted basis gives an SSP of unit mass, the luminosity weighted basis gives an SSP of unitary flux. The conversion formula is:

$$B(\lambda, t, Z(t)) = \frac{B^0(\lambda, t, Z)}{\frac{1}{\Delta\lambda}\int_{\lambda_{\rm min}}^{\lambda_{\rm max}} B^0(\lambda, t, Z)\ {\rm d}\lambda}, \tag{2.3}$$

where $\Delta\lambda = \lambda_{\rm max} - \lambda_{\rm min}$ can be chosen depending on the wavelength range of interest.

Instead of mass contributions we deal with light contributions when using B instead of B^0 thus we replace the SFR with a Luminosity Weighted Stellar Age Distribution (hereafter SAD):

$$\Lambda(t) = \frac{{\rm SFR}(t)}{\Delta\lambda}\int_{\lambda_{\rm min}}^{\lambda_{\rm max}} B^0(\lambda, t, Z)\ {\rm d}\lambda, \tag{2.4}$$

where $\Lambda(t)$ gives the contribution to the total light from the stars of age $[t, t + {\rm d}t]$. With this new unit we can define the SED of a galaxy as:

$$F_{\rm rest}(\lambda) = \int_{t_{\rm min}}^{t_{\rm max}} \Lambda(t)\ B(\lambda, t, Z(t))\ {\rm d}t. \tag{2.5}$$

In Eq. 2.5 we must deal in the real case with light extinction and we must also convolve the data with the proper Spectral Broadening Function (BF). The spectral broadening function can depends both on the properties of the physical sources, e.g. the line of sight velocity distribution (LOSVD) of the galaxy considered, and from instrumental properties, i.e. the PSF of the instrument used in the observations.

For the spectroscopic analysis we fit the continuum using a Non Parametric Estimation of the Continuum (NPEC) that takes into account both the reddening due to the dust absorption and potential flux calibration errors (see App. C). The NPEC method allows us to use the information present in the spectral lines without using the continuum of the spectrum. The continuum in spectral fitting does not

play a relevant role, because the information about the unknowns of the problem depends on the line strengths and depth, and not on the underlying continuum (see Ocvirk et al. (2006a) for further details). Eq. 2.5 becomes:

$$F_{\rm rest}(\lambda) = f_{\rm ext}(\mathbf{E}) \int_{t_{\rm min}}^{t_{\rm max}} \Lambda(t)\, B(\lambda, t, Z(t))\, {\rm d}t, \tag{2.6}$$

in which **E** is a vector providing the extinction factors at a finite number of wavelengths, the anchor points (see App. C for more details).

The observed SED is the convolution of the intrinsic spectrum of the galaxy and an unknown broadening function that collects both physical and instrumental effects. The physical effects are due to the velocity dispersion of the stars along the line of sight. If we assume a global line of sight velocity distribution $g(v)$ for the galaxy we can write:

$$\phi(\lambda) = \int_{v_{\rm min}}^{v_{\rm max}} F_{\rm rest}\left(\frac{\lambda}{1 + v/c}\right) g(v)\, \frac{{\rm d}v}{1 + v/c}, \tag{2.7}$$

in which c is the light velocity and $\int_{v_{\rm min}}^{v_{\rm max}} g(v)\, {\rm d}v = 1$. This formula translates into the usual convolution formula:

$$\tilde{\phi}(\lambda) = c \int_{u_{\rm min}}^{u_{\rm max}} \tilde{F}(w - u)\, \tilde{g}(u)\, {\rm d}u, \tag{2.8}$$

with the reparametrization:

- $w \equiv ln(\lambda), \qquad u \equiv ln(1 + v/c),$
- $\tilde{F}(w) \equiv F_{\rm rest}(e^w) = F_{\rm rest}(\lambda), \qquad \tilde{\phi}(w) \equiv \phi(e^w) = \phi(\lambda),$
- $u_{\rm min} = ln(1 + v_{\rm min}/c), \qquad u_{\rm max} = ln(1 + v_{\rm max}/c).$

The instrumental effect is due to the Point Spread Function (PSF) of the instrument. We can account for this effect by convolving the spectrum $\phi(\lambda)$ with a proper function that smoothes the SSP model spectra to the resolution of the instrument:

$$\phi'(\lambda) = \int_{\lambda_{\rm min}}^{\lambda_{\rm max}} \tilde{\phi}(\lambda)\, {\rm PSF}(\lambda_0 - \lambda)\, {\rm d}\lambda, \tag{2.9}$$

in which ${\rm PSF}(\lambda_0 - \lambda)$ is the response of the instrument corrected for the finite resolution of the SSP model spectra.

In the same way we can associate with each spectrum $B(\lambda, t, Z(t))$ a photometric value for a set of band-passes:

$$B_{\rm phot}(b, t, Z(t)) = \frac{\int_{\lambda_{\rm min}}^{\lambda_{\rm max}} B(\lambda, t, Z(t))\ T_b(\lambda)\ \lambda\ {\rm d}\lambda}{\int_{\lambda_{\rm min}}^{\lambda_{\rm max}} T_b(\lambda)\ \lambda\ {\rm d}\lambda}, \tag{2.10}$$

in which b is the chosen band-pass and T_b is the associated transmission curve. Unobscured photometry of a galaxy $F_{\rm phot}(b)$ is given by:

$$F_{\rm phot}(b) = \int_{t_{\rm min}}^{t_{\rm max}} \Lambda(t) B_{\rm phot}(\lambda, t, Z(t)) dt. \tag{2.11}$$

When analyzing photometry we consider an extinction law from the literature that uses the color excess $E = E(B-V)$ to characterize reddening. Assuming a constant continuum for the spectrum inside the considered filter, Eq.2.12 becomes:

$$F_{\rm phot}(b) = f_{\rm ext}(E, \lambda_{\rm eff}) \int_{t_{\rm min}}^{t_{\rm max}} \Lambda(t)\ B_{\rm phot}(\lambda, t, Z(t))\ {\rm d}t, \tag{2.12}$$

in which $\lambda_{\rm eff}$ is the average wavelength:

$$\lambda_{\rm eff} = \frac{\int_{\lambda_{\rm min}}^{\lambda_{\rm max}} \lambda\ T_b(\lambda)\ {\rm d}\lambda}{\int_{\lambda_{\rm min}}^{\lambda_{\rm max}} T_b(\lambda)\ {\rm d}\lambda} \tag{2.13}$$

2.1.2 Inversion

Our goal is to reconstruct the SFR and/or the SAD from an observed SED and a set of associated photometry. In principle solving the integral equations defined in this section should give us the solution. In reality the solution is not well defined because of noise in the data, errors in the SSPs models, and fundamental issues as the age-metallicity degeneracy (the energy distribution of old stellar populations can be reproduced approximatively by younger populations that are more metal rich).

If the SSPs are inadequate, no acceptable solution is found. More frequently, solutions that are compatible with the data exist, but they are not univocally determined: a set of acceptable solutions is associated with a galaxy SED. Eq. 2.9 and 2.12 are solved using two different approaches:

- A non parametric method that uses Bayesian principles for a statistical analysis. The goodness of fit is estimated with a priori information on some

principles of the solution. We use the same formalism as STECKMAP (Ocvirk et al. 2006b), a method that performs a maximum a posteriori (MAP) estimation of the solutions. We extend this method to perform a combined analysis of spectral and photometric data.

- A parametric method in which we explore sets of possible solutions described by one free parameter. We then find the most probable solution by minimizing the corresponding χ^2 function.

The non parametric method has the advantage of providing star formation history and metallicity evolution of the galaxy with minimal constraints on their shape. On the other hand, the *a priori* of the problem prevents functional forms with large gradients, as it is expected for a ram pressure stripping event. For this reason we introduce a parametric method, that uses a set of analytical star formation histories with minimal assumptions. The parametric method refines the results obtained independently with the non parametric method. In the next sections we explain extensively the two methods.

2.2 Non parametric method

The non parametric method is described in detail in Ocvirk et al. (2006a) and Ocvirk et al. (2006b). Here we extend it to deal with photometry.

2.2.1 Discretizing the basic problem

We proceed to a discretization of the Eq. 2.5 by defining two sets of gate functions:

- $g_i : [\lambda_{\rm min}, \lambda_{\rm max}] \rightarrow \mathbb{R} \qquad i = 1, 2, ...m,$
- $h_j : [t_{\rm min}, t_{\rm max}] \rightarrow \mathbb{R} \qquad j = 1, 2, ...n,$

that sample the wavelengths and the ages. The sets g_i and h_j are two orthonormal bases. If we define the canonical scalar product $\left(\langle f(k), g(k)\rangle = \int f(k)g(k)dk\right)$. We can write:

- $\Lambda(t) \approx \sum_{j=1}^{n} x_j h_j(t), \qquad$ with $\qquad x_j = \int \Lambda(t)\, h_j(t)\, {\rm d}t = \langle \Lambda(t) \rangle_{t \in \Delta_j},$
- $F_{\rm rest}(\lambda) \approx \sum_{i=1}^{m} s_i g_i(\lambda), \qquad$ with $\qquad s_i = \int F_{\rm rest}(\lambda)\, g_i(\lambda)\, {\rm d}\lambda = \langle F_{\rm rest}(\lambda) \rangle_{\lambda \in \Delta_i},$

Eq. 2.5 can be approximated by:

$$s_i \approx B_{i,j} x_j, \tag{2.14}$$

in which:

$$B_{i,j} = \langle B(\lambda, t, Z(t))\rangle_{\lambda\in\Delta\lambda_i, t\in\Delta t_j} \simeq \langle B(\lambda, t, Z_j)\rangle \qquad \text{with} \qquad Z_j = \langle Z(t)\rangle_{t\in\Delta t_j}, \quad (2.15)$$

is some kind of weighted averaging in the interval considered.

In matrix form:

$$\mathbf{y}_{\rm rest} = \mathbf{B}(\mathbf{Z}) \cdot \mathbf{x}, \qquad \text{with} \qquad \mathbf{y}_{\rm rest} = s_1, s_2, ...s_m. \quad (2.16)$$

Note that B is not a linear function of Z. In addition the star formation history summarized in $\mathbf{x}$ must take positive values only. This is implemented by writing $\mathbf{x}$ as the square of a vector $\mathbf{x}'$, where $\mathbf{x}'$ has no positivity requirement. The expression 2.16 is a non linear function of $\mathbf{x}'$.

2.2.2 Discretization of the broadening function

The same methodology is applied when we consider the convolution of the SED with the broadening function BF. This is detailed below in the case of a line of sight velocity distribution. We discretize the problem by defining an evenly spaced grid:

$$u_j = u_{\rm min} + (j - \frac{1}{2})\delta u; \qquad j = 1, 2, ...p, \quad (2.17)$$

spanning $[u_{\rm min}, u_{\rm max}]$, i.e. the velocity space, with constant step $\delta u \equiv (u_{\rm max} - u_{\rm min}/p)$. Eq. 2.7 becomes:

$$\phi(w_i) = \frac{1}{\delta u} \sum_{j=1}^{j=p} \int_{u_{\rm min}}^{u_{\rm max}} F_{\rm rest}(w-u)\, g_j\, \theta\Big(\frac{u-u_j}{\delta u}\Big)\, {\rm d}u \simeq \sum_{j=1}^{j=p} g_j B(w_i - u_j), \quad (2.18)$$

where to each $\{w_j; j = 1, 2....m\}$ corresponds $\phi(w) = [\phi_1, ..., \phi_m]$, a set of logarithmic wavelengths spanning the spectral range with a constant step. In matrix notation we have an extension of Eq. 2.16:

$$\mathbf{y} = \mathbf{K}(\mathbf{y}_{\rm rest}) \cdot \mathbf{g}, \quad (2.19)$$

where this time $\mathbf{y} = (\phi'_1, \phi'_2....., \phi'_m)^\top$ is the product of the convolution of the SED with the spectral broadening function, $\mathbf{g} = (g_1, g_2, ...g_p)^\top$ is the discretized velocity

distribution and $\mathbf{K} = K_{i,j} = F_{\rm rest}(w_i - u_j)$ is a set of spectral models, defined in the vectorial space of wavelength $\times$ velocity.

The convolution theorem (Press 2002) yields an equivalent form of the model spectrum $\mathbf{s} = \mathbf{K} \cdot \mathbf{g}$, which reduces computation times:

$$\mathbf{s} = \mathcal{F}^{-1} \cdot diag(\mathcal{F} \cdot \mathbf{K}) \cdot \mathcal{F} \cdot \mathbf{g}, \tag{2.20}$$

in which $\mathcal{F}$, is the discrete Fourier operator defined in Press (2002) as:

$$\mathcal{F}_{ij} = exp\left(\frac{2i\pi}{m}(i-1)(j-1)\right) \qquad \forall (i,j) \in [1,2,.....m]^2, \tag{2.21}$$

$$\mathcal{F}^{-1} = \frac{1}{m}\mathcal{F}^{*}. \tag{2.22}$$

2.2.3 Application to physical problems

In the observations $\mathbf{y}$ in Eq. 2.19 is contaminated by noise. For this reason we add to the matrix defined in Eq. 2.19 a term:

$$\mathbf{y} = \mathbf{K}(\mathbf{y}_{\rm rest}) \cdot \mathbf{g} + \mathbf{e}. \tag{2.23}$$

In Eq. 2.23 the vector $\mathbf{e} = (e_1, e_2, ...e_m)^{\top}$ takes into account modeling errors and noise in the data. In order to solve this problem the inversion methods perform different tests to recover the best fit solution. The estimation of the best fit is performed using a likelihood method. This same formalism is also valid for the integral equation defined in Eq. 2.12 for the photometry.

Moreover, in Ocvirk et al. (2006a) it is argued that this set of equations is ill posed, i.e. small perturbations of the data, both $F_{\rm rest}(\lambda)$ and $B^0(\lambda, t, Z(t))$, can cause large perturbations in the solutions. In the next section we explain in which way we overcome this problem.

2.2.4 Regularization : Maximum a Posteriori method

Bayes' theorem relates the conditional and marginal probability of stochastic events. We can define a vector $\mathbf{X} = [\mathbf{x}, \mathbf{Z}, \mathbf{E}, E(B-V), \mathbf{g}]$ that collects all the

unknowns that the method determines and deal with it in the rest of the thesis. Applied to $\mathbf{y} = \phi'_1, \phi'_2 ....., \phi'_m$ the theorem states:

$$f_{\text{post}}(\mathbf{X} \mid \mathbf{y}) \propto f_{\text{data}}(\mathbf{y} \mid \mathbf{X}) f_{\text{prior}}(\mathbf{X}), \tag{2.24}$$

where:

- $f_{\text{post}}(\mathbf{X} \mid \mathbf{y})$ is the conditional probability of $\mathbf{X}$ given $\mathbf{y}$.
- $f_{\text{prior}}(\mathbf{X})$ is the prior probability or marginal probability. It does not take into account any information about the the data $\mathbf{y}$ and represents a prior hypothesis on the solutions-space.
- $f_{\text{data}}(\mathbf{y} \mid \mathbf{X})$ is the probability of $\mathbf{y}$ given $\mathbf{X}$.

The value of $\mathbf{X}$ that maximizes $f_{\text{post}}(\mathbf{X} \mid \mathbf{y})$, according to the statement of Bayes' theorem, represents the most adequate solution assuming the $f_{\text{prior}}(\mathbf{X})$ hypotheses for the solutions.

If we assume a Gaussian noise as source of errors in the observations, we have:

$$f_{\text{data}}(\mathbf{y} \mid \mathbf{X}) \propto exp[-\frac{1}{2} \chi^2(\mathbf{y} \mid \mathbf{X})], \tag{2.25}$$

in which:

$$\chi^2(\mathbf{y} \mid \mathbf{X}) = [\mathbf{y} - \mathbf{s}(\mathbf{X})]^\top \cdot \mathbf{W} \cdot [\mathbf{y} - \mathbf{s}(\mathbf{X})], \tag{2.26}$$

where $\mathbf{W} = \text{Cov}(\mathbf{e})^{-1}$ is the weight matrix, equal to the inverse of the covariance matrix of the noise. Maximizing $f_{\text{post}}(\mathbf{X} \mid \mathbf{y})$ is equivalent to minimizing:

$$Q(\mathbf{X}) = \chi^2(\mathbf{y} \mid \mathbf{X}) - 2log[f_{\text{prior}}(\mathbf{X})]. \tag{2.27}$$

If we have no information about the probability distribution of the parameters $\mathbf{X}$, we can suppose that f_{prior} is uniformly distributed, then in the minimization this term can be dropped. However we are then left with the initial ill-posed problem. To overcome this problem we hypothesize, as an *a priori* of the problem, that solutions are smooth and we introduce in $Q(\mathbf{X})$ a penalty function:

$$Q(\mathbf{X}) = \chi^2(\mathbf{y} \mid \mathbf{X}) + \mu P(\mathbf{X}). \tag{2.28}$$

In Eq. 2.28 $P(\mathbf{X})$ smoothes the solutions by taking large values when the unknowns are very irregular functions of time or too chaotic. The adjustable coefficient μ fixes the weight of the penalization in the total estimation. In appendix B there is an extended analysis of the $Q(\mathbf{X})$ function with the analytical expressions of its gradients, that are used for the minimization.

The unknowns of our problem are the star formation history, the metallicity evolution, the spectral broadening function and the prescription for extinction, i.e. the NPEC vector for the spectral analysis and the reddening value for the photometric analysis.

In this way the total Q-function to be minimized is:

$$Q(\mathbf{X}) = (1-\alpha)\cdot\chi^2_{\rm spec}(\mathbf{X}) + \alpha\cdot\chi^2_{\rm phot}(\mathbf{X}) + \mu\cdot P(\mathbf{X}). \tag{2.29}$$

The minimization is obtained using the OPTIMPACK driver (Thiebaut, 2002). In particular we use the *Yorick* implementation of the algorithm VMLM-B (Variable Metric method with Limited Memory requirements and Boundary constraints on the parameters).

In the total Q-function each term represents:

- **Spectral analysis**

$$\chi^2_{\rm spec}(\mathbf{X}) = \frac{1}{N_\lambda}\sum_{i=1}^{N_\lambda}\frac{(F_{\rm mdlspec}(\lambda) - F_{\rm spec}(\lambda))^2}{\sigma^2_{\rm spec}}, \tag{2.30}$$

  is the χ^2 associated with the spectra. $F_{\rm mdlspec}(\lambda)$ is the model spectrum built from a defined $\mathbf{X}$ and $F_{\rm spec}(\lambda)$ is the observed spectrum. $\sigma^2_{\rm spec}$ is the error associated with the observations and N_λ is the number of points in the spectrum. In this case $N_\lambda \sim 10^3$ and we can consider this value approximately equal to the number of degrees of freedom of the problem.

- **Photometric analysis**

$$\chi^2_{\rm phot}(\mathbf{X}) = \frac{1}{N_b}\sum_{i=1}^{N_b}\frac{(F_{\rm mdlphot}(b) - F_{\rm phot}(b))^2}{\sigma^2_{\rm phot}}, \tag{2.31}$$

  is the χ^2 associated to the photometry. $F_{\rm mdlphot}(b)$ represents the photometric model obtained from the defined $\mathbf{X}$, $F_{\rm phot}(b)$ are the photometric data, $\sigma^2_{\rm phot}$ the errors in the measures and N_b are the number of band-passes used.

- **Penalty function**

  $\mu P(\mathbf{X})$ is the penalty function necessary to regularize the problem. We define for $P(\mathbf{X})$ a quadratic function:

$$P(\mathbf{X}) = \mathbf{X}^\top \cdot \mathbf{L}^\top \cdot \mathbf{L} \cdot \mathbf{X}, \tag{2.32}$$

  with derivative:

$$\frac{\partial P}{\partial \mathbf{X}} = 2\mathbf{L}^\top \cdot \mathbf{L} \cdot \mathbf{X}. \tag{2.33}$$

  The term $\mathbf{L}$ is a matrix (called *kernel*) that may correspond to different differential operators:

  - $\mathbf{L} = \mathbf{D}_1$ where $\mathbf{D}_1 \equiv diag[-1, 1]$.

    $\mathbf{L}$ calculates the first derivative and the penalization smoothes only the gradient of the solution. The penalization in this case assumes large values when the solution is an irregular function of time.

  - $\mathbf{L} = \mathbf{D}_2$ where $\mathbf{D}_2 \equiv diag[-1, 2, -1]$.

    The operator $\mathbf{D}_2$ computes the Laplacian of $\mathbf{X}$, as defined in Pichon et al. (2002). The penalization smoothes the second derivative, preventing then large curvature in the solution.

  We regularize the solution by penalizing the second derivative for the star formation and the first derivative for the metallicity evolution.

  To ensure solutions in the range of metallicities available in the SSPs we introduce a binding function $c(\mathbf{Z})$:

$$c(Z) = \begin{cases} (Z - Z_{\min})^2 & \text{if } Z \leq Z_{\min}\,, \\ (Z - Z_{\max})^2 & \text{if } Z \geq Z_{\max}\,, \\ 0 & \text{otherwise} \end{cases} \tag{2.34}$$

  with gradient:

$$\left(\frac{\partial C}{\partial \mathbf{Z}}\right)_j = \begin{cases} 2\,(Z_j - Z_{\min}) & \text{for } Z_j < Z_{\min}\,, \\ 2\,(Z_j - Z_{\max}) & \text{for } Z_j > Z_{\max}\,, \\ 0 & \text{otherwise}\,. \end{cases} \tag{2.35}$$

  This function assumes high values only outside the boundary $[Z_{\min}, Z_{\max}]$ and is zero-valued otherwise. We can write explicitly the term that collects all the

penalties terms:

$$\mu \cdot P_{\rm tot}(\mathbf{X}) = \mu_x P(\mathbf{x}) + \mu_Z P(\mathbf{Z}) + \mu_C C(\mathbf{Z}) + \mu_g P(\mathbf{g}). \tag{2.36}$$

- In eq. 2.29 α determines the weight of the photometric and spectroscopic constraints.

2.3 Parametric method

In the parametric analysis we fix a star formation history and we create a time-dependent set of associated spectra. We cut the star formation at a fixed age to simulate the ram pressure stripping episode and we study the passive evolution of the stellar populations since the truncation.

In practice, we considered exponentially decreasing star formation rates (SFR):

$$\mathrm{SFR}(t) = A \cdot e^{-t/\tau}, \tag{2.37}$$

in which A is a constant (the initial SFR) and τ is a characteristic timescale that controls the flexure of the curve. We cut the SFR after 13.5 Gyr, and we built a set of spectra following the passive evolution of the stellar populations afterwards. Similarly we created a set of photometric values extracted from the same set of spectra.

We compare the set of spectra obtained analytically with the observations. We set the initial parameters that create the family of spectra directly from the results of non parametric inversion method. We define the variable $\Delta t = t_{\rm trunc} - t_{\rm now}$, i.e. the difference between the time at which occurred the truncation and the present time, and using a χ^2 function as best fit estimator we study the fit as a function of Δt. The goal of the parametric method is to find the Δt that minimizes the χ^2 function. This corresponds to the stripping age.

The total χ^2 is similar to the one defined in the Eq. 2.29:

$$\chi^2_{\rm tot}(\mathbf{X}) = (1-\alpha) \cdot \chi^2_{\rm spec}(\mathbf{X}) + \alpha \cdot \chi^2_{\rm phot}(\mathbf{X}), \tag{2.38}$$

with the difference that $\mathbf{X}$ represents here the star formation rate and the extinction prescription only. The star formation history, the metallicity evolution and the BF

are fixed from the non parametric results. For each stripping age in the minimization of $\chi^2_{\rm tot}$ the only unknowns are the NPEC vector **E** for the spectroscopic analysis and the color excess $E(B-V)$ for the photometric analysis.

2.4 Summary

In this chapter:

- we defined an integral equation associated with the spectral energy distribution of a galaxy (Eq. 2.6);
- we discretized the spectral energy distribution and we transformed it into an equivalent set of equations (Eq. 2.19);
- using Bayesian methods the solution for the star formation history, the metallicity evolution, the spectral broadening function and the continuum correction is recovered since the minimization of a function (Eq. 2.29) that contains the usual χ^2 as best fit estimator. We circumvent the problem of ill conditioning using a penalty function that imposes the smoothness of the solutions (Eq. 2.36);
- we developed a parametric method that more specifically addresses the problem of stripping age determination. The parametric method use assumptions in agreement with the results obtained from the non parametric method;

Chapter 3

Testing the non parametric method with artificial data

In Ocvirk et al. (2006a) the non parametric method has been tested for a set of artificial spectra, with a resolution $R = 10000$ and a signal to noise ratio $S/N = 100$ per pixel. As we will see in detail in Chapt. 4, in our case we want to apply the method to spectra with an intermediate resolution $R \sim 800$. Moreover, we extend the work of Ocvirk et al. (2006a) to deal with photometric data, and this new tool has not been tested yet. For these reasons in this chapter we will proceed to an investigation of the non parametric method through appropriate mock models.

The unknowns of our problem are the star formation history, the metallicity evolution, the non parametric estimation of the continuum, the parameter characterizing the dust extinction, and the spectral broadening function.

In Eq. 2.29 the smoothing functions $P(\mathbf{X})$ regularize the problem, and the weight in the final estimation of each penalty is set by the coefficients μ (Eq. 2.36).

Setting the weight coefficients is not a trivial point, since there is no automatic method to fix them. At the same time an optimal weighting between the likelihood and the priors of the methods is crucial in order to obtain reliable solutions. In the case of linear problems, a method widely used is the *Generalized cross validation* (GCV, Wahba 1990). In GCV we define a function GCV(μ) that involves the spectral basis and the data, depending on a parameter μ. The value of μ that minimizes the GCV function corresponds to the weight coefficient that gives the best solution.

This method, conceived for the linear problems, provides only an useful starting point for μ_x, for our non linear problem that not necessarily gives the best solution. This is because non linear problems have a solutions space more complex than the linear one.

The better way to proceed is to create artificial data and then to perform a

campaign of inversions in which the weight coefficients vary around a range of values centered on the GCV results.

According to the value of the weight coefficient we can identify different regimes. If the problem is under-smoothed, i.e. the value of μ is too low, the solutions will show fluctuations and irregularities that we can easily classified as artifacts. If the problem is over-smoothed, i.e. we use high μ, the solutions will be excessively flat. The range of acceptable μ is between these two regimes, and needs extensive campaigns to be fixed empirically (Craig & Brown, 1986).

Since in Eq. 2.36 the weight coefficient μ_C confines the metallicity solution in the range of metallicities allowed by the spectral basis, its value determination does not need any test. We will fix for it high values, $\mu_C = 10^8$, preventing radically any solution inconsistent with the input spectral basis.

The weight coefficient μ_g control the flatness of the spectral broadening function. It does not need high values, because the spectral broadening function is expected to show a bell-like, with a peak velocity equal to the rotation velocity of the galaxy at the observed radius. In this case the penalization $\mu_g \cdot P(\mathbf{g})$ prevents possible wavy structures in regions far from the velocity-peak and does not need high values to give acceptable solutions. After extensive tests we fix $\mu_g = 10^{-2}$.

The weight coefficients crucial in final results are then μ_x and μ_Z, that regularize the star formation and the metallicity, respectively.

In this chapter we investigate the results of the non parametric method for different configurations, using artificial data. With these pseudo-data we want to explore the space of the solutions in the μ_x - μ_Z plane.

The chapter is structured as follows: in Section 3.1 we present the models used to build the artificial data. In Section 3.2 and 3.3 we investigate the influence of the initial condition and the penalization in spectral and photometric inversion, respectively. In Section 3.4 we will show he results obtained for the joint analysis, and in Section 3.5 we address the problem of the stripping age determination for a model with truncated star formation.

3.1 Semi analytical models

We choose two different semi-analytical models of Boissier & Prantzos (2000). The selected models reproduce the chemical and spectrophotometric evolution of a spiral galaxy at different radii using simple 'scaling laws', and are calibrated on the Milky Way. The models study the evolution of spirals simulating the disk as

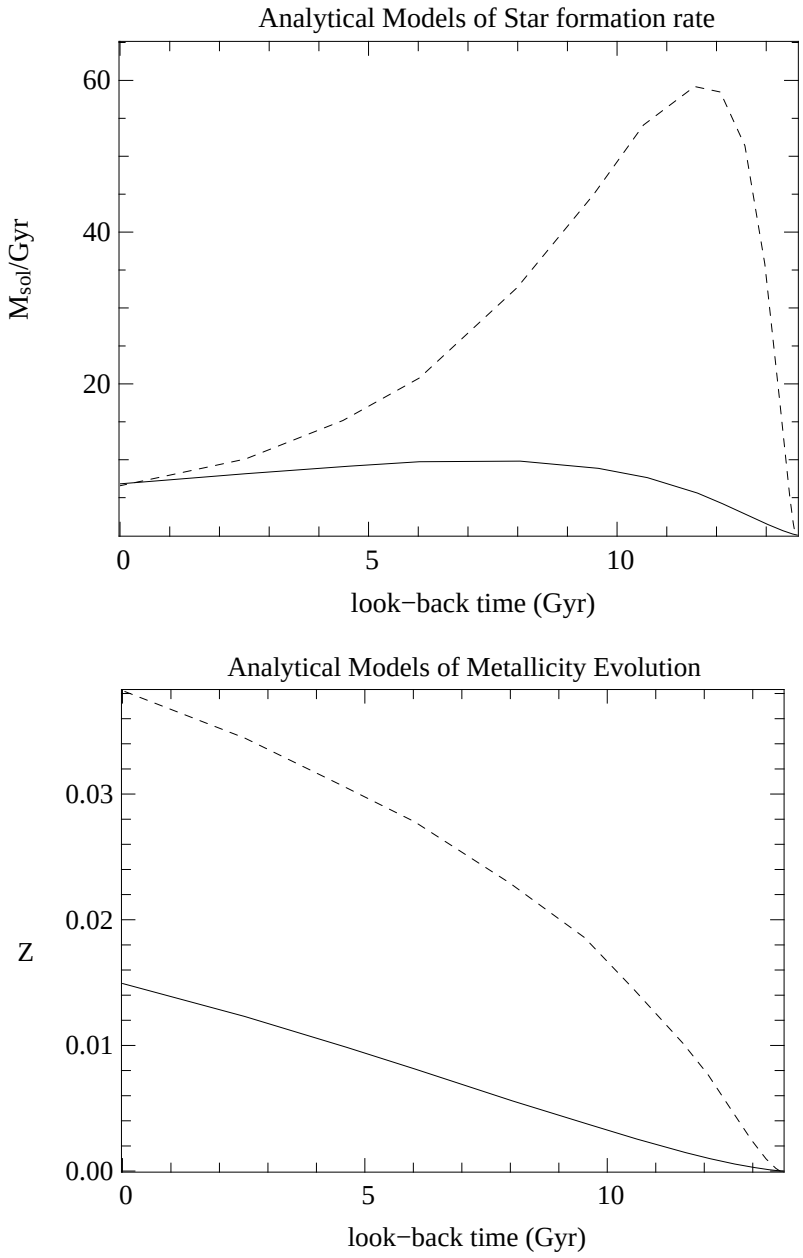

Figure 3.1: Local star formation history (top panel) and metallicity evolution (bottom panel) of the two semi-analytical models of Boissier & Prantzos (2000) at a radius R = 4.5 kpc. The dashed and solid line represents SAM1 (λ = 0.03, V_C = 230 km/s) and SAM2 (λ = 0.06, V_C = 190 km/s), respectively.

independent concentric rings. This approach allows to reproduce the star formation and the metallicity evolution of the galaxy at a defined radius.

In our case we choose to study the star formation history and metallicity evolution at a radius R = 4.5 kpc from the center of the disk. We chose this radius to match the observations detailed in Chapt. 4. The models of Boissier & Prantzos

(2000) are characterized by two parameters, λ and V_C. The spin parameter λ (Mo et al. 1998) is related to the halo mass and its angular momentum J. High λ correspond to large disks and small λ correspond to compact smaller disks. As a reference value we can take the Milky Way, for which $\lambda = 0.03$. The maximum circular velocity V_C is related to the mass of the halo that formed the disk, i.e. $M \propto V_C^3$. As a reference value we take the Milky Way galaxy, for which $V_C = 220$ km/s (Boissier & Prantzos, 2000).

The first model is built using $\lambda = 0.03$ and $V_C = 230$ km/s. It represents a galaxy similar to the Milky Way, in which the local star formation has a huge peak after 2 Gyr (dashed line in top panel of Fig. 3.1). After the peak the profile decreases exponentially with characteristic timescale $\tau = 6$ - 8 Gyr (Eq. 2.37). To this model is associated a metallicity evolution that increases rapidly with time. The metallicity is sub-solar only in the first 4 Gyr of galaxy's life (dashed line in bottom panel of Fig. 3.1) and reaches values above $Z = 0.03$ in the last 5 Gyr. From now on we refer to this model as SAM1.

The second model has a $\lambda = 0.06$ and $V_C = 190$ km/s and describes a spiral galaxy less compact and less massive than the Milky Way. The star formation rate increases slowly for the first 4 Gyr, and then evolves with an approximatively constant star formation rate until now (solid line in top panel of Fig. 3.1). The associated metallicity increases slowly until Z = 0.015 and is always sub-solar (solid line in bottom panel of Fig. 3.1). We refer to this model as SAM2.

The 2 semi-analytical models chosen represent different spiral galaxies (see Fig. 3.1). This choice is made to test the pertinence of the method for a variety of spiral galaxies.

Using the star formation rate and metallicity evolution of the models, we build, using Eq. 2.6, two spectra at a wavelength range $\lambda\lambda$ = [3330 - 6360] Å. We chose the spectral library of Bruzual & Charlot (2003), with an average resolution $R \sim 2000$ at optical wavelengths. To deal with light extinction we apply the Calzetti (2001) law (see App. D). We reddened the artificial spectra with $E(B-V)_{\rm gas} = 0.5$ and we added a gaussian noise that gives $S/N = 50$. The optical wavelength and the signal to noise ratio are chosen to match the observations (see Chapt. 4).

We use for the inversion a flux-normalized basis (Eq. 2.3), in which each spectrum has a unitary flux. To be consistent with this formalism, we normalize the input spectrum and the spectral broadening function in order to have unitary mean and we impose to the non parametric estimation of the continuum an unitary average value. In the same way in photometric inversion we reddened the model

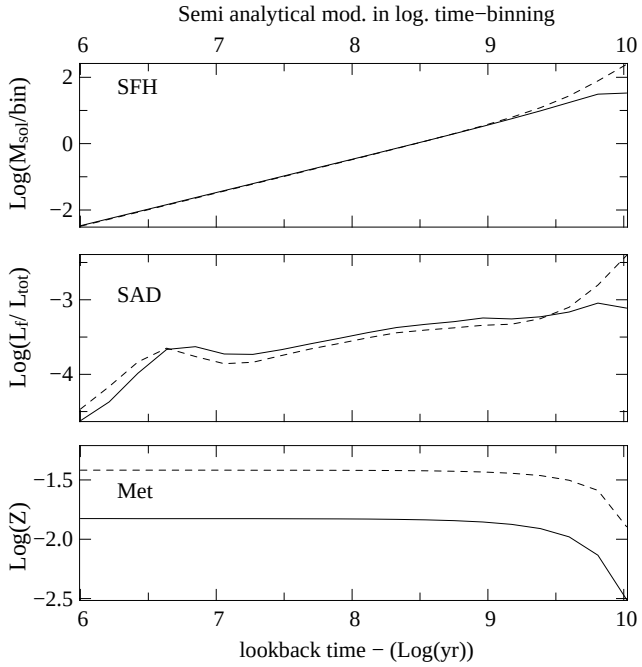

Figure 3.2: Local star formation history (top panel), luminosity weighted stellar age distribution (middle panel) and metallicity evolution (bottom panel) of the two semi-analytical models of Boissier & Prantzos (2000) shown in Fig. 3.1 at a radius R = 4.5 kpc and using a logarithmical time-binning. The dashed and solid line represents SAM1 (λ = 0.03, V_C = 230 km/s) and SAM2 (λ = 0.06, V_C = 190 km/s), respectively.

spectrum using an extinction law normalized to have a unitary mean.

The stellar populations in which we are interested are the younger populations at lookback times $t < 1$ Gyr. Ram pressure stripping occurs in fact when the galaxies transit the central regions of the cluster, for a few Myr. For this reason we chose a logarithmical time binning with higher resolution in time at young ages. Before starting the inversion we proceed to the new age-binning integrating over the selected age-intervals and we convert the star formation rate (mass per unit time) in star formation history (mass per time-bin). Then we convert the star formation history in luminosity weighted stellar age distribution (luminosity fraction per time-bin) dividing the star formation history for a time-binned mass to light ratio. The results of this conversion are shown in Fig. 3.2.

The shape of the star formation history and the luminosity weighted stellar age distribution are quite similar, except at lookback time $t \sim 10^7$ Myr. This is due to the uncertainties of the SSP models at these ages. If we look at the M/L ratio versus lookback time (Fig. 3.3) we can see that for different metallicities the M/L ratio increases at lookback times $t \leq 10^7$ Myr. Dividing the star formation history for the M/L ratio we have then a decreases in luminosity weighted stellar

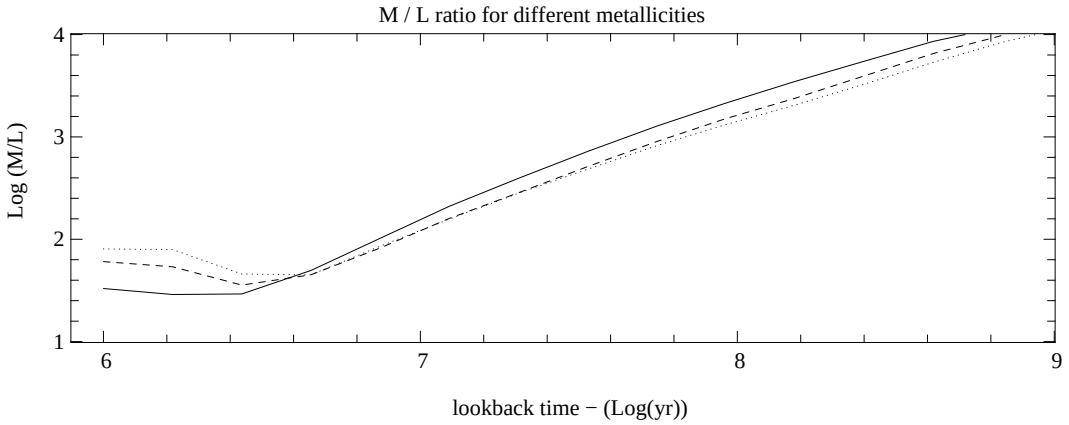

Figure 3.3: M/L ratio versus lookback time for Bruzual & Charlot (2003) SSP basis at $Z = 0.05$ (solid line), $Z = 0.08$ (dashed line) and $Z = 0.004$ (dotted line).

age distribution. We will see that this uncertainties affect the solutions, showing systematically disagreement with the model at these lookback times.

The stability of the results is tested with Monte Carlo simulations. Iteratively we add to the input spectrum a gaussian noise and we perform ten inversions. The error bars are given by the root mean square of the obtained results.

3.2 Testing the spectral inversion with artificial data

3.2.1 Weight of penalization

In this section we investigate how the variations of μ_x, μ_Z affect the results of the spectral inversion, i.e. $\alpha = 0$ in Eq. 2.29.

The functions $P(\mathbf{x})$ and $P(\mathbf{Z})$ in Eq. 2.36 regularize the solutions, i.e. they assume large values when the star formation history and metallicity evolution are irregular functions of time, and negligible values when the solutions are sufficiently smooth. The penalization values are ultimately multiplied with the coefficients μ_x and μ_Z, that fix their weight in the final result.

In the total Q-function (Eq. 2.29) the component $\mu \cdot P(\mathbf{X})$ must be smaller than the χ^2 component, otherwise the penalization dominates the solution. Proper values for the component $\mu_x \cdot P(\mathbf{x})$ and $\mu_Z \cdot P(\mathbf{Z})$ are of the order of 10^{-1}-10^{-3}, at least ten times lower than the χ^2 component (that for normalized distribution $\chi^2 \approx 1$).

As an example, in Fig. 3.4 are shown two spectral inversions realized with $\mu_Z = 10^2$ and $\mu_x = 10^2$, $\mu_x = 10^{-2}$. For the left panel of Fig. 3.4 (inversion with $\mu_x = 10^2$ and $\mu_Z = 10^2$), the χ^2 minimum is $\chi^2_{\rm spec} = 1.01$, and the results

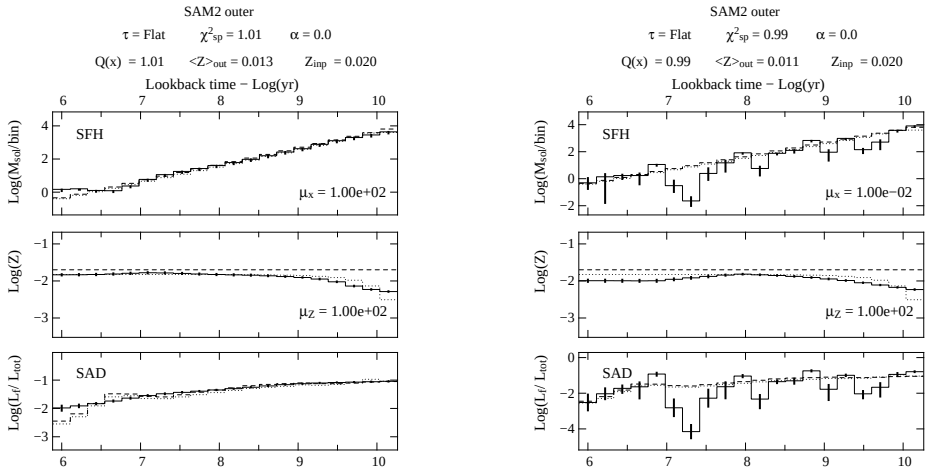

Figure 3.4: Results for non parametric inversion of a synthetic spectrum corresponding to the galaxy model SAM2 for $\mu_Z = 10^2$, and $\mu_x = 10^2$ (left panel) and $\mu_x = 10^{-2}$ (right panel). In each figure the top, middle and bottom panels represent the star formation history in solar masses per time-bin, the metallicity evolution and the luminosity weighted stellar age distribution as a function of lookback time, respectively. In each panel the dotted line shows the input model and the dashed lines the initial guess. The solid lines shows the results of the inversion with associated error bars, estimated calculating the root mean square of 10 Monte Carlo simulations. Above the panels are marked the τ used (see Eq. 2.37) as initial guess for the star formation history, the χ^2 and the weight parameter α in Eq. 2.29, the time-bin averaged metallicity $\langle Z \rangle_{\rm out}$ and the constant value of metallicity $Z_{\rm inp}$ used for the initial guess. In right bottom of top and middle panels of each figure are marked the value of penalization μ_x, μ_Z (see Eq. 2.36).

are in agreement with the input model. This confirms the proper convergence of the procedure towards the absolute minimum. The value of the penalty function associated to the star formation history, before the last iteration is $P(\mathbf{x}) = 5.7 \cdot 10^{-5}$ and $\mu_x \cdot P(\mathbf{x}) \sim 0.006$.

The inversion with $\mu_x = 10^{-2}$ and $\mu_Z = 10^2$ gives different results (right panel of Fig. 3.4). The penalization under-smoothes the solution and the resulting star formation is irregular. For this case $P(\mathbf{x}) = 0.42$ and $\mu_x \cdot P(\mathbf{x}) \sim 0.0042$. The high value of the penalty $P(\mathbf{x})$ is consistent with the irregularities of the solution, and the $\chi^2 = 0.99$ confirms the proper convergence of the minimization towards the absolute minimum. This is an example of a μ_x value that is not acceptable, because the solution is in disagreement with the input model, and the weight coefficient does not smooth sufficiently the solution. We stress here that the value of $\mu \cdot P(\mathbf{X})$ in Eq. 2.28 is negligible compared to χ^2 once the minimization has converged to a solution.

Since an empirical fine tuning of the weight coefficients is necessary, the better

way to proceed is to investigate the influence of μ_x, μ_Z, through a campaign of inversions. In the next sections we will show some of the results of this campaign together with an investigation of the influence of the chosen initial guess on the results. In App. E we show the complete set of penalties explored. A first set of values presented here is $[\mu_x, \mu_Z] = [10^{-1}, 10^{-1}]$, $[10^{-1}, 10^{2}]$, and $[10^{-1}, 10^{4}]$ (Fig. 3.5). The second set of values is $[\mu_x, \mu_Z] = [10^{1}, 10^{-1}]$, $[10^{1}, 10^{2}]$, and $[10^{1}, 10^{4}]$ (Fig. 3.6). A third set of values is $[\mu_x, \mu_Z] = [10^{2}, 10^{-1}]$, $[10^{2}, 10^{2}]$, $[10^{2}, 10^{3}]$, and $[10^{2}, 10^{4}]$ (Fig. 3.7).

We performed this campaign of inversion for model SAM2 using a flat star formation history and a constant metallicity evolution ($Z = 0.02$) as initial condition of the problem.

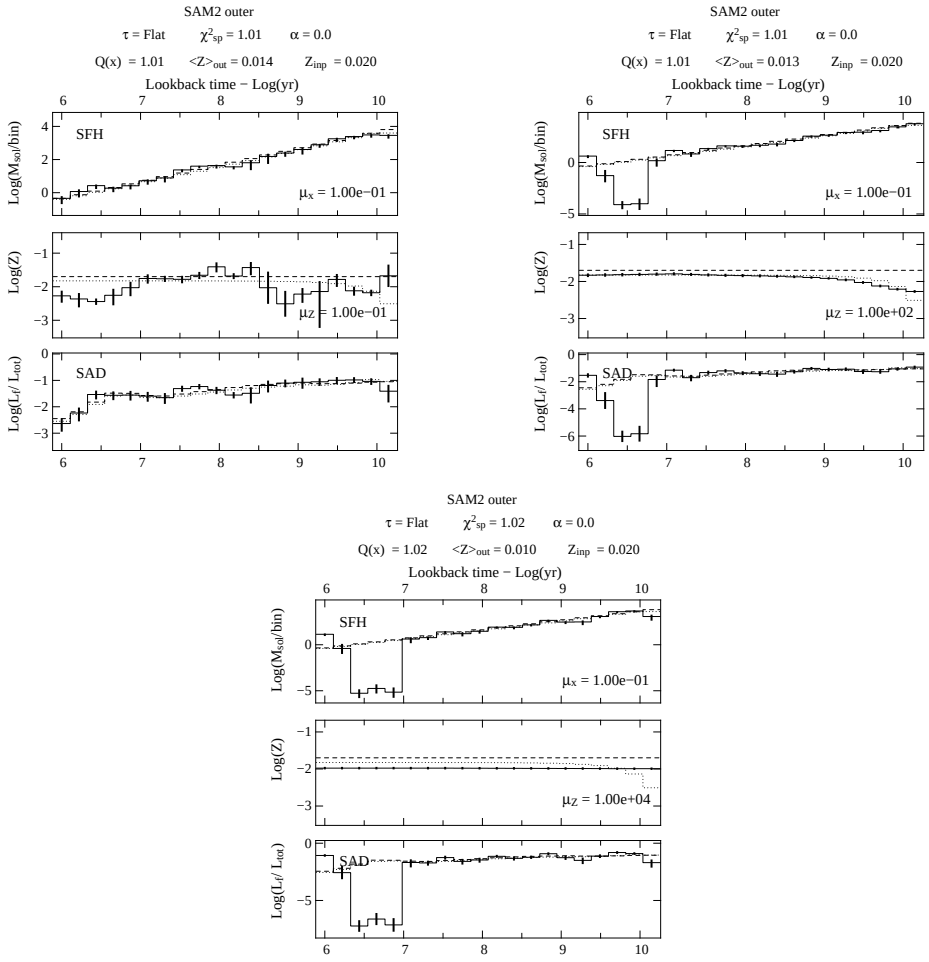

Figure 3.5: Results for non parametric inversion of a synthetic spectrum corresponding to the galaxy model SAM2 for $[\mu_x, \mu_Z] = [10^{-1}, 10^{-1}]$ (left panel), $[\mu_x, \mu_Z] = [10^{-1}, 10^{2}]$ (right panel) and $[\mu_x, \mu_Z] = [10^{-1}, 10^{4}]$ (bottom panel). For a detailed description see Fig. 3.4.

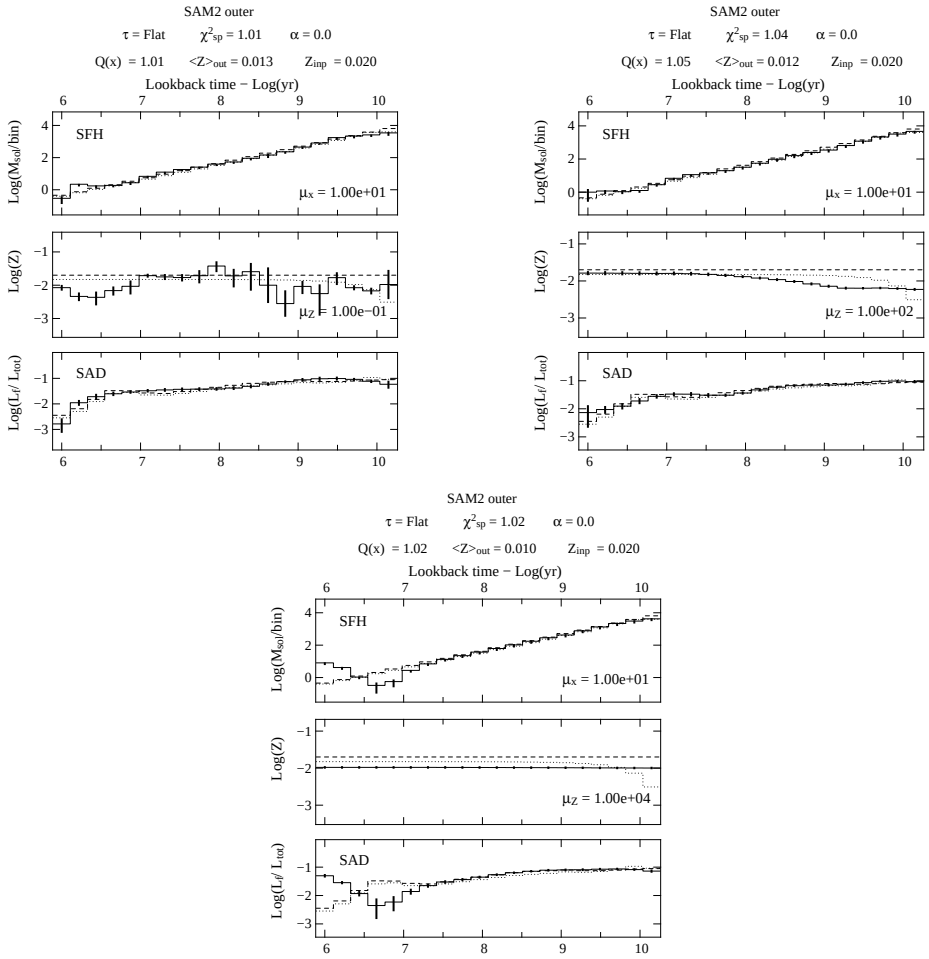

Figure 3.6: Results for non parametric inversion of a synthetic spectrum corresponding to the galaxy model SAM2 for $[\mu_x, \mu_Z] = [10^1, 10^{-1}]$ (left panel), $[\mu_x, \mu_Z] = [10^1, 10^2]$ (right panel) and $[\mu_x, \mu_Z] = [10^1, 10^4]$ (bottom panel). For a detailed description see Fig. 3.4.

Star formation penalty (μ_x)

In Eq. 2.36 the factor $\mu_x \cdot P(\mathbf{x})$ smoothes the star formation preventing large curvature in the solution. Lower μ_x gives larger fluctuations, and this is confirmed in Fig. 3.5. The solutions with lower star formation penalty, $\mu_x = 10^{-1}$ and $\mu_Z > 10^{-1}$, show fluctuations at lookback times of $t \leq 10$ Myr, in disagreement with the input model.

The acceptable fluctuations around the minimum $\chi^2 = 1$, due to the noise in the data, are inversely proportional to the square root of the number of degrees of freedom of the problem (standard property of a χ^2 distribution). In our case the tolerance level is ~ 0.02. Acceptable solutions are found for $[\mu_x, \mu_Z] = [10^{-1}, 10^{-1}]$, $[10^{-1}, 10^2]$, $[10^{-1}, 10^4]$, $[10^1, 10^{-1}]$, $[10^1, 10^4]$, $[10^2, 10^2]$, and $[10^2, 10^4]$. We conclude that for a constant metallicity the solutions for all μ_x are acceptable. From Fig. 3.5 and 3.6 we determine two different regimes of solutions: for $\mu_x = 10^{-1}$

the recovered star formation shows irregularities and the error bars are larger than those of the solutions for $\mu_x \geq 10^1$. This means that for $\mu_x = 10^{-1}$ the penalization under-smoothes the solutions and we can exclude $\mu_x < 10^{-1}$.

For $\mu_x \geq 10^1$ the star formation is in agreement with the input model, showing only differences at lookback times $t \leq 10$ Myr. As already seen in Sect. 3.1, this is due to the particular shape of the mass to light ratio of the SSP basis at these lookback times (see Fig. 3.3). The small increase of the mass to light ratio at lookback times $t \leq 10$ Myr affects the solutions when we convert the luminosity fraction per time-bin, into solar masses per time-bin. For this reason, the recovered small differences at these lookback times can be considered as artifacts of the SSP models. The associated μ_x values are acceptable.

From this analysis we conclude that a campaign of inversions applied to mock spectra is necessary to give a criterion that determines the appropriate value for the penalization coefficients, and also to fix a range of allowed μ values consistent with the χ^2 statistical properties.

The campaign of inversion performed for model SAM2 determined the values of μ_x giving reliable solutions. The range of acceptable values is $\mu_x \geq 10^1$.

Metallicity penalty (μ_Z)

The coefficient μ_Z determines the weight of the metallicity penalty function $P(\mathbf{Z})$ in the final solution. (see Eq. 2.36). From Fig. 3.5, 3.6, and 3.7 we recover a trend similar to the μ_x analysis. For $\mu_Z \leq 10^{-1}$ the solutions show irregularities and large error bars, that is a sign of an under-smoothing of the solution. For increasing μ_Z the metallicity solutions become smoother. According to the models of Boissier & Prantzos (2000) the metallicity of a spiral galaxies, at a given radius, evolve weakly at lookback times $t < 1$ Gyr. This trend is consistent with the *a priori* of the method, i.e. the smoothness of the solutions. At lookback times $t \geq 1$ Gyr the metallicity profile decreases steeply by a factor $\sim$ 3-4, and to reproduce such a curve, the minimization requires low penalty values for μ_Z.

Only solutions for $\mu_Z \geq 10^{-1}$ can reproduce the smooth metallicity evolution for lookback times $t < 1$ Gyr. For $\mu_Z \geq 10^3$ the metallicity evolution is flat everywhere. In summary, a high value of μ_Z, preventing large curvature in the solutions, is preferable to reproduce the smooth metallicity at lookback times $t \leq 1$ Gyr. A lower μ_Z is instead required to reproduce the trend of the profile at lookback times $t \geq 1$ Gyr.

We investigate the possibility of a compromise able to reproduce the steep gradient of the SAM2 metallicity model at lookback times $t \geq 1$ Gyr and the flat

profile at lookback times $t \leq 1$ Gyr, performing four different inversions. We set the penalty of star formation $\mu_x = 10^2$, that reproduces the input star formation history for a wide range of μ_Z (see Fig. 3.5 and 3.6). The values of μ_Z are 10^1, 10^2, 10^3, and 10^4. They span the range of transition between a low-value regime, with fluctuations in the solution allowed, and a high-value regime, that imposes flat solutions. The results show that for an appropriate setting of $\mu_x = 10^2$ and $\mu_Z = 10^2$ (Fig. 3.7), we can reproduce an increasing metallicity evolution for the spectral analysis of the model SAM2.

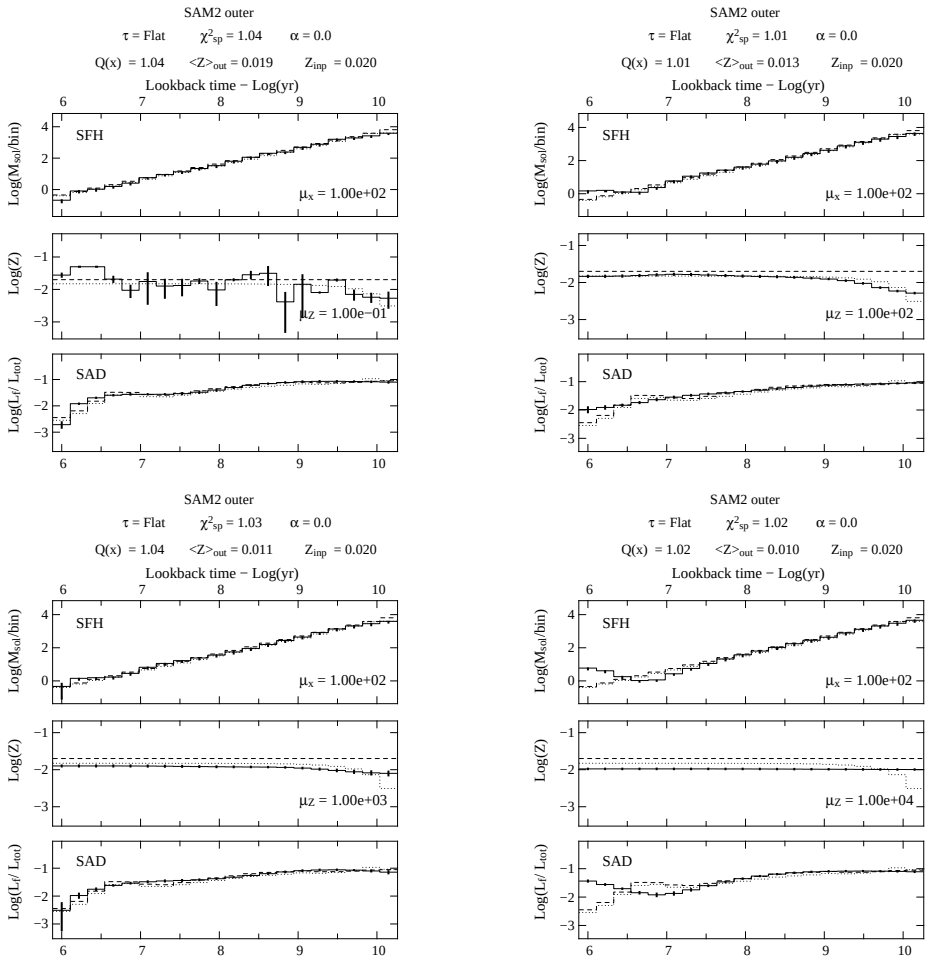

Figure 3.7: Results for non parametric inversion of a synthetic spectrum corresponding to the galaxy model SAM2 for $[\mu_x, \mu_Z] = [10^2, 10^{-1}]$ (top left panel), $[\mu_x, \mu_Z] = [10^2, 10^2]$ (top right panel), $[\mu_x, \mu_Z] = [10^2, 10^3]$ (bottom left panel) and $[\mu_x, \mu_Z] = [10^2, 10^4]$ (bottom right panel). For a detailed description see Fig. 3.4.

For $\mu_Z \geq 10^4$, as shown in left and bottom panels of Fig. 3.6, the penalization imposes a flat solution, and the average value recovered can be considered as a time-bin averaged metallicity. We verify that this averaged value is systematically below the input model at lookback times $t < 1$ Gyr. By imposing the flatness of the

solution we underestimate the metallicity at lookback times t <1 Gyr, at epochs that are relevant for the stripping age determination.

Moreover, when using observations, the choice of μ_Z is still more difficult and not trivial, because of varying noise and emission lines changing the depth of absorption lines. We can overcome this problem by imposing a high penalization for the metallicity, e.g. $\mu_Z = 10^4$. With this value we recover a flat metallicity evolution that corresponds to a time-bin averaged metallicity (see bottom panel of Fig. 3.5 and 3.6). Since metallicity increases with time in the first 5 Gyr and then keeps an approximatively constant value, for $\mu_Z = 10^4$ we verify that the imposed flat metallicity evolution systematically underestimates the metallicity evolution at lookback time $t \leq 5$ Gyr. Comparing different models with different star formation and metallicity evolution we can quantify the amount of this underestimation.

For the SAM2 model, the time-bin averaged metallicity is $\langle Z \rangle = 0.015$, and the value recovered from the inversion when $\mu_Z = 10^4$ is $\langle Z \rangle = 0.01$, both for low ($\mu_x = 10^{-1}$) and high ($\mu_x = 10^2$) star formation penalties. The difference with respect to the input model is $\Delta Z = 0.005$. The gradient of metallicity evolution for SAM2 shows a steep slope (see Fig. 3.2) at lookback times $t > 5$ Gyr, that reduces the time-bin averaged value of the metallicity.

We verify that the underestimation of the metallicity is related both to the steepness of the metallicity profile and to the slope of the considered star formation history. To show better this relation, we realized two inversions for the SAM1 and SAM2 model, considering a flat star formation, and a constant metallicity evolution $Z = 0.02$ as initial conditions. We fix the value of $\mu_x = 10^2$ and $\mu_Z = 10^4$ (top panels in Fig. 3.8). The time-bin averaged metallicity of model SAM2 is $\langle Z \rangle = 0.015$ and the inversion recovers a time averaged metallicity of $\langle Z \rangle = 0.01$, with an underestimation of $\Delta Z = 0.005$ of the metallicity at lookback time $t < 5$ Gyr (left panel of Fig. 3.8). For the model SAM1 the time-bin averaged metallicity is $\langle Z \rangle = 0.035$ and the recovered solution has a time-bin averaged metallicity of $\langle Z \rangle = 0.026$, with an underestimation of $\Delta Z = 0.008$, larger than the model SAM2. The larger underestimation is due to the steeper curvature of the metallicity evolution (see Fig. 3.1) for the model SAM1, that decreases the time-bin averaged value.

As last test we realized the same inversion of the model SAM2 shown in the left panel of Fig. 3.8, but as input metallicity we impose that of the SAM1 model. As shown in the bottom panel of Fig. 3.8 the time-bin averaged metallicity of the SAM1 model is $\langle Z \rangle = 0.035$, and the recovered averaged metallicity is $\langle Z \rangle = 0.033$, with a difference $\Delta Z = 0.002$, a lower value with respect to the SAM2 model inversion

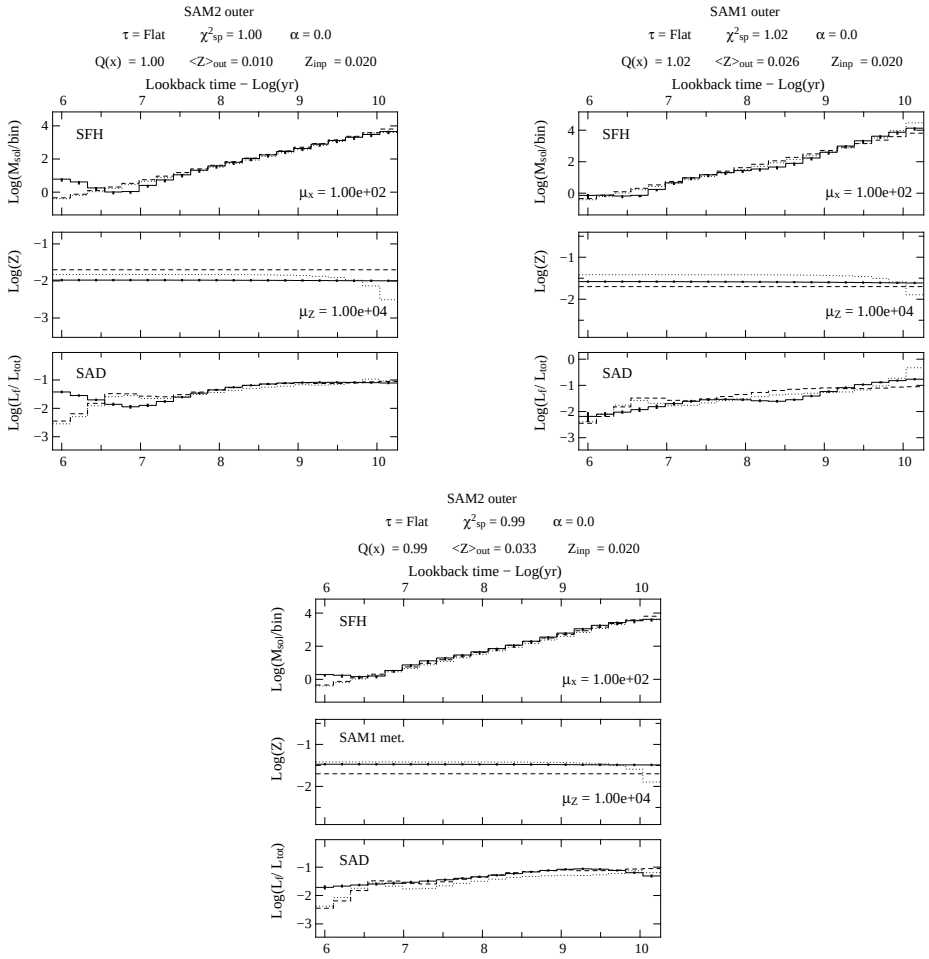

Figure 3.8: Results for non parametric inversion of a synthetic spectrum corresponding to the galaxy model SAM2 (left panel) and SAM1 (right panel) and model SAM2 using the metallicity of model SAM1 (bottom panel). For a detailed description see Fig. 3.4.

with the proper metallicity evolution. As already seen the metallicity evolution of the SAM1 model (dashed lines in Fig. 3.1) is steeper than that of the SAM2 model (solid lines in Fig. 3.1). At the same time the luminosity weighted metallicity of these stellar populations, using the star formation of SAM2 model, is lower with the respect to the model SAM1 and in the final averaging these lookback times have a lower weight in the solution. In summary the underestimation produced by a time-bin averaging of the metallicity evolution depends on the metallicity gradient at lookback times $t > 1$ Gyr, and on the light contribution of the the stellar populations at lookback times $t > 1$ Gyr. Mixing SAM2 star formation and SAM1 metallicity evolution is intrinsically inconsistent. This last test has been conceived only to determine the influence of the star formation history in the underestimation produced by a time-bin averaging of the metallicity, without any physical purpose.

In conclusion the basic trend of the metallicity evolution of the analyzed models is well recovered when $\mu_Z = 10^2$. In the observations the solutions can show irregular shape also for larger values of μ_Z, making it difficult to select reliable solutions. In this case it is preferable to use high values of penalization that give flat metallicity evolution corresponding to a time-bin averaged metallicity. Since the metallicity increases with time, the time-bin averaging produces an underestimation of the metallicity at lookback time $t < 5$ Gyr, that depends on the steepness of the metallicity profile and the star formation slope. Using Boissier & Prantzos (2000) models we estimate this underestimation to be $0.005 \leq \Delta Z \leq 0.008$.

3.2.2 Initial guess

The choice of the initial guess in non parametric methods is not trivial. As shown in Ocvirk et al. (2006a) the problem of the minimization of the Q-function for spectral inversion is ill-posed. This means that tiny variations in the initial condition can give huge variations in the results. The solution space of the non linear problem is complex and a bad choice of the initial conditions could make the algorithm converge to a local minimum. We chose as a reasonable initial guess for star formation history a decreasing exponential and a constant metallicity. The exponential law is characterized by a timescale τ that determines the slope of the curve (Eq. 2.37). In our case, it is necessary to investigate how the initial star formation history and the initial metallicity affect the results.

We analyze the spectrum of model SAM1 and SAM2. In order to minimize the effects due to the metallicity penalization we set a constant metallicity evolution $Z = 0.02$ for SAM2 model, and $Z = 0.03$ for SAM1 model. We fix the penalization $\mu_Z = \mu_x = 10^2$. This value has been fixed according to the results showed in Sect. 3.2.1 for model SAM2.

For the star formation initial guess we use two extremely different cases. The first case is an exponentially decreasing law with $\tau = 1$ Gyr (see Eq. 2.37) that represents an early type galaxy with a huge peak in the local star formation history at lookback times $t \geq 10$ Gyr. The spectral energy distribution in this case is dominated by old populations and the current star formation is negligible. The second case corresponds to a flat star formation history, in which the stellar component due to the young and intermediate stellar populations in total light is not negligible. Since a peaked star formation is more similar to the SAM1 shape (top panel in Fig. 3.1), we expect that the model with $\tau = 1$ Gyr gives better results than a constant star formation. As shown in the top row of Fig. 3.9 this is not the case. The chosen initial conditions leads to results that are in good agreement with the input for both

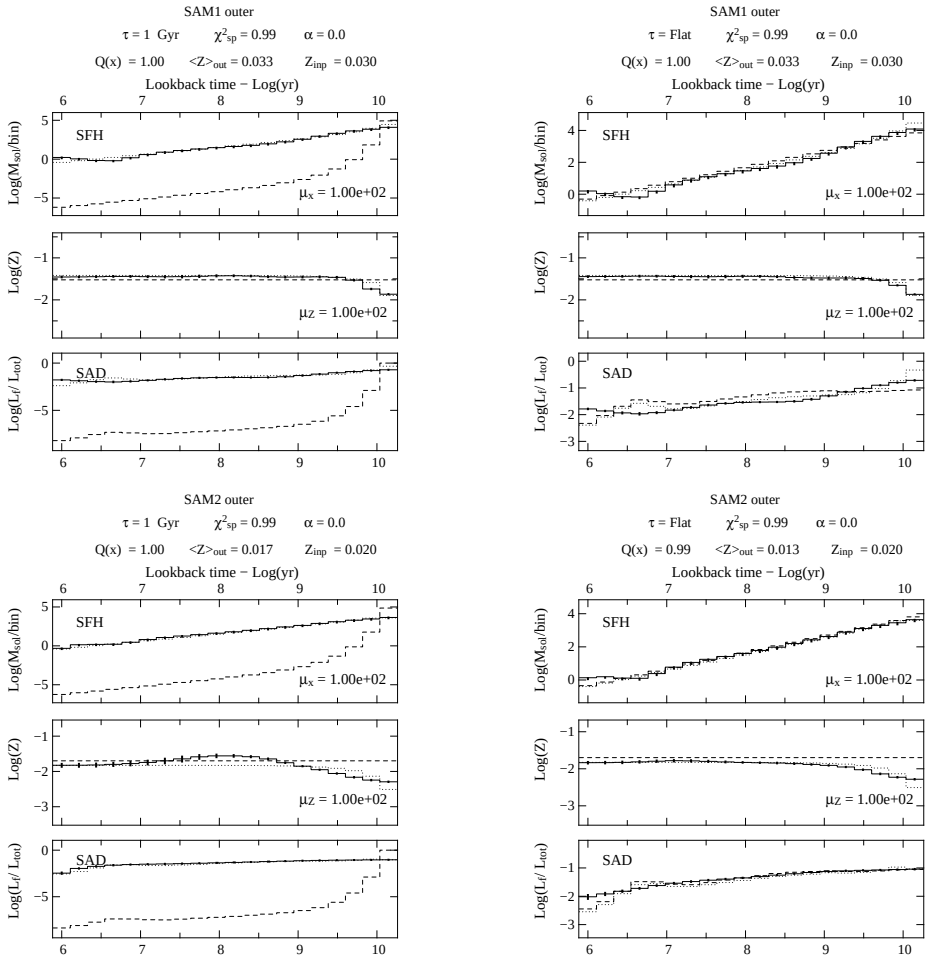

Figure 3.9: Results for the non parametric inversion of a synthetic spectrum corresponding to the galaxy model SAM1 (figures in top row) and SAM2 (figures in bottom row) for different star formation history as initial guess : a flat star formation history (figures in right column) and an exponentially decreasing law with timescale $\tau = 1$ Gyr (figures in left column). For a detailed description see Fig. 3.4.

models, and obtain the same $\chi^2_{\rm spec} = 0.99$. The results are stable, as the error bars show, and the evolution of the metallicity is traced relatively well. In the case of the model SAM1, the time-bin averaged metallicity is $\langle Z \rangle = 0.035$ and the recovered metallicity is for both initial guess $\langle Z \rangle = 0.033$.

For model SAM2 the time-bin averaged metallicity is $\langle Z \rangle = 0.015$ and the recovered averaged metallicity is $\langle Z \rangle = 0.017$ for the model with an exponential with $\tau = 1$ Gyr and $\langle Z \rangle = 0.013$ for a flat star formation history as initial guess.

The difference between the model and the solution for the star formation history of both models increases at lookback times $t < 10$ Myr. At these small time scales, the chosen models contribute little to the total light and the uncertainties become relevant. Also, we require that the luminosity weighted stellar age distribution is flat, which leads to a bump in the star formation history (see Fig. 3.3).

We also note that for model SAM1 there is a systematic underestimation of stars produced at lookback times $t > 8.6$ Gyr, i.e. the first time-bin. This is another effect due to the penalization. For the model SAM1 the galaxy has produced most of its stars in the first 8 Gyr (Fig. 3.1). Binning the time-axes logarithmically, the mass of stars produced in the first time-bin (lookback times $8.6 \leq t \leq 14$ Gyr) corresponds to the 64% of the mass of stars produced during the galaxy's life. This produces a decrease in the star formation history by a factor 3 between the first and the second time-bin that the penalization, when μ_x is sufficiently high, smoothes. Obviously the penalization can be reduced by reducing μ_x, allowing more irregular solutions. We investigate this effect later on.

For model SAM2 the parameter τ of the initial guess does not affect the recovered solution. Again we have higher uncertainties in the younger component, as for model SAM1, but in this case the inversion reproduces quite well the star formation history at lookback time $t \geq 9$ Gyr. This is due to the different shapes of the two models. The star formation history of model SAM2 is flatter than SAM1 (Fig. 3.1). This means that the curvature between the first time-bin and the others is less pronounced with respect to SAM1 and the penalization does not prevent the overall curvature at these ages. The metallicity is well reproduced until lookback times of $\sim$ 2 Gyr. For lookback times $t > 5$ Gyr, the penalization regularizes the gradient by replacing the steep curvature of the input model with a smoothly decreasing profile.

As a further test we investigated the effect of starting with unphysical initial guesses. We chose for the metallicity a flat evolution with the same value shown in Fig. 3.9, i.e. $Z = 0.03$ for model SAM1 and $Z = 0.02$ for model SAM2. For the star

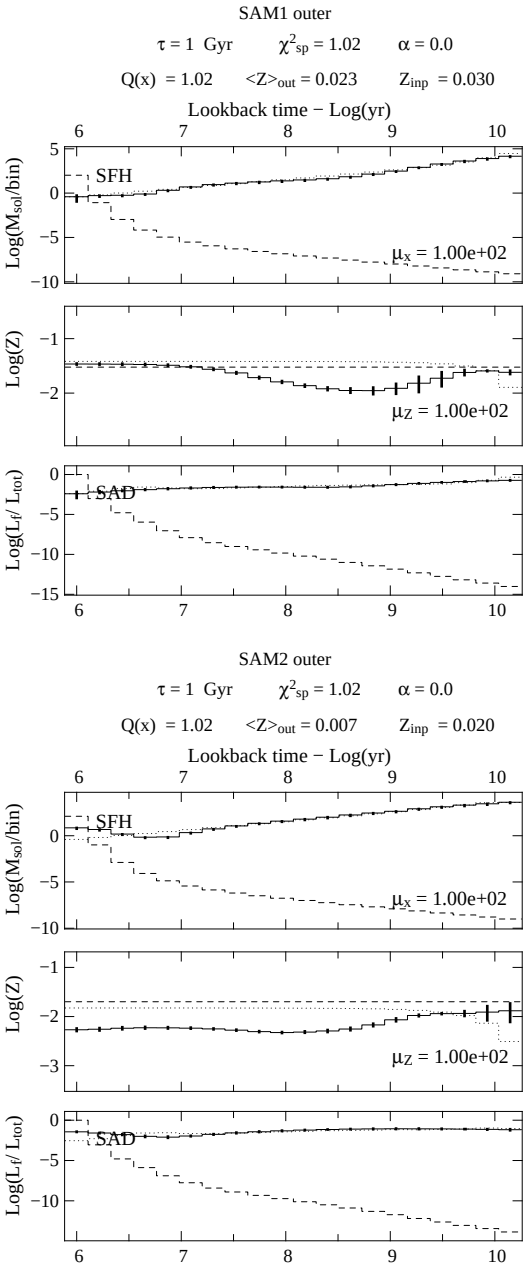

Figure 3.10: Results for non parametric inversion of a synthetic spectrum corresponding to the galaxy model SAM1 (top) and SAM2 (bottom) for an increasing star formation history as initial guess (dashed line). For a detailed description see Fig. 3.4.

formation history we chose instead of a decreasing exponential, an exponentially increasing star formation history, with a short timescale (τ = 1 Gyr). As shown in Fig. 3.10, also in this case, the inversion is able to reproduce the reference star formation histories for both models.

An interesting effect of the choice of such unphysical initial guess, is that the recovered metallicity is less precise and its evolution is not well reproduced. For model SAM1 the time-bin averaged metallicity of the input model is $\langle Z \rangle = 0.035$, and we find an average metallicity of $\langle Z \rangle = 0.022$. For model SAM2 we have a time-bin averaged metallicity $\langle Z \rangle = 0.015$ and we recover $\langle Z \rangle = 0.007$. The metallicities are quite different from the input models and they show also an unphysical evolution with lookback time. In the case of model SAM1 the profile increases at lookback times $t < 1$ Gyr to merge with the model at recent epochs. The metallicity at old ages is relatively high since the first time-bin. The spectral energy distribution of the first guess is then dominated by the very young component, contrary to the models that we want to reproduce. The chosen μ_x and the μ_Z values reproduce the input models when the initial guess is a flat star formation history or an exponential with timescale of τ = 1 Gyr (Fig. 3.9). With this unphysical initial guess instead during the minimization procedure, we lose the informations about the trend of metallicity and we obtain unphysical profiles (Fig. 3.10).

We can preserve the information about the overall metallicity, by increasing the penalization of μ_Z. We then obtain a constant solution that can be considered as a representative metallicity. For this latter choice of penalization the inversion shows a systematic underestimation in recovering the metallicity of the models. This underestimation spans a range ΔZ = 0.05 - 0.008, as seen in Sect. 3.2.1.

The test shown in Fig. 3.10 is an extreme case that is not realistic and that we reject in the rest of the analysis. For reasonable initial guesses for the star formation history the spectral inversion reproduces both flat and peaked star formation histories and the solutions are not strongly dependent on the slope of the chosen initial guess.

We saw that for particular choices of the initial guesses for the star formation history, we obtain consistent star formation histories but metallicity evolutions in disagreement with the input model. Now we investigate the influence of different initial guesses for the metallicity evolution. We start using the same configuration as in the right bottom panel of Fig. 3.9. In that case we used as initial guess a flat metallicity evolution $Z = 0.02$, that is a slight overestimation of the time-bin averaged metallicity of the model, $\langle Z \rangle = 0.015$.

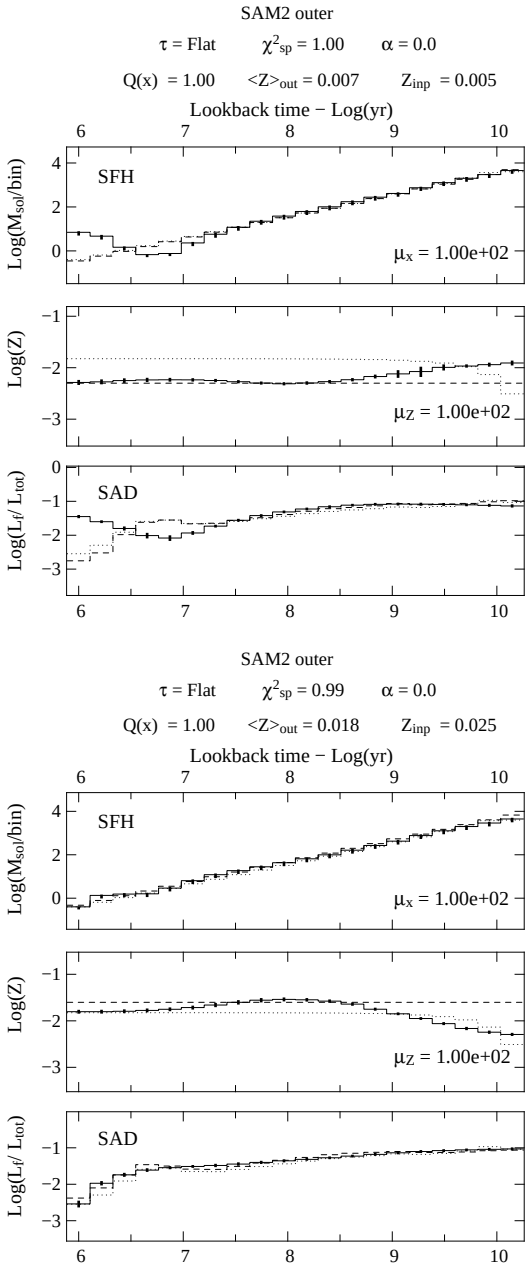

Figure 3.11: Results for non parametric inversion of a synthetic spectrum corresponding to the galaxy model SAM2 for a constant metallicity initial guess that starts from an higher (top panel) and lower (bottom panel) value respect to the model solution. For a detailed description see Fig. 3.4.

We perform the same inversion using as initial guess a constant metallicity, with $Z = 0.025$ and $Z = 0.005$. In this way we explore the effect of an overestimation and an underestimation of the input metallicities. As shown in Fig. 3.11, if the minimization starts from an initial value that is an overestimation of the input model, the solution reproduces the basic trend of the metallicity evolution, leading to an

average metallicity $\langle Z \rangle = 0.018$, consistent with the model. For the inversion that uses an initial condition that underestimates the real solution (top panel in Fig. 3.11), the recovered time-bin averaged metallicity is too low: $\langle Z \rangle = 0.007$.

Metallicity is less constrained by the method, and differences of the order $0.005 \leq \Delta Z \leq 0.01$ in the initial guess lead to different solutions. For observed spectra, in which we do not know how to fix this value, we can overcome the problem in different ways. We can recover the metallicity from independent methods, e.g. studying the emission lines of the spectrum, if present, or analyzing the features that are metal-dependent. Then we explore for which configuration the inversion gives consistent solutions. Another way is to increase μ_Z to a value that imposes a flat metallicity evolution. In this case the metallicity has the same value at all the ages, that we can consider as a time-bin averaged value of the metallicity evolution along the galaxy's life. This means that we lose informations about profile-curvature at lookback times $t > 9$ Gyr. For $t < 9$ Gyr metallicity stays almost constant and the minimization does not need high penalizations.

For the stripping age determination we are interested in stellar populations spanning lookback times $0 < t < 1$ Gyr. The flat metallicity solution obtained for high value of μ_Z is a time-bin averaged metallicity that underestimates the value of the metallicity in the last Gyr, giving a lower limit to the metallicity of stellar populations at these ages.

In conclusion, the metallicity evolution is less constrained than the star formation history in the spectral analysis, and the problem can be solved using independent methods or assuming penalization values that give a time-bin averaged metallicity, leading to an underestimation of the metallicity between $\Delta Z = 0.005$ and 0.01 (see Sect. 3.2.1). The initial guess assumed for the metallicity leads to an underestimation of the metallicity at lookback time $t < 1$ Gyr

3.3 Testing the photometric inversion with artificial data

In this section we investigate the results of the non parametric method for the photometric analysis ($\alpha = 1$ in Eq. 2.29). We used, as input data, the model SAM2 of Boissier & Prantzos (2000) (see Fig.3.1). The photometric pass-bands considered are FUV, NUV, u', g', i', r', z', J, H, and K. We applied to the model spectrum a Calzetti (2001) extinction law with $E(B-V) = 0.5$ normalized to have a unit mean.

The non parametric inversion method acts in both kind of analysis in the same way, performing the minimization under the same hypothesis. What is changed are the input data. In spectral analysis we have a small wavelength range, $\lambda\lambda = 3300$ -

6300 Å, a high resolution, R ∼780, and the problem has a high number of degrees of freedom, $N \sim 2600$. For the photometry we have a large wavelength coverage, from 1530 Å of FUV to 22000 Å of K-band, but each filter produces a point value, that collects all the informations inside the associated wavelength domain. We have less degrees of freedom ($N \sim 7$). In addition, the GALEX spatial resolution is low and the UV emission of the outer region is very faint (number of counts inside the chosen regions: 5-6 DN). Despite these problems, the advantages of such a large wavelength domain, from UV (GALEX) to Infra Red (2MASS), is that we have a direct information about stellar populations of ages at lookback times $t < 1$ Gyr and $t > 10$ Gyr, an important constraint not available in the spectrum.

The problem associated to the photometric analysis is ill-posed and needs regularization. We investigate here in detail the weight coefficients μ_x and μ_Z by performing a campaign of inversion spanning the same ranges explored in the spectral analysis: $[\mu_x, \mu_Z] = [10^{-1}, 10^{-1}]$, $[10^{-1}, 10^{2}]$, and $[10^{-1}, 10^{4}]$ (Fig. 3.13). The second set of values is $[\mu_x, \mu_Z] = [10^{1}, 10^{-1}]$, $[10^{1}, 10^{2}]$, and $[10^{1}, 10^{4}]$ (Fig. 3.14). A third set of values is $[\mu_x, \mu_Z] = [10^{2}, 10^{-1}]$, $[10^{2}, 10^{2}]$, $[10^{2}, 10^{3}]$, $[10^{2}, 10^{4}]$ (Fig. 3.15), and a fourth set of values $[\mu_x, \mu_Z] = [10^{3}, 10^{-1}]$, $[10^{3}, 10^{2}]$, $[10^{3}, 10^{4}]$ (Fig. 3.16).

3.3.1 Numerical Stability without regularization

Ocvirk et al. (2006a) showed that the problem associated to the spectral inversion is ill-posed. We realized an inversion in which the initial guesses are equal to the model used to generate the input data. No noise is added. The χ^2 contribution to $Q(\mathbf{X})$ is minimal, but the functions and their derivatives are not. Therefore the first iteration of the minimization steps away from the desired solution.

First, we consider low penalization values : $\mu_x = \mu_Z = \mu_C = 10^{-20}$. We use a mass normalized and a flux normalized spectral basis (Eq. 2.3 and 2.1).

As shown in Fig. 3.12 in both cases the star formation history is recovered properly. On the contrary the metallicity evolution is in disagreement with the input data. We cannot expect any variation in the metallicity evolution on short timescale to be reliable. This is expected, because there is not enough information in the photometry. Therefore, we need to penalize at least the metallicity to smooth the solution.

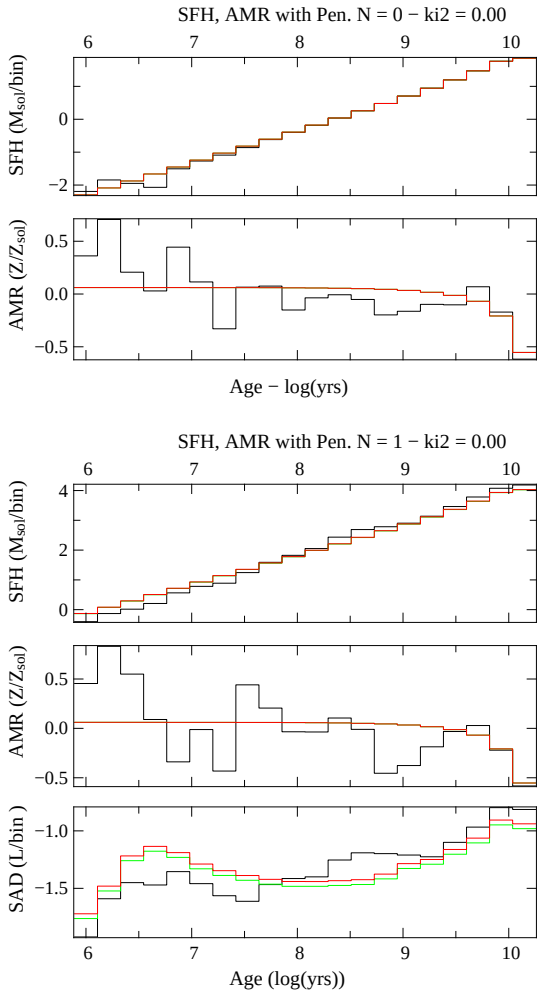

Figure 3.12: Results for non parametric inversion of photometric values corresponding to the SAM2 model (Boissier & Prantzos, 2000). In all the panels the red histogram represents the input data, that are also the initial conditions, and the black histogram represents the recovered solution from inversion. The ages are measured in lookback time ([$\log_{10}$(yr)] with the convention that $t_{\rm now} = 0$. Top figure : star formation history (top panel) and metallicity evolution (bottom panel) for a mass weighted spectral basis (Eq. 2.1). Bottom panel : star formation history (top panel), metallicity evolution (middle panel) and luminosity weighted stellar age distribution (bottom panel) for a luminosity weighted spectral basis (Eq. 2.3).

3.3.2 Weight of penalization

Star formation penalty(μ_x)

In the spectral analysis the recovered star formation history is in agreement with the model for $\mu_x \geq 10^{-1}$. As shown in Fig. 3.13 and 3.14 the photometric analysis needs higher regularization than the spectral analysis to give stable solutions. If we consider the recovered star formation when $\mu_x = 10^1$, we can note that we have large fluctuations at lookback time $t \sim 800$ Myr and $t \sim 10$ Myr. For the same value in the

spectral analysis we obtain results in agreement with the input model (see Fig. 3.6).

For the photometric analysis the number of degrees of freedom of the problem leads to a tolerance threshold for the χ^2 of 0.4, because we have few data-points and thus the noise in the data can produce large fluctuations of χ^2 values. The χ^2 values vary between 0.6 ± 0.4, and all inversions are acceptable. The photometric inversion requires higher penalization for the star formation history ($\mu_x \geq 10^3$). Moreover, the metallicity is not well constrained by the photometry and also needs a high penalization ($\mu_Z \geq 10^2$).

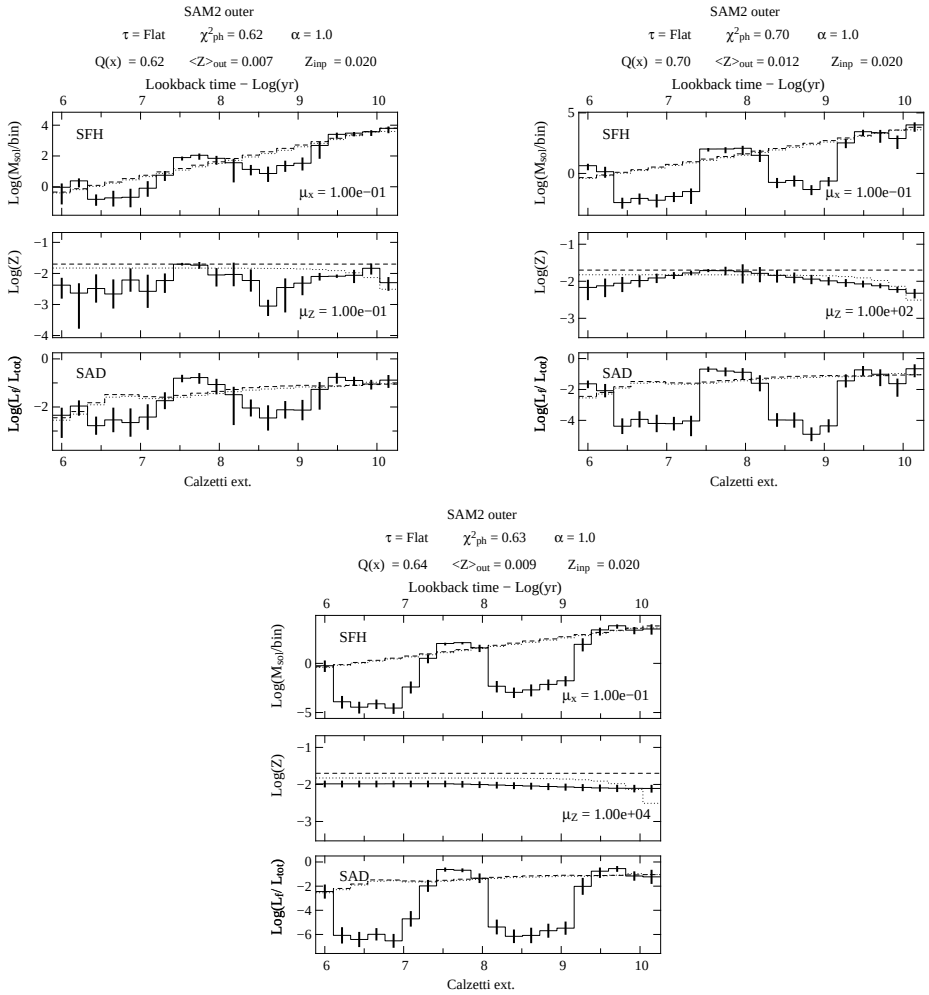

Figure 3.13: Results for non parametric inversion of photometric values corresponding to the galaxy model SAM2 for $[\mu_x, \mu_Z] = [10^{-1}, 10^{-1}]$ (left panel), $[\mu_x, \mu_Z] = [10^{-1}, 10^{2}]$ (right panel) and $[\mu_x, \mu_Z] = [10^{-1}, 10^{4}]$ (bottom panel). For a detailed description see Fig. 3.4.

Penalization of metallicity evolution

We proceed to a test in which varying μ_Z we investigate the convergence of the minimization. The solution is not improved for $10^{-20} \leq \mu_Z \leq 10^{-6}$, and we explore

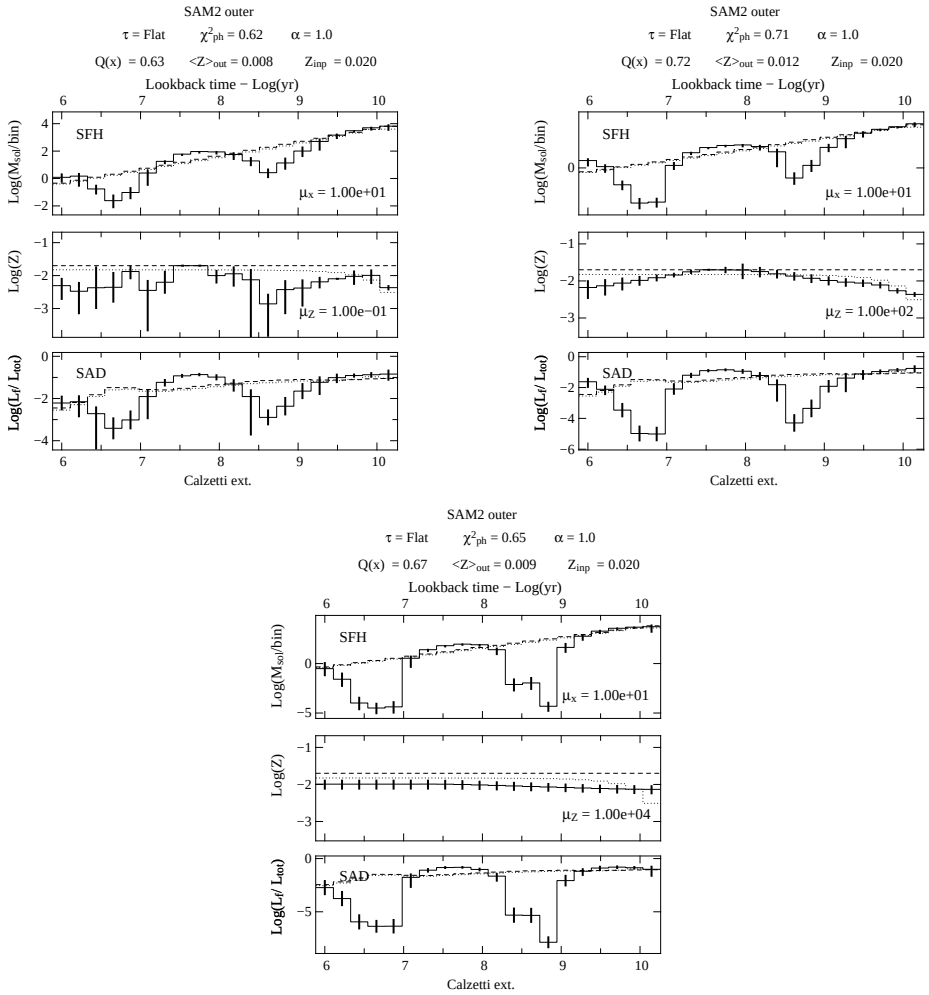

Figure 3.14: Results for non parametric inversion of photometric values corresponding to the galaxy model SAM2 for $[\mu_x, \mu_Z] = [10^1, 10^{-1}]$ (left panel), $[\mu_x, \mu_Z] = [10^1, 10^2]$ (right panel) and $[\mu_x, \mu_Z] = [10^1, 10^4]$ (bottom panel). For a detailed description see Fig. 3.4.

the range $10^{-2} \leq \mu_Z \leq 10^2$ while keeping $\mu_x = \mu_C = 10^{-20}$ (see Eq. 2.36). In Fig. 3.17 are shown the results and in Fig. 3.18 are shown the differences between the recovered solution and the injected histories.

As long as we keep μ_Z low, we find large fluctuations in the resulting metallicity evolution (bottom panel of Fig. 3.18). For the highest $\mu_Z \geq 10^2$ the metallicity residuals stay almost flat. This is the better solution for this family of penalization. An opposite behavior is shown by the star formation history. If μ_Z is low the star formation history prefers solutions similar to the initial condition. As we increase μ_Z the star formation history increases its fluctuations around the input star formation history. For the highest μ_Z, i.e. the best metallicity model, we find the worst star formation history, but we must consider that the penalization is negligible ($\mu_x = 10^{-20}$) and the problem remains ill-posed.

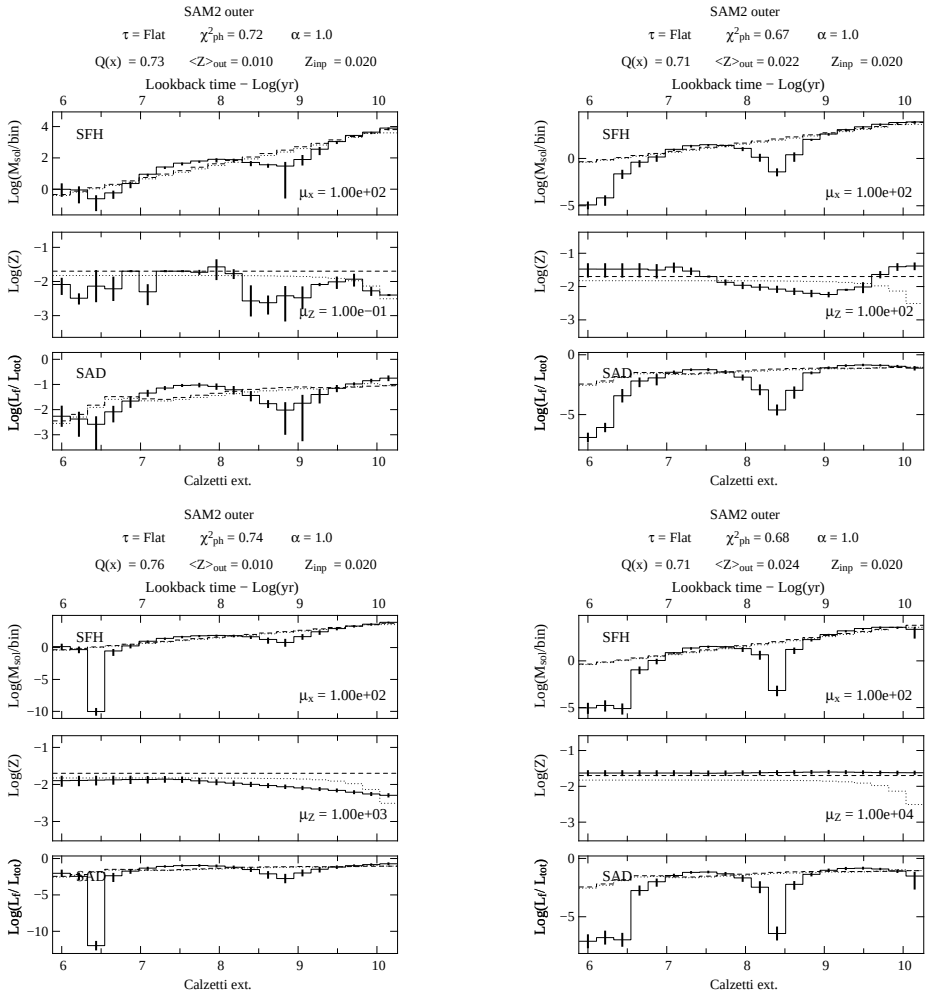

Figure 3.15: Results for non parametric inversion of photometric values corresponding to the galaxy model SAM2 for $[\mu_x, \mu_Z] = [10^2, 10^{-1}]$ (top left panel), $[\mu_x, \mu_Z] = [10^2, 10^2]$ (top right panel), $[\mu_x, \mu_Z] = [10^2, 10^3]$ (bottom right panel), $[\mu_x, \mu_Z] = [10^2, 10^4]$ (bottom left panel). For a detailed description see Fig. 3.4.

The results of the photometric inversion, shown in Fig. 3.13, 3.14, and 3.15, are quite different with respect to the spectral results of Fig. 3.5, 3.6, and 3.7. Both the star formation history and metallicity evolution are less constrained by the photometry with respect to the spectral analysis. This means that the regularization of the problem needs higher values of the penalization. The star formation history for $\mu_x \geq 10^3$ is in agreement with the input model, if we exclude the youngest populations at lookback times $t < 10$ Myr. This effect has also been observed in the spectral analysis, and it is due to the uncertainties in the stellar population models at these ages. These uncertainties affect then both kinds of analysis, spectral and/or photometric.

If we increase μ_Z we obtain flat solutions with acceptable χ^2 values, and we

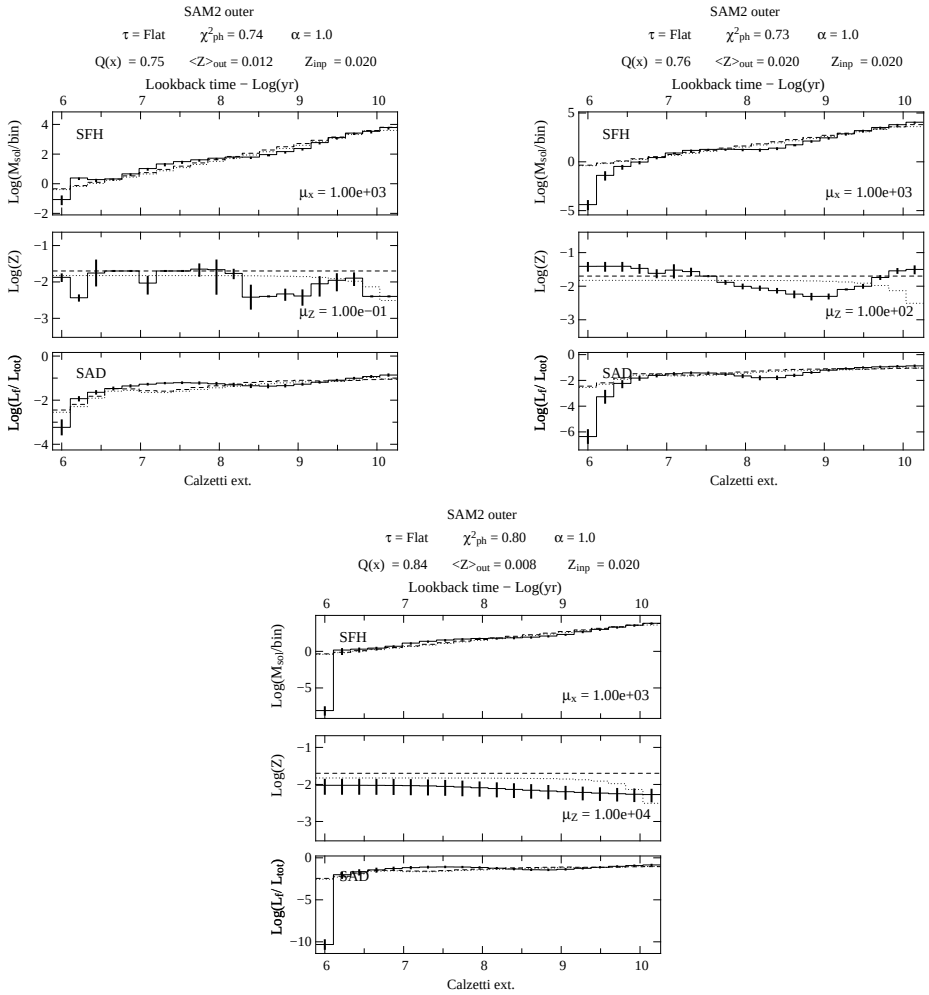

Figure 3.16: Results for non parametric inversion of photometry values corresponding to the galaxy model SAM2 for $[\mu_x, \mu_Z] = [10^3, 10^{-1}]$ (left panel), $[\mu_x, \mu_Z] = [10^3, 10^2]$ (right panel) and $[\mu_x, \mu_Z] = [10^3, 10^4]$ (bottom panel). For a detailed description see Fig. 3.4.

obtain time-bin averaged metallicity evolutions that produce an underestimation of the metallicity at lookback times $t < 1$ Gyr. The time-bin averaged metallicity of the model SAM2 is $\langle Z \rangle = 0.015$ and the flat metallicity obtained for $\mu_Z = 10^4$ produces an underestimation of $\Delta Z = 0.009$. The underestimation produced in photometric inversion is higher than the spectral analysis, i.e. $0.005 \geq \Delta Z \geq 0.008$. This is expected, since the determination of the metallicity evolution in photometric analysis is less constrained.

The photometric inversion produces large fluctuations also for values of μ_x and μ_Z for which the spectral analysis gave consistent results. At this stage, we conclude that metallicity is not well constrained and the most reliable procedure is to fix a high value of metallicity penalization to recover systematically flat metallicity solutions.

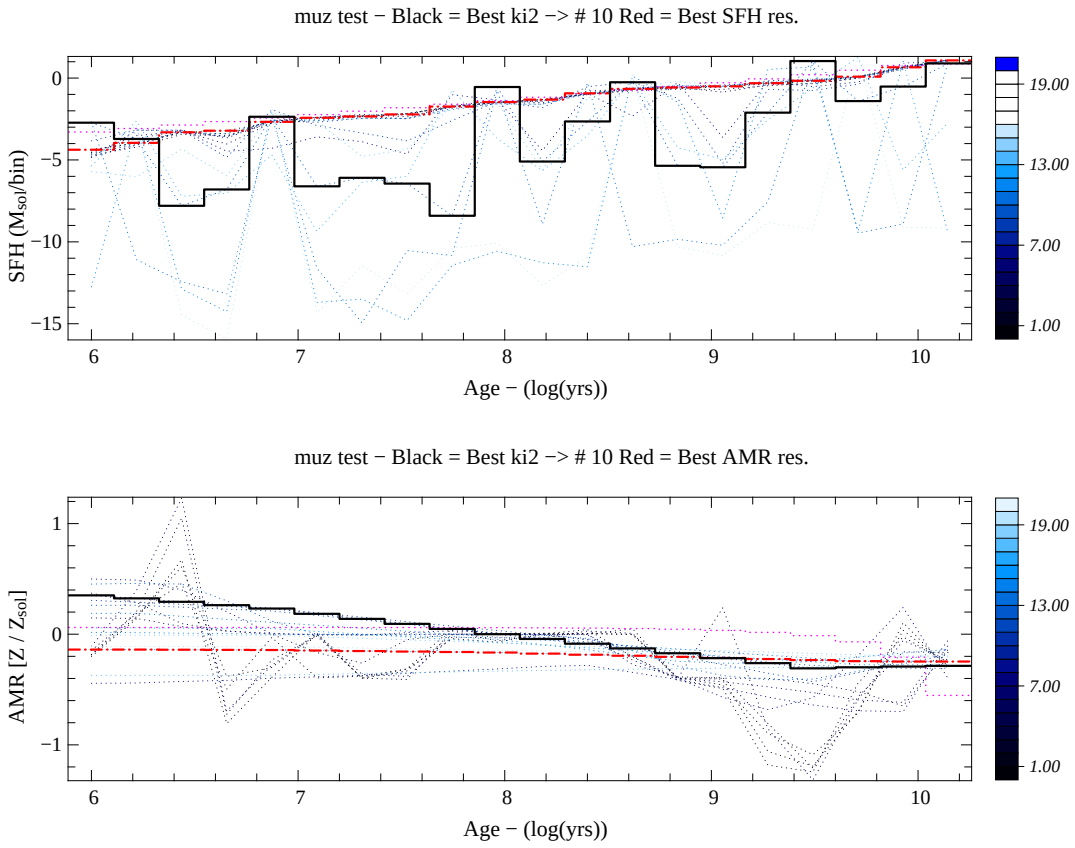

Figure 3.17: Top panel: star formation history vs. lookback time [$\log_{10}$(yr)] for different $10^{-2} \leq \mu_Z \leq 10^2$ (increasing number of realizations in right column represents increasing μ_Z). Bottom panel: metallicity evolution vs. lookback time [$\log_{10}$(yr)]. In each plot the black the red and the magenta histograms shows the best χ^2 solution, the solution that has the lowest differences with the input solution and the initial condition, respectively.

3.3.3 Initial Condition

We use a light weighted basis (Eq. 2.3) and we investigate the recovered metallicity evolution for the photometric analysis without penalization. We set different initial conditions: the SAM2 model of Boissier & Prantzos (2000) (see Fig. 3.2), an exponentially decreasing star formation law with characteristic timescale $\tau = 10$ Gyr and a constant luminosity weighted stellar age distribution. For all initial conditions used, we recover star formation histories in agreement with the input solution, but again the metallicity evolutions show large fluctuations (Fig. 3.19).

The photometric inversion is not very sensitive to the initial condition, the only effect is in terms of uncertainties of the results. To demonstrate this we proceed to an inversion using $\mu_x = 10^4$ and $\mu_Z = 10^4$. In one case we use as initial guess for the star formation, an exponential with characteristic timescale $\tau = 1$ Gyr instead of a flat star formation. In another case we use as initial guess for the metallicity

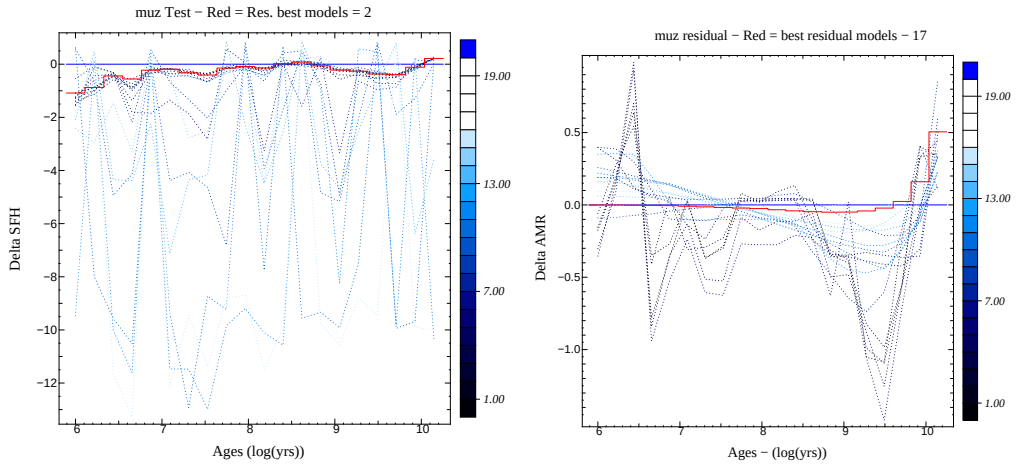

Figure 3.18: Left panel: ΔSFH = (recovered SFH - input SFH) vs. lookback time [$\log_{10}$(yr)] for $10^{-2} \leq \mu_Z \leq 10^2$ (increasing numbers of realizations represents increasing μ_Z). Right panel: ΔAMR = (recovered metallicity - input metallicity) vs. lookback time [$\log_{10}$(yr)]. In each plot the black, the red and the magenta histograms shows the best χ^2 solution, the solution that has the lowest differences with the input solution and the initial condition, respectively.

a constant evolution with $Z = 0.005$ instead of $Z = 0.02$. The results are shown in Fig. 3.20 for the three cases. The χ^2 of all inversions are acceptable. The star formation histories are well reproduced for lookback times $t > 10$ Myr for all initial guesses. The initial conditions which are closest to the input lead to the smallest uncertainties of the metallicity evolution.

3.4 Combined Analysis

In this section we investigate the effect of different penalization on the solution for a joint spectral and photometric analysis. We fix $\alpha = 0.5$ in Sect. 2.29 and we proceed to a campaign of inversions spanning the same ranges explored in the spectral and photometric analysis: $[\mu_x, \mu_Z] = [10^{-1}, 10^{-1}]$, $[10^{-1}, 10^2]$, $[10^{-1}, 10^4]$ shown in Fig. 3.21, $[\mu_x, \mu_Z] = [10^1, 10^{-1}]$, $[10^1, 10^2]$, $[10^1, 10^4]$ shown in Fig. 3.22, and $[\mu_x, \mu_Z] = [10^2, 10^{-1}]$, $[10^2, 10^2]$, $[10^2, 10^3]$, $[10^2, 10^4]$, shown in Fig. 3.23.

We saw in Sect. 3.2 and 3.3 that the photometric and the spectral inversion have a different answer to the penalties. As a general trend we saw that the photometry needs higher penalization both for the star formation and the metallicity. The metallicity is not well constrained by the photometry and for this reason we use a high penalization imposing a constant evolution. In summary, for the spectral analysis a value of $\mu_x \geq 10^{-1}$ gives results in agreement with the input models, but for the photometry this value is not sufficient. Performing a campaign we

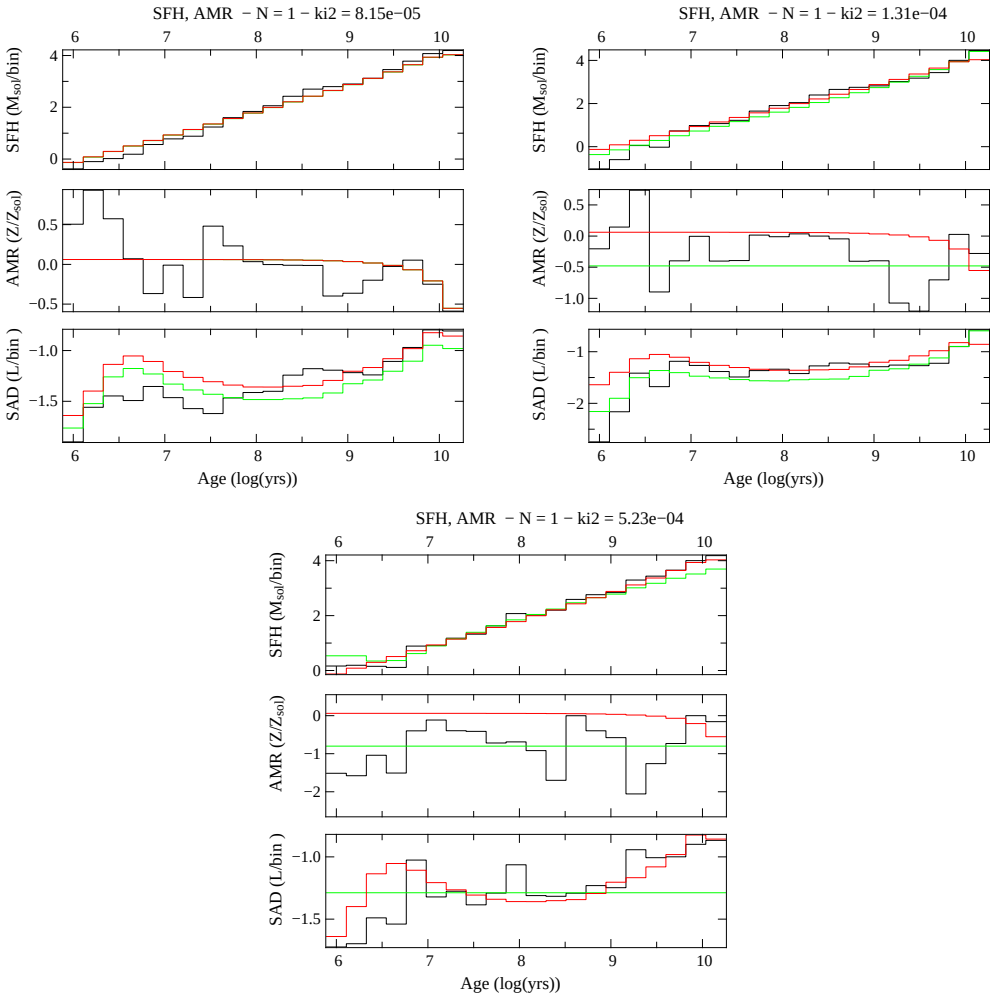

Figure 3.19: Results for non parametric inversion of photometric values corresponding to the SAM2 model (Boissier & Prantzos, 2000). In all the panels the red histograms represent the input data, the green histograms are the initial conditions, and the black histograms represents the recovered solution from inversion. The ages are measured in lookback time ([$\log_{10}$(yr)]) with the convention that $t_{\rm now} = 0$. In each figure is plotted the star formation history (top panel), the metallicity evolution (middle panel) and the luminosity weighted stellar age distribution (bottom panel). The results are obtained for different initial guesses for the star formation history: the model SAM2 (Boissier & Prantzos, 2000) (left figure), an exponential (Eq. 2.37) with $\tau = 10$ Gyr (right figure) and a constant luminosity weighted stellar age distribution (bottom figure).

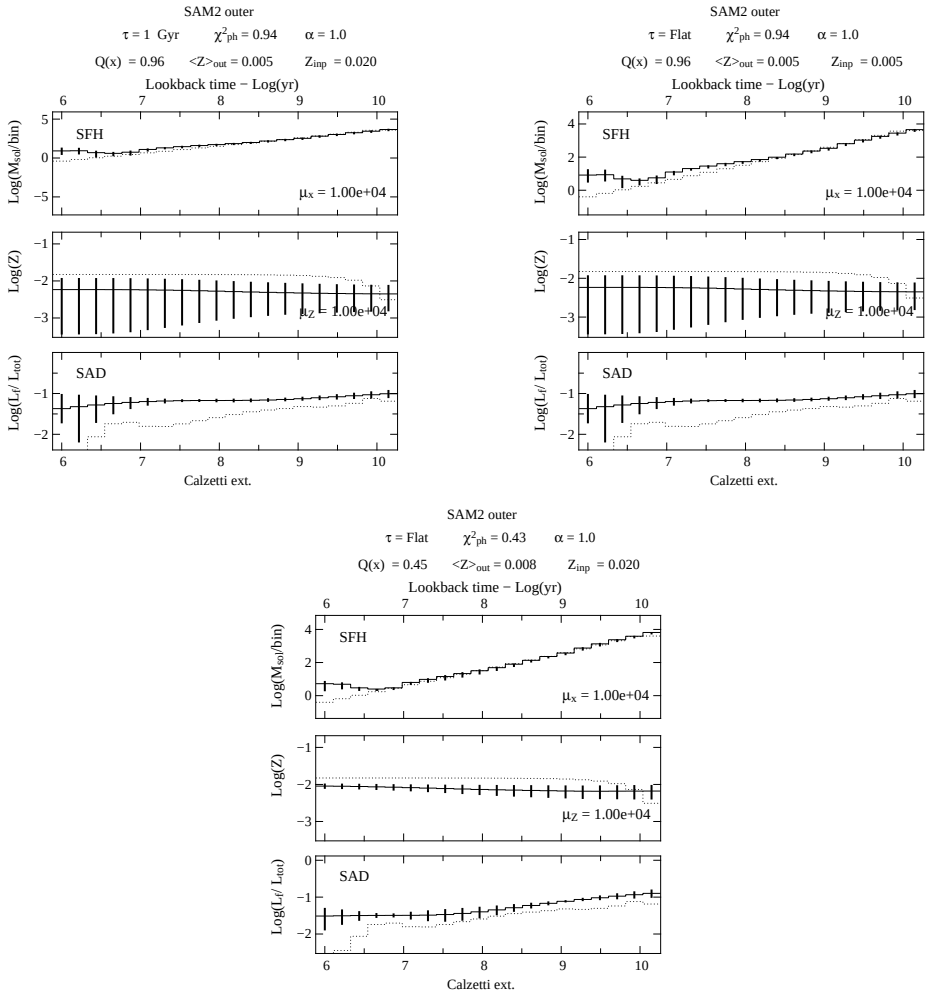

Figure 3.20: Results for non parametric inversion of photometric values corresponding to the galaxy model SAM2 for $\mu_Z = \mu_x = 10^4$. As initial guesses for the star formation and the metallicity evolution we have : an exponential with characteristic timescale $\tau = 1$ Gyr and a constant metallicity $Z = 0.02$ (left panel), a flat star formation and a constant metallicity $Z = 0.005$ (right panel) and a flat star formation with a constant metallicity $Z = 0.02$ (bottom panel). In each figure the top, middle and bottom panels represent the star formation history, the metallicity evolution and the luminosity weighted stellar age distribution, respectively. In each panel the dotted and dashed lines show the input model and the solid lines the results with associated error bars. The errors are obtained via Monte Carlo simulations. In top of panels are marked the τ used in star formation initial guess, the spectral χ^2, the weight parameter α in Eq. 2.29, the value of the total Q-function (Eq. 2.29), the time-bin averaged metallicity recovered from the inversion and the constant value of metallicity $Z_{\rm inp}$ used for the initial guess. In right bottom of top and middle panel of each figure are marked the value of penalization μ_x, μ_Z (see Eq. 2.36).

realized that star formation histories in agreement with the models are obtained when $\mu_x \geq 10^2$.

For the metallicity the trends were similar: for $\mu_Z \geq 10^2$ in the spectral analysis we reproduce the trend of the input metallicity evolution. For the photometry

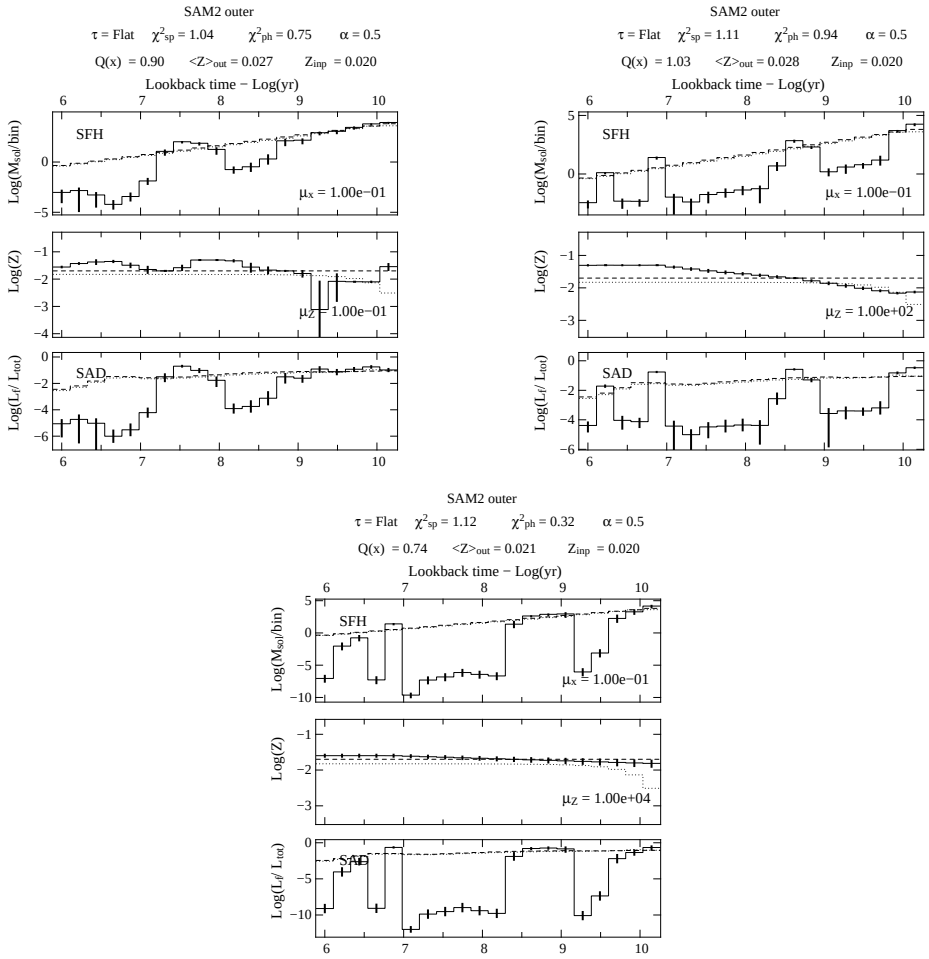

Figure 3.21: Results for non parametric inversion of combined analysis (spectral and photometric) corresponding to the galaxy model SAM2 for $[\mu_x, \mu_Z] = [10^{-1}, 10^{-1}]$ (left panel), $[\mu_x, \mu_Z] = [10^{-1}, 10^{2}]$ (right panel) and $[\mu_x, \mu_Z] = [10^{-1}, 10^{4}]$ (bottom panel). For a detailed description see Fig. 3.4.

the metallicity is highly unstable at $\mu_Z = 10^2$ and if we increase the penalization, the recovered solution becomes flat. The problem is not well constrained and we use values of $\mu_Z = 10^4$ to impose a constant evolution. The joint analysis shows that combining the two sets of data the solution is a balance between the separate analysis. In Fig. 3.21, 3.22, and 3.23 we show the results for different sets of μ_x and μ_Z. For small star formation penalties ($\mu_x = 10^{-1}$), the star formation history is strongly irregular. For $\mu_x = 10^1$ the recovered star formation histories are smooth for lookback times $t \geq 10$ Myr. For $\mu_x = 10^2$ the recovered star formation history shows a drop at a lookback time of $t = 300$ Myr for $\mu_Z = \mu_x = 10^{-1}$. For larger μ_Z the star formation history is smooth. It is not possible to recover the metallicity. A large metallicity penalization imposing a constant metallicity is thus necessary. In this case $\mu_x \geq 10^1$ leads to an acceptable solution.

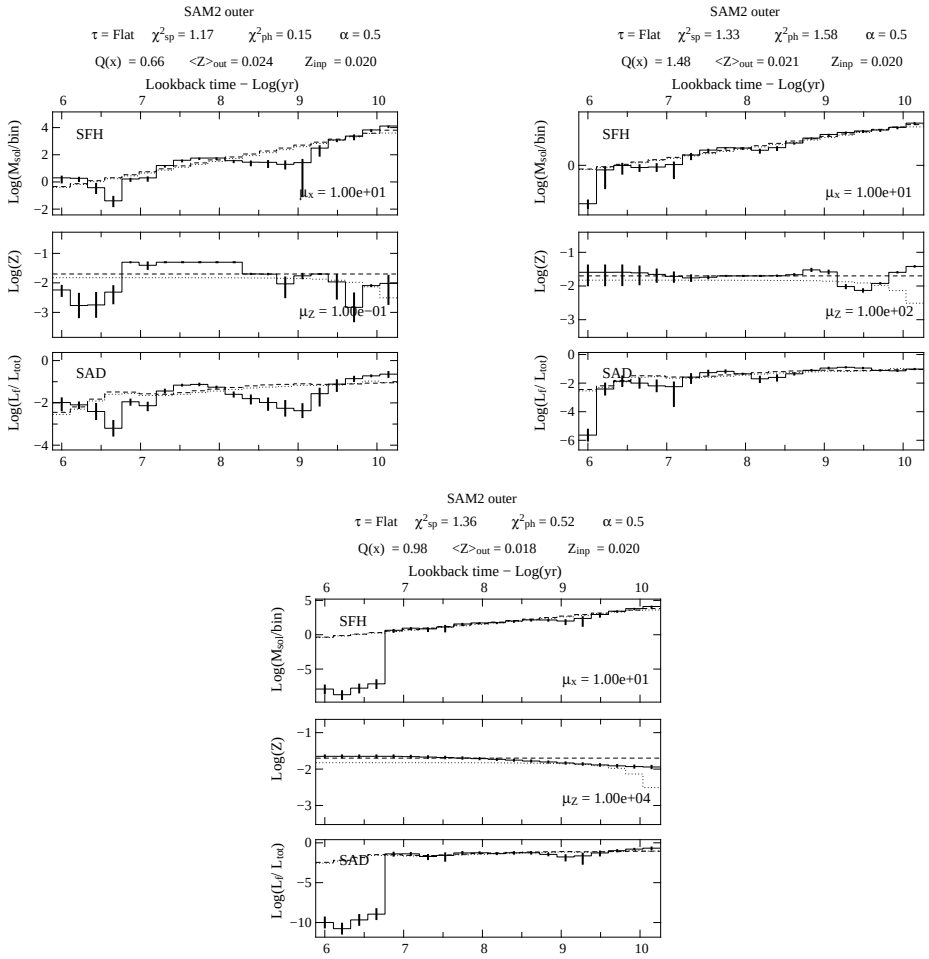

Figure 3.22: Results for non parametric inversion of combined analysis (spectral and photometric) corresponding to the galaxy model SAM2 for $[\mu_x, \mu_Z] = [10^1, 10^{-1}]$ (left panel), $[\mu_x, \mu_Z] = [10^1, 10^2]$ (right panel) and $[\mu_x, \mu_Z] = [10^1, 10^4]$ (bottom panel). For a detailed description see Fig. 3.4.

3.5 Stripping age determination

We are interested to study the effect of ram pressure stripping in the optical spectrum and photometry. Until now we studied semi analytical models that reproduce isolated spiral galaxies with current star formation. Ram pressure removes a fraction of the gas disk and quenches the star formation.

In this section we investigate the performance of the non parametric inversion in recovering a cut in the star formation history. We take the SAM2 model (Boissier & Prantzos 2000) and we cut the star formation history at a lookback time of t = 130 Myr. We then perform a spectral, a photometric, and a joint inversion of the mock data and we analyze the results. We investigate here in detail the weight coefficients μ_x and μ_Z by performing a campaign of inversion spanning the same ranges explored in the spectral and photometric analysis: $[\mu_x, \mu_Z] =$

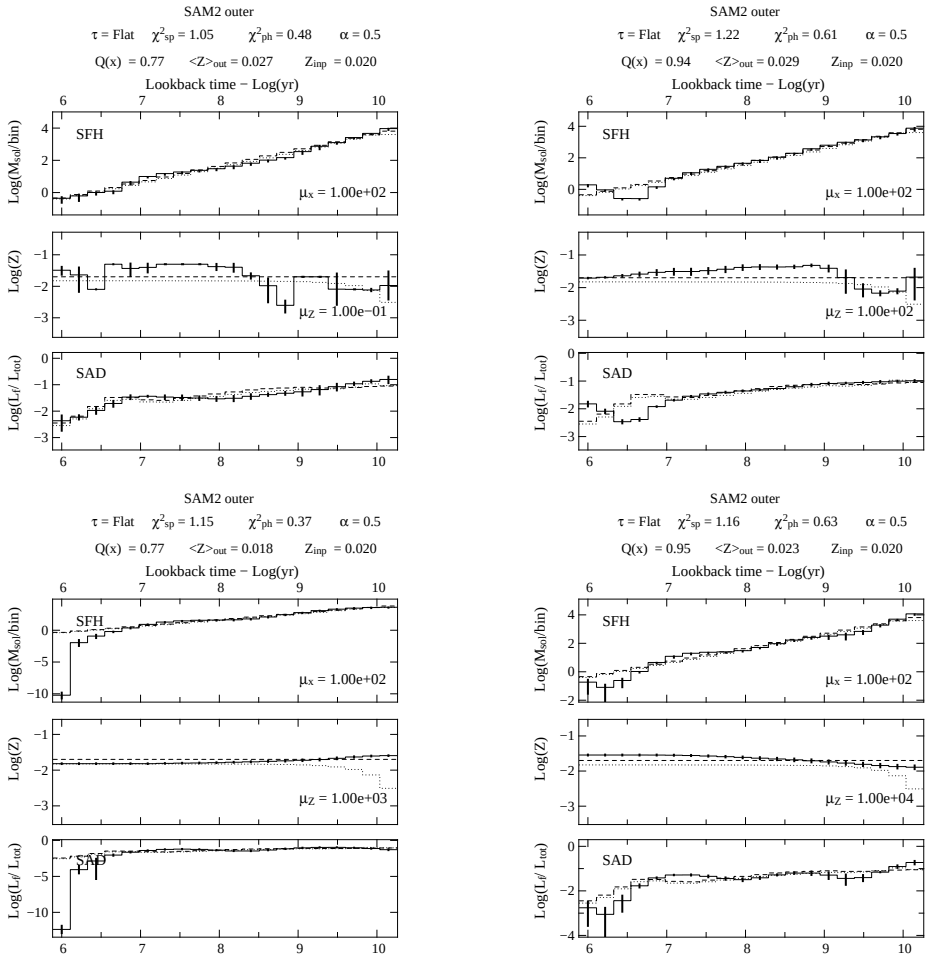

Figure 3.23: Results for non parametric inversion of combined analysis (spectral and photometric) corresponding to the galaxy model SAM2 for $[\mu_x, \mu_Z] = [10^2, 10^{-1}]$ (top left panel), $[\mu_x, \mu_Z] = [10^2, 10^2]$ (top right panel), $[\mu_x, \mu_Z] = [10^2, 10^3]$ (bottom left panel), and $[10^2, 10^4]$ (bottom right panel). For a detailed description see Fig. 3.4.

$[10^{-1}, 10^{-1}]$, $[10^{-1}, 10^2]$, and $[10^{-1}, 10^4]$ (Fig. 3.27). The second set of values is $[\mu_x, \mu_Z] = [10^1, 10^{-1}]$, $[10^1, 10^2]$, and $[10^1, 10^4]$ (Fig. 3.25). A third set of values is $[\mu_x, \mu_Z] = [10^2, 10^{-1}]$, $[10^2, 10^2]$, $[10^2, 10^3]$, and $[10^2, 10^4]$ (Fig. 3.26).

3.5.1 Spectral analysis

As initial conditions we use a flat star formation and a constant metallicity $Z = 0.02$. Based on the χ^2 all solutions are acceptable, and show a rapid decrease in star formation between 100 and 130 Myr. The star formation history before truncation is smooth for all penalizations μ_x and μ_Z. Due to the small penalization for $\mu_x \leq 10^{-1}$ star formation residuals can appear at lookback times $t < 100$ Myr, e.g. for $[\mu_x, \mu_Z] = [10^{-1}, 10^{-1}]$, $[10^{-1}, 10^{-2}]$, $[10^{-1}, 10^4]$, and $[10^1, 10^4]$. Only for $[\mu_x, \mu_Z] = [10^{-1}, 10^4]$ the stripping age is exactly reproduced. For $\mu_x = 10^1$ the stripping age

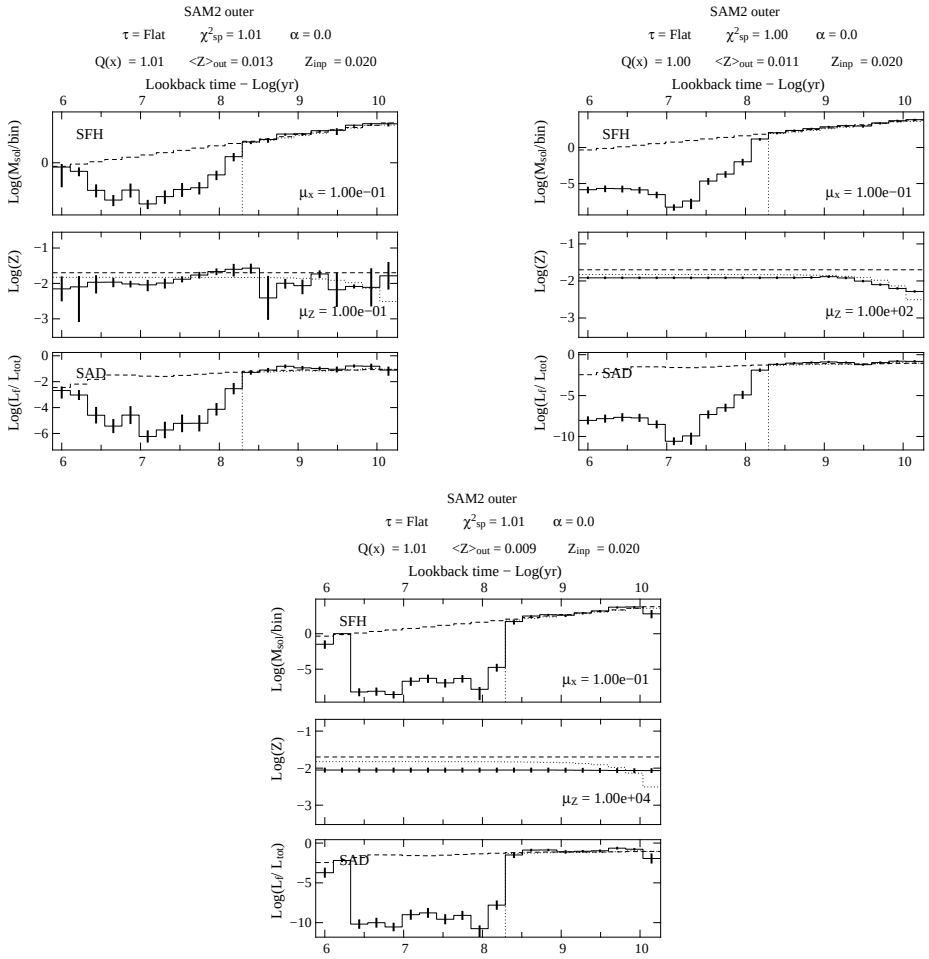

Figure 3.24: Results for non parametric inversion of a synthetic spectrum corresponding to the galaxy model SAM2 with truncated star formation history at lookback time $t = 130$ Myr for: $[\mu_x, \mu_Z] = [10^{-1}, 10^{-1}]$ (left panel), $[\mu_x, \mu_Z] = [10^{-1}, 10^{2}]$ (right panel) and $[\mu_x, \mu_Z] = [10^{1}, 10^{4}]$ (bottom panel). For a detailed description see Fig. 3.4.

is underestimated by one, for $\mu_x = 10^2$ by two time bins, i.e. ~ 80 Myr. As for the isolated disk models, the trend of the metallicity evolution can be reproduced for $\mu_Z = 10^2$.

3.5.2 Photometric analysis

We use the same configuration of Sect. 3.5.1 and we perform photometric inversions. Based on the χ^2 all solutions are acceptable. For $\mu_x = 10^{-1}$ the star formation history for lookback times $t > 130$ Myr is irregular, for $\mu_x \geq 10^1$ it is smooth. There is residual star formation for lookback times $t \leq 300$ Myr, e.g. for $[\mu_x, \mu_Z] = [10^{-1}, 10^2]$, $[10^1, 10^{-1}]$, $[10^1, 10^2]$, $[10^2, 10^{-1}]$, and $[10^2, 10^3]$. These residuals occur at lookback times $t \leq 10$ Myr, and they are mainly due to the uncertain M/L ratio of these young stellar populations (see Fig. 3.3). For $[\mu_x, \mu_Z]$

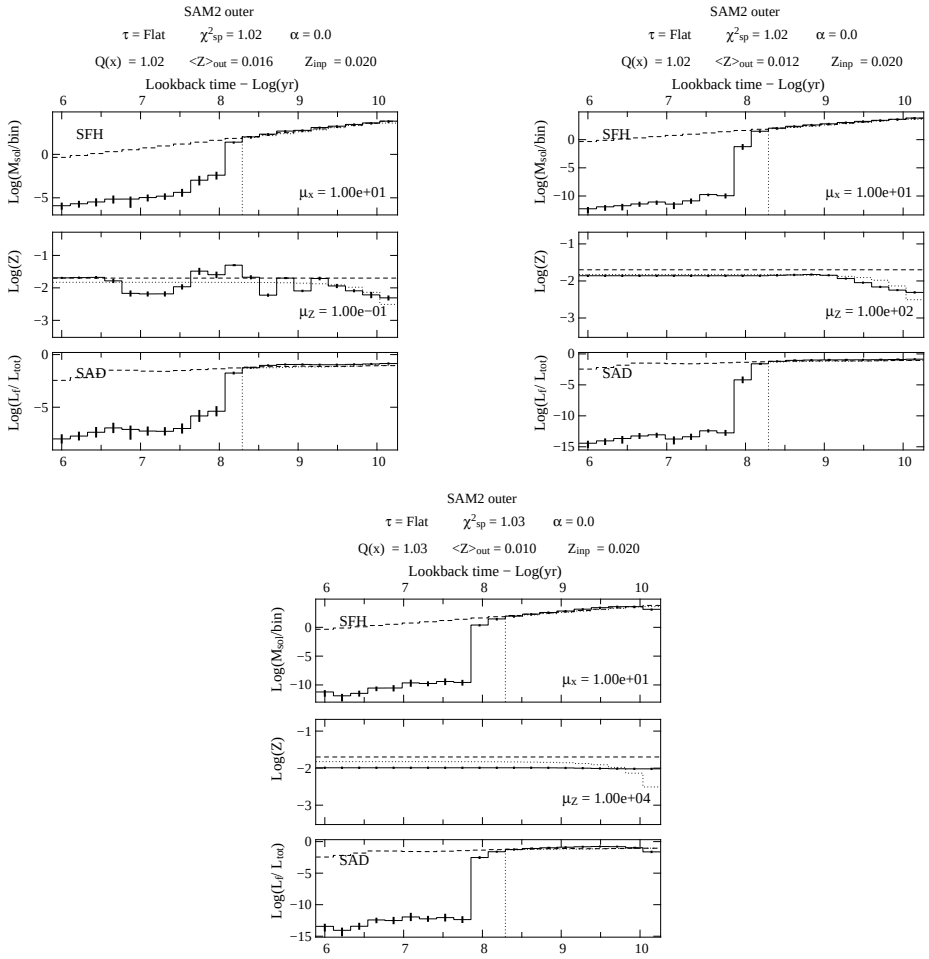

Figure 3.25: Results for non parametric inversion of a synthetic spectrum corresponding to the galaxy model SAM2 with truncated star formation history at lookback time $t = 130$ Myr for: $[\mu_x, \mu_Z] = [10^1, 10^{-1}]$ (left panel), $[\mu_x, \mu_Z] = [10^1, 10^2]$ (right panel) and $[\mu_x, \mu_Z] = [10^1, 10^4]$ (bottom panel). For a detailed description see Fig. 3.4.

$= [10^1, 10^4]$ and $[10^2, 10^4]$ the stripping age is underestimated by one time bin, i.e. 50 Myr. As for the isolated disk the metallicity cannot be reproduced and we have to impose a constant metallicity ($\mu_Z = 10^4$).

3.5.3 Combined Analysis

The analysis of spectral and photometric inversion showed separately slightly different behavior. Photometry requires high penalization to give consistent solutions and the metallicity is not well constrained. The best fit is obtained imposing a constant metallicity with $\mu_Z = 10^4$ that leads to an underestimation of the time-bin averaged metallicity at lookback times $t < 5$ Gyr.

The spectral analysis needs lower penalizations than the photometry and with adequate metallicity penalization it is able to reproduce the basic trends of

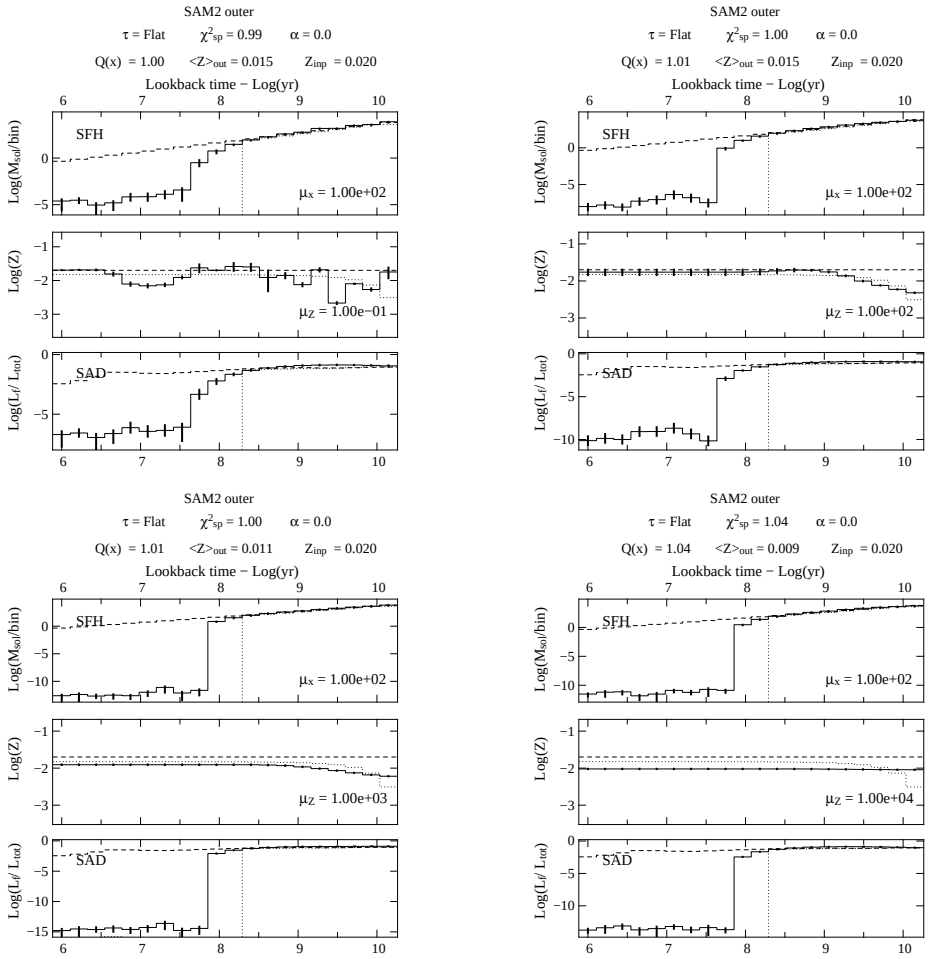

Figure 3.26: Results for non parametric inversion of a synthetic spectrum corresponding to the galaxy model SAM2 with truncated star formation history at lookback time t = 130 Myr for: $[\mu_x, \mu_Z] = [10^2, 10^{-1}]$ (top left panel), $[\mu_x, \mu_Z] = [10^2, 10^1]$ (top right panel), $[\mu_x, \mu_Z] = [10^2, 10^3]$ (bottom right panel) and $[\mu_x, \mu_Z] = [10^2, 10^4]$ (bottom left panel). For a detailed description see Fig. 3.4.

metallicity at lookback times $t < 5$ Gyr. The combined analysis of the spectral and photometric data is a compromise between the results obtained for the separate cases.

According to the results of Sect. 3.4, we investigate here in detail the weight coefficients μ_x and μ_Z by performing a campaign of inversion spanning the same ranges explored in the spectral and photometric analysis: $[\mu_x, \mu_Z] = [10^{-1}, 10^{-1}]$, $[10^{-1}, 10^2]$, and $[10^{-1}, 10^4]$ (Fig. 3.30). The second set of values is $[\mu_x, \mu_Z] = [10^1, 10^{-1}]$, $[10^1, 10^2]$, and $[10^1, 10^4]$ (Fig. 3.31). A third set of values is $[\mu_x, \mu_Z] = [10^2, 10^{-1}]$, $[10^2, 10^2]$, $[10^2, 10^3]$, and $[10^2, 10^4]$ (Fig. 3.32).

For small $\mu_x \leq 10^{-1}$ the solutions are irregular for all μ_Z and all lookback times. For $\mu_x = 10^1$ the star formation history is smooth for lookback times $t \geq 300$ Myr

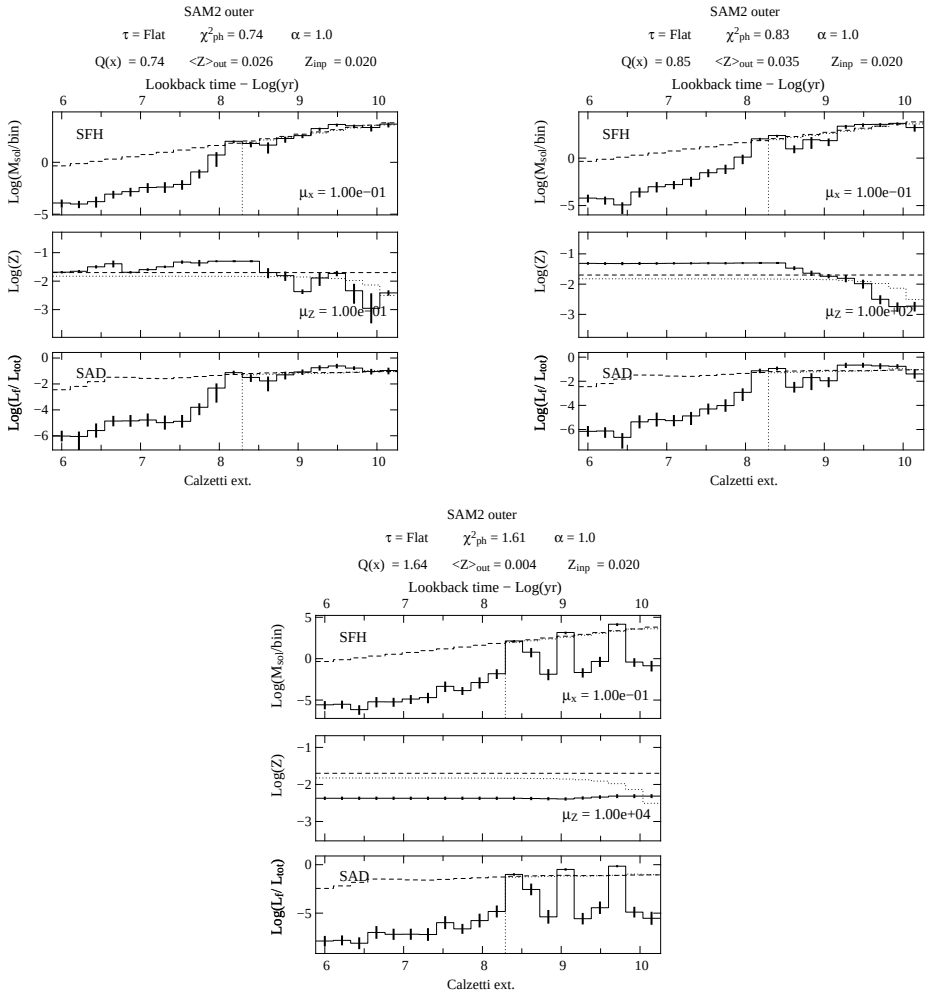

Figure 3.27: Results for non parametric inversion of photometric values corresponding to the galaxy model SAM2 with truncated star formation history at lookback time $t = 130$ Myr for: $[\mu_x, \mu_Z] = [10^{-1}, 10^{-1}]$ (left panel), $[\mu_x, \mu_Z] = [10^{-1}, 10^{2}]$ (right panel) and $[\mu_x, \mu_Z] = [10^{1}, 10^{4}]$ (bottom panel). For a detailed description see Fig. 3.4.

and the cut is well reproduced. On the other hand, the star formation history is smooth for these lookback times for $\mu_x = 10^2$ and all μ_Z. The stripping time is underestimated by one time bin, i.e. 50 Myr, except for $\mu_Z = 10^3$, in which the stripping time is underestimated by two time-bins, i.e. 80 Myr. The results for $\mu_x = 1$ reproduce well the model, but have an higher χ^2, because of the residuals star formation at younger ages, in disagreement with the model.

Thus, the combined analysis is more robust than the separate analysis in the sense that it gives consistent results for $\mu_x = 10^2$. However, the stripping age is underestimated by at least 50 Myr. We recall that the combined analysis of the isolated disk models also give consistent results for $\mu_x = 10^2$.

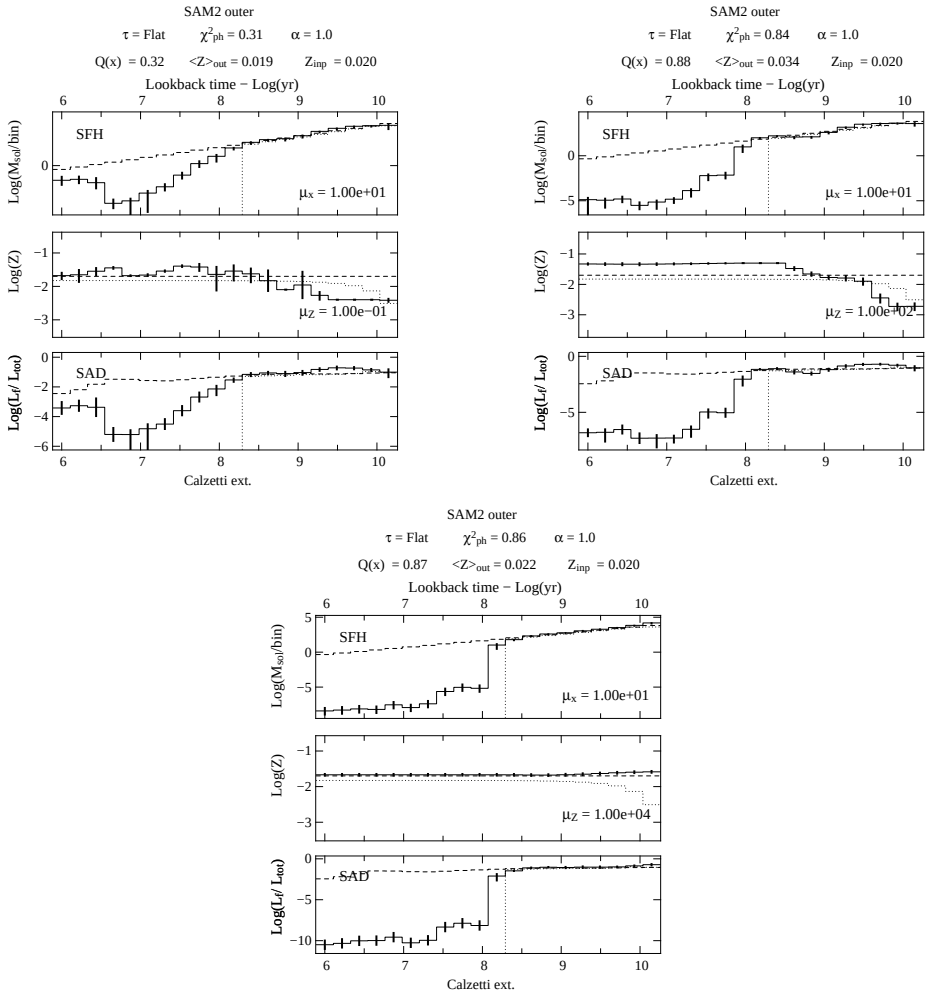

Figure 3.28: Results for non parametric inversion of photometric values corresponding to the galaxy model SAM2 with truncated star formation history at lookback time $t = 130$ Myr for: $[\mu_x, \mu_Z] = [10^1, 10^{-1}]$ (left panel), $[\mu_x, \mu_Z] = [10^1, 10^2]$ (right panel) and $[\mu_x, \mu_Z] = [10^1, 10^4]$ (bottom panel). For a detailed description see Fig. 3.4.

3.6 Summary

In this chapter:

- we performed a campaign of inversion using semi analytical model of Boissier & Prantzos (2000) to explore the answer of the method to different mock data. The campaign investigated the spectral inversion, the photometric inversion, and the combined analysis. We tested the effect of the initial condition, both for metallicity and the star formation. We investigated the influence in the results of different weight coefficients.

  The choice of the initial conditions has no effect on the recovered solution as long as it is reasonable. The trend of the metallicity evolution can be recovered

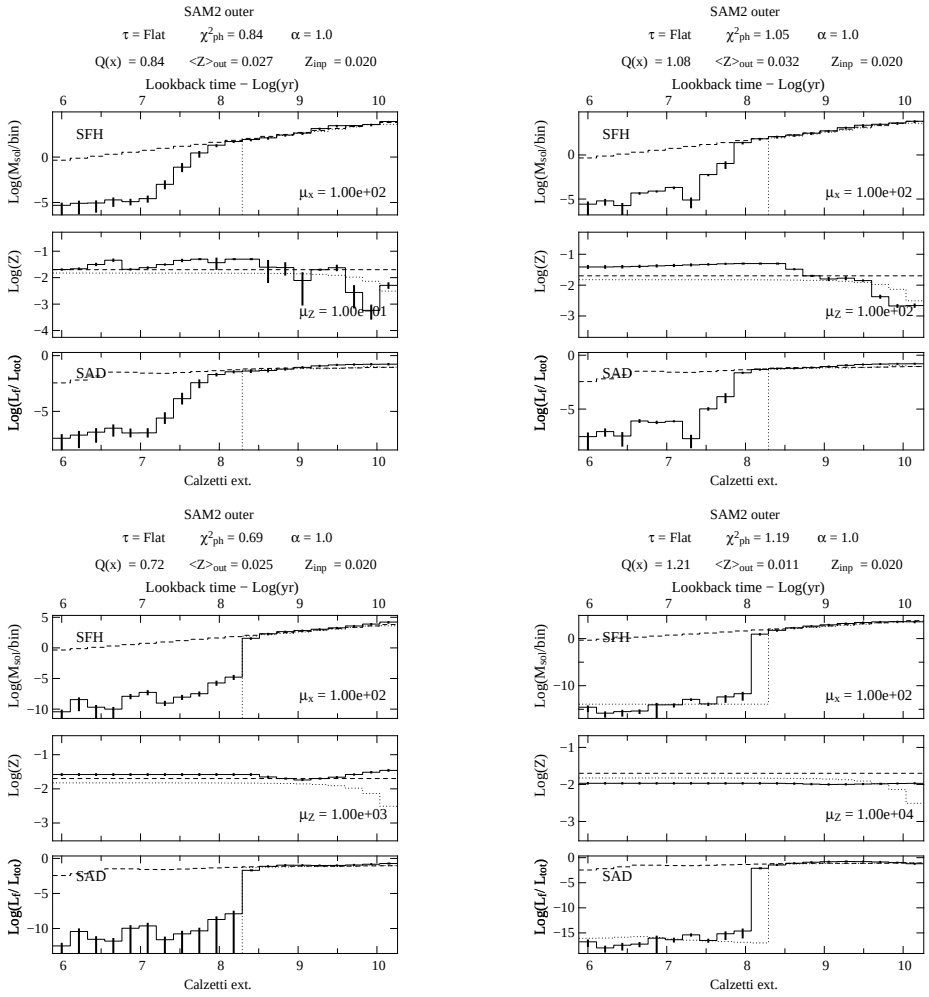

Figure 3.29: Results for non parametric inversion of photometric values corresponding to the galaxy model SAM2 with truncated star formation history at lookback time $t = 130$ Myr for: $[\mu_x, \mu_Z] = [10^2, 10^{-1}]$ (top left panel), $[\mu_x, \mu_Z] = [10^2, 10^1]$ (top right panel), $[\mu_x, \mu_Z] = [10^2, 10^3]$ (bottom right panel) and $[\mu_x, \mu_Z] = [10^2, 10^4]$ (bottom left panel). For a detailed description see Fig. 3.4.

for $\mu_Z = 10^2$ in the spectral analysis. For all other cases we have to impose a constant metallicity evolution ($\mu_Z = 10^4$). The star formation history is well reproduced for $\mu_x \geq 10^{-1}$. For the photometric analysis a higher star formation penalization is needed $\mu_x \geq 10^3$ and the combined analysis works best with $\mu_x = 10^2$.

- we analyzed specifically the solution for spectral, photometric and combined inversion for a ram pressure stripping scenario. We studied the recovered star formation solutions for a model in which the star formation is truncated at 130 Myr.

  For $\mu_x = 10^1$ the cut is well reproduced, but a residual star formation at

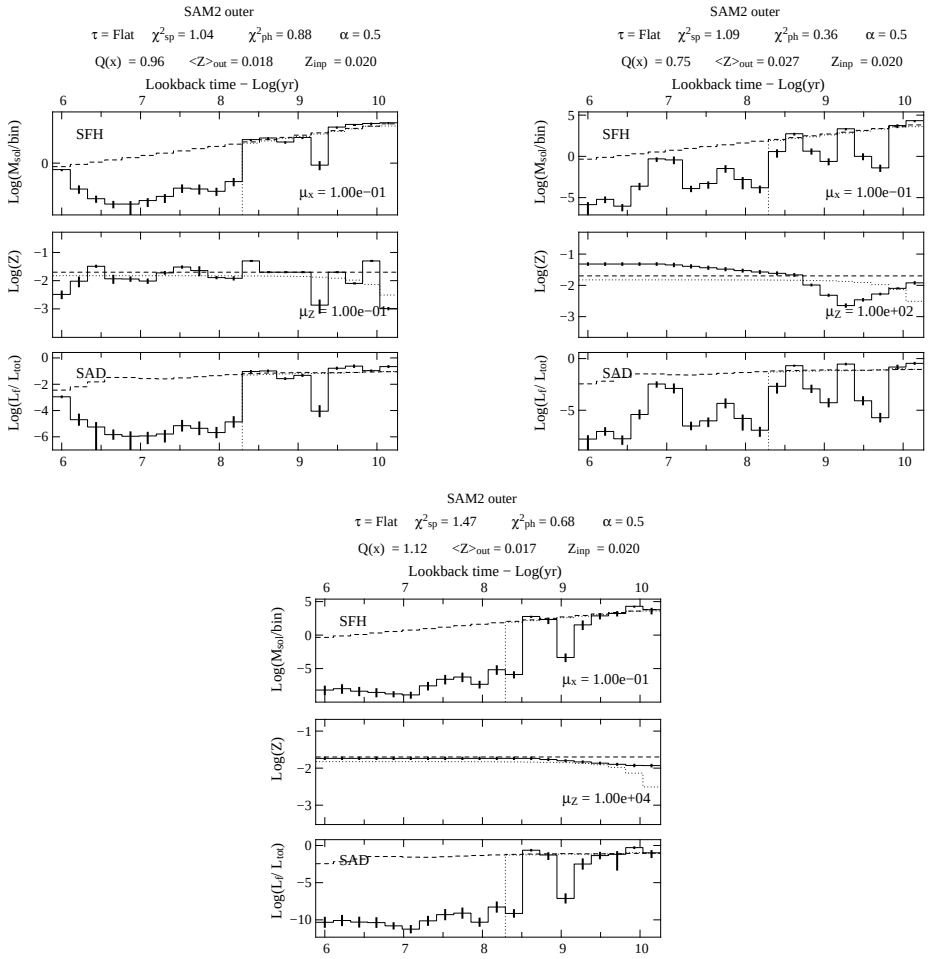

Figure 3.30: Results for non parametric inversion of combined analysis (spectral and photometric) corresponding to the galaxy model SAM2 with truncated star formation history at lookback time $t = 130$ Myr for: $[\mu_x, \mu_Z] = [10^{-1}, 10^{-1}]$ (left panel), $[\mu_x, \mu_Z] = [10^{-1}, 10^{2}]$ (right panel) and $[\mu_x, \mu_Z] = [10^{-1}, 10^{4}]$ (bottom panel). For a detailed description see Fig. 3.4.

looback times $t < 10$ Myr increases the χ^2 to higher values. The uncertainties at these lookback times are due to the uncertainties in the SSP models, and are not physical. In any case the χ^2 increase to unacceptable values and for this reason we prefer to use the results obtained for $\mu_x = 10^2$, in which the χ^2 assumes lower values. The stripping age, in this case, is underestimated by at least 50 Myr.

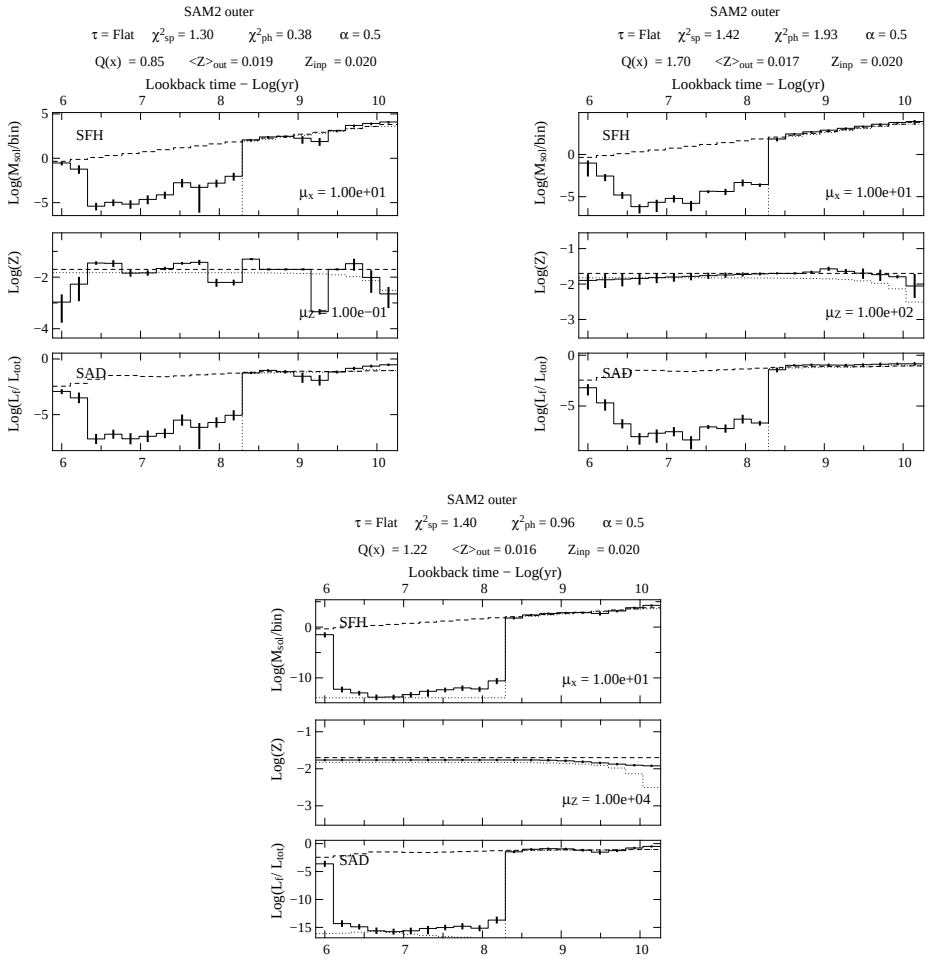

Figure 3.31: Results for non parametric inversion of combined analysis (spectral and photometric) corresponding to the galaxy model SAM2 with truncated star formation history at lookback time t = 130 Myr for: $[\mu_x, \mu_Z] = [10^1, 10^{-1}]$ (left panel), $[\mu_x, \mu_Z] = [10^1, 10^2]$ (right panel) and $[\mu_x, \mu_Z] = [10^1, 10^4]$ (bottom panel). For a detailed description see Fig. 3.4.

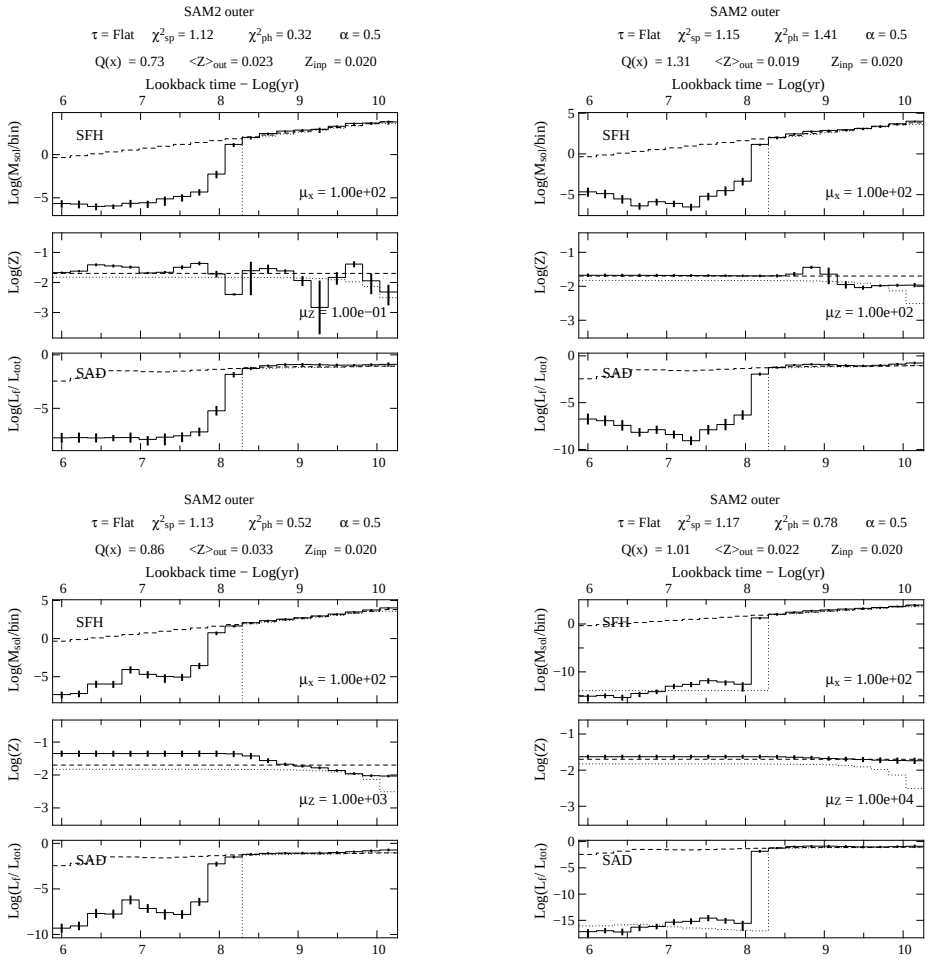

Figure 3.32: Results for non parametric inversion of combined analysis (spectral and photometric) corresponding to the galaxy model SAM2 with truncated star formation history at lookback time t = 130 Myr for: $[\mu_x, \mu_Z] = [10^2, 10^{-1}]$ (top left panel), $[\mu_x, \mu_Z] = [10^2, 10^1]$ (top right panel), $[\mu_x, \mu_Z] = [10^2, 10^3]$ (bottom right panel) and $[\mu_x, \mu_Z] = [10^2, 10^4]$ (bottom left panel). For a detailed description see Fig. 3.4.

Chapter 4

NGC 4388

4.1 Observations

The spectroscopic observations of NGC 4388 were performed over two nights (May 2-3, 2006) at the European Southern Observatory (ESO) Very Large Telescope (VLT) facility Cerro Paranal, Chile as part of the program ID 77.B-0039(A) (P.I. B. Vollmer). The instrument used was the FOcal Reducer and low dispersion Spectrograph 2 (FORS2, Appenzeller et al. 1998) in Long Slit Spectroscopy (LSS) observing mode. The detector system consisted of two 4096 $\times$ 2048 CCD with a pixel size of 15 μm. The slit dimesion was 418$''$ $\times$ 1$''$ and we chose a 2 $\times$ 2 binning of the pixels with high gain readout and standard resolution. The resulting image scale is 0.252$''$ / binned pixel. The selected grism was the GRIS-600B with a wavelength range of 3350 - 6330 Å, a central wavelength of 4650 Å. The pixel scale is 1.48 Å/pixel, which, with the selected slit, yields a spectral resolution of $\lambda/\Delta\lambda \approx 780$.

4.1.1 Data set

We adopt for NGC 4388 a distance of 16.7 Mpc (Yasuda et al. 1997), yielding a scale of 81 pc/arcsecond. For the acquisition the slit was pointed at two different regions of NGC 4388 (Fig. 4.1). We chose an inner region at about 1.5 kpc towards East direction from the galaxy center. We did not take exactly the center of the galaxy to avoid bulge contamination. The selected outer region lies just outside the HI disc, at about 4.5 kpc from the center. Individual exposure times were 600 sec for the inner region and 1350 sec for the outer. The total integration time for each region was 3600 and 9450 s, respectively (Tab. 4.1). Because of the bad weather conditions we used only the data obtained at the first night, which reduces the total integration to 1800 s for the inner region.

We used LTT4816, a white dwarf with $m_V = 13.96$ (Bakos et al., 2002) and

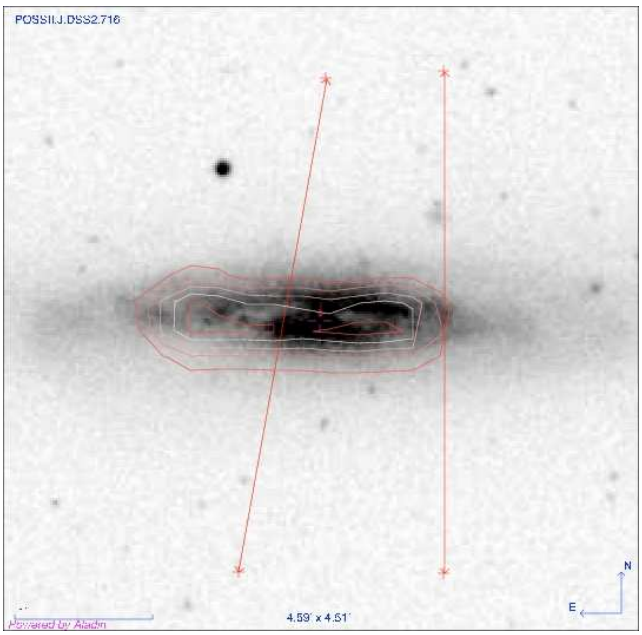

Figure 4.1: B-band POSSII image of NGC 4388 with superimposed HI density (red contours). The vertical red lines represents the slit positions.

LTT7987, a white dwarf with $m_V = 12.23$ (Perryman et al., 1997) as flux calibrators.

In addition to the spectroscopic observations we obtained during daytime calibration measurements (flat-field and bias), and wavelength calibration exposures (Hg-Cd-He lamps).

4.1.2 Data reduction

We performed Data Reduction procedures using the Image Reduction and Analysis Facilities (IRAF)[1] (Tody, 1993). We realized an average of the five bias frames using the IRAF **imcombine** task on **images.immatch** package.

In order to remove the cosmic rays and the bad pixels we applied to the combined images the **crreject** criterion of IRAF. Within this task we define a parameter *hsigma* and we reject only the positive pixels that are above *hsigma* time the average value of the input frame. In our case we defined a 3σ rejection criterion.

Although the aspect and the histograms of the five biases were similar, it turned out that two of them were corrupt. The consequence were low level periodic patterns in the residuals of the spectral fits. These suspicious patterns made us go back to the very first steps of the reduction, after we had checked all other potential sources (sky subtraction, flatfield, fringes). We summed in each bias frame all the selected

[1]IRAF is distributed by the National Optical Astronomy Observatory, which is operated by the Association of Universities for Research in Astronomy, Inc., under cooperative agreement with the National Science Foundation.

Table 4.1: Journal of Observations (ESO program ID 77.B-0039(A)). Seeing, airmass and UT (Universal Time) refer to the beginning of each observation.

Observation	Frame	Exp. Time (sec)	Seeing	Airmass	Date	UT
LTT4816 Ph.St.	1	35	0.91″	1.484	2006 May, 2	23:06
NGC4388 Inner	1	600	0.9″	1.688	2006 May, 2	23:45
NGC4388 Inner	2	600	1.11″	1.616	2006 May, 2	23:56
NGC4388 Inner	3	600	1.10″	1.554	2006 May, 3	00:07
NGC4388 Outer	1	1350	0.89″	1.330	2006 May, 3	01:11
NGC4388 Outer	2	1350	0.83″	1.289	2006 May, 3	01:34
NGC4388 Outer	3	1350	0.96″	1.264	2006 May, 3	01:58
NGC4388 Outer	4	1350	0.67″	1.256	2006 May, 3	02:21
NGC4388 Outer	5	1350	0.61″	1.423	2006 May, 3	04:10
NGC4388 Outer	6	1350	0.55″	1.519	2006 May, 3	04:33
NGC4388 Outer	7	1350	0.55″	1.651	2006 May, 3	04:57
LTT7987 Ph.St.	1	40	1.34″	1.010	2006 May, 3	10:35
NGC4388 Inner	1	600	-1.00″	1.690	2006 May, 4	04:59
NGC4388 Inner	2	600	-1.00″	1.861	2006 May, 4	05:09
NGC4388 Inner	3	600	-1.00″	1.868	2006 May, 4	05:20

rows and we subtracted subsequent frames from each other (i.e. we subtracted 1^{st} minus the 2^{nd}, the 2^{nd} minus the 3^{rd} and so on).

In Fig. 4.2 the second plot from the top shows the difference between the 3^{rd} and the 4^{th} bias frame. This new average value stays also in the 5^{th} frame, that shows no significant difference from the 4^{th} (plot on the top). In other words the bias frames underwent a significant change between 3^{rd} and 4^{th} exposure.

We iteratively reduced the data and analyzed the results of the spectral fit until there were no obvious periodic residuals in the fit. After this process we used only the first 3 frames to estimate the underlying level of the observations and we rejected the last two.

The response of the detector is not uniform mainly for two reasons:

- Each single pixel has a different answer to the same signals. To solve this problem we used quartz lamp flatfield exposures. We combined the flatfield frames using the median with no rejection criterion. We then subtracted the bias. The obtained frame removes the small scale effects due to the single pixel variations.

- The flatfield itself is not uniform on large scales, and in particular it has its own wavelength dependence. We account for this effect using the task **response**. The CCD used for the extraction has a dimension of 4096×2048 pix^2. We associate to each pixel a coordinate in the $x - y$ plane. We define the x-axis along the CCD-highest dimension (4096 pix) and the y-axis in the direction of

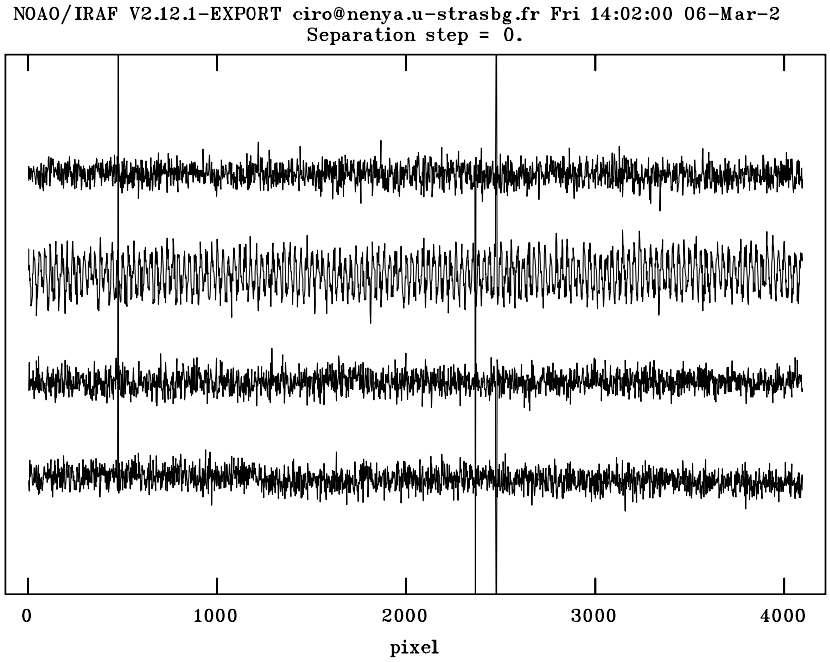

Figure 4.2: Difference between the bias frames in chronological order taken during daytime calibration of ESO program ID 77.B-0039(A). The results are offset for clarity.

lower dimension. The slit is aligned with y-axes. The task **response** averages along the CCD *y*-axis and extracts a one dimensional spectrum in *x* direction. We search then a function along this axis to fit the obtained profile. We use a cubic spline interpolation of 15^{th} order and we then divide the flatfield by this function along the y-axes.

The final result of these processes is a normalized flat-field. We subtracted the average bias from the raw data and we divided the result by the normalized flat-field. After carefully checking the average levels of the various frames, we combined all the data using the **imcombine** task to take the median of all the images.

We proceeded to the wavelength calibration, by extracting the spectra of an appropriate Hg-Cd-He lamp with known lines. We identified these same known emission lines in our calibration frame using the tasks **identify** and **reidentify** from **noao.twodspec** package. In this way we determined the function that transforms the *x*-axis coordinate of the CCD in wavelengths. The spectral lines of the lamp are almost, but not perfectly, aligned with the *y*-axis. We took into account this effect when using the task **reidentify**.

We applied the wavelength calibration to the data and we extracted a one-dimensional spectrum using the IRAF task **apall** from the **apextract** package. We

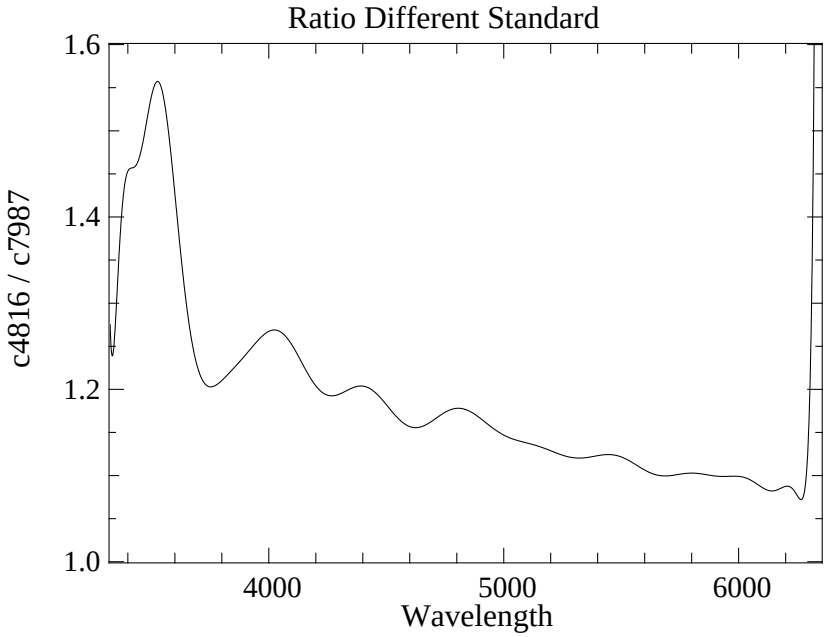

Figure 4.3: Ratio between the inner spectra of NGC 4388 obtained using LTT 4816 an LTT 7987 as flux calibrators. Large values below 3700 Å are due to the low signal level at these wavelengths. This is a consequence of the poor quantum efficiency of FORS2 CCD.

used an aperture of 32.76″ for both the inner and the outer region (lines [53-183] and [58-188] of the images, respectively) and two sky windows above and below the aperture (Fig. 4.11).

We finally proceeded with the flux calibration, i.e. the definition of a function that converts the number of ADU (Analogical Digital Unit) detected in physical units of flux per unit wavelength $F(\lambda)$, through the ”photometric standard” stars observed at the VLT. We used the spectrum of LTT 4816 and its intrinsic spectrum (Hamuy et al., 1992) to calibrate the flux of the spectra.

The absolute flux calibration has an accuracy of $\sim$ 20 % above 3700 Å at best. As a test we extracted two spectra for the inner region using respectively LTT 4816 and LTT 7987 as flux calibrators. In Fig. 4.3 is shown the ratio between the spectra obtained, that is in average $\sim$ 1.2. Note that LTT 7987 was observed far in time from the galaxy observations, with different seeing and airmass.

The wavelength-scale for the oscillations in Fig. 4.3 is approximatively 200 Å. This trend is taken into account for the continuum correction of the spectrum explained in App. C. Despite uncertainties in the flux calibration, our spectral analysis method is in fact able to correct this kind of errors, and an accuracy of 20% is sufficient for our purpose. The final reduced spectra are shown in Fig. 4.5.

To convert the spectra from Analogical Digital Unit (ADU), that are the output

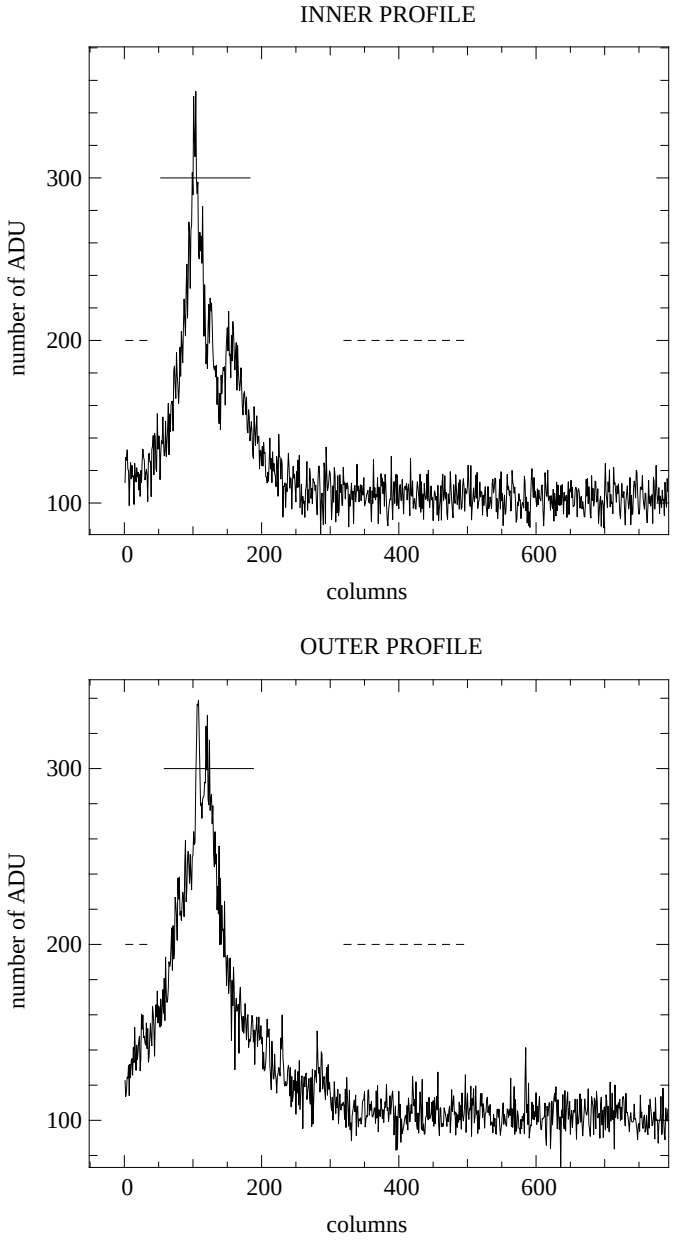

Figure 4.4: Top panel: Number of ADU versus number of column for the inner region CCD frame. The solid line shows the chosen window for the spectrum extraction and the dashed line show the window chosen for the sky determination. Bottom panel: same as the top panel for the CCD frame of the outer region.

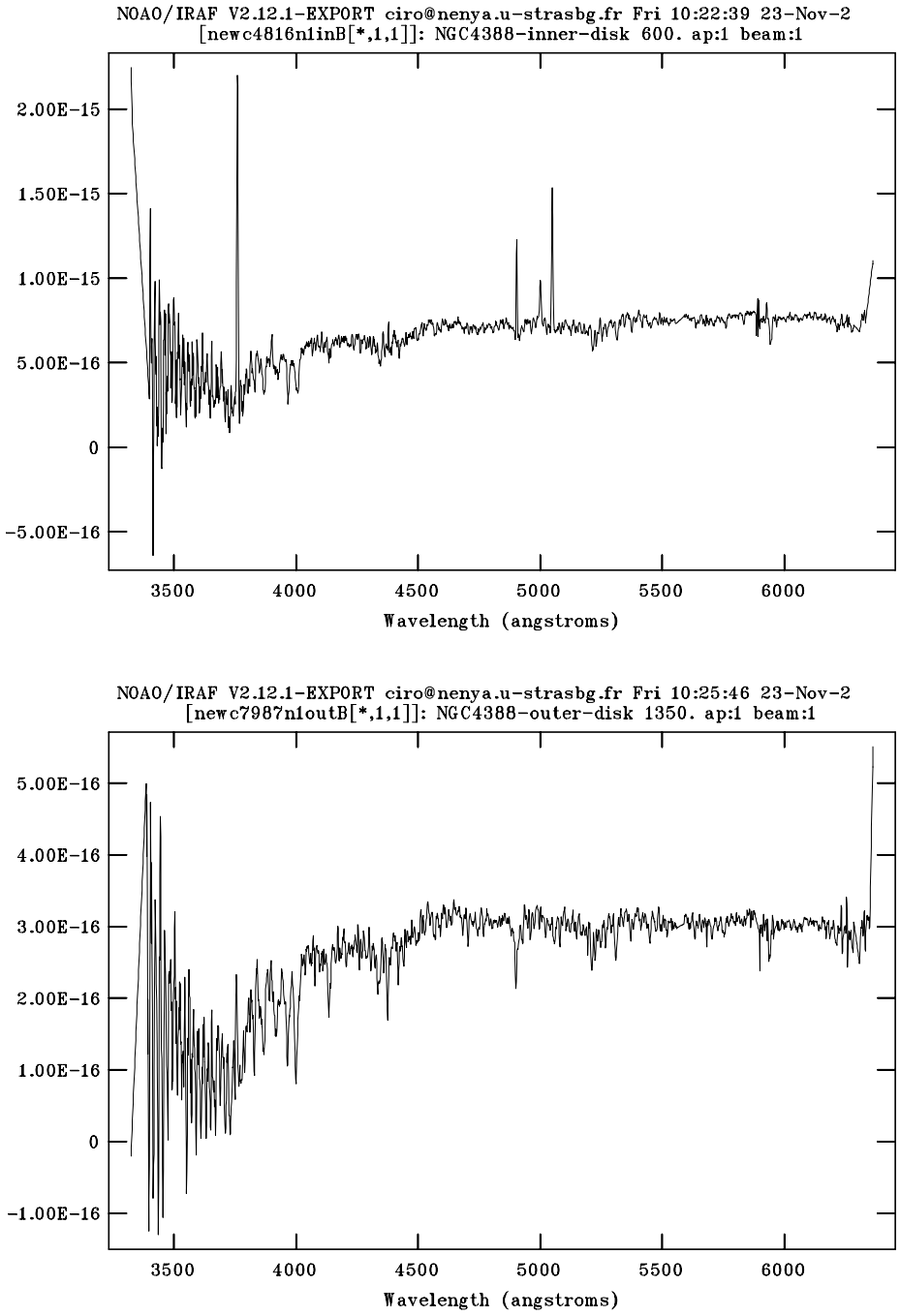

Figure 4.5: Integrated flux energy in erg/cm^2/sec /Å for the inner (top panel) and outer (bottom panel) regions of NGC 4388 in B-Band.

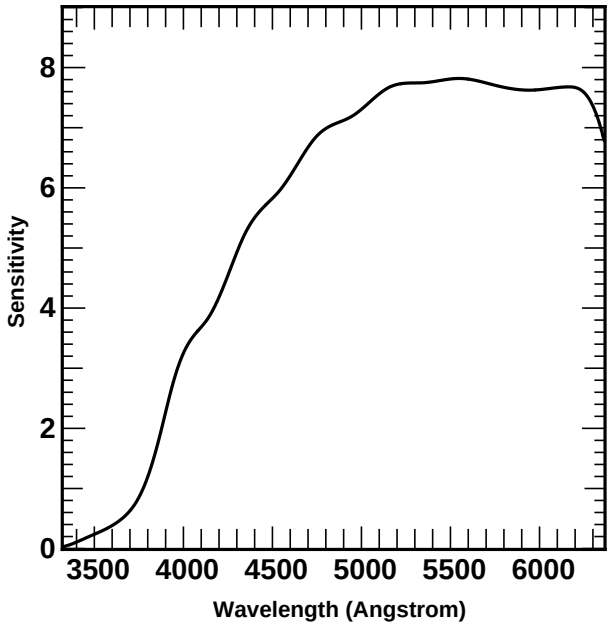

Figure 4.6: Normalized global sensitivity function in FORS2 observations. It is the sensitivity of the grism + optics + filter and detector.

unit of a CCD, to flux, we divide the spectra by the sensitivity function of the detector (Fig. 4.6). If the curve takes values close to zero, slight variations of the spectra become great oscillations in the final spectra. The sensitivity function decreases steeply for $\lambda < 3700$ Å (Fig. 4.6) and this affects the spectra, in which the noise increases dramatically at these wavelenghts.

For these reasons we did not use the shortest wavelengths in the analysis, multiplying the final spectra with a gate function, that is zero at the wavelengths that we do not want to consider, and one otherwise. The gate function is also useful to mask bad pixels and emission lines.

The final spectra for the inner and the outer regions are shown in Fig. 4.7 and Fig. 4.8. The average SNR per pixel for the inner and outer region are approximatively 60 and 26, respectively.

4.2 Photometry

In this section we show how we extracted the photometry of NGC 4388 using the same apertures as for the spectroscopic observations. We considered 10 broad passbands and for this purpose we retrieved NGC 4388 images from archives (Fig. 4.9):

- GALEX (Gil de Paz et al. 2007) provided images at Ultraviolet wavelengths

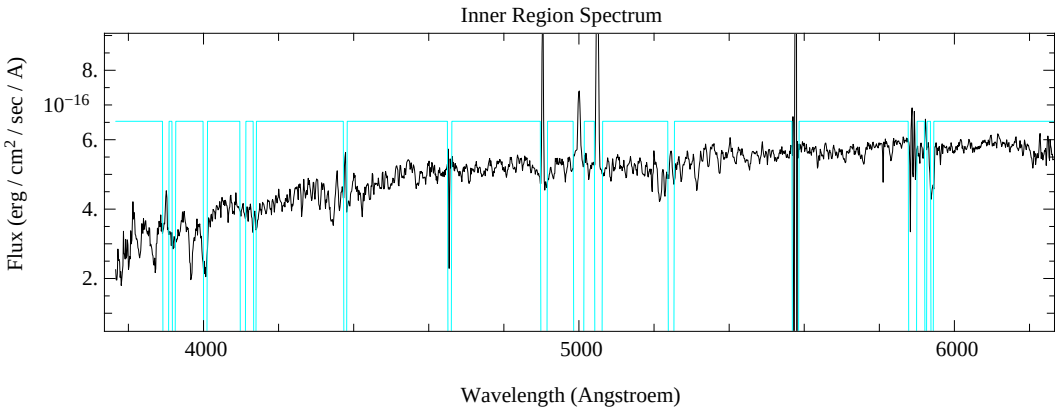

Figure 4.7: Integrated energy flux (in approximate units of [erg/cm^2/sec/Å]) for the inner region of NGC 4388 in B-band. The cyan line shows the gate function used to mask the bad pixels and the emission lines.

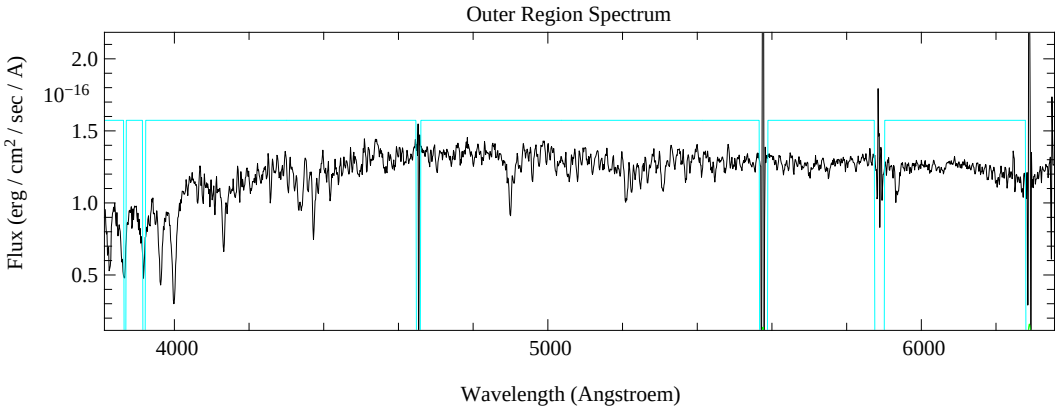

Figure 4.8: Integrated energy flux (in approximate units of [erg/cm^2/sec/Å]) for the outer region of NGC 4388 in B-band. The cyan line shows the gate function used to mask the bad pixels and the emission line.

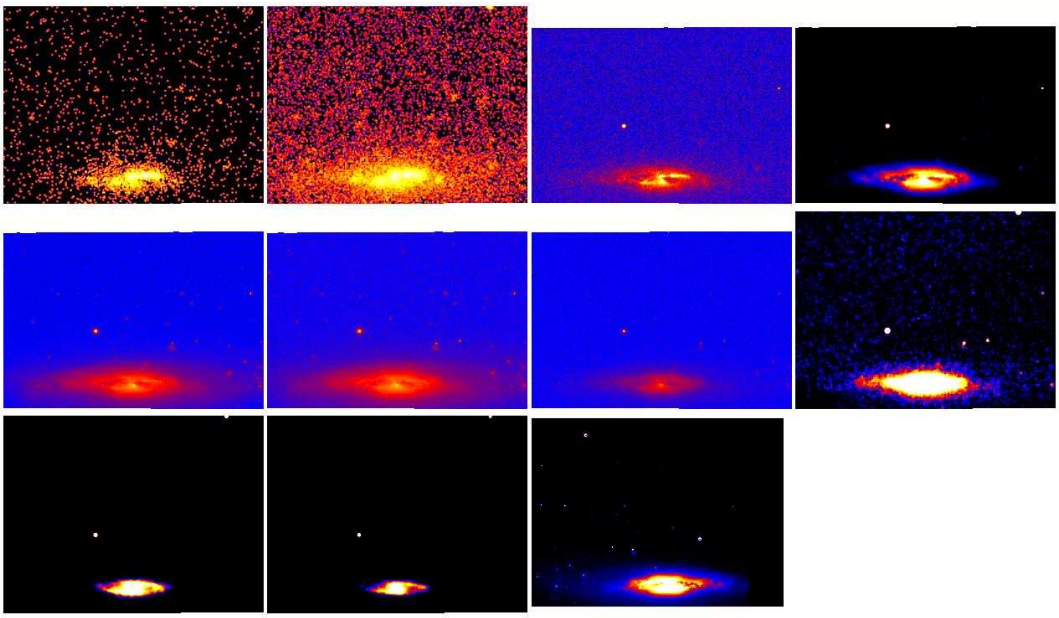

Figure 4.9: Images with different filters used for the photometric analysis. From the left to the right and from the top to the bottom are shown: $FUV, NUV, u', g', r', i', z', J, H, K$. The last image in the right of bottom row shows the acquisition frame image from VLT telescope without slit in the B-Band.

in FUV and NUV (courtesy of S. Boissier).

- SDSS-R6 (Adelman-McCarthy et al. 2008) provided u', g', r', i' and z' images.

- Near-Infrared J, H and K were taken from 2MASS (Skrutskie et al. 2006).

All images were resampled onto the coordinate grid used in FORS2 acquisition observations using ALADIN (Bonnarel et al. 2000).

In Fig. 4.10 is shown, as an example, the FORS2 spectroscopic CCD image for the outer region of NGC 4388. This image has been corrected for the bias, divided by the flatfield and summed to the other frames of the same observation block. From the spectroscopic images, collapsing along the wavelength axis, we recovered the light profile of the inner and the outer region (Fig. 4.11).

The exact locations of the two spectroscopic apertures on the broad-band images were determined by comparing the wavelength averaged profile along the FORS2 slits with cuts through the SDSS g' image (the filter that matches the transmission curve of GRISM-600B grism in FORS2 best). In both cases a clean peak in the cross correlation function allowed us to identify the slit position (Fig. 4.12) to within ± 1 pixel.

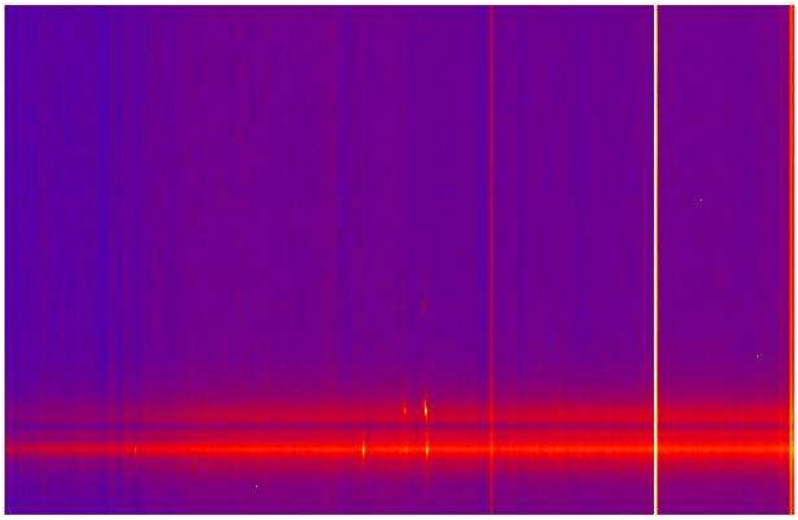

Figure 4.10: CCD image of the outer region of NGC 4388 corrected for the bias and the flatfield.

The pointing error for each magnitude was estimated by shifting the slit by one column to the left and one column to the right. We subtracted the new magnitudes from the reference value and took the highest difference as a measure of the uncertainty.

The photometric zero points of the optical and near-IR images were derived using star $J122549.86 + 124047.9$ (see Fig. 4.13), for which SDSS and 2MASS magnitudes are available (see Tab. 4.2).

For the GALEX images, we used the recipe of Morrissey et al. (2007) to convert count per second (CPS) into AB magnitudes (Oke, 1990):

$$m_{\mathrm{FUV}}(AB) = -2.5 log_{10}(CPS) + 18.82, \tag{4.1}$$

$$m_{\mathrm{NUV}}(AB) = -2.5 log_{10}(CPS) + 20.08. \tag{4.2}$$

The zero point defined in Eq. 4.2 are accurate within ±10% (Morrissey et al. 2007). GALEX images have a resolution of 4″. Therefore our aperture fluxes are contaminated by light outside the 1″ slit width. However this is a negligible effect with respect to the other sources of errors in the UV fluxes.

From the header file of the inner and the outer spectrum and from the cross-correlation test we recovered :

- The pixel scale : 0.252″ /binned pixel.

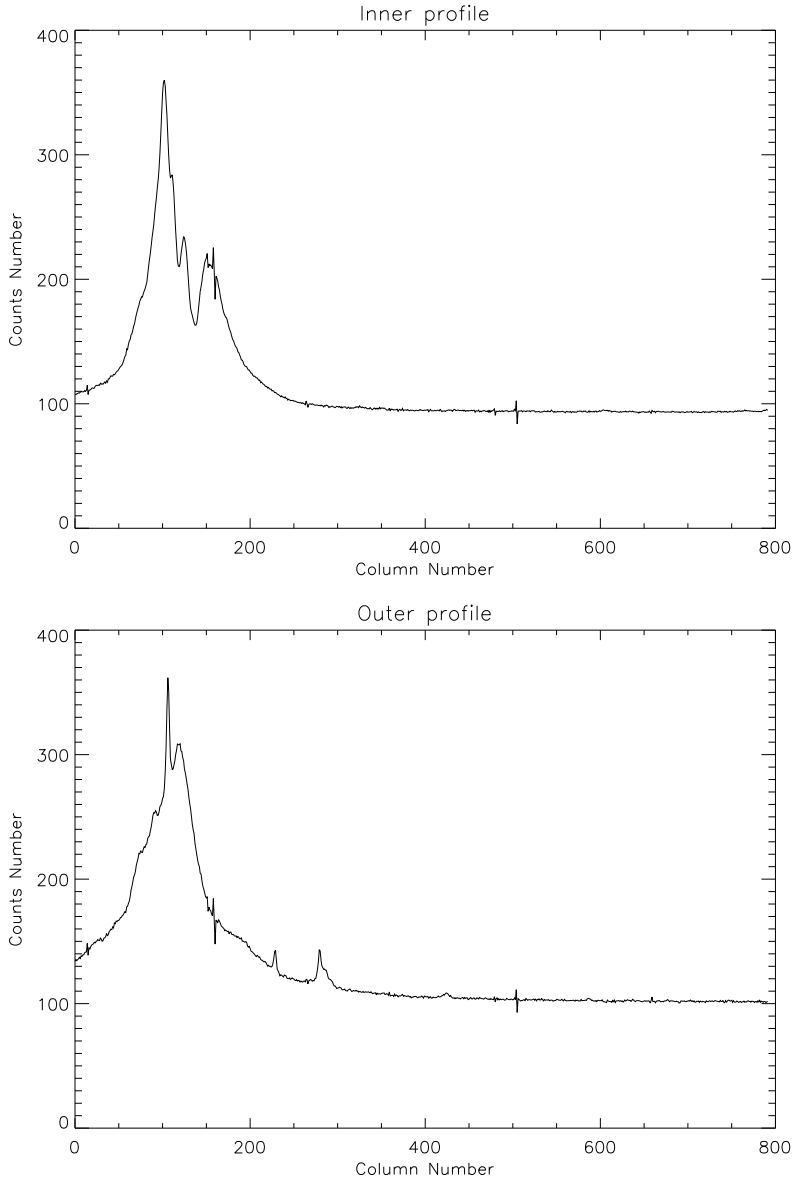

Figure 4.11: Light profile of the observations (number of counts vs. column number) for the inner (top panel) and the outer (bottom panel) region for NGC 4388. In the outer profile, as background galaxy column 280 is particularly useful for positioning.

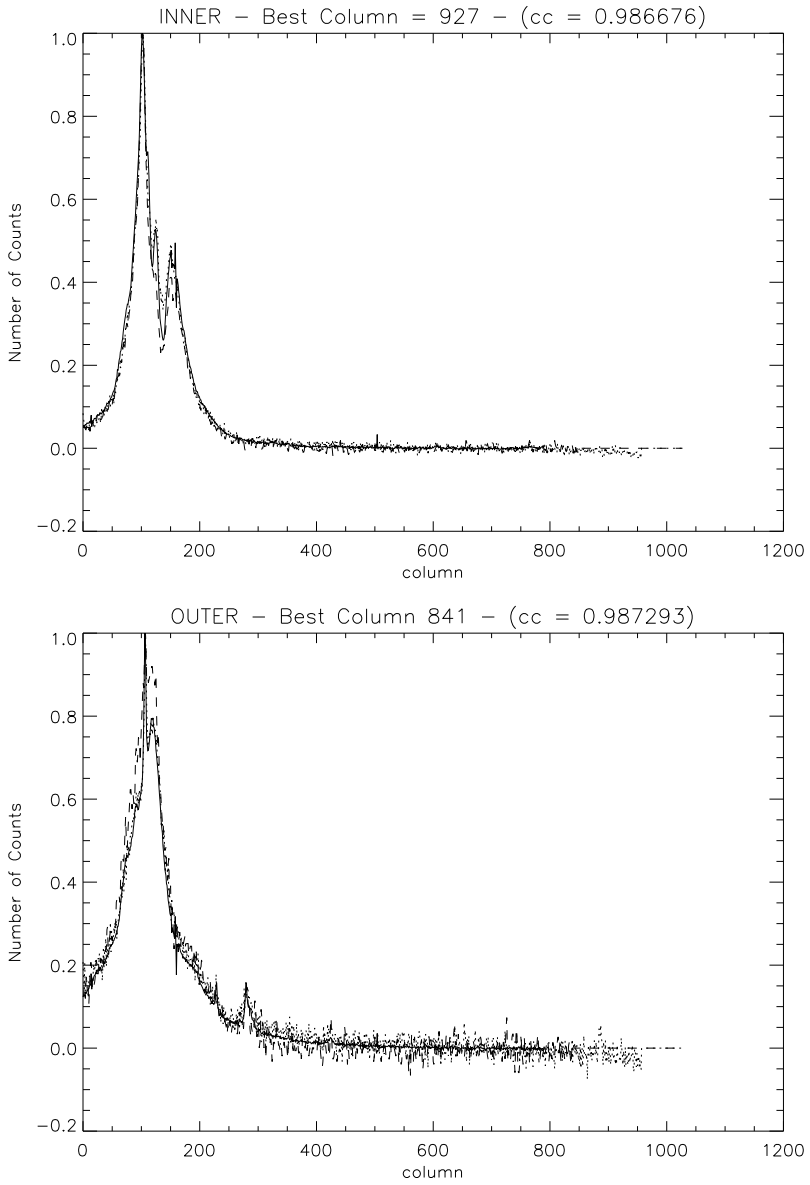

Figure 4.12: Best cross-correlation between the profile of g' image and the inner (top panel) and the outer (bottom panel) regions of NGC 4388 with the relative column number (top of each panel).

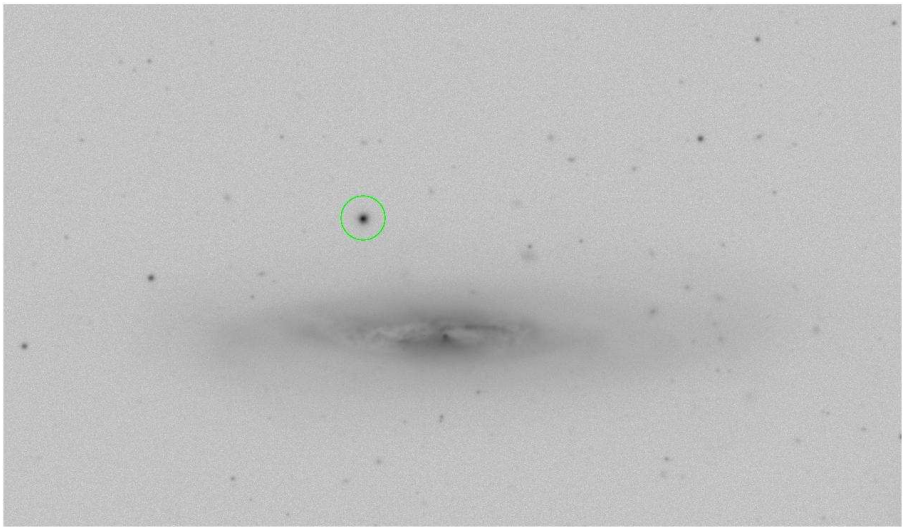

Figure 4.13: SDSS g' filter image with reference star $J122549.86+124047.9$ (green circle).

- The slit width : $\approx 1'' \approx 4$ pixels.
- The rows chosen for the extraction of the spectrum: [53 : 183] for the Inner and [58 : 188] for the Outer.
- The best cross correlation column : 927 and 814 for the inner and the outer respectively.

We defined then the extraction windows for the photometry,

- Inner : Column [926 : 929] Row [53 : 183]
- Outer : Column [813 : 816] Row [58 : 188],

and we applied:

$$m_{\text{band}} = -2.5 log_{10} \frac{F_{\text{obj}}(DN)}{F_{\text{star}}(DN)} + m_{\text{star}}, \tag{4.3}$$

where $F_{\text{obj}}, F_{\text{star}}$ are respectively the number of counts of the observed object and the number of counts of the reference star with magnitude m_{star} through the considered filter.

The measurement of $F_{\text{star}}(DN)$ requires a careful sky-subtraction. As reference image we take the SDSS g' filter and we estimate the sky-background considering a circle centered on the star. We find a value of 1069 DN, consistent with the sky value defined in the header file of the SDSS image ($\approx$ 1070 DN). If we overestimate the sky-level a fraction of the measured DN that are considered sky, belong to in reality to the star. As we increase the integrated area the DN subtracted to the

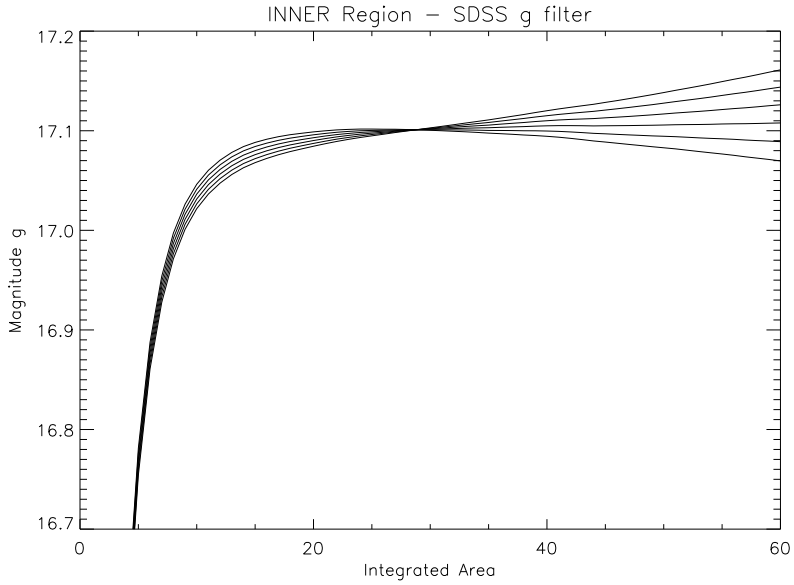

Figure 4.14: Inner region Magnitude versus integrated area of the reference star for a family of sky values. The correct sky value provides stable magnitude at large integrated areas.

real emission increases, and the magnitude decreases with increasing integrated area. The correct sky values gives increasing magnitude for the star until a *plateau*, and the corresponding asymptotic value corresponds the best estimation of the magnitude.

In Fig. 4.14 we show a family of curves obtained by varying the sky value. We estimate the average sky as the value that keeps the magnitude constant at large integrated areas, and this asymptote correspond to the magnitude value. Applying this method to all the filters for the inner and outer region we obtained the values in Tab. 4.2. We estimated the uncertainties on the final magnitudes for the galaxy apertures from a combination of the uncertainties of the flux measurements of the reference star (zero point) and those of the positioning of the slit:

$$\sigma^2_{\mathrm{TOT}} = \sigma^2_{\mathrm{SLIT}} + \sigma^2_{\mathrm{STAR}}. \tag{4.4}$$

Filter	FUV	NUV	u'	g'	r'	i'	z'	J	H	K
m_{AB}	–	–	16.78	15.06	14.35	14.69	14.07	13.08	12.65	12.52
σ_{star}	–	–	0.025	0.034	0.017	0.002	0.016	0.021	0.03	0.024
Inner	20.40	19.95	18.45	17.10	16.37	16.03	15.76	14.38	13.60	13.32
σ_s-In	0.17	0.04	0.01	0.02	0.04	0.04	0.04	0.04	0.02	0.05
Outer	22.21	21.30	19.49	18.07	17.47	17.18	17.03	16.08	15.06	14.75
σ_s-Out	0.31	0.07	0.08	0.06	0.07	0.07	0.03	0.33	0.04	0.12
σ_{tot}-In	0.2	0.1	0.03	0.04	0.04	0.04	0.04	0.05	0.04	0.06
σ_{tot}-Out	0.33	0.12	0.07	0.07	0.07	0.07	0.03	0.33	0.05	0.12

Table 4.2: NGC 4388 Photometry Determination. $1^{st}-2^{nd}$ row : Magnitude and error for the reference star 2MASS J122549.86 + 124047.9. For the UV filters (GALEX) we converted count per second (CPS) into AB magnitude using Morrissey et al. (2007). 3^{rd} – 4^{th} row: magnitude and error for the inner region. 5^{th} – 6^{th} row : magnitude and error for the outer regions. 7^{th} – 8^{th} row : total uncertainty for inner and outer region.

4.3 Pinning down the ram pressure induced halt of star formation in the Virgo cluster spiral galaxy NGC 4388

In this section we attached the paper showing the main results of the method. The paper has been accepted for publication with minor revision in Astronomy & Astrophysics.

Astronomy & Astrophysics manuscript no. draft˙v5
November 4, 2009

Pinning down the ram-pressure-induced halt of star formation in the Virgo cluster spiral galaxy NGC 4388.

A joint inversion of spectroscopic and photometric data.

C. Pappalardo[1], A. Lançon[1], B. Vollmer[1], P. Ocvirk[2], S. Boissier[3], & A. Boselli[3]

[1] Observatoire astronomique de Strasbourg, Université de Strasbourg & CNRS UMR7550, 11 rue de l'Université, 67000 Strasbourg, France e-mail: ciro.pappalardo@astro.u-strasbg.fr
[2] Astrophysikalisches Institut Potsdam, An der Sternwarte 16, 14482 Potsdam, Germany
[3] Laboratoire d'Astrophysique de Marseille, OAMP, Université Aix-Marseille & CNRS UMR6110, 38 rue Frédéric Joliot Curie, 13388 Marseille Cedex 13, France

Preprint online version: November 4, 2009

ABSTRACT

Context. In a galaxy cluster, the evolution of spiral galaxies depends on their cluster environment. Ram pressure due to the rapid motion of a spiral galaxy within the hot intracluster medium removes the galaxy's interstellar medium from the outer disk. Once the gas has left the disk, star formation stops. The passive evolution of the stellar populations should be detectable in optical spectroscopy and multi-wavelength photometry.
Aims. The goal of our study is to recover the stripping age of the Virgo spiral galaxy NGC 4388, i.e. the time elapsed since the halt of star formation in the outer galactic disk using a combined analysis of optical spectra and photometry.
Methods. We performed VLT FORS2 long slit spectroscopy of the inner star-forming and outer gas-free disk of NGC 4388. We developed a non-parametric inversion tool that allows us to reconstruct the star formation history of a galaxy from spectroscopy and photometry. The tool is tested on a series of mock data using Monte Carlo simulations. The results from the non-parametric inversion are refined by applying a parametric inversion method.
Results. The star formation history of the unperturbed galactic disk is flat. The non-parametric method yields a rapid decline of star formation $\sim$ 300 Myr ago in the outer disk. Due to the necessary regularization of the inversion, the derived star formation truncation is not sharp. The parametric method gives a final stripping age of 190 $\pm$ 30 Myr.
Conclusions. We are able to give a precise stripping age which is consistent with revised dynamical models.

Key words. Galaxies: evolution – Galaxies: clusters: individual: Virgo cluster – Galaxies: individual: NGC 4388 – Galaxies: stellar content

1. Introduction

Depending on the environment in which they move, spiral galaxies undergo different processes that can modify their structure significantly (see Boselli & Gavazzi 2006 and references therein):

- gravitational effects (e.g. tidal interactions in galaxy-galaxy encounters),
- hydrodynamical effects (e.g. ram pressure stripping or thermal evaporation),
- hybrid processes, i.e. those involving both types of effects, such as preprocessing and starvation.

The closest cluster of galaxies in the northern hemisphere is the Virgo cluster ($d \approx 16.7$ Mpc, Yasuda et al. 1997), with a mass of $M = 1.2 \times 10^{15} M_{\odot}$ and a radius of about 2.2 Mpc (Fouqué et al. 2001). Virgo is an evolving cluster that is still dynamically active. The cluster-core is centered on M87, the most massive elliptical galaxy. Other sub-clumps are falling into the potential well of the cluster.

One important characteristic of Virgo spiral galaxies is their lack of gas (Giovanelli & Haynes 1983, Chamaraux et al. 1980). The amount of atomic gas in Virgo spirals is up to 80% less than that of field galaxies of the same size and morphological type. Virgo spirals show truncated HI disks (Giovanelli & Haynes 1983, Cayatte et al. 1990) with respect to their optical disks. The galaxies on radial orbits are on average more HI deficient than the ones on circular orbits (Dressler 1986). Chung et al. (2009) found long HI tails associated with spiral galaxies located at distances from 0.5 to 1 Mpc from the cluster center. For these cases, ram pressure stripping is the most probable cause. The interstellar medium (ISM) of a spiral galaxy that is moving inside the potential well of a cluster, undergoes a pressure due to the intracluster medium (ICM), that is hot ($T_{\rm ICM} \approx 10^7 - 10^8$ K) and tenuous ($\rho_{\rm ICM} \approx 10^{-3} - 10^{-4}$ atoms cm^{-3}). If this pressure is larger than the restoring force due to the galactic potential, the galaxy loses gas from the outer disk. Quantitatively this is expressed by the Gunn & Gott (1972) criterion:

$$\rho_{\rm ICM} v_{\rm gal}^2 \geq 2\pi G \Sigma_{\rm star} \Sigma_{\rm gas}, \quad (1)$$

where $\rho_{\rm ICM}$ is the density of the ICM, $v_{\rm gal}$ is the peculiar velocity of the galaxy inside the cluster, $\Sigma_{\rm star}$ and $\Sigma_{\rm gas}$ are the surface density of stars and gas, respectively. Ram pressure stripping has been studied theoretically (e.g. Vollmer et al. 2001, Schulz & Struck 2001, Quilis et al. 2000, Abadi et al. 1999, Roediger & Brüggen 2008) and observationally (e.g. Kenney et al. 2004, Solanes et al. 2001, Cayatte et al. 1990, Warmels 1988, Chung et al. 2009).

NGC 4388 is a highly inclined Seyfert 2 spiral galaxy (of type Sab) with $m_B = 12.2$ mag and radial velocity of $V_{\rm rad} \sim 1400$ km s^{-1} with respect to the cluster mean. It is located at a projected distance of 1.3° (≈ 400 kpc at 16.7 Mpc distance) from the Virgo cluster center (M87). NGC 4388 has lost 85% of its HI gas mass (Cayatte et al. 1990). The HI distribution is strongly truncated within the optical disk. By observing the galaxy in Hα Veilleux et al. (1999b) found a large plume of ionized gas extending 4 kpc above the plane. In subsequent SUBARU observations Yoshida et al. (2002) revealed a more extended tail out to 35 kpc to the North-East. Vollmer & Huchtmeier (2003) performed 21-cm line observations with the Effelsberg 100-m radio telescope. They discovered neutral gas associated with the Hα plume out to at least 20 kpc NE of NGC 4388's disk, with an HI mass of 6×10^7 M$_\odot$. With interferometic observations Oosterloo & van Gorkom (2005) showed that this HI tail is even more extended, with a size of 110×25 kpc and a mass of 3.4×10^8 M$_\odot$.

In the case of NGC 4388 Vollmer & Huchtmeier (2003) estimated that ram pressure stripping is able to remove more than 80% of the galaxy's ISM, consistently with the observations of Cayatte et al. (1990). They also estimated that the galaxy passed the cluster center ∼ 120 Myr ago. However this estimation is based on the observations of Vollmer & Huchtmeier (2003). The more extended HI tail found by Oosterloo & van Gorkom (2005) implies that this time-scale increases.

Once the gas has left the galactic disk, star formation, that is ultimately fueled by the neutral hydrogen, stops. Stripping is believed to progress inwards from the outermost disk on timescales of order 10^8 years. But at any given radius stripping happens within a shorter timescale. The stellar populations then evolve passively and this is detectable both in optical spectra and in the photometry. The detailed analysis of the stellar light provides essential information on the stripping age, i.e. the time elapsed since the halt of star formation. These constraints are independent of dynamical models, and can be compared to those derived from the gas morphology and kinematics. Crowl & Kenney (2008) analyzed the stellar populations of the gas-free outer disk of NGC 4388, 5.5 kpc off the center (with our adopted distance of 16.7 Mpc). They used SparsePak spectroscopy and GALEX photometry. Their age diagnostics are based on Lick indices and UV fluxes which they compare to stellar population synthesis predictions (models of Martins et al. 2005). Assuming that the past star formation rate in the galaxy has been constant over long timescales, they conclude the stripping of the gas from the outer disk occured 225 ± 100 Myr ago. Our renewed analysis is based on VLT FORS2 long slit spectroscopy of NGC 4388 taken at two positions:

- The first slit was pointed at 1.5 kpc from the center, in a gas-normal star-forming region of the disk. We did not take exactly the center to avoid bulge contamination.
- The second slit was pointed at 4.5 kpc from the center, just outside the star-forming gas disk.

The spectra are combined with multi-wavelength photometry. The long term star formation history of the galaxy is obtained using an extension of the non parametric inversion method of Ocvirk et al. (2006). It combines the information provided by the spectroscopic and photometric data, and determines the star formation history using minimal constraints on the solutions. The results are then refined using a parametric method that assumes the halt of star formation at the observed outer position in the disk occurs quasi-instantaneously.

The paper is structured as follows: in Sect.s 2 and 3 we describe the observations and we explain how we extract the photometry that we use as input data. In Sect. 4 we introduce the new approach used in this paper that combines spectral and photometric analysis. In Sect. 5 and 6 we detail the results of this new method in the case of NGC 4388 and we discuss them. Finally, in Sect. 7 we give our conclusions and compare our results to previous work.

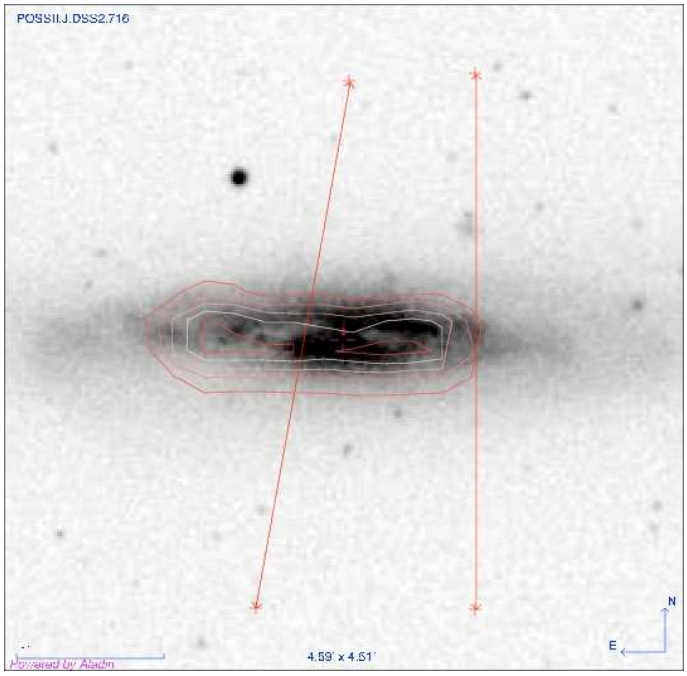

Fig. 1. B-band POSSII image of NGC4388 with HI contours. The slit positions for the inner and the outer regions are overlaid.

2. Observations

2.1. Data Set

We performed observations of NGC4388 on May 2, 2006 at the European Southern Observatory Very Large Telescope (VLT) facility on Cerro Paranal, Chile. The instrument used was the FOcal Reducer and low dispersion Spectrograph 2 (FORS2, Appenzeller et al. 1998) in Long Slit Spectroscopy observing mode. The detector system consisted of two 4096 × 2048 CCD. We chose 2 × 2 binning of the pixels (image-scale 0.252″/ binned pixel) and high gain readout. We selected grism GRIS-600B with a wavelength range of 3350 – 6330 Å and a resolution of 1.48 Å / binned pixel. The data were acquired through a 1″ slit, yielding a resolving power of $\lambda/\Delta\lambda \approx 780$ at the central wavelength.

The two slit positions used for the acquisition are shown in Fig. 1 together with HI contours. Individual exposure times were 600 s for the inner region and 1350 s for the outer. The total integration time for each region were of 1800 s and 9450 s respectively (Table 1). We used LTT 4816 and LTT 7987, two white dwarfs respectively with $m_V = 13.96$ and $m_V = 12.23$ (Bakos et al. 2002, Perryman et al. 1997) as spectrophotometric standards.

2.2. Data Reduction

Data reduction procedures were performed using the `images` and `noao.twodspec` packages of the Image Reduction and

Table 1. Journal of Observations (ESO program ID 77.B-0039(A)). Seeing, airmass and UT (Universal Time) refer to the beginning of each acquisition.

Observation	Frame	Exp. Time (sec)	Seeing	Airmass	Date	UT
LTT4816 Ph.St.	1	35	0.91″	1.484	2006 May, 2	23:06
NGC4388 Inner	1	600	0.9″	1.688	2006 May, 2	23:45
NGC4388 Inner	2	600	1.11″	1.616	2006 May, 2	23:56
NGC4388 Inner	3	600	1.10″	1.554	2006 May, 3	00:07
NGC4388 Outer	1	1350	0.89″	1.330	2006 May, 3	01:11
NGC4388 Outer	2	1350	0.83″	1.289	2006 May, 3	01:34
NGC4388 Outer	3	1350	0.96″	1.264	2006 May, 3	01:58
NGC4388 Outer	4	1350	0.67″	1.256	2006 May, 3	02:21
NGC4388 Outer	5	1350	0.61″	1.423	2006 May, 3	04:10
NGC4388 Outer	6	1350	0.55″	1.519	2006 May, 3	04:33
NGC4388 Outer	7	1350	0.55″	1.651	2006 May, 3	04:57
LTT7987 Ph.St.	1	40	1.34″	1.010	2006 May, 3	10:35

Analysis Facility (IRAF)[1] (Tody, 1993). We created average bias and flat-field images using daytime calibration and we removed cosmic ray hits using a 3σ-clipping rejection.

After bias and flat-field correction, we combined the individual galaxy exposures and applied the wavelength calibration to the spectral axis of the images. The aperture used for the extraction of 1D spectra covers a length of 32.76″ along the slit for both the inner and the outer regions of NGC 4388. The sky subtraction was based on a linear fit to the sky windows on either side of the aperture. Finally, we used the spectrum of LTT 4816 and its intrinsic fluxes (Hamuy et al., 1992) to calibrate the flux of the spectra. The flux calibration is $\approx$ 20% accurate, based on the comparison of the energy distributions obtained using either LTT4816 or LTT7987 as a standard.

The final reduced spectra for the inner and outer regions are shown in section 5. The average signal-to-noise ratio per pixel for the inner and outer region are $\approx$ 60 and $\approx$ 26 respectively inside the wavelength ranges used in the analysis.

3. Photometry

For the photometry we use the following archive data:

- GALEX (Gil de Paz et al. 2007): FUV and NUV.
- SDSS (Rel. 6, Adelman-McCarthy et al. 2008): u', g', r', i', and z'.
- 2MASS (Skrutskie et al. 2006) : J, H, and K.

The archive images were resampled onto the coordinate grid used in FORS2 observations using ALADIN (Bonnarel et al. 2000). The photometric zero points were derived using the star 2MASS $J122549.86 + 124047.9$ (Table 2).

For the GALEX images, we used the formulae of Morrissey et al. (2007) to convert counts per second (CPS) into AB magnitudes. The zero points defined are accurate to within ±10% (Morrissey et al. 2007).

The exact locations of the two spectroscopic apertures on the images were determined by comparing the wavelength-averaged profile along the FORS2 slits with cuts through the SDSS g' image. In both cases a clean peak in the cross correlation function allowed us to identify the slit position to within 1 pixel size. The GALEX images have a spatial resolution of about 4″. Light measured within a 1″ aperture is contaminated by neighbouring areas, but this effect is smaller than the uncertainties already accounted for, which are large, because of low signal levels.

We estimate the uncertainties on the final magnitudes for the galaxy apertures from a combination of the uncertainties on the flux measurements of the reference star (zero point) and those of the positioning of the slit (see Table 2):

$$\sigma^2_{\rm TOT} = \sigma^2_{\rm SLIT} + \sigma^2_{\rm STAR}. \quad (2)$$

4. Method

The spectral energy distribution (SED) of a galaxy can be considered as the integrated light produced by different stellar populations with different ages and metallicities. The light and mass contributions of each population depend on the star formation history of the observed region during the galaxy's life.

If we define an Initial Mass Function and a set of stellar libraries, we can obtain, integrating over the stellar masses, the intrinsic spectrum $B^0(\lambda, t, Z)$ of the single stellar population of age t, metallicity Z and unit mass. Assuming that the metallicities of the stars can be described by a single valued Age-Metallicity Relation $Z(t)$, we can derive the unobscured SED of a galaxy at rest:

$$F_{\rm rest}(\lambda) = \int_{t_{\rm min}}^{t_{\rm max}} SFR(t)\; B^0(\lambda, t, Z(t))\; {\rm d}t, \quad (3)$$

in which $SFR(t)$ represents the mass of new stars born per unit time, with the convention that $t_{\rm min} = 0$ is today, and $t_{\rm max}$ is the Hubble time.

Since we observe the light and not the mass in a galaxy, it is more convenient to convert the mass weighted spectral basis $B^0(\lambda, t, Z)$ into a luminosity weighted basis. The difference is that $B^0(\lambda, t, Z)$ defines the spectrum of a Single Stellar Population (SSP) of unit mass, and $B(\lambda, t, Z)$ defines a SSP spectrum of unit flux. Instead of mass contributions we deal with light contributions, thus converting the SFR into the Luminosity Weighted Stellar Age Distribution (hereafter SAD):

$$\Lambda(t) = \frac{SFR(t)}{\Delta\lambda} \int_{\lambda_{\rm min}}^{\lambda_{\rm max}} B^0(\lambda, t, Z)\; {\rm d}\lambda, \quad (4)$$

where $\Delta\lambda = \lambda_{\rm max} - \lambda_{\rm min}$ is the available wavelength domain, and $\Lambda(t)$ gives the contribution to the total light from the stars of age $[t, t + {\rm d}t]$.

[1] IRAF is distributed by the National Optical Astronomy Observatory, which is operated by the Association of Universities for Research in Astronomy, Inc., under cooperative agreement with the National Science Foundation.

Filter	FUV	NUV	u'	g'	r'	i'	z'	J	H	K
m_{AB}	–	–	16.78	15.06	14.35	14.69	14.07	13.08	12.65	12.52
σ_{star}	–	–	0.025	0.034	0.017	0.002	0.016	0.021	0.03	0.024
Inner	20.40	19.95	18.45	17.10	16.37	16.03	15.76	14.38	13.60	13.32
σ_{SLIT}-Inner	0.17	0.04	0.01	0.02	0.04	0.04	0.04	0.04	0.02	0.05
Outer	22.21	21.30	19.49	18.07	17.47	17.18	17.03	16.08	15.06	14.75
σ_{SLIT}-Outer	0.31	0.07	0.08	0.06	0.07	0.07	0.03	0.33	0.04	0.12
σ_{TOT}-Inner	0.2	0.1	0.03	0.04	0.04	0.04	0.04	0.05	0.04	0.06
σ_{TOT}-Outer	0.33	0.12	0.07	0.07	0.07	0.07	0.03	0.33	0.05	0.12

Table 2. NGC 4388 photometry. $1^{st} - 2^{nd}$ row : magnitude and error for the reference star 2MASS $J122549.86 + 124047.9$. For the UV filters (GALEX) we converted counts per second (CPS) into AB magnitude using Morrissey et al. (2007). $3^{rd} - 4^{th}$ row: magnitude and error for the inner region. $5^{th} - 6^{th}$ row : magnitude and error for the outer regions. $7^{th} - 8^{th}$ row : total uncertainty for inner and outer region.

With

$$B(\lambda, t, Z) = \frac{B^0(\lambda, t, Z)}{\frac{1}{\Delta\lambda}\int_{\lambda_{\min}}^{\lambda_{\max}} B^0(\lambda, t, Z)\,\mathrm{d}\lambda}, \quad (5)$$

Eq. 3 becomes:

$$F_{\rm rest}(\lambda) = \int_{t_{\min}}^{t_{\max}} \Lambda(t) B(\lambda, t, Z(t))\,\mathrm{d}t. \quad (6)$$

In the same way we can associate with each spectrum $B(\lambda, t, Z(t))$ a photometric value for the set of bandpasses defined in Table 2:

$$B_{\rm phot}(y, t, Z(t)) = \frac{\int_{\lambda_{\min}}^{\lambda_{\max}} B(\lambda, t, Z(t)) \cdot T_y(\lambda)\,\lambda\,\mathrm{d}\lambda}{\int_{\lambda_{\min}}^{\lambda_{\max}} T_y(\lambda)\,\lambda\,\mathrm{d}\lambda}, \quad (7)$$

in which $y = [FUV, NUV, u', g', i', r', z', J, H, K]$ and T_y is the transmission curve associated with each y. Unobscured photometry $F_{\rm phot}(y)$ is given by:

$$\begin{aligned} F_{\rm phot}(y) &= \int_{t_{\min}}^{t_{\max}} SFR(t)\, B^0_{\rm phot}(y, t, Z(t))\,\mathrm{d}t \\ &= \int_{t_{\min}}^{t_{\max}} \Lambda(t)\, B_{\rm phot}(y, t, Z(t))\,\mathrm{d}t. \end{aligned} \quad (8)$$

Eq. 6 is not complete, because it does not take into account other effects that can modify the final shape of the SED of a galaxy:

• Extinction : when fitting spectroscopic data we use a flexible continuum correction that can account both for the reddening due to dust and for flux calibration errors. The method allows us to use the information present in the spectral lines without using the continuum of the spectrum, which is preferable when the flux calibration is not perfect. In practice, we define a set of equally spaced anchor points across the wavelength range of the optical spectra. Their ordinates are then optimized in a way that the cubic spline interpolation through the points cancels out any SED difference between models and data. We refer to this adjustable correction as NPEC hereafter (for "Non Parametric Estimate of the Continuum").

For the photometry however extinction must be accounted for explicitly. We adopt the attenuation law of Calzetti (2001), that uses the color excess $E(B-V)$ as a single parameter (see however Sect. 6).

• Radial velocities of the stars : we assume that the velocities of stars of all ages along the line of sight have the same velocity distribution. The galaxy spectrum $F_{\rm spec}$ results from the convolution of the spectrum at rest $F_{\rm rest}$ with a line of sight velocity distribution. Note that the comparison between models and data also requires to smooth the models to the spectral resolution of the observations. For brevity, and because kinematics are not the purpose of this article, we will often refer to both effects as the spectral broadening function (BF) below.

Recovering the star formation history ultimately means finding a $\Lambda(t)$ that fulfills Eqs. 6 and 8 while accounting for the corrections just described. To do this we use two different approaches:

- a non parametric method in which we recover the star formation history by resolving the associated inverse problem with regularized methods (see Ocvirk et al. 2006);
- a parametric method in which we define a set of possible $\Lambda(t)$ depending on one free parameter, the time elapsed since the stripping event. We then find the most probable solution by minimizing the classical χ^2 function.

The non parametric method has the advantage of providing the star formation history and trends in the age-metallicity relation of the galaxy with minimal constraints on their shape. On the other hand, the regularization of the problem does not allow us to recover functional forms with large gradients, such as those expected for a ram pressure stripping event. This is why we combine the results from the non-parametric analysis with a parametric analysis.

We chose as SSP library the models of Bruzual & Charlot (2003), that cover a time interval $\Delta t = [0 - 19.5]$ Gyr, a wavelength range $\lambda\lambda = [100 - 24850]$Å with a spectral resolution (FWHM) $R = 2000$. These SSP spectra are constructed with stellar spectra from Le Borgne et al. (2003). The underlying stellar evolution tracks are those of Alongi et al. (1993), Bressan et al. (1993), Fagotto et al. (1994a), Fagotto et al. (1994b) and Girardi et al. (1996).

4.1. Non Parametric Method

The non parametric method is described in detail in Ocvirk et al. (2006). Here we extend it to deal with spectroscopy and photometry jointly.

Assuming gaussian noise in the data we estimate the most likely solution by minimizing the following $Q_\mu(\mathbf{X})$ function for the star formation history and age-metallicity relation:

$$Q_\mu(\mathbf{X}) = (1-\alpha)\cdot\chi^2_{\rm spec}(\mathbf{X}) + \alpha\cdot\chi^2_{\rm phot}(\mathbf{X}) + \mu\cdot P(\mathbf{X}), \quad (9)$$

in which:

- $\mathbf{X}$ is a vector that includes the SAD, the metallicity evolution, the color excess $E(B-V)$ for the photometry, the NPEC correction vector for spectral analysis and a spectral broadening

function (BF). The latter includes the effects due to the line of sight velocity distribution and the broadening introduced by the instrumentation.

– $$\chi^2_{\rm spec}(\mathbf{X}) = \frac{1}{N_\lambda}\sum_{i=1}^{N_\lambda}\frac{\left(F_{\rm mdlspec}(\lambda) - F_{\rm spec}(\lambda)\right)^2}{\sigma^2_{\rm spec}}, \quad (10)$$
is the χ^2 associated with the spectrum. $F_{\rm mdlspec}(\lambda)$ is the model with a defined $\mathbf{X}$ and $F_{\rm spec}(\lambda)$ is the observed spectrum, $\sigma^2_{\rm spec}$ is the associated error in the observations and $N_\lambda \sim 1700$ is the number of points in the spectrum, that we can consider approximately equal to the number of degrees of freedom of the problem.

– $$\chi^2_{\rm phot}(\mathbf{X}) = \frac{1}{N_y}\sum_{i=1}^{N_y}\frac{\left(F_{\rm mdlphot}(y) - F_{\rm phot}(y)\right)^2}{\sigma^2_{\rm phot}}, \quad (11)$$
is the χ^2 associated with the photometry, where $F_{\rm mdlphot}(y)$ is the model photometry obtained from Eq. 8 with a chosen $\mathbf{X}$, $F_{\rm phot}(y)$ are the photometric data and $\sigma^2_{\rm phot}$ are the errors in the measures, N_y represents the number of bandpasses used.

– $$\mu P(\mathbf{X}) = \mu_x P(\rm SAD) + \mu_Z P(\rm AMR) + \mu_{NPEC} P(\rm E) + \mu_{BF} P(\rm BF) \quad (12)$$
is a penalty function necessary to regularize the problem. As shown in Ocvirk et al. (2006) the inverse problem associated with Eqs. 6 and 8 is ill-posed. The function $P(\mathbf{X})$ is chosen to yield large values when the SAD and AMR are very irregular function of time, or when the BF or the NPEC correction are too chaotic. The set of $\mu = (\mu_x, \mu_Z, \mu_{NPEC}, \mu_{BF})$ are adjustable parameters that control the weight of each $P(\mathbf{X})$ in the final estimation.
– α determines the relative weights of the photometric and spectroscopic constraints.

4.2. Parametric Method

In this case we assume an exponential star formation history before the stripping event, a metallicity and a BF, all consistent with the non parametric results. We reproduce the stripping by cutting the star formation at different look-back times $0 \leq t \leq 1$ Gyr. For each of these times, we calculate the NPEC correction and $E(B-V)$ that produce the lowest χ^2. The minimum of $\chi^2(t)$ is taken to provide the most likely stripping age. The spectroscopic and photometric contributions to the χ^2 are weighted as before:

$$\chi^2_{\rm tot}(\mathbf{X}, t) = (1-\alpha)\cdot\chi^2_{\rm spec}(\mathbf{X}, t) + \alpha\cdot\chi^2_{\rm phot}(\mathbf{X}, t), \quad (13)$$

where $\alpha, \chi^2_{\rm spec}(\mathbf{X}, t), \chi^2_{\rm phot}(\mathbf{X}, t)$ have the same meaning as in Sect. 4.1.

5. Results

5.1. Non Parametric Inversion

First we point out that the weightings μ for the penalty are a central issue of the non parametric method and that their determination is not a trivial problem. There are different ways of fixing these values (Titterington, 1985). Following Ocvirk et al. (2006) we used a generalized cross validation method (GCV) just as a starting point. GCV is designed for linear problems, and gives a starting value for μ_x for the restricted problem with no metallicity evolution, spectral broadening and extinction. In the case of non linear problems one has to proceed via empirical tuning (Craig & Brown, 1986) to define the values of μ below which the results present artifacts, and above which the smoothness of the solution is completely due to the penalty.

We chose a penalization that favours smooth first derivatives of the AMR and smooth second derivatives of the SAD and BF. We explored the effect of the weight coefficients μ through a campaign of inversions of artificial spectra. For the NPEC correction, we found it was not necessary to require smoothness explicitely, and the penalization simply acts to normalize the continuum correction (thus avoiding the degeneracy between the absolute values of this correction and the star formation rates). The method recovers similar well-behaved BF for a wide range of μ_{BF}. The campaign showed that it is not possible to recover more than a tentative linear trend in the AMR with the data available to us, and we chose to simplify the problem with constant metallicity (i.e. large μ_Z). A realistic metallicity evolution shows a rapid increase at large lookback times and little increase over the last 5 Gyr (Boissier & Prantzos 2000). From our method we derive a metallicity average over a Hubble time $\langle Z\rangle$. For typical models of Boissier & Prantzos (2000) this mean metallicity is $\Delta Z \sim 0.005$-0.01 lower than the metallicity averaged over the last 5 Gyr.

For the stellar age distribution, we adopt the the smallest μ_x that provides robust solutions, i.e. small sensitivity to the noise in the data. This choice was based on successive inversions of pseudo-data after addition of artificial noise (we refer to these tests as Monte Carlo simulations later on). Above this threshold in μ_x, the sensitivity of the star formation history to the actual value of μ_x is low.

In the campaign of tests, we also verified that within reasonable limits, the shape of the initial guess does not affect the recovered solution. We ended up taking a semi-analytical model of Boissier & Prantzos (2000) as an initial guess for the star formation rate and the age-metallicity relation, and a constant for the BF and the NPEC correction.

For each region we reconstruct the star formation history using the VLT spectrum alone, the photometry alone and spectrum/photometry at the same time.

5.1.1. Inner Region

– VLT spectrum ($\alpha = 0$).
The spectrum shows a fit (top panel in Fig. 2) with $\chi^2_{\rm spec} = 2.2$ and a star formation history (top panel of Fig. 3) that is approximately flat. The metallicity is nearly solar, $\langle Z\rangle = 0.018 \pm 0.003$. For comparison we took three emission lines ([OII]3727, Hβ4861, [OIII]5007) to recover the metallicity using the strong line method (Pilyugin 2000). We obtained $\langle Z\rangle \approx 0.021$ consistent with the results of the inversion. The broadening function is centered on -100 km/s. The shift and the width of the broadening function are consistent with expectation based on galactic rotation and non-circular motions in a barred potential (Veilleux et al. 1999b).
– Photometry ($\alpha = 1$)
The fit reproduces well the observations with a $\chi^2 = 0.36$ (middle panel of Fig. 2). The star formation history (bottom panel of Fig. 3) is quite similar to the star formation history recovered in the case $\alpha = 0$, except in the last 10 Myr. The metallicity is consistent with the spectroscopic results with larger error bars. From the photometric inversion we recovered the average reddening of the stars in the region, $E(B-V) = 0.18$.
– VLT spectrum + Photometry ($\alpha = 0.5$)

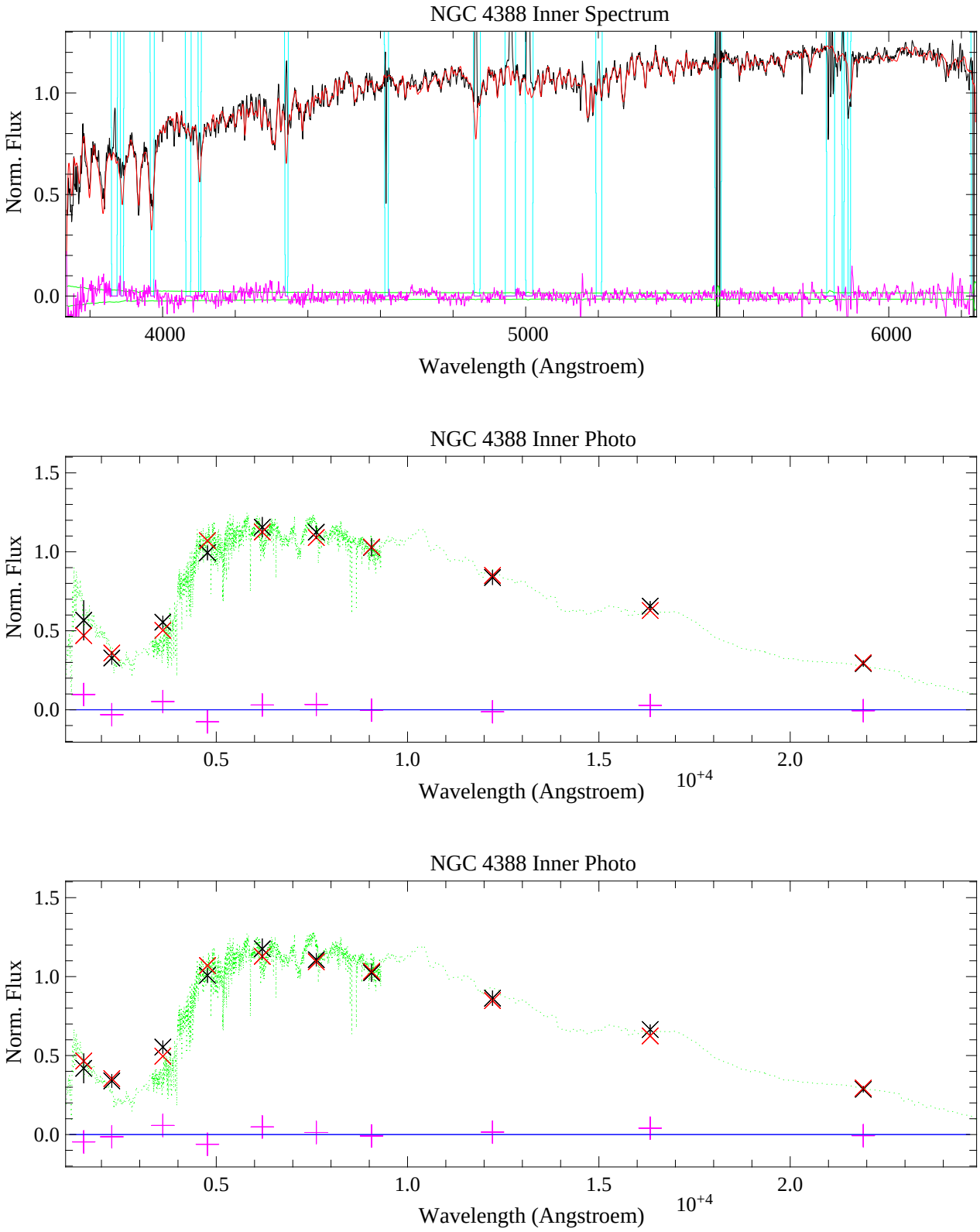

Fig. 2. NGC 4388 inner region fits. Top panel: spectra (black line) and best fit (red line) obtained from inversion with $\alpha = 0$. In the bottom of the panel are shown the residuals (magenta line) and the σ (green line). The cyan vertical lines shows the mask used for emission and sky lines. Middle panel: photometry (black crosses) and best fit (Red crosses) obtained from inversion with $\alpha = 1$ overplotted to the corresponding flux (green dotted line). In the bottom of the panel are shown the residuals (magenta crosses). Bottom panel: same as the middle panel, but using $\alpha = 0.5$. We do not show the fit of the spectrum for the case $\alpha = 0.5$, because is indistinguishable by eye from the top panel.

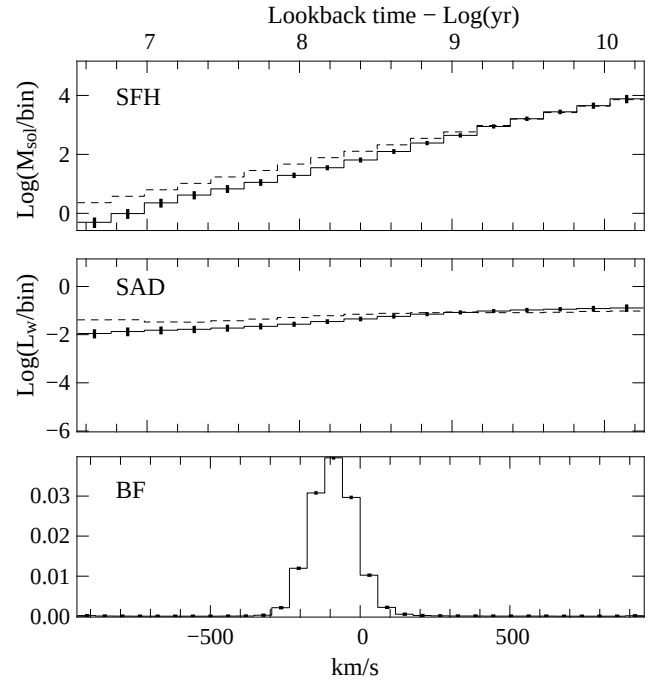

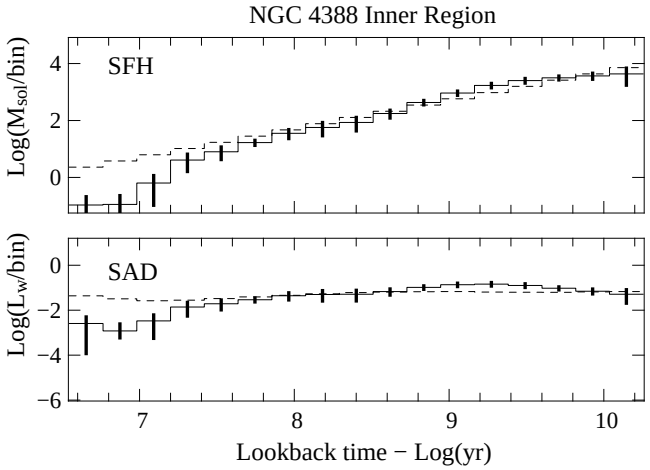

Fig. 3. NGC 4388 inner region results. Top figure: star formation history (SFH), stellar age distribution (SAD) vs. lookback time and broadening function (BF) for the $\alpha = 0$ case. Bottom figure: SFH and SAD vs. look-back time for photometric analysis ($\alpha = 1$). In each figure are plotted the error bars obtained from 30 Monte Carlo simulations. The dashed line represents a flat SFH.

The fit of the spectrum is essentially identical to the case $\alpha = 0$ and we do not show it. The photometry is shown in the bottom panel of Fig. 2. The total $\chi^2_{\rm tot} = 1.4$ is intermediate between the two former cases. The star formation history and the luminosity weighted stellar age distribution are shown in Fig. 4.

5.1.2. Outer Region

– VLT spectrum ($\alpha = 0$)
We obtain a fit (top panel of Fig. 5) with a $\chi^2_{\rm spec} = 0.43$. The recovered star formation history (top panel of Fig.6) is flat until a look-back time of ∼ 300 Myr, then it shows a drop, as expected from the ram pressure stripping scenario. The time-bin averages metallicity is $\langle Z \rangle = 0.01 \pm 0.006$, about half of that of the inner region. The broadening function is centered on ≈ 200 km/s, consistent with galactic rotation (Veilleux et al. 1999b). Its width is dominated by the spectral broadening of the instrument.

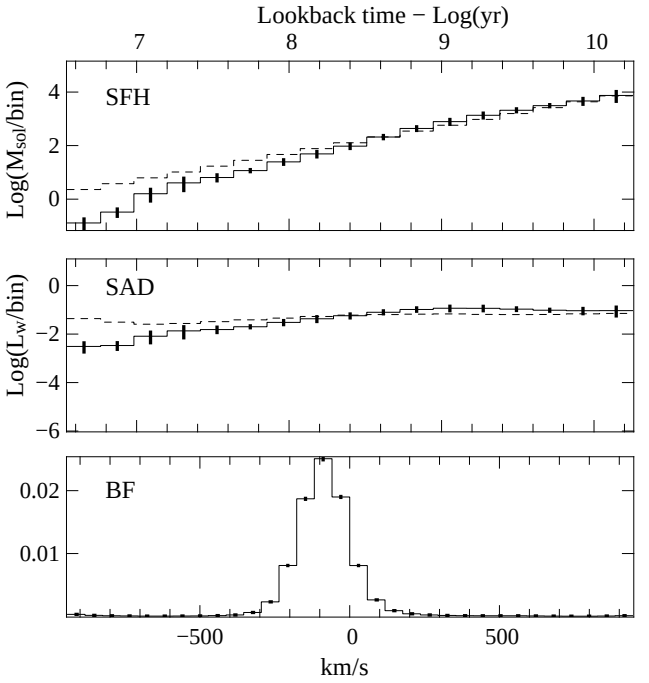

Fig. 4. Combined analysis of the inner region ($\alpha = 0.5$): top and middle panel: star formation history in $M_\odot$/bin and luminosity weighted stellar age distribution vs. look-back time in $\log_{10}$(yr), with error bars derived from Monte Carlo simulations. The dashed line in both panels shows a flat SFH. Bottom panel: line of sight velocity distributioin in km/s with errors from Monte Carlo simulations.

– Photometry ($\alpha = 1$)
The star formation history shows a shape similar to the $\alpha = 0$ case, with a departure from a constant value at a lookback time of ∼ 300 Myr (bottom panel of Fig. 6). The extinction is $E(B-V) = 0.07$ and the $\chi^2_{\rm phot} = 1.1$ (middle panel of Fig. 5).
– VLT spectrum + Photometry ($\alpha = 0.5$)
The total fit (bottom panel of Fig. 5) has a $\chi^2_{\rm tot} = 0.51$. The spectral fit is very similar to the case $\alpha = 0$ and is not shown. The total star formation history is flat until ∼ 300 Myr ago, then it decreases steeply (Fig. 7). The gas stripping of NGC 4388 truncated the star formation history between 100 and 500 Myr ago.
In Fig. 4 and 6 compare the recovered star formation history for the inner and the outer regions to a flat star formation. While the inner region shows a good agreement, the outer region, at around 300 Myr, significantly deviates from a flat star formation history. The truncation is not sharp, because of the chosen penalization, that smoothes the solution.

As expected the non parametric method:

1. provides constraints on the long term star formation history of the galaxy,
2. confirms a recent radical change in the star formation history of the outer disk,
3. cannot provide a precise stripping age.

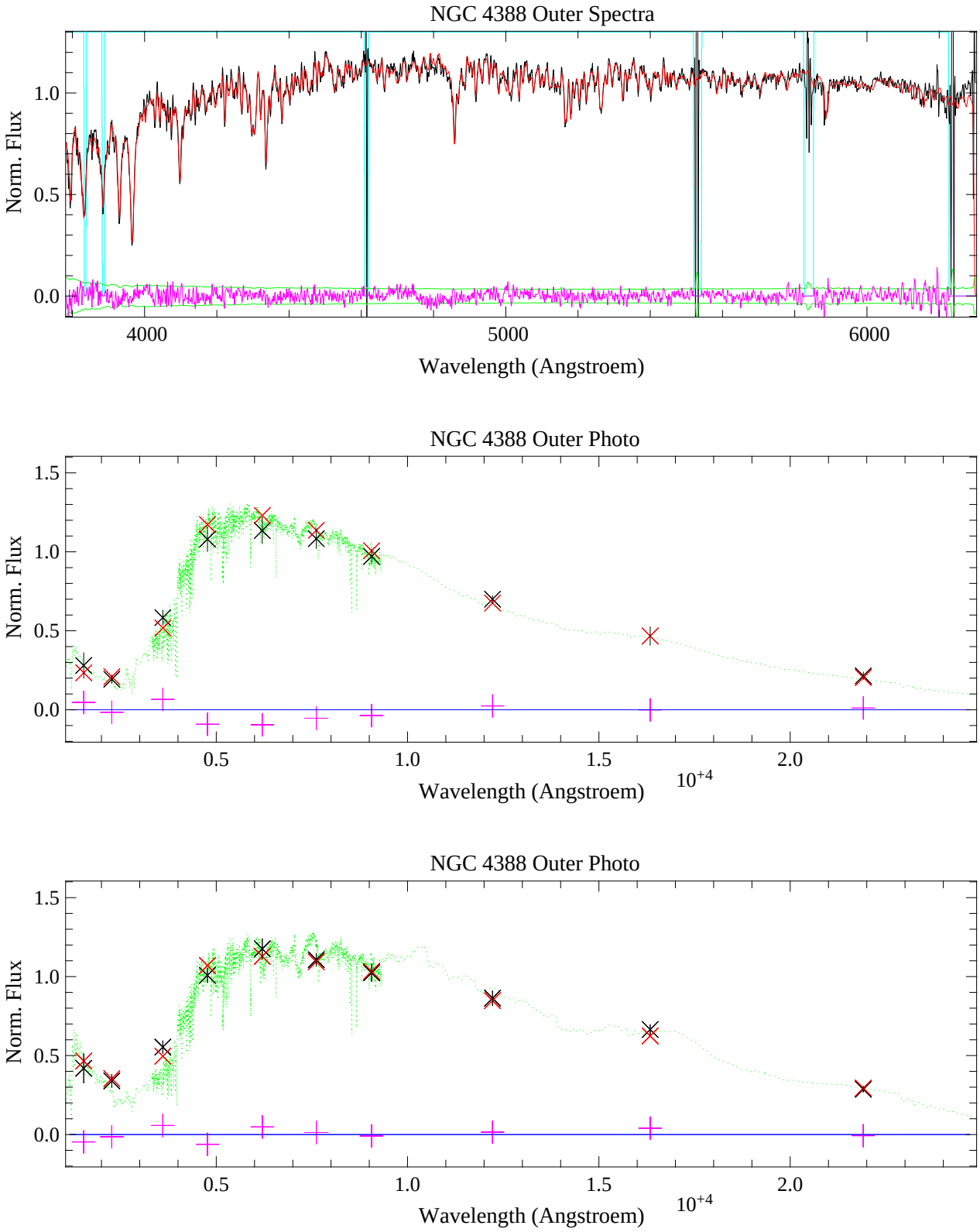

Fig. 5. NGC 4388 outer region fits: top panel: spectra (black) and best fit (red) obtained from inversion with $\alpha = 0$. In the bottom of the panel are shown the residuals (magenta) and the observational errors (green). The cyan vertical lines show the mask used for emission and sky lines. Middle panel: photometry of NGC 4388 (black crosses and error bars) and best fit (red crosses) obtained from inversion with $\alpha = 1$. The best model spectrum is overplotted. The photometric residuals are also shown (magenta crosses). Bottom panel: same as the middle panel, but using $\alpha = 0.5$. We do not shown the fit of the spectrum for the case $\alpha = 0.5$, because it is indistinguishable from the top panel by eye.

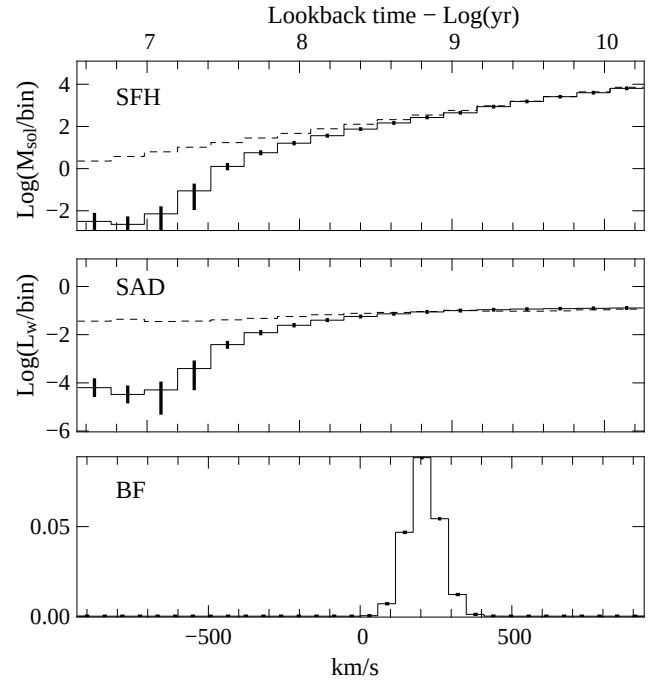

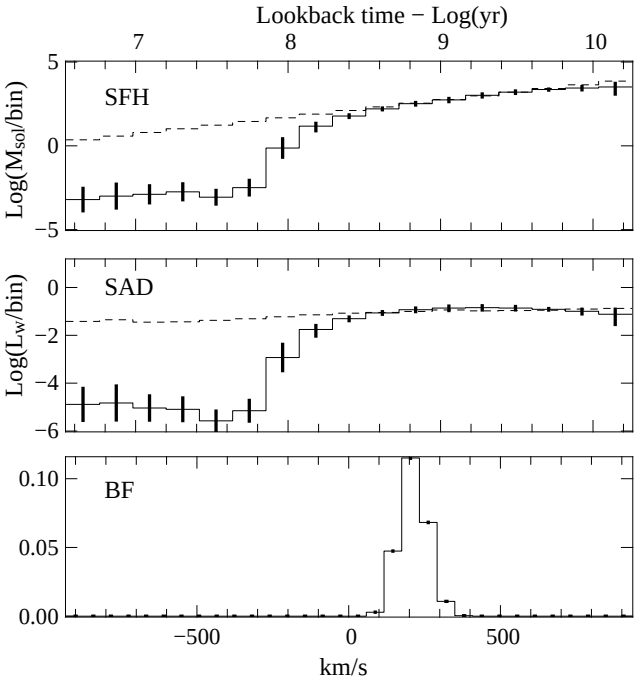

Fig. 7. Combined analysis of the outer region ($\alpha = 0.5$): star formation history in $M_\odot$/bin and luminosity weighted stellar age distribution vs. look-back time in $\log_{10}$(yr) for the outer region of NGC 4388, with error bars derived from Monte Carlo simulations. The dashed lines show a flat SFH. Bottom panel: spectral broadening function in km/s with errors from Monte Carlo simulations.

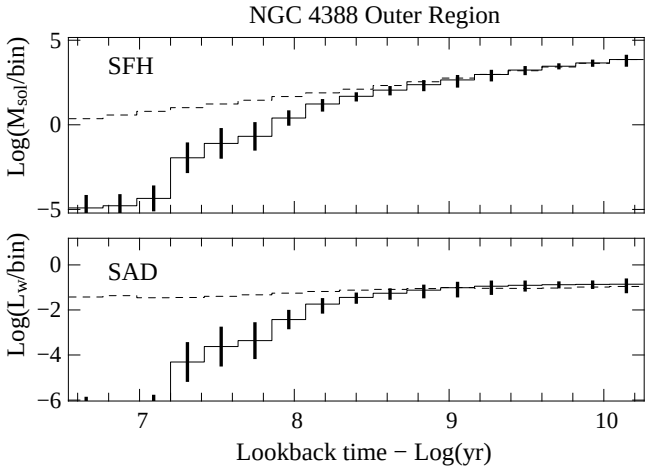

Fig. 6. NGC 4388 outer region results. Top figure: SFH, SAD vs. look-back time and BF for the $\alpha = 0$ case. Bottom figure: SFH and SAD vs. lookback time for photometric analysis ($\alpha = 1$). In each figure are plotted the error bars obtained from 30 Monte Carlo simulations. The dashed line in all the figures represents a flat SFH.

5.2. Parametric Inversion

We applied the parametric method to the spectrum of the outer region of NGC 4388 to quantify the time elapsed since the star formation truncation. For the pre-stripping star formation history and metallicity, we use the results of Sect. 5.1. This is essential because, as explained below, the derived stripping age depends on the luminosity weighted Z and on the ratio of young-to-old stars at the time of stripping. The first point to clarify is the importance of the choice of metallicity evolution in the stripping age determination.

To test the influence of different AMRs on the determination of the stripping age, we used a grid of constant metallicity models as well as two AMRs from the galaxy evolution models of Boissier & Prantzos (2000). We find that the stripping age decreases when the average metallicity increases. The stripping age of the parametric method is only sensitive to the metallicity averaged over the last 5 Gyr. Since the mean metallicity from the non-parametric method, which is averaged over a Hubble time, is lower by $\Delta Z \sim 0.005$-0.01 (cf. Sect. 5.1), we take a constant metallicity of $Z = 0.018$ for the parametric method. We study the χ^2 as a function of the time elapsed since the truncation of the star formation. As done for the non parametric method, we apply the parametric method to the VLT spectrum, the photometry alone, and then spectrum and photometry together.

- VLT spectrum ($\alpha = 0$)
  The top panel of Fig. 8 shows the value of χ^2 as a function of the stripping age, yielding a most likely stripping age of 190 Myr.
- Photometry ($\alpha = 1$)
  We obtain a $\chi^2_{\rm phot} = 0.54$ (middle panel of Fig. 8) and a stripping age of 190 Myr consistent with the result obtained for the VLT spectrum analysis. We recovered also an $E(B-V) = 0.1$ in good agreement with the reddening obtained in the equivalent non parametric problem.
- VLT spectrum + Photometry ($\alpha = 0.5$)
  The minimum $\chi^2_{\rm tot}$ is 0.57 and the stripping age is again of 190 Myr (bottom panel of Fig. 8).

With the non parametric method we fixed an upper limit for the stripping age of $\sim$ 300 Myr. The parametric method improved the precision giving a stripping age of 190 Myr. It is remarkable that the photometric and spectroscopic data provide good agreement on the stripping age. Uncertainties on this value are discussed in the next section.

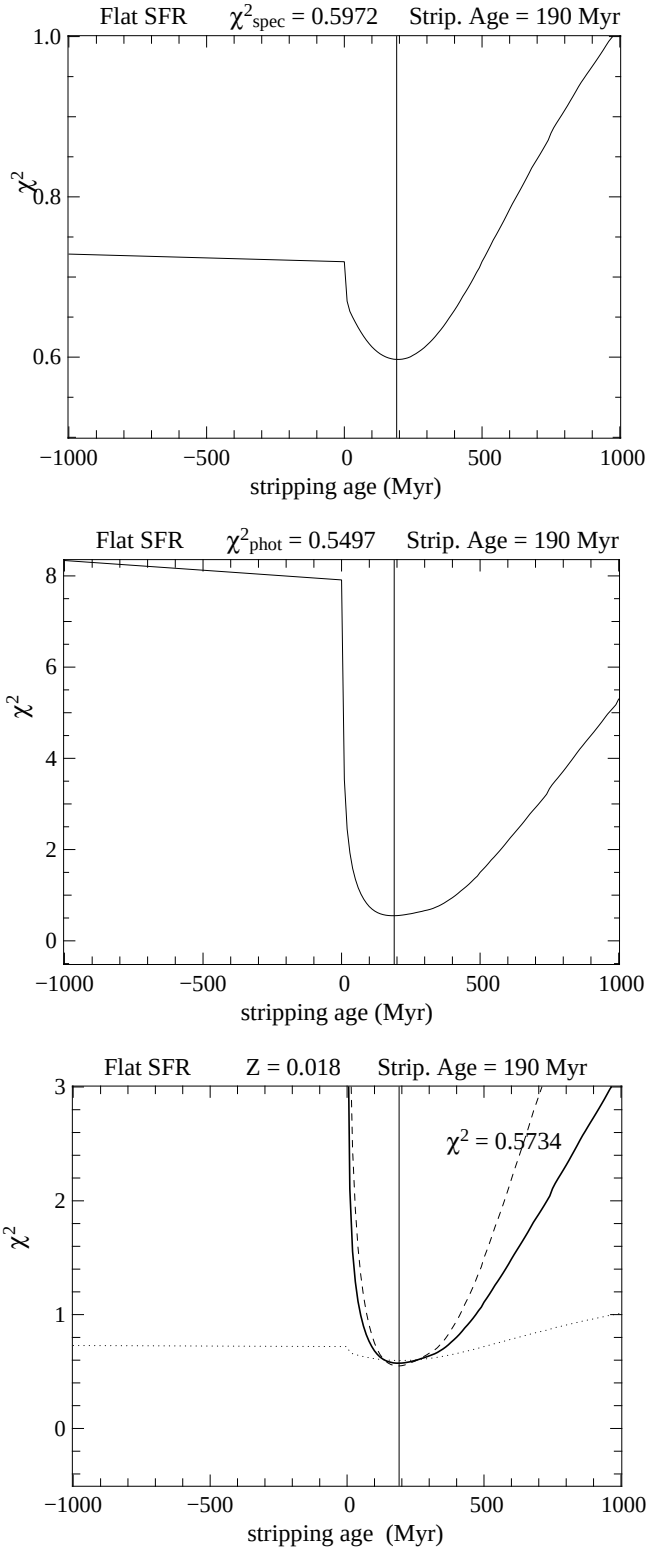

Fig. 8. Parametric inversion of the outer region. χ^2 as a function of the time elapsed since the truncation of star formation. The underlying SFR is flat. Top panel: spectral analysis with $\alpha = 0$. Middle panel: photometric analysis with $\alpha = 1$. Bottom panel: spectro/photometric analysis with $\alpha = 0.5$. In this figure the dotted line represents the spectral χ^2, the dashed line the photometric χ^2, and the black line shows the total χ^2. The vertical line in each panel shows the stripping age.

6. Discussion

6.1. Uncertainties in the parametric method

In the determination of the stripping age a crucial point is to determine the uncertainty of the result. In order to clarify this point we discuss here the influence of the potential sources of errors in the method:

- **Monte Carlo simulations**
  We add a gaussian noise to the spectral and photometric data, and perform 500 Monte Carlo simulations that way. As expected from statistics, the absolute values of the minimum χ^2 vary and the dispersion is of the order of $1/\sqrt{N}$, where N is the number of degrees of freedom (> 1700 for the spectroscopic analysis, 7 for the photometric analysis). However, the location of the minimum in the χ^2 curves varies very little. The error on the stripping age associated with the noise is ∼ 20 Myr.
- **Extinction law**
  The extinction law of Calzetti (2001) was designed to provide a reasonable correction for starburst galaxies. Compared to other laws in the literature, such as the standard Milky Way extinction laws, it is relatively flat. The choice of the extinction law affects the UV-optical colours particularly strongly. However, in the external regions of NGC 4388 from which gas has been mostly removed by ram pressure stripping, the effect of the choice of the extinction law can only be small. As a test, we apply to the model spectra two different extinction laws (Calzetti 2001, Cardelli et al. 1989) and we compare the recovered stripping ages. The results differ by ∼ 10 Myr.
- **Long term star formation history**
  At fixed metallicity, we build families of model spectra with different star formation histories. We consider exponentially decreasing star formation rates (SFR $\propto e^{-\tau/t}$) with timescales τ =6, 10 and 50 Gyr, as well as a flat SFR. The stripping age increases from 100 Myr for τ = 6 Gyr to 190 Myr for a flat SFR, because the ratio of young-to-old stars before the ram pressure stripping event is larger with flatter star formation rates. Shorter timescales are excluded, because the corresponding spectra are too heavily dominated by old stars even before any cut in the SFR is considered. In our study the long term star formation history is constrained strongly by the non parametric inversion of Sect. 5.1. For a wide range of penalization weights, constant star formation rates are favoured. The uncertainty on the stripping age obtained when considering only regular star formation histories consistent with the non parametric results is reduced to about 10 Myr.
- **Metallicity**
  At fixed star formation, we build sets of model spectra using different metallicity values. The stripping age increases with increasing metallicity. With our study the average metallicity over the last 5 Gyr is established through the non-parametric analysis. The error on the metallicity is ∼ 20%. The resulting error on the stripping age is ∼ 10 Myr. It is worth noting that the agreement between the stripping ages determined from the photometry only and from the spectroscopy only is best with the flat star formation history and the quasi-solar metallicity found by the non-parametric analysis. With other assumptions, this agreement is lost.

6.2. Gas dynamics and star formation

With the non-parametric method we find an upper limit for the stripping age of 300 Myr with a smooth decline of star formation during 100-200 Myr. Numerical simulations (Abadi et al. 1999, Vollmer et al. 2001, Rödiger & Brüggen 2006) show that the ISM located at a given distance from the galaxy center is stripped rapidly within a few 10 Myr. Therefore, the smooth decline of the star formation rate derived from the non-parametric method is most probably not physical, but due to regularization of the inversion. A rapid halt of star formation suggested by the dynamical models can only be studied with a parametric method, where we make the simplifying assumption that the gas is stripped instantaneously. The derived stripping age of 190 Myr is consistent with the extent of the observed HI tail (Oosterloo & van Gorkom 2005): a tail extent of 80 kpc in the plane of the sky and along the line of sight with the given stripping age leads to a total velocity of $\sim 570\,\mathrm{km\,s^{-1}}$ and a radial velocity of $\sim 400\,\mathrm{km\,s^{-1}}$. The latter corresponds to the difference between the galaxy's systemic velocity and the velocity of the HI tail (Oosterloo & van Gorkom 2005). The full extent of the HI tail was not known at the time when Vollmer & Huchtmeier (2003) presented their dynamical model. Their tail has an extent of 40 kpc with an associated stripping age of 120 Myr. A new, revised dynamical model (Vollmer, in prep.) with the observed extent yields a stripping age consistent with our findings.

7. Conclusions

VLT FORS2 spectroscopic observations of the inner star-forming and outer gas-free disk of the Virgo spiral galaxy NGC 4388 are presented. Previous observations indicate that this galaxy has undergone a recent ram pressure stripping event. Once the galaxy's ISM is stripped by ram pressure star formation stops. We detect this star formation truncation in the spectrum and the multiwavelength photometry of the outer disk region of NGC 4388.

To derive star formation histories we extend the non parametric inversion method of Ocvirk et al. (2006) making a joint analysis of spectroscopic and photometric data possible. The new code has been tested on a series of mock data using Monte Carlo simulations. We find that the results are stable, once that minimization has converged. The uncertainties for the young stellar ages ($\leq$ 100 Myr) can be large due to the uncertainties of stellar models. Whitin the reasonable limits, the shape and absolute value of the initial guess does not affect the recovered solution (at fixed signal-to-noise ratio).

The new inversion tool is applied to our spectroscopic and photometric data of NGC 4388. We explore the effect of different penalizations in case of spectral analysis, photometric analysis and combined analysis. The main results are: (i) for the inner disk spectrum the recovered star formation history is flat and (ii) for the outer disk region the inversion yields a star formation drop at a look-back time of $\sim$ 300 Myr. Due to the penalization this truncation is not sharp.

We introduce a parametric method that refines the precision of the determination of the stripping age. Based on the non parametric results we assume a flat star formation before the stripping event and an almost solar metallicity. We approximate the effect of gas stripping by cutting the star formation at different look-back time $0 \leq t \leq 1$ Gyr. The obtained set of spectra is compared with the observed spectrum of the outer disk of NGC 4388. The effect of the potential sources of error in the stripping age determination are evaluated.

The parametric method leads to a stripping age for NGC 4388 of $\sim 190 \pm 30$ Myr. This result is in agreement with the results of a previous work of Crowl & Kenney (2008) and with revised dynamical models.

Acknowledgements. This publication makes use of data products from the Two Micron All Sky Survey, which is a joint project of the University of Massachusetts and the Infrared Processing and Analysis Center/California Institute of Technology, funded by the National Aeronautics and Space Administration and the National Science Foundation.

Funding for the SDSS and SDSS-II has been provided by the Alfred P. Sloan Foundation, the Participating Institutions, the National Science Foundation, the U.S. Department of Energy, the National Aeronautics and Space Administration, the Japanese Monbukagakusho, the Max Planck Society, and the Higher Education Funding Council for England. The SDSS Web Site is http://www.sdss.org/.

We would like to thank D. Munro for freely distributing his Yorick programming language (available at `http://www.maumae.net/yorick/doc/index.html`)

References

Abadi, M. G., Moore, B., & Bower, R. G. 1999, MNRAS, 308, 947
Adelman-McCarthy, J. K., et al. 2008, ApJS, 175, 297
Alongi, M., Bertelli, G., Bressan, A., Chiosi, C., Fagotto, F., Greggio, L., & Nasi, E. 1993, A&AS, 97, 851
Appenzeller, I., et al. 1998, The Messenger, 94, 1
Bakos, G. Á., Sahu, K. C., & Németh, P. 2002, ApJS, 141, 187
Boissier, S., & Prantzos, N. 2000, MNRAS, 312, 398
Bonnarel, F., et al. 2000, A&AS, 143, 33
Boselli, A., & Gavazzi, G. 2006, PASP, 118, 517
Bressan, A., Fagotto, F., Bertelli, G., & Chiosi, C. 1993, A&AS, 100, 647
Bruzual, G., & Charlot, S. 2003, MNRAS, 344, 1000
Calzetti, D. 2001, PASP, 113, 1449
Cardelli, J. A., Clayton, G. C., & Mathis, J. S. 1989, ApJ, 345, 245
Cayatte, V., van Gorkom, J. H., Balkowski, C., & Kotanyi, C. 1990, AJ, 100, 604
Chamaraux, P., Balkowski, C., & Gerard, E. 1980, A&A, 83, 38
Chung, A., van Gorkom, J. H., Kenney, J. D. P., Crowl, H., & Vollmer, B. 2009, AJ, in press; arXiv:0909.0781
Craig, I. J. D., & Brown, J. C. 1986, Research supported by SERC. Bristol, England and Boston, MA, Adam Hilger, Ltd., 1986, 159 p.,
Crowl, H. H., & Kenney, J. D. P. 2008, AJ, 136, 1623
Dressler, A. 1986, ApJ, 301, 35
Fagotto, F., Bressan, A., Bertelli, G., & Chiosi, C. 1994, A&AS, 105, 29
Fagotto, F., Bressan, A., Bertelli, G., & Chiosi, C. 1994, A&AS, 104, 365
Fouqué, P., Solanes, J. M., Sanchis, T., & Balkowski, C. 2001, A&A, 375, 770
Gil de Paz, A., et al. 2007, ApJS, 173, 185
Giovanelli, R., & Haynes, M. P. 1983, AJ, 88, 881
Girardi, L., Bressan, A., Chiosi, C., Bertelli, G., & Nasi, E. 1996, A&AS, 117, 113
Gunn, J. E., & Gott, J. R. I. 1972, ApJ, 176, 1
Hamuy, M., Walker, A. R., Suntzeff, N. B., Gigoux, P., Heathcote, S. R., & Phillips, M. M. 1992, PASP, 104, 533
Kenney, J. D. P., Crowl, H., van Gorkom, J., & Vollmer, B. 2004, Recycling Intergalactic and Interstellar Matter, 217, 370
Le Borgne, J.-F., et al. 2003, A&A, 402, 433
Martins, L. P., González Delgado, R. M., Leitherer, C., Cerviño, M., & Hauschildt, P. 2005, MNRAS, 358, 49
Morrissey, P., et al. 2007, ApJS, 173, 682
Ocvirk, P., Pichon, C., Lançon, A., & Thiébaut, E. 2006, MNRAS, 365, 46
Oosterloo, T., & van Gorkom, J. 2005, A&A, 437, L19
Perryman, M. A. C., et al. 1997, A&A, 323, L49
Pilyugin, L. S. 2000, A&A, 362, 325
Quilis, V., Moore, B., & Bower, R. 2000, Science, 288, 1617
Roediger, E., & Brüggen, M. 2006, MNRAS, 369, 567
Roediger, E., & Brüggen, M. 2008, MNRAS, 388, L89
Schulz, S., & Struck, C. 2001, MNRAS, 328, 185
Skrutskie, M. F., et al. 2006, AJ, 131, 1163
Solanes, J. M., Manrique, A., García-Gómez, C., González-Casado, G., Giovanelli, R., & Haynes, M. P. 2001, ApJ, 548, 97
Titterington, D. M. 1985, A&A, 144, 381
Tody, D. 1993, Astronomical Data Analysis Software and Systems II, 52, 173
Veilleux, S., Bland-Hawthorn, J., Cecil, G., Tully, R. B., & Miller, S. T. 1999, ApJ, 520, 111
Veilleux, S., Bland-Hawthorn, J., & Cecil, G. 1999, AJ, 118, 2108
Vollmer, B., Cayatte, V., Balkowski, C., & Duschl, W. J. 2001, ApJ, 561, 708

Vollmer, B., & Huchtmeier, W. 2003, A&A, 406, 427
Warmels, R. H. 1988, A&AS, 72, 57
Yasuda, N., Fukugita, M., & Okamura, S. 1997, ApJS, 108, 417
Yoshida, M., et al. 2002, ApJ, 567, 118

4.4 Test of the non parametric method

4.4.1 Comparison with different spectral libraries

In the non parametric inversion we use the single stellar population (SSP) library of Bruzual & Charlot (2003) (BC03), that covers a time interval Δt = [0 - 19.5] Gyr, a wavelength range $\lambda\lambda$ = [100 - 24850] Å, a metallicity Z = [0.001,0.05] with an average spectral resolution (FWHM) R = 2000 at optical wavelengths.

The Bruzual & Charlot (2003) basis uses Padova 1994 (Alongi et al. 1993, Bressan et al. 1993, Fagotto et al. 1994a, Fagotto et al. 1994b, Girardi et al. 1996) evolutionary tracks and the models are built using the Stelib library (Le Borgne et al., 2003), with a resolution of 3 Å at optical wavelength. This library has been widely used by the scientific community and tested in different research domains. Different analysis investigated the potential sources of errors, revealing for example a systematic wavelength calibration error (Koleva et al. 2007) or a small correction in the spectral resolution (MacArthur et al. 2009).

In order to study the influence of the chosen spectral basis in the results, we consider another spectral library of Vazdekis et al. (2007), from now on SSP-MILES. It uses the spectral library MILES (Sánchez-Blázquez et al. 2006, Cenarro et al. 2007), uses the Padova 2000 isochrones and covers a wavelength range of $\lambda\lambda$ = [3525 - 7500] Å with a resolution of R = 4300 (2.3 Å). SSP-MILES reproduces spectra with ages spanning Δt = [100 - 17780] Myr and metallicity of ΔZ = [0.0004,0.03].

This basis has the advantage of the high resolution, but unfortunately it covers only a limited wavelength range and for this reason it cannot be used for photometric analysis. We consider two spectral inversions obtained using the Bruzual & Charlot (2003) (BC03) and the Vazdekis et al. (2007) SSP-MILES libraries.

The results are consistent (see Fig. 4.15), showing that the solution recovered with the minimization is independent from the used library. This is confirmed by the χ^2 value, that varies of 0.02 between the two basis. The tolerance of the χ^2 is the threshold above the minimum, at which we can still consider a solution acceptable. The fluctuation of the minimum value of a χ^2 function under the tolerance-level are completely due to the noise. For each χ^2 the tolerance depends on the degrees of freedom of the problem, i.e. the number of the independent parameters in the data minus the number of parameters to estimate. In our case, the number of points in the spectra $N_\lambda > 2000$, largely above the number of parameters that we want to estimate. In this case we can approximate the degree of freedom of the problem as the number of independent points in the spectra. For BC03 we have a tolerance of

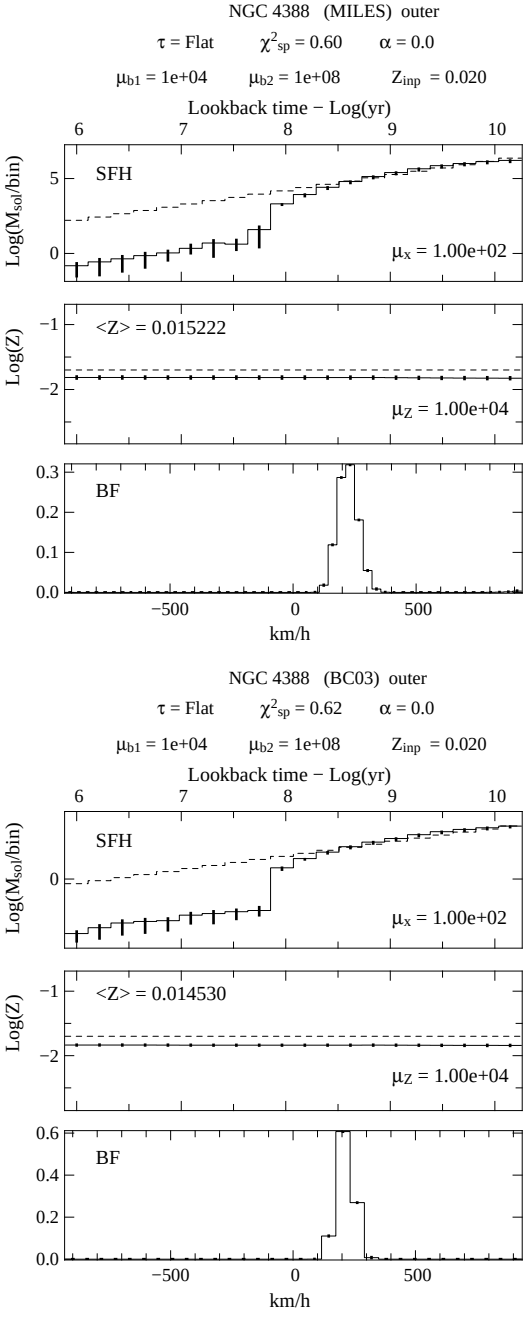

Figure 4.15: Results for non parametric inversion of NGC 4388 (outer region) for SSP-MILES (Vazdekis et al. 2007, top panel) and Bruzual & Charlot (2003) (bottom panel). In each figure the top, middle and bottom panels represent the star formation history, the metallicity evolution and the spectral broadening function, respectively. In each panel the dashed lines show the initial condition and the solid lines show the results with associated error bars. The error are obtained via Monte Carlo simulations. In top of panels are marked the τ used in star formation, the spectral χ^2, the weight parameter α in Eq. 2.29, the penalization for boundary condition (μ_C in Eq. 2.36), and the constant value of metallicity $Z_{\rm inp}$ used for the initial guess. In right bottom of top and middle panel of each figure are marked the value of penalization μ_z, μ_Z (see Eq. 2.36). In top left of middle panel is marked the time-bin average metallicity of the profile.

0.03, that define a range of $0.63 \geq \chi^2 \geq 0.60$. The shape of the spectral broadening function in case of SSP-MILES is narrower, because of the better resolution, and the drop in the star formation occurs approximatively at the same lookback time for the two spectral libraries.

In conclusion the solution of the non parametric method is independent from the chosen spectral libraries, under the condition that the minimization procedure converges to the absolute minimum. This is strictly related to the weight of penalization μ_x, μ_Z, confirming the necessity of an adequate regularization in order to obtain reliable solutions.

4.4.2 Comparison with different initial conditions

In Sect. 3.2.2 we investigated the influence of different initial guess for the star formation history on the inversion of mock spectra. In this section we perform the same kind of investigation for the outer region of NGC 4388. We use the same penalization $\mu_x = 10^2$ and $\mu_Z = 10^2$ and a constant metallicity evolution $Z = 0.025$. We fix as initial guess a flat star formation history, an exponentially decreasing law with $\tau = 5$ Gyr and an increasing exponential with $\tau = 5$ Gyr.

As shown in Fig. 4.16 the models with flat and decreasing star formation law are consistent, leading to a common solution, and the model with an increasing star formation law shows some difference both in star formation history and metallicity evolution. In this last case the minimization does not converge to the right minimum and this is confirmed by $\chi^2 = 0.74$, higher than the value of the first two models, with $\chi^2 = 0.66$. The tolerance of χ^2 function, considering the degrees of freedom of the problem, is for spectral analysis ~ 0.03. The obtained fit shows also a larger spectral broadening function and an unphysical metallicity evolution. The fit obtained with an increasing star formation as initial guess is not acceptable, as expected from the analysis of mock data. We note that notwithstanding the bad fit of the spectrum, the last model shows a drop in the star formation at lookback time $t < 300$ Myr, but this drop is not as evident as in the first two models.

The metallicity found for the inner region is solar, consistent with the results of the strong line method (Pilyugin 2000). The metallicity recovered from the outer region inversion is systematically above the solar value. As explained in Sect. 4.16 also in real observations the metallicity evolution is not well constrained by the method. For this reason in Sect. 4.3 we chose to fix an high value of penalization for the metallicity $\mu_Z = 10^4$, recovering in this way a time-bin averaged metallicity.

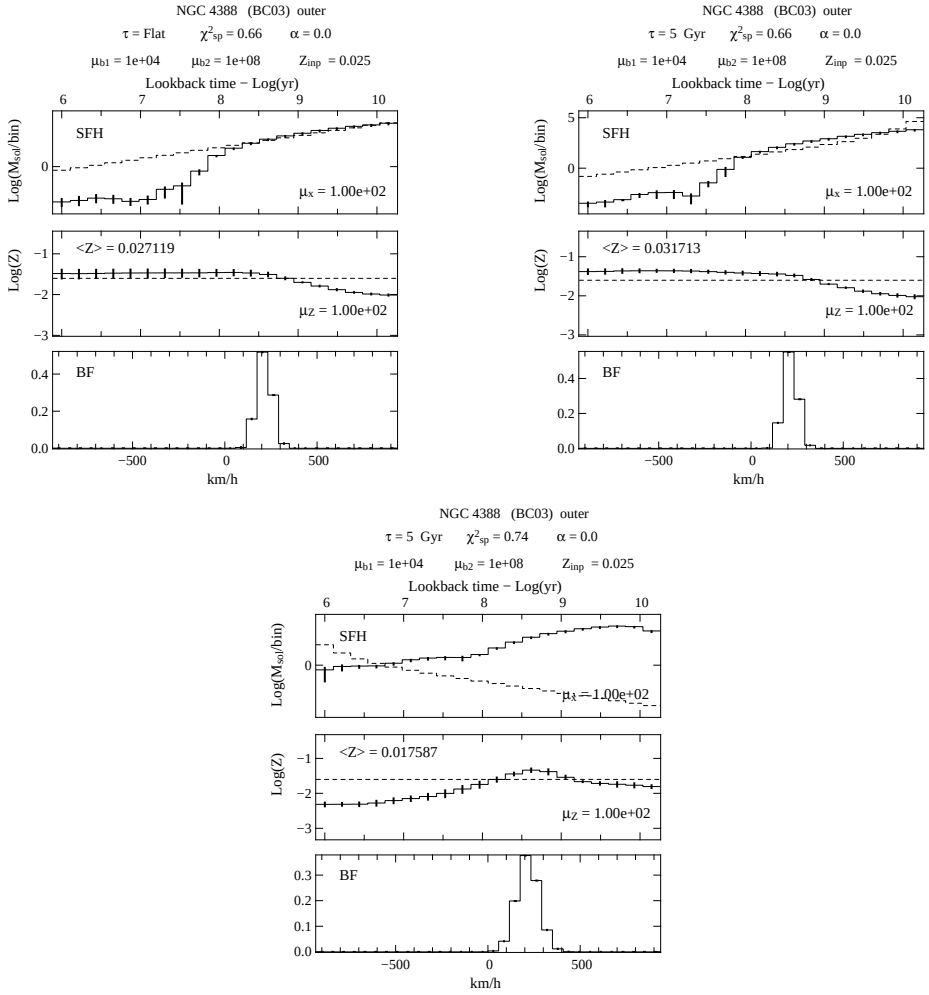

Figure 4.16: Inversion of the outer region of NGC 4388, for different initial guesses for the star formation: a flat star formation history (left panel), an exponentially decreasing star formation law with characteristic timescale $\tau = 5$ Gyr (right panel) and an exponentially increasing star formation law with characteristic timescale $\tau = 5$ Gyr (bottom panel). In each figure the top, middle and bottom panels represent the star formation history, the metallicity evolution and the spectral broadening function, respectively. In each panel the dashed lines show the initial guess and the solid lines the results with associated error bars. The errors are obtained via Monte Carlo simulations. In top of panels are marked the τ used in star formation initial guess, the spectral χ^2, the weight parameter α in Eq. 2.29, the penalizations used for boundary condition (μ_C in Eq. 2.36), and the constant value of metallicity $Z_{\rm inp}$ used for the initial guess. In right bottom of top and middle panel of each figure are marked the value of penalization μ_x, μ_Z (see Eq. 2.36). In top left of middle panel is marked the time-bin averaged metallicity of the profile.

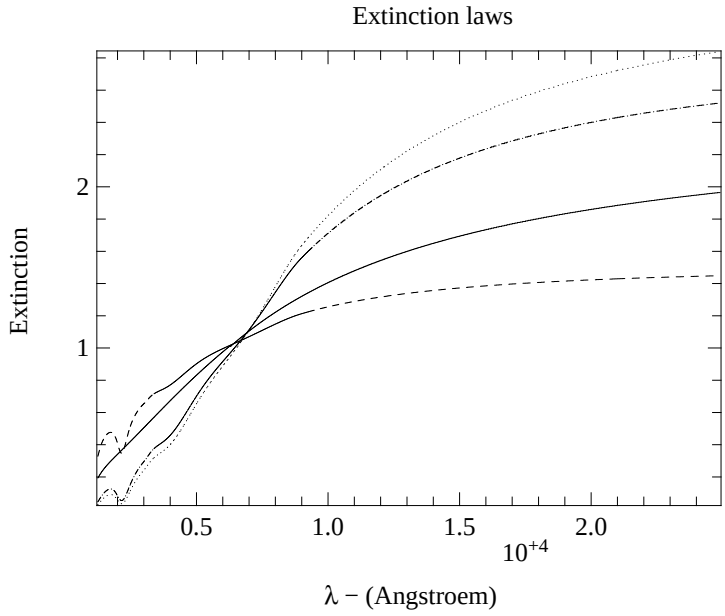

Figure 4.17: Interstellar extinction ($e^{-\tau(\lambda)}$) for Calzetti (2001), solid line, and different Cardelli et al. (1989) as a function of wavelength. In Cardelli et al. (1989) law we use $R_V = 1$ (dashed line), $R_V = 2.7$ (dot-dashed line) and $R_V = 3.1$ (dotted line) (see App. D for details).

4.4.3 Comparison with different extinction laws

The non parametric inversion of the photometry applies to the photometric basis the extinction law of Calzetti (2001). This law depends on a free parameter, the color excess $E(B-V)$. This parameter characterizes the light extinction due to the interstellar dust. The shape of the law is calibrated by nearby star forming galaxies. For the inner spectrum we observe in optical spectroscopy the typical emission lines of star forming galaxies and a Calzetti (2001) extinction law is reasonable. The spectrum of the outer region does not show emission lines and for this reason we investigate the influence on the results of a different extinction law. We chose an extinction law of Cardelli et al. (1989) (see app. D) that can be used both in dense and diffuse interstellar medium. The law depends on $E(B-V)$ parameter and R_V, that is the ratio of the absolute extinction at reference wavelength in V and the color excess. In our case we fixed $R_V = 3.1$. The shape of the law is quite similar to that of Calzetti (2001) except in the blue region of the spectrum (see Fig. 4.17).

In Fig. 4.18 and 4.19 are shown the recovered star formation history and the photometric fit for a combined inversion of the outer region of NGC 4388, respectively. The drop in the star formation in both cases is at $\sim$ 300 Myr and the recovered profiles are in good agreement. The differences in shape between the

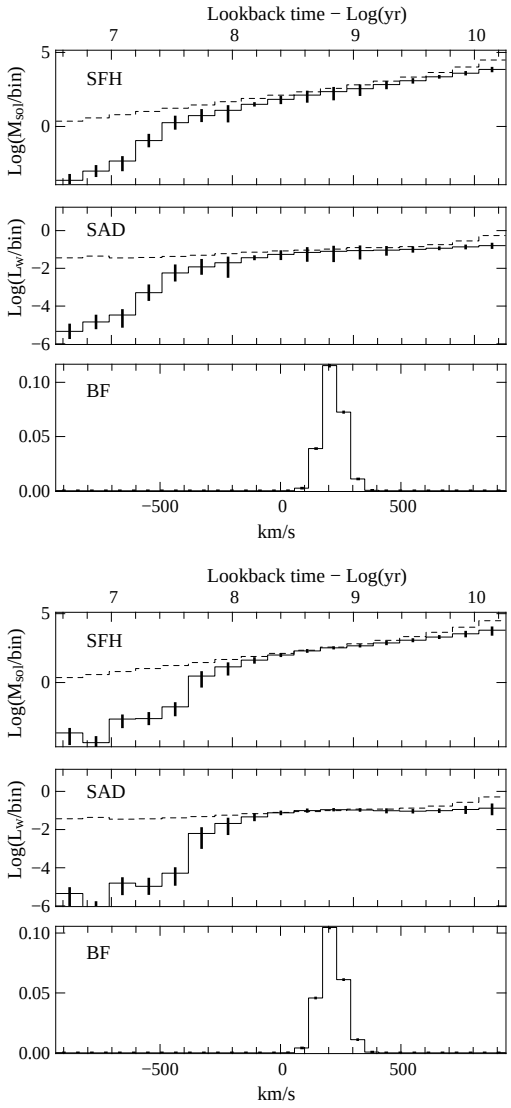

Figure 4.18: Non parametric inversion of the outer region of NGC 4388 for spectral and photometric analysis (α = 0.5). The top panels show the star formation history versus the lookback time. The middle panels show the luminosity weighted stellar age distribution versus lookback time and in the bottom panels is shown the spectral broadening function. In all panels the dashed line represents an exponentially decreasing star formation law with τ = 10 Gyr. The error bars are estimated via Monte Carlo simulations. The photometric inversion is obtained using a Calzetti (2001) law in the top panel and a Cardelli et al. (1989) law in the bottom panel.

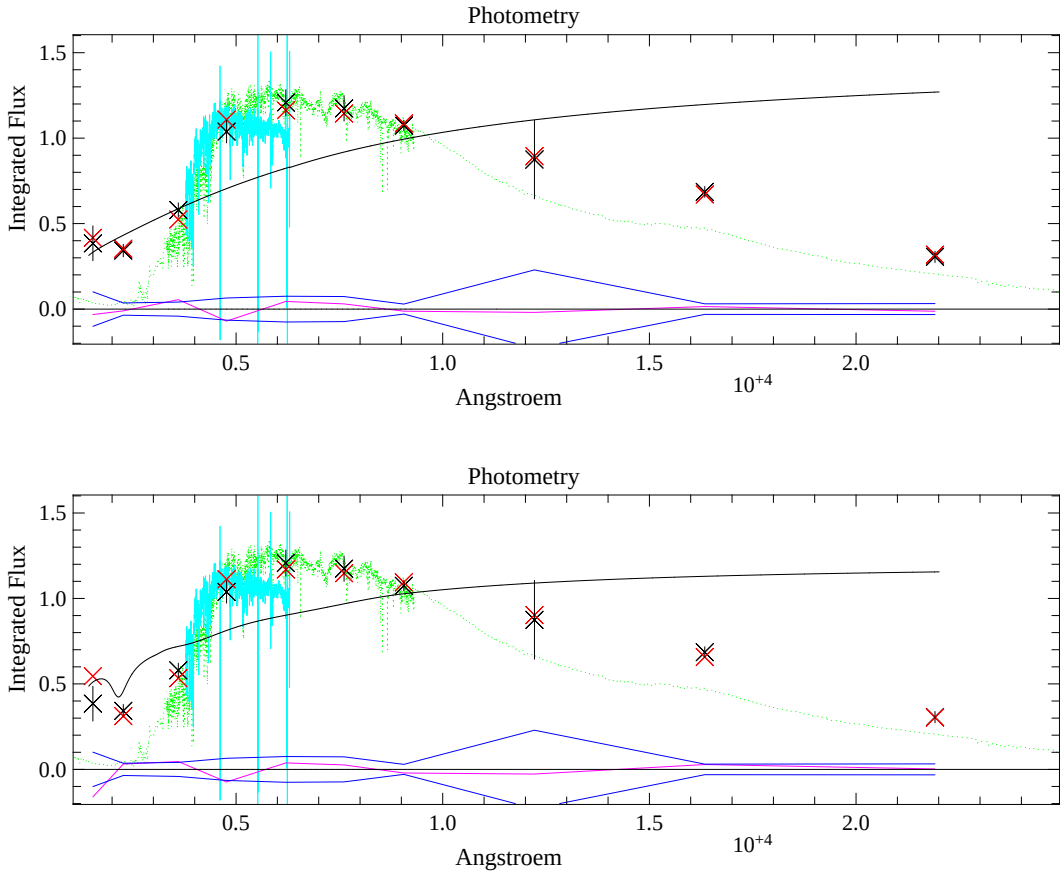

Figure 4.19: Photometric fir of the combined non parametric inversion of the outer region of NGC 4388. In both panels are shown ; the input photometric data with associated error (black crosses), the best-fit model (red crosses), the observed spectrum (cyan line), the photometric noise (blue line) and the residuals (magenta line). To guide the eye, an arbitrary unobscured spectrum of the basis is also shown (green line). Finally the black line show the extinction law applied to the models, a Calzetti (2001) (top panel) and Cardelli et al. (1989) (bottom panel) extinction law, respectively.

chosen extinction laws are significant at wavelength below $\sim$ 8000 Å. For filters in the wavelength range below the SDSS i' filter the Calzetti (2001) law decreases faster than the Cardelli et al. (1989) law, as shown in Fig. 4.19, and the extinction has in Cardelli et al. (1989) a bump at 2200 Å, which falls within the NUV GALEX filter. The bump in the FUV filter of the Cardelli et al. (1989) law produces bad fit of this point, that is about 40% higher the the model value.

The outer region gas of the galaxy has been stripped, and we expect for this region a low extinction. The minimization procedure used for the inversion confirmed the lack of gas, leading for the outer region to an $E(B-V) = 0.07$ using a Calzetti (2001) law and $E(B-V) = 0.05$ using a Cardelli et al. (1989) law. This means that lower extinction reproduces better the input data. In conclusion using a Cardelli et al. (1989) extinction law the non parametric inversion recovers a drop in star formation history at lookback time $t <\sim 300$ Myr consistent with the results obtained using a Calzetti (2001) law. The different shape of the two laws affects only the curvature of the star formation history and the general trend of the solution is preserved.

4.4.4 Effect of Spectral Broadening function

The best fit model recovered with the non parametric method is the result of the convolution of the spectral energy distribution of the galaxy at rest and the spectral broadening function, that takes in account the effect of the instrumental point spread function and the line of sight velocity distribution. In our work we estimated this last effect to be negligible with respect to the broadening induced by the instrumentation. But as we show in this section, the star formation history and the metallicity are robust with respect to changes in the way the two sources of broadening are treated.

Taking the lamp spectra used for the wavelength calibration and fitting a gaussian to different lines we recovered for our observations a FWHM = 4.71 Å. The spectral basis of Bruzual & Charlot (2003) has at optical wavelength a FWHM = 3.375 Å (MacArthur et al., 2009). The broadening introduced by the instrumental PSF is :

$$\sigma_{\rm PSF} = \sqrt{\sigma^2_{\rm obs} - \sigma^2_{\rm BC03}} = 3.3 \text{ Å}. \tag{4.5}$$

We can express the spectral resolution both in terms of wavelengths or in terms of physical quantities, using :

$$\frac{\lambda}{\Delta\lambda} = \frac{c}{\Delta v}, \tag{4.6}$$

in which $\Delta\lambda$ represents the smallest wavelength distinguishable in the observations.

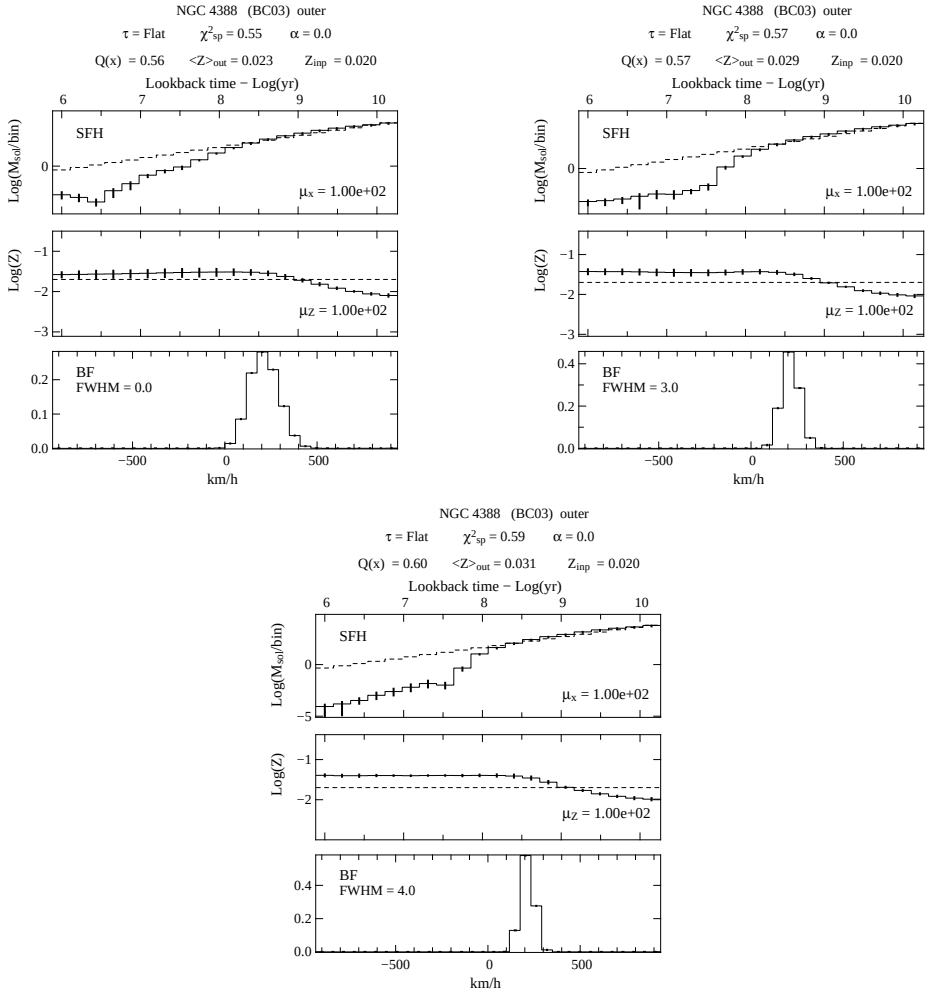

Figure 4.20: Results for non parametric inversion of the outer region of NGC 4388. We use the stellar population basis of Bruzual & Charlot (2003) (left panel) and before the minimization we convolve the basis with a gaussian of FWHM = 3 Å (right panel) and FWHM = 4 Å (bottom panel). In each figure the top, middle and bottom panels represent the star formation history, the metallicity evolution and the spectral broadening function, respectively. In each panel the dashed lines show the initial guess and the solid lines show the results with associated error bars. The errors are estimated via Monte Carlo simulations. In top of panels are marked the τ used in star formation initial guess, the spectral χ^2, the weight parameter α in Eq. 2.29, the Q-function value (Eq. 2.29), the recovered time-bin averaged metallicity evolution $\langle Z_{\rm out}\rangle$ and the constant value of metallicity $Z_{\rm inp}$ used for the initial guess. In right bottom of top and middle panel of each figure are marked the value of penalization μ_x, μ_Z (see Eq. 2.36). In top left of bottom panel is marked the FWHM of the gaussian convolved with the spectral basis before the minimization.

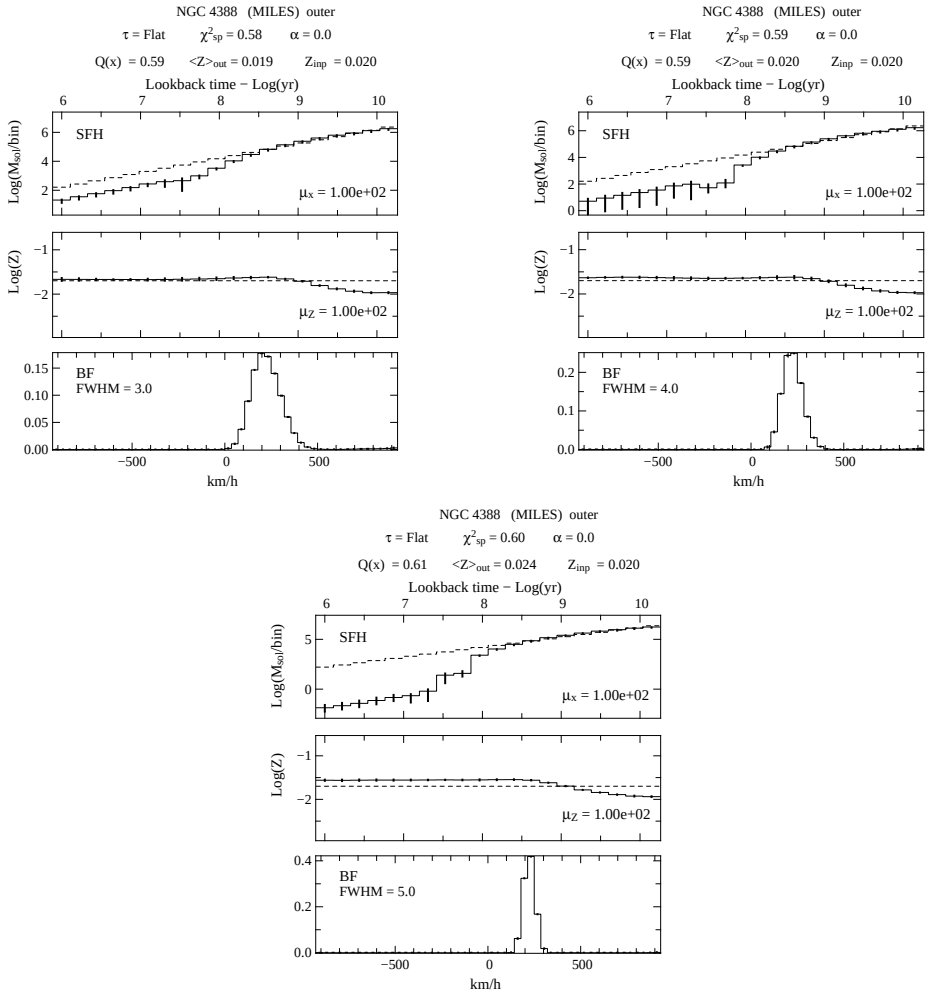

Figure 4.21: Results for non parametric inversion of the outer region of NGC 4388. We convolve the basis of Vazdekis et al. (2007) with a gaussian of FWHM = 3 Å (left panel), FWHM = 4 Å (right panel) and FWHM = 5 Å (bottom panel). In each figure the top, middle and bottom panels represent the star formation history, the metallicity evolution and the spectral broadening function, respectively. In each panel the dashed lines show the initial guess and the solid lines show the results with associated error bars. The errors are estimated via Monte Carlo simulations. In top of panels are marked the τ used in star formation initial guess, the spectral χ^2, the weight parameter α in Eq. 2.29, the Q-function value (Eq. 2.29), the recovered time-bin averaged metallicity evolution $\langle Z_{\rm out}\rangle$ and the constant value of metallicity $Z_{\rm inp}$ used for the initial guess. In right bottom of top and middle panel of each figure are marked the value of penalization μ_x, μ_Z (see Eq. 2.36). In top left of bottom panel is marked the FWHM of the gaussian convolved with the spectral basis before the minimization.

In our case the FORS2 instrument has a constant $\Delta\lambda$ overall the optical spectrum. Δv represents the minimal variation of velocity that we can distinguish though the Doppler effect, and c is the speed of light.

If we assume a stellar velocity dispersion of 40 km/s (typical of a spiral galaxy) from Eq. 4.6 we can determine $\Delta\lambda$, that is a function of wavelength, assuming larger value for increasing λ. The wavelength range used for our observations spans $\lambda\lambda$ = [3300 - 6360]. This means that for the higher λ a velocity dispersion of 40 km/s introduce a broadening in the observations of $\Delta\lambda$ = 0.84 Å, small with respect to the $\Delta\lambda$ = 3.3 Å introduced by the observations.

We performed inversions using the same formalism developed in Chapt. 2 except that we convolved the spectral SSP basis of Bruzual & Charlot (2003) with a gaussian before the minimization. We chose two gaussians with FWHM = 3 and FWHM = 4 Å to investigate the results around the $\sigma_{\rm PSF}$ = 3.3 Å defined in Eq. 4.5.

The results are shown in Fig. 4.20. For the three cases the star formation deviates from the flat star formation history at lookback time $t \sim 300$ Myr. We note that the results obtained for the inversion with FWHM = 0 (left panel in Fig. 4.20 and FWHM = 3 (right panel in Fig. 4.20) have a χ^2 acceptable because they vary by $\Delta\chi^2 = 0.03$, and this variation is below the tolerance level of the χ^2. The model in which the stellar population basis is convolved with a gaussian with a FWHM = 4 Å gives a $\chi^2 = 0.59$, that is not acceptable as a good fit. This is expected, since the smoothing produced is higher than allowed for the spectral resolution of the observations, producing a worse fit. The FWHM of the spectral broadening function recovered for this case is very narrow but it should be a Dirac peak. Nevertheless, the star formation and metallicities are still reasonable.

The results obtained using the spectra of Bruzual & Charlot (2003) are independent from the chosen basis. To verify this we performed the same test using the spectral library of Vazdekis et al. (2007), with a spectral resolution FWHM = 2.3 Å. The higher spectral resolution of the basis increase $\sigma_{\rm PSF}$ = 4.1 Å. For this reason we convolve the SSP-MILES basis with a gaussian of FWHM = 3 Å, below the resolution limit, FWHM = 4 Å, the adequate smoothing level, and a FWHM = 5 Å, that 'degrades' the data beyond the spectral resolution of the observations (see Fig. 4.21). The results are consistent, both for the star formation history and the metallicity evolution. The χ^2 values show the same trend observed for the basis Bruzual & Charlot (2003), with increasing values at higher FWHM. The better resolution of SSP-MILES allows to recover narrower structure of the spectral broadening function.

4.4.5 Effect of penalizations

In Sect. 3.2.1 we studied the effect of different penalizations on the spectral inversion. In this section we apply the method to one observations of the outer region of NGC 4388. The main goal here is to confirm that the behavior of the penalization is similar to what was seen with pseudo-data. We choose the SSP library of SSP-MILES (Vazdekis et al. 2007), and we fix a flat star formation history and a constant solar metallicity, as initial guess for the minimization. We proceed as in Sect. 3.2.1, modifying μ_x and μ_Z for three different values, 10^{-4}, 10^2, 10^4.

Spectral analysis

Increasing the penalization μ_x we prevent large curvature in the star formation history (Fig. 4.22). The same trend observed for artificial data in Sect. 3.5 is reproduced with the observations. The solution with higher $\mu_x = 10^4$ does not show a truncation in star formation history. The fluctuations in the first $\sim$ 10 Myr are due to the uncertainties in the stellar populations models at these ages and the slope of the M/L ratio versus lookback time. The flat star formation history recovered from the non parametric method for this μ_x value is unphhysical, because from different observations we know that the galaxy underwent ram pressure stripping in the last few 100 Myr. The lack of star formation should be detectable in the spectrum, and the star formation should show a drop. In Sect. 3.5 we saw that increasing μ_x the cut in the stripping age disappears and the drop in the star formation is underestimatd. For NGC 4388 we observe the same effect, and despite the χ^2 has an acceptable value we can reject this solution because of the higher penalization.

The solutions for $\mu_x < 10^4$ show a drop in the star formation at about 250 Myr for $\mu_x = 10^{-4}$ and 130 Myr for $\mu_x = 10^2$. The χ^2 values are similar and also the time-bin averaged metallicity varies by only $\Delta Z = 0.002$. The χ^2 analysis allows to reject all the solutions that are above the tolerance level of the χ^2 distribution, but is not decisive in the choice of the best model. This is due to the minimization procedure that, for a sufficiently regularized problem, assures always the convergence towards a minimum. To show this we perform a campaign of inversions spanning both for μ_x and μ_Z the range $10^{-4}, 10^4$. In Fig. 4.23 is shown a map of χ^2 values in the μ_x - μ_Z plane. According to the minimum $\chi^2 = 0.416$ and the tolerance level of 0.03 for our problem, we can accept all the $\chi^2 < 0.446$, condition that covers all the map. A campaign of inversion to explore μ_x, μ_Z parameter can reject some solutions but to select the best physical model a detailed analysis of the results is necessary.

The spectral analysis is not able, as seen for the artificial data (Sect. 3.5), to

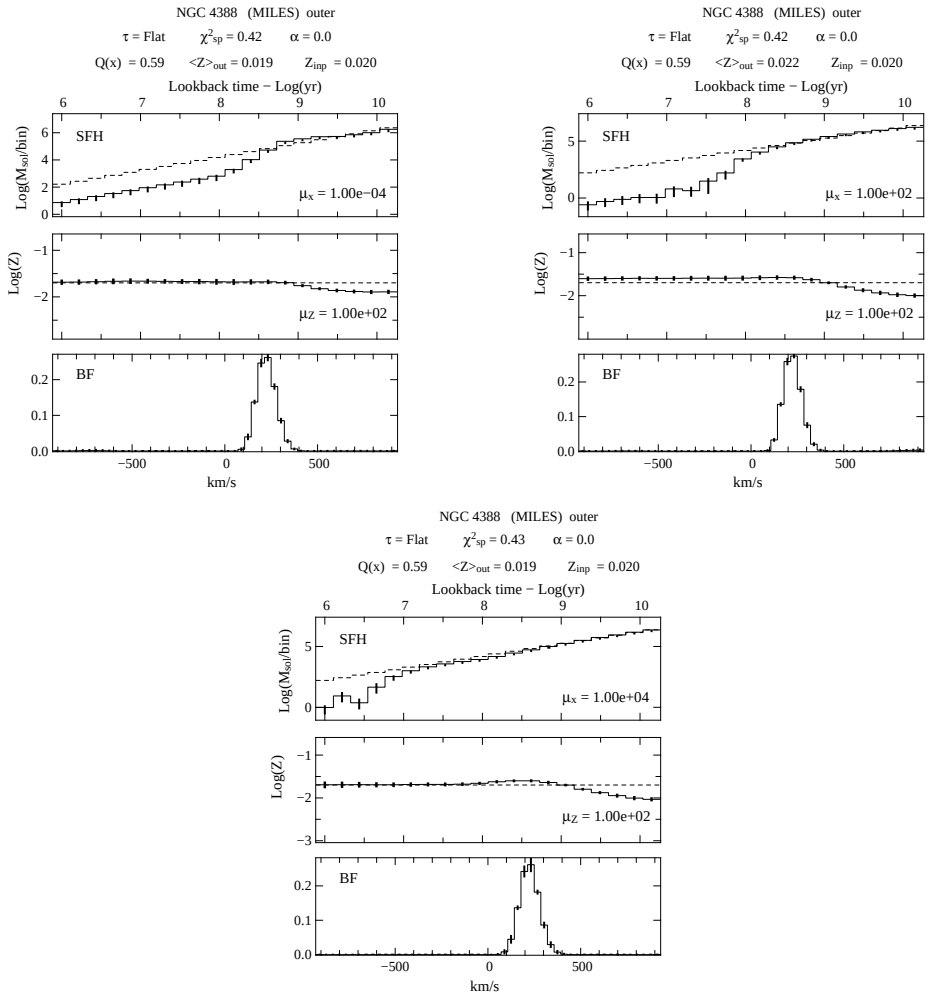

Figure 4.22: Non parametric inversion of the outer region of NGC 4388 for $\mu_x = 10^{-4}$ (left panel), $\mu_x = 10^2$ (right panel), and $\mu_x = 10^4$ (bottom panel). In each figure the top, middle and bottom panels represent the star formation history, the metallicity evolution and the spectral broadening distribution, respectively. In each panel the dashed lines show the initial condition and the solid lines show the results with associated error bars. The errors are obtained via Monte Carlo simulations. In top of panels are marked the τ used for the initial guess in star formation, the spectral χ^2, the weight parameter α in Eq. 2.29, the value of the total $Q(\mathbf{X})$ function (Eq. 2.29), the constant value of metallicity $Z_{\rm inp}$ used for the initial guess and the time-bin average metallicity recovered with the inversion. In right bottom of top and middle panel of each figure are marked the value of penalization μ_x, μ_Z (see Eq. 2.36).

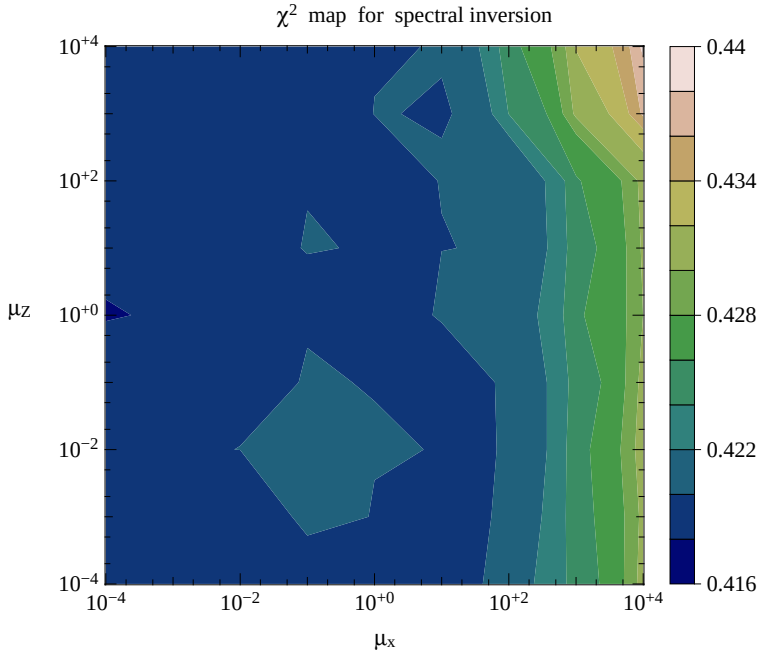

Figure 4.23: χ^2 map for spectral inversion of the outer region of NGC 4388 in the μ_x - μ_Z plane.

recover a clear truncation in the star formation. We can estimate grossly, from this analysis, that the stripping for NGC 4388 occurred between 130 and 250 Myr.

Photometric analysis

We performed a photometric inversion of the outer region of NGC 4388. Since we know from the campaign of pseudo-data that the photometric problem is less constrained in metallicity, we set two different values for $\mu_x = 10^0, 10^2$ and $\mu_Z = 10^2, 10^4$.

The results, shown in Fig. 4.24 are very similar to the one obtained using the semi analytical model of Boissier & Prantzos (2000), in particular Fig. 3.29. For $\mu_x = 10^2$ and $\mu_Z = 10^4$ (right top panel of Fig. 3.29) the mock campaign shows a cut in the star formation that underestimates the input model by one time-bin, i.e.50 Myr, and a constant metallicity value $Z = 0.011$. In the bottom right panel of Fig. 4.24 we have the equivalent trend for NGC 4388 observations. The star formation history shows a cut at lookback time $t = 200$ Myr, and a constant metallicity value $Z = 0.009$. The results are consistent with the spectral inversion, which recovered a stripping age between 130 and 250 Myr. For $\mu_Z = 10^2$ we recover an increasing metallicity with time-bin averaged metallicity of $\langle Z \rangle = 0.023$ for $\mu_x = 10^2$ and $\langle Z \rangle = 0.014$ for $\mu_x = 10^0$, but this last case can be rejected

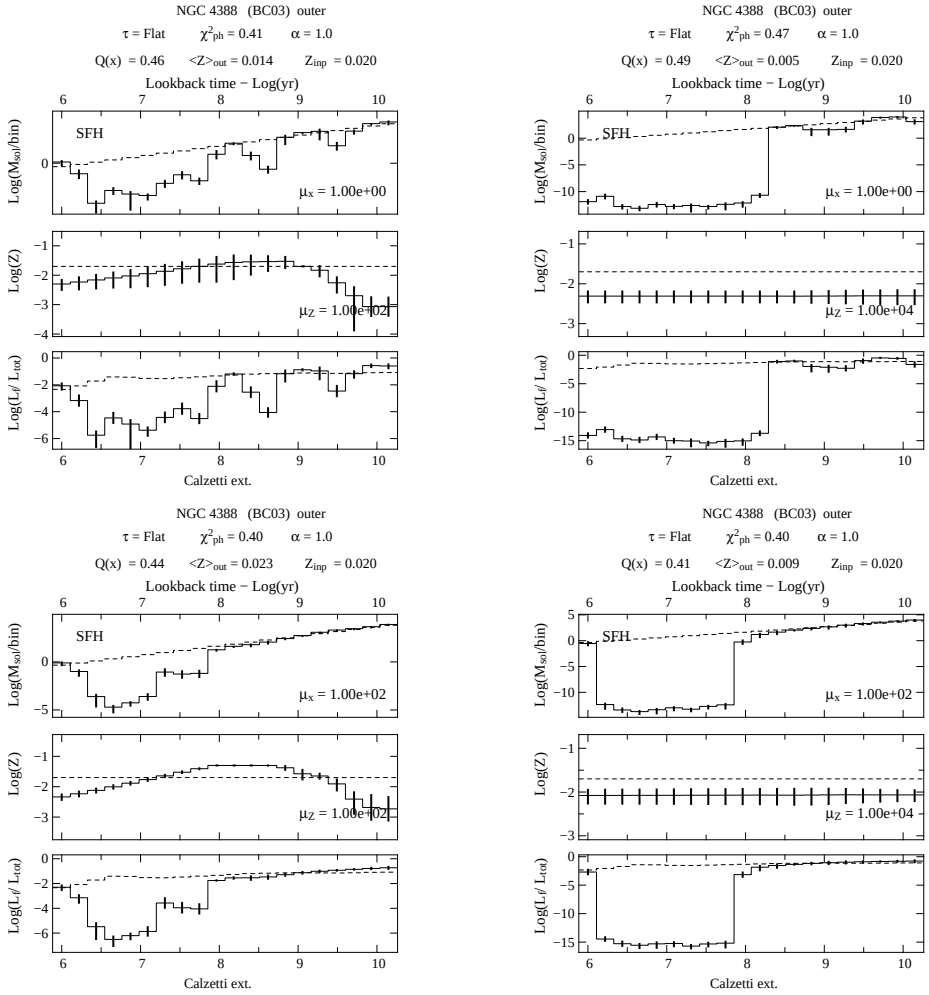

Figure 4.24: Photometric inversion of the outer region of NGC 4388 for : $\mu_x = 10^0$, $\mu_Z = 10^2$ (top left panel), $\mu_x = 10^0$, $\mu_Z = 10^4$ (top right panel), $\mu_x = 10^2$, $\mu_Z = 10^2$ (bottom left panel) and $\mu_x = 10^2$, $\mu_Z = 10^4$ (bottom right panel). In each figure the top, middle and bottom panels represent the star formation history, the metallicity evolution and the spectral broadening distribution, respectively. In each panel the dashed lines show the initial condition and the solid lines show the results with associated error bars. The error are obtained via Monte Carlo simulations. In top of panels are marked the τ used for the initial guess in star formation, the spectral χ^2, the weight parameter α in Eq. 2.29, the value of the total $Q(\mathbf{X})$ function (Eq. 2.29), the constant value of metallicity $Z_{\rm inp}$ used for the initial guess and the time-bin average metallicity recovered with the inversion. At the bottom right of the top and middle panels of each figure are marked the value of penalization μ_x, μ_Z (see Eq. 2.36).

because the star formation penalty is too low, as shown by the fluctuation of the star formation history recovered. Using a $\mu_x = \mu_Z = 10^2$ we obtain flat star formation history at lookback time $t > 200$ Myr and an increasing metallicity until the drop in star formation, very similar to the results showed in top left panel of Fig. 3.29 for the mock data. This can be explained in term of information about the stellar populations at these ages. Since the star formation is low, the metallicity is not well constrained and also a decreasing evolution, as in this case, converge to an acceptable minimum with a $\chi^2 = 0.40$.

The campaign with artificial data showed us that the metallicity is less constrained by the photometry with respect to the spectral analysis. For this reason we prefer to impose a constant solution for the metallicity using, $\mu_Z = 10^4$. In the bottom right panel of Fig. 4.24 the stripping is shifted toward younger ages, and the deviation from a flat star formation history starts when the steep truncation of the star formation in top right panel of Fig. 4.24 occurs. The bump in star formation history is not relevant because it happens at lookback time $t < 10$ Myr, in a range of ages for which the stellar models are uncertain.

Combined analysis

The combined spectral and photometric inversion is shown in Fig. 4.25. The spectral analysis recovered reliable solution for $\mu_x = \mu_Z = 10^2$, and the photometric analysis showed a minimum χ^2 for $\mu_x = 10^2$ and $\mu_Z = 10^4$. The combined analysis seems to prefer the photometric constraint in the combined analysis. Setting $\alpha = 0.5$ we gave the same weight to the spectral and photometric minimization, but as seen in Sect. 4.4.5, the metallicity is not well constrained in photometric analysis. These uncertainties affect the combined analysis, for which the model with $\mu_x = \mu_Z = 10^2$ shows larger error bars at lookback time $t < 1$ Gyr. For this reason again we prefer to keep the metallicity constant and determine the stripping age using the solution for $\mu_x = 10^2$ and $\mu_Z = 10^4$. For this set of weight coefficients the star formation shows a drop at lookback time between $130 \leq t \leq 200$.

In conclusion the spectral analysis reproduces more realistic trends for metallicity than the photometric analysis, but in case of a truncation of the star formation, the regularization does not allow the method to be precise in the stripping age determination. The photometry instead reproduces better the cut of star formation, but does not allow to reproduce reliable metallicity values. Finally the combined analysis reproduces some trends for the metallicity, but the high uncertainties of the photometry in the metallicity solution affects the final solution also in the combined analysis.

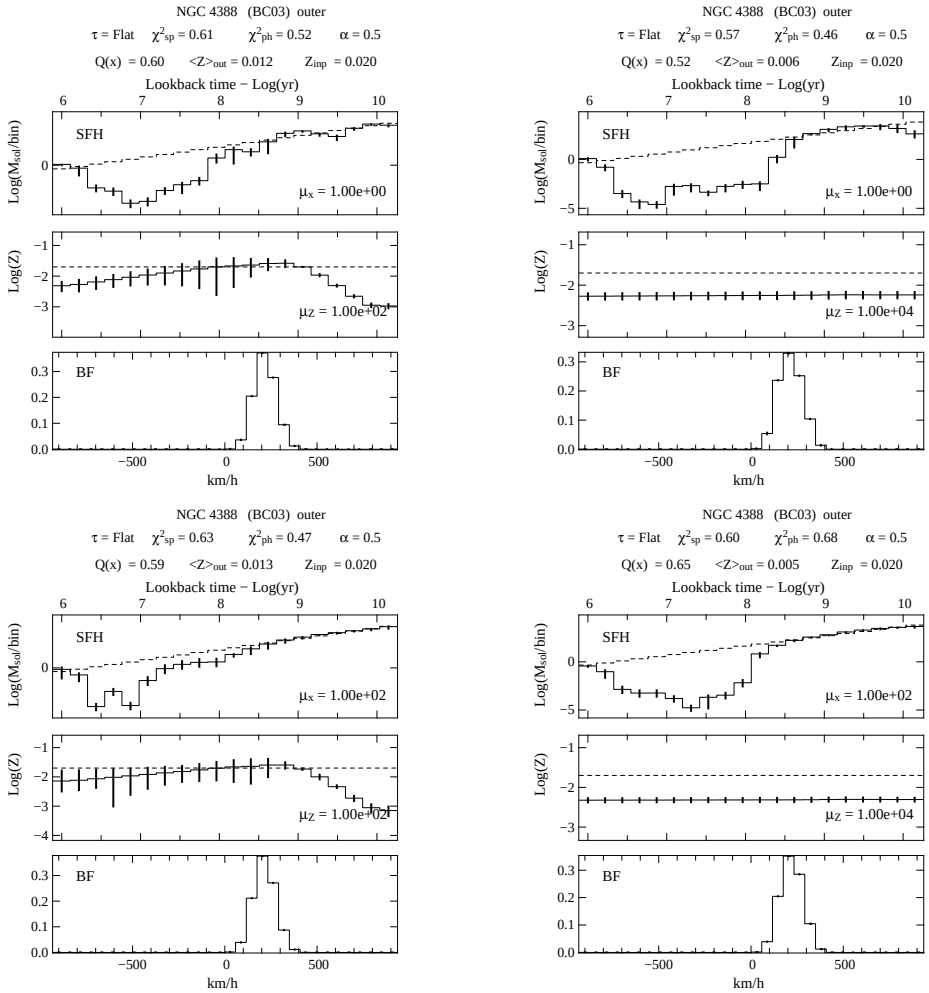

Figure 4.25: Combined inversion of the outer region of NGC 4388 for : $\mu_x = 10^0$, $\mu_Z = 10^2$ (top left panel), $\mu_x = 10^0$, $\mu_Z = 10^4$ (top right panel), $\mu_x = 10^2$, $\mu_Z = 10^2$ (bottom left panel) and $\mu_x = 10^4$, $\mu_Z = 10^4$ (bottom right panel). In each figure the top, middle and bottom panels represent the star formation history, the metallicity evolution and the spectral broadening distribution, respectively. In each panel the dashed lines show the initial condition and the solid lines show the results with associated error bars. The error are obtained via Monte Carlo simulations. In top of panels are marked the τ used for the initial guess in star formation, the spectral χ^2, the weight parameter α in Eq. 2.29, the value of the total $Q(\mathbf{X})$ function (Eq. 2.29), the constant value of metallicity $Z_{\rm inp}$ used for the initial guess and the time-bin average metallicity recovered with the inversion. In right bottom of top and middle panel of each figure are marked the value of penalization μ_x, μ_Z (see Eq. 2.36).

4.5 Test of the parametric method

The purpose of these tests presented here is to investigate the robustness of the determination of the stripping age, under the assumption that the quenching of star formation occurs locally on very short timescales. This assumptiion is based on independent dynamical models (Abadi et al. 1999, Roediger & Brüggen 2006, Vollmer et al. 2001).

4.5.1 Stability of the Parametric method via Monte Carlo simulations

We add a random gaussian noise to the photometry and to the observed spectrum of the outer region of NGC 4388 and we perform 500 Monte Carlo simulations. The results are shown in Fig. 4.26. Both for the spectroscopy and photometry the shape is quite similar for all the realizations. We calculate then the $\chi^2_{\rm tot}$ as in Eq. 2.38 and we show in the bottom panel of Fig. 4.26 the distribution of stripping ages. The results show that the χ^2 minimum oscillates between 180 and 200 Myr, with a peak at 180 Myr. Between 180 and 200 Myr we have $\sim$ 85% of the realizations. The recovered values of minima for χ^2 are in both cases comparable, $\chi^2_{\rm spec}(\rm min) = 0.63$ and $\chi^2_{\rm phot}(\rm min) = 0.60$. The dashed lines in Fig. 4.26 show the tolerance levels of the χ^2 function, that is inversely proportional to the square root of the degrees of freedom of the problem (standard property of χ^2 distribution). This threshold defines the acceptable solutions, in which the fluctuations are generated from the noise in the data, and are not due to potential error in the modelization. In our case the minimum χ^2 for all the realizations are below this threshold.

From our analysis we conclude that the uncertainties in the stripping age are due to the noise from the Monte Carlo simulation, i.e. adding a gaussian noise to the spectral and photometric data. The uncertainties of the stripping age is $\sim$ 20 Myr.

4.5.2 Influence of τ and metallicity evolution

We perform different tests to verify the efficiency of the parametric method in recovering the stripping age. We use the spectra and the photometry of the outer region of NGC 4388, as defined in Sect. 4.1.1 and 4.2. We take the star formation history defined in Eq. 2.37 with $\tau = \{2, 3, 6, 10, 15, 50\}$ Gyr and a constant metallicity evolution $Z = \{0.004, 0.008, 0.02, 0.03\}$ (n.b. $Z = 0.02$ corresponds to solar metallicity). For each couple (τ, Z) we build spectra and photometry at different cut ages and we study the evolution of $\chi^2_{\rm tot}$ as a function of the lookback time for the outer region. For the rest of the section the weight parameter α in

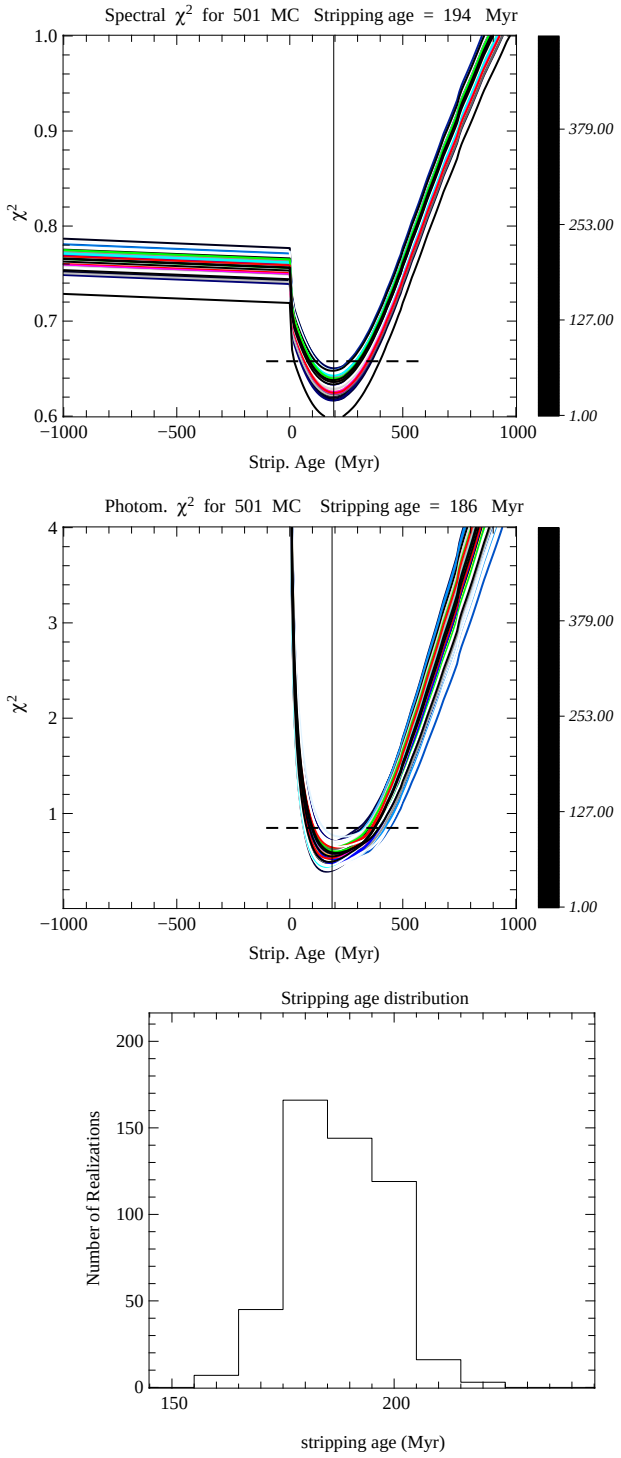

Figure 4.26: $\chi^2_{\rm spec}$ (top panel) and $\chi^2_{\rm phot}$ (middle panel) evolution versus stripping age for 500 Monte Carlo realizations. The dashed line represents the tolerance threshold for the χ^2. Note the different amplitudes of the spectroscopic and photometric curves, which is related to the difference in the number of degrees of freedom of the two problems. Bottom panel : histogram showing the number of Monte Carlo realizations of $\chi^2_{\rm tot}$ as a function of the stripping age.

Eq. 2.38 is been fixed at 0.5. The main results of this analysis are:

- The stripping age decreases with increasing metallicity. In Fig. 4.28 are shown the evolution of $\chi^2_{\rm tot}$ at fixed $\tau = 50$ Gyr with increasing metallicities. The stripping age spans from 650 to 150 Myr and the value of the minimum $\chi^2_{\rm tot}$ decreases with increasing metallicity. The variation of the stripping age becomes less dramatic if we decreases the value of τ, i.e. if we increase the slope of the star formation history. In Fig. 4.29 are shown the variation of the $\chi^2_{\rm tot}$ at a lower $\tau = 15$ Gyr and different metallicites. Note that this star formation history is not compatible with the non-parametric results for NGC 4388. The stripping ages span a smaller range (475-150 Myr) than in the previous case. By decreasing τ we ultimately decrease the weight of the younger populations with respect to the older ones. This means that the variations of the spectra at different cut ages are small. The evolution of the spectral χ^2, shown as dotted lines in Fig. 4.28 and 4.29, is not affected dramatically by the variations of the metallicity. The photometric χ^2, shown as dashed lines in Fig. 4.28 and 4.29, instead shows very different profiles, that modify in a relevant way the total $\chi^2_{\rm tot}$. The photometry is more sensitive to the metallicity variation than the spectra in the stripping age determination.

- The stripping age decreases with the decreasing τ. In Fig. 4.27 are shown for a fixed metalllicity $Z = 0.02$ the evolution of the stripping age with increasing τ. The observed trend is due to the ratio young/old stars. For lower τ the younger component is negligible with respect to the older stellar populations. In the case of $\tau = 2$ Gyr the stripping age is negative and the old stars dominate the light even before the cut in the star formation. As a consequence the spectral $\chi^2_{\rm spec}$ (dotted line) remains almost flat after the star formation cut. The photometric $\chi^2_{\rm phot}$ (dashed line in Fig. 4.27) is more sensitive to the variations of τ compared to the spectral $\chi^2_{\rm spec}$ (dotted line in Fig. 4.27). For $\tau > 2$ Gyr, the $\chi^2_{\rm tot}$ has stables minima, 0.70, 0.62, 0.66. The drop in $\chi^2_{\rm tot}$ values, from $\chi^2_{\rm tot} \sim 4$ to 0.8 immediately after the cut in star formation, means that a star formation with a cut reproduces better the observed spectrum than a continuous one, if the underlying star formation history is sufficiently flat.

A realistic metallicity evolution is not necessarily flat. In the examples illustrated below we show what part of the age-metallicity relation is most relevant in determining the stripping age. We build three different sets of spectra using the same underlying star formation history (exponential with $\tau = 50$ Gyr) and three

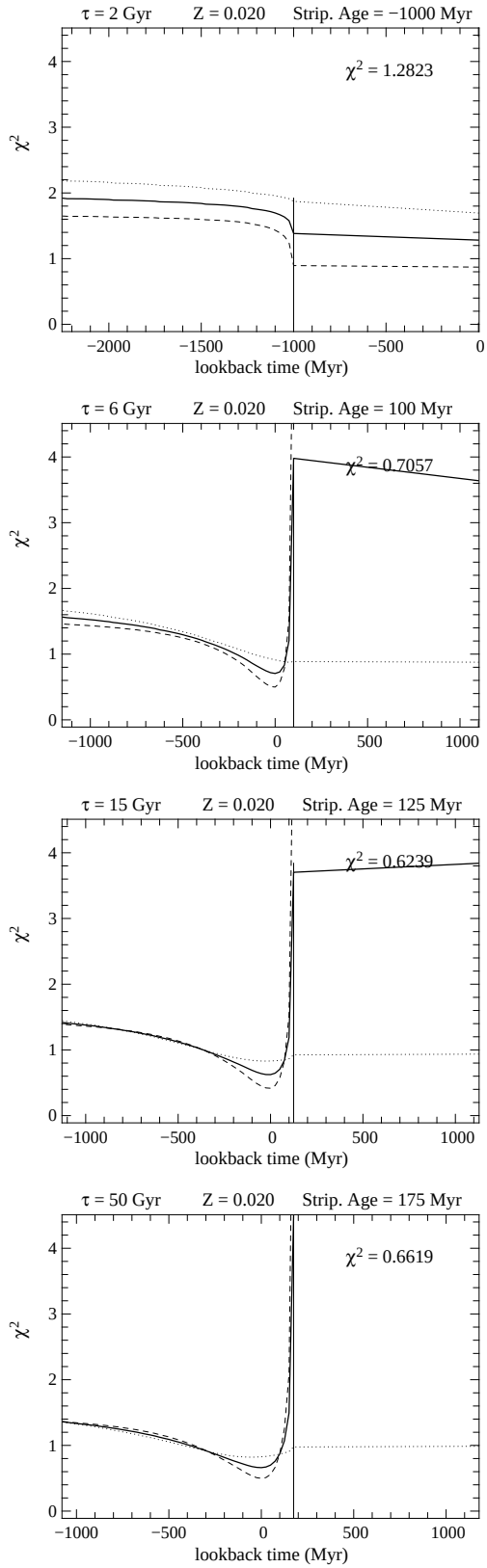

Figure 4.27: Evolution of χ^2 as a function of lookback time for different assumed τ. In each panel the solid lines show $\chi^2_{\rm tot}$, the dashed lines $\chi^2_{\rm phot}$ and the dotted lines $\chi^2_{\rm spec}$. On the top of each panel are marked the characteristic timescale of the underlying star formation history (τ), the constant metallicity value (Z), and the recovered stripping age. Inside each plot is marked the minimum $\chi^2_{\rm tot}$.

different metallicity histories: a constant solar metallicity and the semi-analytical models of Boissier & Prantzos (2000) SAM1 and SAM2 (see Fig. 3.1).

The evolution of $\chi^2_{\rm tot}$ as a function of lookback time for these three cases is shown in Fig. 4.30. The metallicity of SAM2 model (solid line in Fig. 3.1) is always below the solar value. The corresponding stripping age, 200 Myr, is below the stripping age recovered for a solar metallicity evolution, 175 Myr. This result is in agreement with the analysis shown in Fig. 4.29, in which decreasing metallicities leads to higher stripping ages.

The case for the evolution of the metallicity of SAM1 model (dashed line in Fig. 3.1) is different, that is below a solar value only for the first 5 Gyr. Since we are investigating variations in the model spectra occurred in the last $\sim$ 500 Myr, the metallicity variations of the last few Gyr dominates the shape of $\chi^2_{\rm tot}$. For time $t > 11$ Gyr the metallicity $Z > 0.03$ and the recovered stripping age is $t_{\rm strp} = 100$ Myr, i.e. shorter than for a constant solar metallicity. This is in agreement with the results of Fig. 4.28 and 4.29, in which order of magnitude of $\sim$ 100 Myr are reached only for metallicities $Z = 0.02$.

In conclusion, the determination of the stripping age using the parametric method is influenced both by star formation and metallicity.

The choice of τ in Eq. 2.37 determines the star formation at lookback time $t < 300$ Myr, ages relevant in stripping age determination. Steep star formation histories produce negligible star formation at present, compared to the old stellar populations. The light contribution from young ages in the observed spectrum is low and if you want to reproduce this, you have to cut a lot when we use a constant star formation history, because the young populations dominates the light in this case. For a decreasing star formation the young ages contributes less light to the final spectrum. Therefore the stripping age is smaller than that for a constant star formation history.

Using semi-analytical models of Boissier & Prantzos (2000) we will show in Sect. 4.5.6 that the metallicity of stellar populations at lookback time $t < 5$ Gyr are critical for the stripping age determination. Because of the age-metallicity degeneracy, the metal rich populations look older. Thus the stripping age becomes smaller than that for metal poor populations.

4.5.3 Influence of the chosen Spectral Broadening Function

The spectral library chosen to build the model spectra is the Bruzual & Charlot (2003) library, with an average resolution $R \sim 2000$. The VLT observations have a

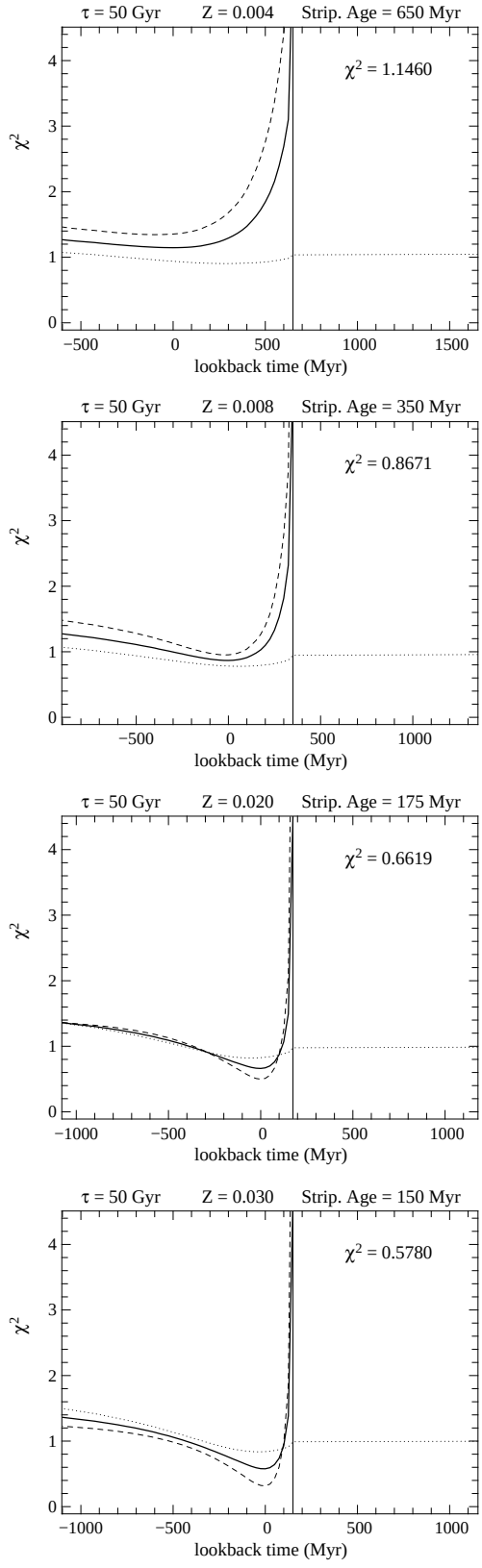

Figure 4.28: Evolution of $\chi^2_{\rm tot}$ as a function of lookback time for different assumed metallicities (solid lines). For a detailed description see Fig. 4.27.

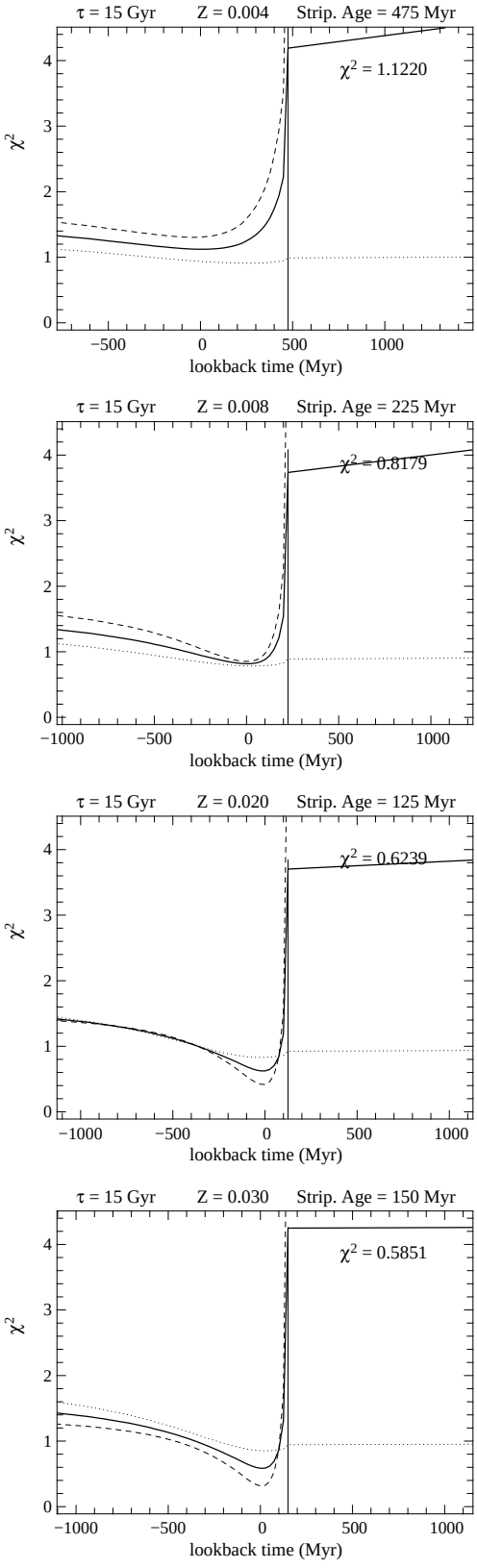

Figure 4.29: Evolution of $\chi^2_{\rm tot}$ as a function of lookback time for different assumed metallicities (solid lines). For a detailed description see Fig. 4.27.

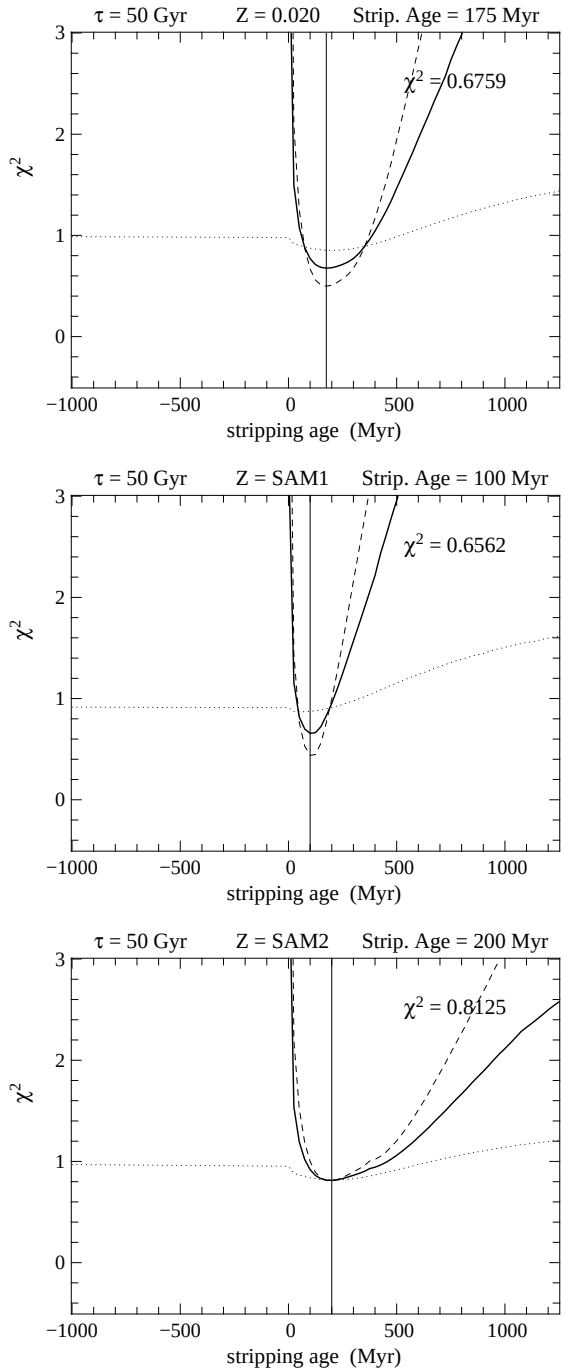

Figure 4.30: $\chi^2_{\rm tot}$ as a function of lookback time for a family of spectra built with a fixed exponential star formation history (τ = 50 Gyr) and different metallicity evolutions : a constant solar metallicity (top panel), SAM1 metallicity model (middle panel) and SAM2 metallicity model (Boissier & Prantzos, 2000). The solid, dotted and dashed lines show the total $\chi^2_{\rm tot}$, the spectral $\chi^2_{\rm spec}$ and the photometric $\chi^2_{\rm phot}$, respectively. To build the model spectra we used a τ = 50 Gyr (Eq. 2.37). On top of each panel are marked the value of the τ, the metallicity used and the stripping age recovered. In the right corner of each panel is marked the minimum $\chi^2_{\rm tot}$ of the plotted distribution.

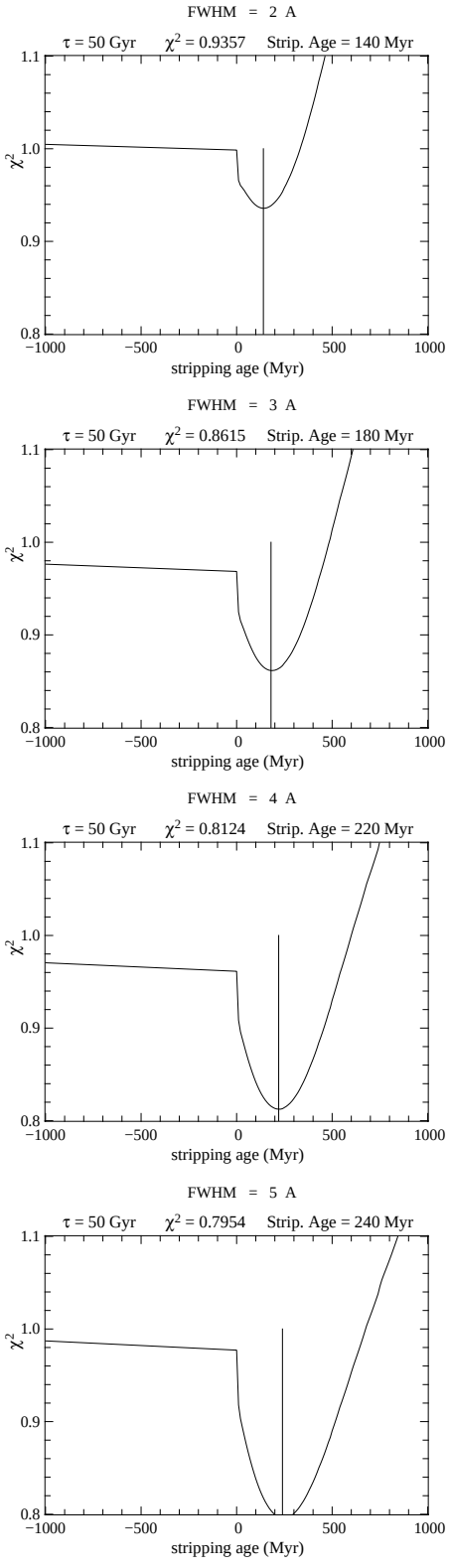

Figure 4.31: $\chi^2_{\rm spec}$ evolution versus stripping age for a set of spectra reproduced from a cut star formation convolved with a gaussian. On the top of each panel are shown the characteristic timescale of the underlying star formation law (τ), the minimum $\chi^2_{\rm spec}$, the FWHM of the convolved gaussian, and the recovered stripping age. The vertical bar marks the minimum position.

resolution $R \sim 800$. To be consistent with the observations we smooth the spectral library to match the observations. The non parametric method is able to recover a spectral broadening function that collects the effect of the instrumental point spread function and the effect due to the line of sight stellar velocity distribution.

We can convolve the model spectra used in the parametric method analysis with a Gaussian of FWHM = 3.3 Å that "degrades" the models to the spectral resolution of the observations, or we can convolve the models with the spectral broadening function recovered from the non parametric inversion of the outer region.

In Fig. 4.32 and 4.33 are shown the best fit spectrum with the associated $\chi^2_{\rm spec}$ (see Eq. 2.38). The residuals are quite similar, and the non parametric correction of the continuum has almost the same shape in both cases. Despite this similarity the recovered stripping ages are different. For the models convolved with a gaussian $t_{\rm strp} = 190$ Myr and the minimum $\chi^2_{\rm tot} = 0.84$, for the models convolved with the spectral broadening function $t_{\rm strp} = 170$ Myr and the minimum $\chi^2_{\rm tot} = 0.62$. Convolving the spectra with a broadening function obtained from the non parametric inversion we better reproduce the observations.

The smoothing plays an important role in the determination of the stripping age. We investigate this effect by convolving the model spectra with gaussians of different FWHM. No extra broadening is allowed (i.e. the search for a line of sight velocity distribution is switched off in the minimization procedure). In Fig. 4.31 are shown some results. The stripping age increases with the FWHM used for the convolution, but this dependence becomes weaker with increasing FWHM: between 2 and 3 Å the stripping ages varies of 40 Myr and between 5 and 6 Å the stripping ages varies of 20 Myr. This is expected. If the models are not smooth enough, their absorption lines are deep and they look older.

4.5.4 Influence of the extinction law

The parametric method applies to the photometry an extinction law of Calzetti (2001) that was calibrated on nearby star forming galaxies. Among extinction law in the literature, this law is one of the flattest, because it results from a spatial configuration where stars and dust are mixed. We investigate the effect of a different choice of extinction. We take the Cardelli et al. (1989) law with $R_V = 3.1$ (see app. D) and we study the evolution of $\chi^2_{\rm phot}$. The results (Fig. 4.34) vary by 20 Myr and the $\chi^2_{\rm phot}$ vary by less than 0.01. The ligh extinction in spectral analysis is taken into account using the same Non Parametric Estimation of the Continuum (NPEC) used in non parametric method (see App. C). For this reason this source of errors involved only the photometric analysis.

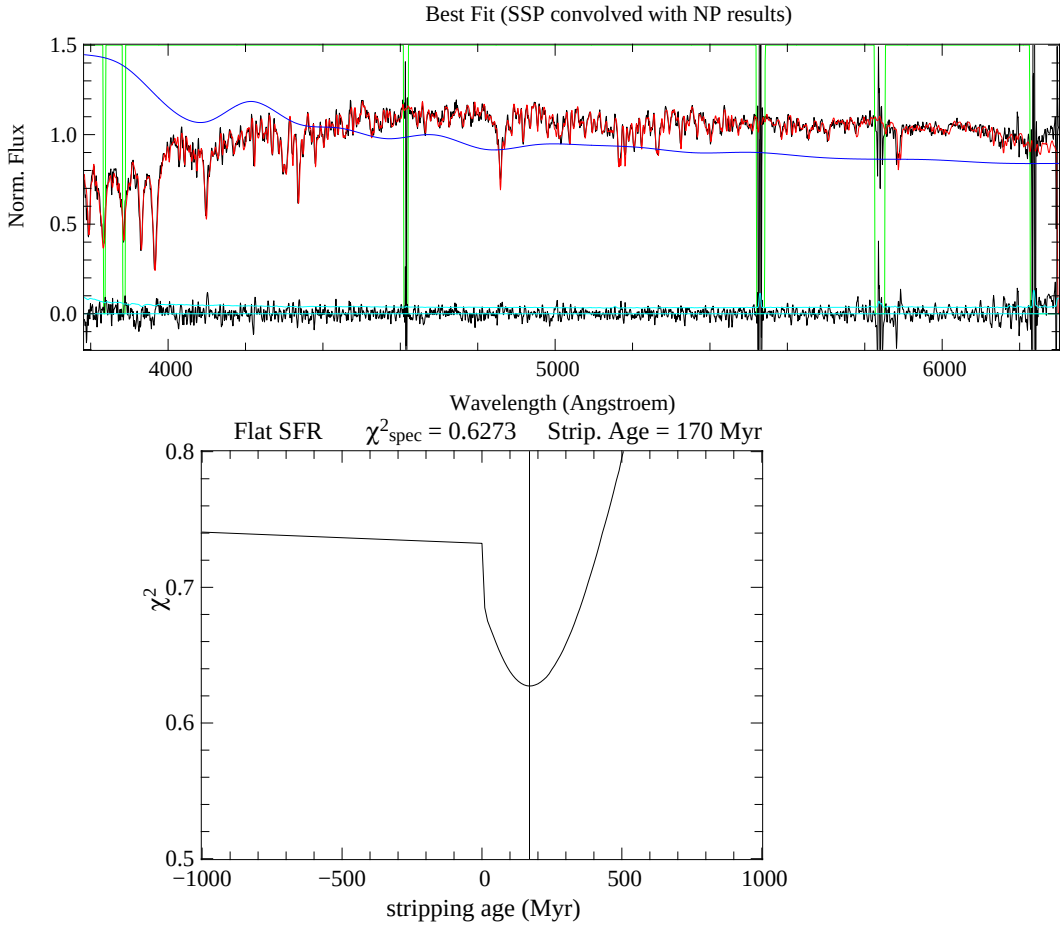

Figure 4.32: Top panel: Best fit for a set of spectra that reproduce the spectral energy distribution of different stellar populations at different ages after the cut in their star formation history. The underlying conditions are a flat star formation history and a constant solar metallicity. The set of spectra have been convolved with the spectral broadening function obtained from non parametric inversion of the outer region of NGC 4388. The red line shows the best fit, the black line are the observations, the green line shows the used mask for the bad pixels and the blue line show the non parametric extinction correction. Bottom panel : Evolution of the χ^2_{spc} (see Eq. 2.38) versus stripping age. The vertical line shows the minimum.

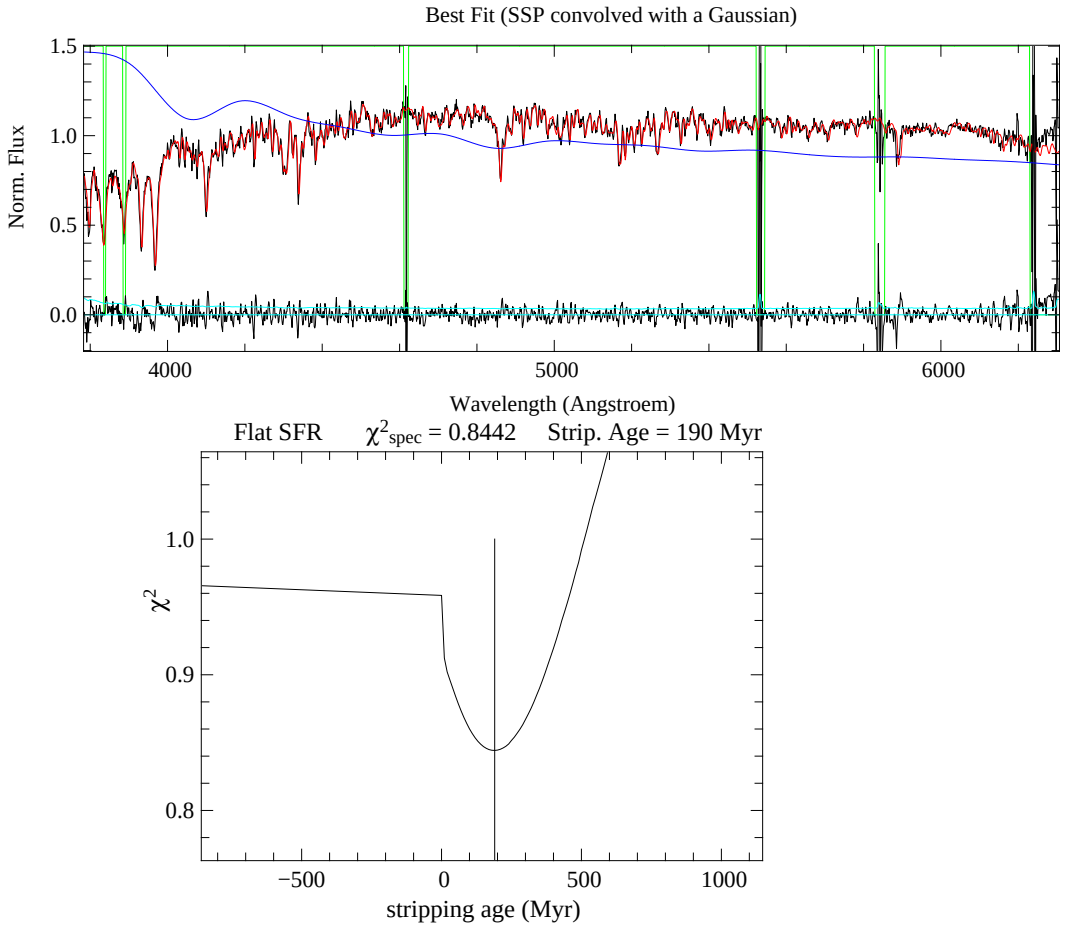

Figure 4.33: Top panel: Best fit for a set of spectra that reproduce the spectral energy distribution of different stellar populations at different ages after the cut in their star formation history. The underlying conditions are a flat star formation history and a constant solar metallicity. The set of spectra have been convolved with a Gaussian distribution with a FWHM = 3.3 Å. The red line shows the best fit, the black line are the observations, the green line shows the used mask for the bad pixels and the blue line show the non parametric extinction correction. Bottom panel : Evolution of the χ^2_{spec} (see Eq. 2.38) versus stripping age. The vertical line shows the minimum.

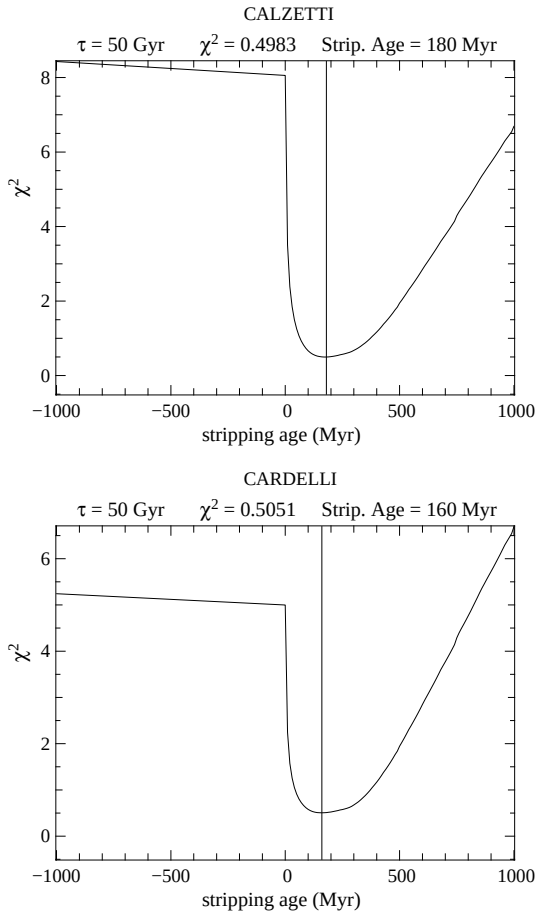

Figure 4.34: $\chi^2_{\rm phot}$ evolution versus stripping age for a set of spectra from a truncated star formation. In the top and bottom panels are plotted the results obtained using a Calzetti (2001) and Cardelli et al. (1989) extinction law, respectively. On the top of each panel are shown the characteristic timescale τ used for the star formation before the cut, the minimum $\chi^2_{\rm phot}$ and the recovered stripping age.

4.5.5 Metallicity error from the NP method and stripping age

We use for the estimation of the stripping age in the outer region the metallicity value recovered from the non parametric inversion. Performing 10 Monte Carlo simulations we gave also an error bar associated to the non parametric result. To be consistent with this incertitude in the metallicity value we build 3 set of spectra with a flat star formation history cut at different ages. We take a constant metallicity evolution with 3 different values corresponding to the value recovered from the non parametric inversion, the lower limit and the upper limit, as determined from the Monte Carlo simulations. The result are shown in Fig. 4.35 the fluctuation of the recovered stripping age is of the order of 15 Myr.

4.5.6 Metallicity dependence of the stripping age determination

In Sect. 4.5.2 we built a grid of spectra using different metallicity evolutions and different star formation models and we showed that the stripping age decreases with increasing metallicity. In this section we investigate which stellar populations are critical in the stripping age determination. We use four different metallicity evolutions. For one model the metallicity is $Z = 0.02$ since lookback time $t = 13.5$ Gyr. For the second model $Z = 0.01$ except for the last 12 Myr, where it rises to $Z = 0.02$. Between these two extremes, we build two models in which the metallicity increases abruptly from $Z = 0.01$ to $Z = 0.02$ at intermediate ages, at lookback times $t_{\rm inc} = 2.5$ Gyr, and $t_{\rm inc} = 5$ Gyr. We study the χ^2 evolution and the effect on the stripping age for spectral, photometric and joint analysis.

- **Spectral analysis**

The case with $t_{\rm inc} = 12$ Myr corresponds to a constant metallicity evolution of $Z = 0.01$ and the case $t_{\rm inc} = 13.5$ Gyr is a constant metallicity of $Z = 0.02$. These cases give a stripping age of 240 Myr and 180 Myr, respectively. The spectral χ^2 decreases with $t_{\rm inc}$ and the stripping age increases when the metallicity decreases, in agreement with results of Sect. 4.5.2 (left column in Fig. 4.36). The difference in stripping age between $Z = 0.01$ and $Z = 0.02$ is then 60 Myr. If we use a constant metallicity of $Z = 0.01$ and we increase the value to $Z = 0.02$ only in the last 2.5 Gyr, we obtain a stripping age that is 30 Myr above the value that we obtain if the metallicity is solar for an Hubble time. If we extend this interval to the last 5 Gyr we obtain a stripping age that is 20 Myr above the reference value of 180 Myr. The χ^2, on the contrary, is not very sensitive to the variation of metallicity in the last 5 Gyr. As already said the tolerance level for the χ^2 function in our case is $\Delta\chi^2 = 0.02$. The value of the minimum χ^2 obtained when we increase the metallicity in the last 5 Gyr is $\chi^2 =$

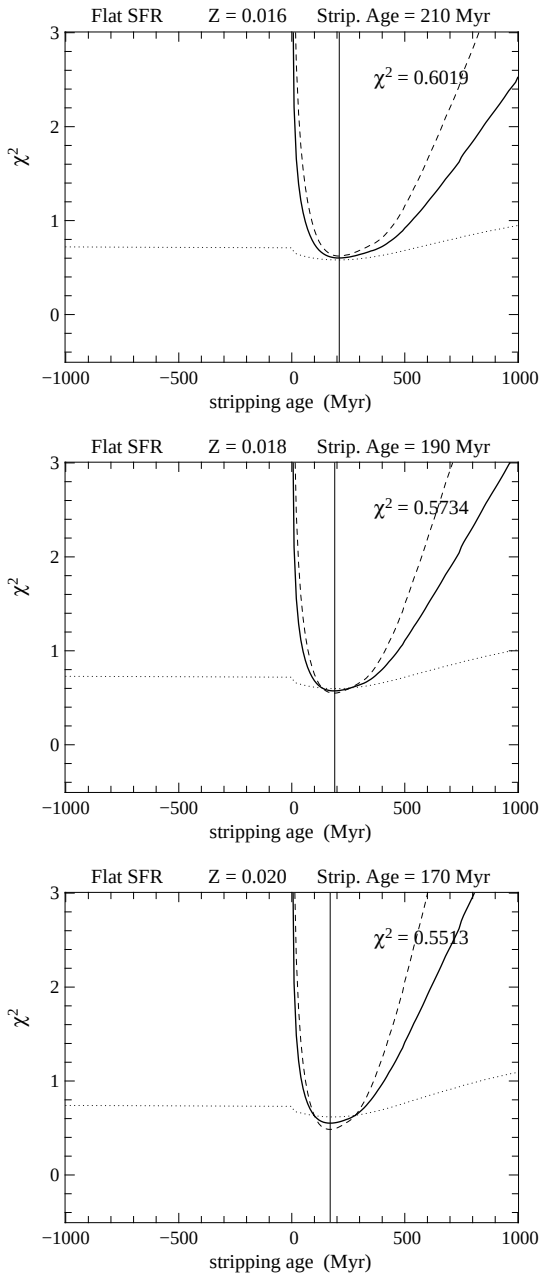

Figure 4.35: Evolution of $\chi^2_{\rm tot}$ as a function of lookback time for different assumed metallicities (solid lines). For a detailed description see Fig. 4.27.

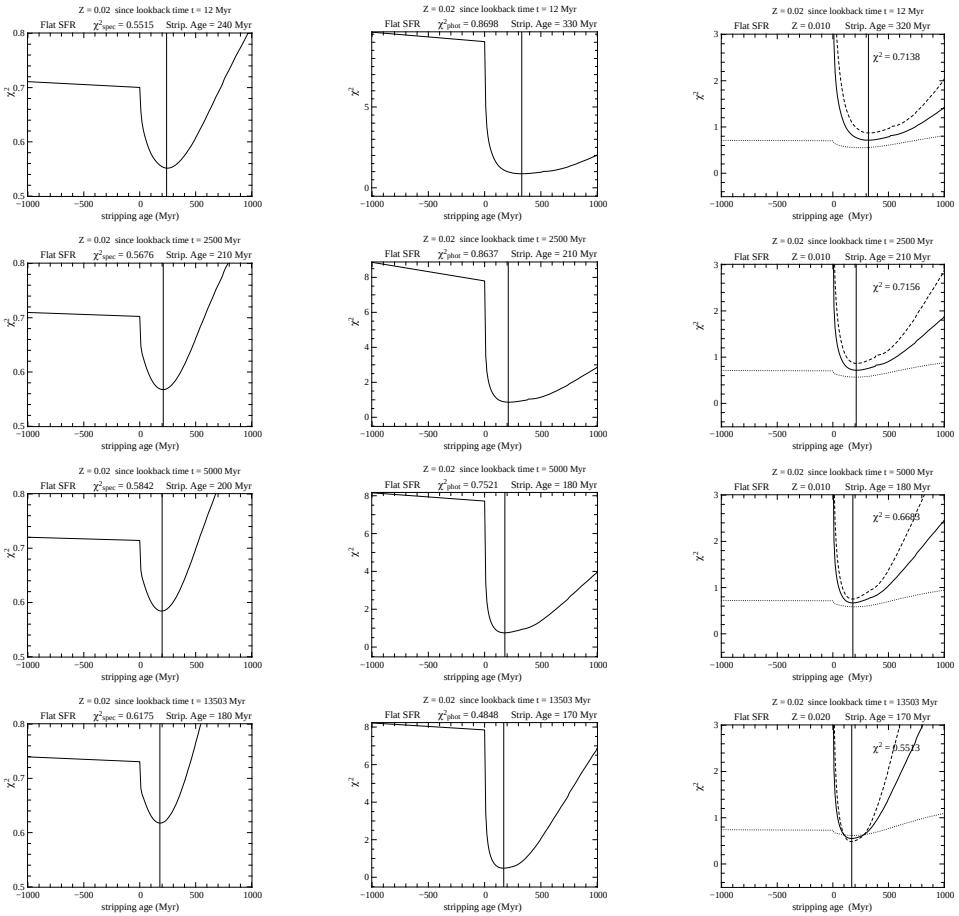

Figure 4.36: Evolution of spectral χ^2 (left column), photometric χ^2 (middle column) and total χ^2 (right column) as a function of the stripping age. In the right column the dashed and dot lines represents the photometric and spectral χ^2, respectively. Each row corresponds to a different metallicity evolution, depending on the lookback time $t_{\rm inc}$ since when the metallicity increases from $Z = 0.01$ to $Z = 0.02$. We show models with $t_{\rm inc} = 12$ Myr (first row), 2.5 Gyr (second row), 5 Gyr (third row) and 13.5 Gyr (bottom row). On top of each panel are marked the minimum χ^2, the corresponding stripping age and the star formation used.

0.57, $\Delta\chi^2 = 0.03$ above the value obtained when the metallicity is constantly $Z = 0.01$. The uncertainty in the stripping age estimated with the parametric method is $\sim$ 30 - 35 Myr. In this sense the stripping age is strictly dependent only on the metallicity evolution of the last 5 Gyr, and this result is inside the errors determined summing all the sources of potential errors.

- **Photometric analysis**

Photometry shows an opposite trend with metallicity with respect to the spectral analysis (middle column of Fig. 4.5.2). The χ^2 decreases with increasing metallicity and the minimum value is obtained for a constant metallicity evolution of $Z = 0.02$. The tolerance of the χ^2 for the photometric analysis is 0.35. The value

obtained for a solar metallicity in the last 5 Gyr is $\chi^2 = 0.75$. This value is acceptable and leads to a stripping age of 180 Myr, 10 Myr under the estimation obtained using a constant solar metallicity. Also for photometric analysis the metallicity of the last 5 Gyr is crucial in stripping age determination. We note that between a constant solar metallicity over all time and a constant solar metallicity only during the last 2.5 Gyr the stripping age varies by 40 Myr. Once we include these early ages and we consider a constant metallicity evolution of $Z = 0.01$, the stripping age increases rapidly to 330 Myr. The dependence of the stripping age on the metallicity of intermediate populations is more pronounced in the photometric analysis, where the sensitivity to the variation of metallicity in stripping age is largely due to the metallicity evolution during the last 2.5 Gyr.

• **Combined analysis**

The joint analysis of photometry and spectrum shows the same trends observed for the separate analysis (right panel in Fig. 4.5.2). The χ^2 is minimum for a constant solar metallicity. The total χ^2 is dominated by the photometric χ^2. The best spectral χ^2 is always smaller than the best photometric χ^2, except for the solar case, and using a constant metallicity $Z = 0.01$, we obtain a stripping age that is completely dominated by the result of the photometric analysis.

From this analysis we infer that the stripping age estimated using our parametric method is not influenced by the chosen long term metallicity evolution. The relevant part of the age-metallicity relation that determines the final stripping age estimation, is that of the intermediate age and young stellar populations. In particular we note that spectral analysis is able to reproduce the same results that we would obtain with a constant metallicity, by imposing this value only in the last 5 Gyr of galaxy's life. This dependence is more pronounced for photometric analysis, in which the epoch relevant for stripping age determination is the evolution over the last 2.5 Gyr.

In this section the variation of the stripping ages $t_{\rm strp}$ has been extensively investigated. The main results are:

- we check the stability of the results performing 500 Monte Carlo simulations, recovering a $\Delta t_{\rm strp} \simeq 20$ Myr;
- we fix a constant metallicity $Z = 0.02$ and varying $2 \leq \tau \leq 50$ Gyr we built different families of spectra. We obtained $\Delta t_{\rm strp} = 175$ Myr;
- defining for the star formation $15 \leq \tau \leq 50$ Gyr and for the metallicity

$0.004 \leq Z \leq 0.03$ we built different families of spectra. We obtained $315 \leq \Delta t_{strp} \leq 500$ Myr;

- for $\tau = 50$ Gyr and $Z = 0.02$ we built a family of spectra in which we convolve, before the minimization procedure, the model spectra with gaussians of different FWHM. For $2 \leq$ FWHM ≤ 5 Å we recovered $\Delta t_{strp} = 100$ Myr;
- we applied to the model spectra an extinction law of Calzetti (2001) and Cardelli et al. (1989) and applying the non parametric method to the photometric analysis we recovered a $\Delta t_{strp} = 20$ Myr;
- we built three families of spectra using a flat star formation history and metallicity values consistent with the error bars recovered in the non parametric method $0.016 \leq Z \leq 0.02$. For the chosen metallicity we recovered $\Delta t_{strp} = 40$ Myr;
- for a flat star formation history, we built a family of spectra in which the metallicity increases abruptly from $Z = 0.01$ to $Z = 0.02$ at different time t_{inc}. For $12 \leq t_{inc} \leq 13503$ Myr we recovered $\Delta t_{strp} = 150$ Myr.

Chapter 5

NGC 4522

2008, A&A, 491, 455.

Astronomy & Astrophysics manuscript no.
(will be inserted by hand later)

Ram-pressure stripped molecular gas in the Virgo spiral galaxy NGC 4522⋆

B. Vollmer[1], J. Braine[2], C. Pappalardo[1], P. Hily-Blant[3]

[1] CDS, Observatoire astronomique de Strasbourg, 11, rue de l'université, 67000 Strasbourg, France
[2] Laboratoire d'Astrophysique de Bordeaux (OASU), Université de Bordeaux, UMR 5804, CNRS/INSU, B.P. 89, F-33270 Floirac, France
[3] IRAM, Domaine Universitaire, 300 rue de la Piscine, 38406 Saint-Martin d'Hères, France

Received / Accepted

Abstract. IRAM 30m ^{12}CO(1–0) and ^{12}CO(2–1) HERA observations are presented for the ram-pressure stripped Virgo spiral galaxy NGC 4522. The CO emission is detected in the galactic disk and the extraplanar gas. The extraplanar CO emission follows the morphology of the atomic gas closely but is less extended. The CO maxima do not appear to correspond to regions where there is peak massive star formation as probed by Hα emission. The presence of molecular gas is a necessary but not sufficient condition for star formation. Compared to the disk gas, the molecular fraction of the extraplanar gas is 30 % lower and the star formation efficiency of the extraplanar gas is about 3 times lower. The comparison with an existing dynamical model extended by a recipe for distinguishing between atomic and molecular gas shows that a significant part of the gas is stripped in the form of overdense arm-like structures. It is argued that the molecular fraction depends on the square root of the total large-scale density. Based on the combination of the CO/Hα and an analytical model, the total gas density is estimated to be about 4 times lower than that of the galactic disk. Molecules and stars form within this dense gas according to the same laws as in the galactic disk, i.e. they mainly depend on the total large-scale gas density. Star formation proceeds where the local large-scale gas density is highest. Given the complex 3D morphology this does not correspond to the peaks in the surface density. In the absence of a confining gravitational potential, the stripped gas arms will most probably disperse; i.e. the density of the gas will decrease and star formation will cease.

Key words. Galaxies: individual: NGC 4522 – Galaxies: interactions – Galaxies: ISM – Galaxies: kinematics and dynamics – Stars: formation – Radio lines: ISM

1. Introduction

The best-studied case of active ram-pressure stripping of a cluster galaxy is NGC 4522 located in the Virgo cluster. Only in this cluster is the resolution of radio telescopes sufficient ($\sim 20'' = 1.6$ kpc[1]) for a detailed analysis of the gas morphology and kinematics. NGC 4522 is a rather small ($D_{25} = 4' = 20$ kpc) edge-on Sc galaxy with a rotation velocity of ~ 100 km s^{-1}. It is strongly HI deficient ($DEF = 0.6$; Helou et al. 1984). Its projected distance to the cluster center (M 87) is large (~ 1 Mpc), and its radial velocity with respect to the Virgo cluster mean is high (1150 km s^{-1}). HI and Hα observations (Kenney et al. 2004; Kenney & Koopmann 1999) show a heavily truncated gas disk at a radius of 3 kpc, which is $\sim 40\%$ of the optical radius, and a significant amount of extraplanar gas to the west of the galactic disk. The one-sided extraplanar atomic gas distribution shows high column densities, comparable to those of the adjacent galactic disk. The 6 cm polarized radio continuum emission shows a maximum at the eastern edge of the galactic disk, on the opposite side of the extraplanar gas and star formation. Since the stellar disk is symmetric and undisturbed (Kenney & Koopmann 1999), a tidal interaction is excluded as the origin of the peculiar gas distribution of NGC 4522. Thus, this galaxy undergoes ram-pressure stripping due to the galaxy's rapid motion within the hot and tenuous intracluster gas (ICM) of the Virgo cluster.

Vollmer et al. (2006) made a dynamical model that includes the effects of ram pressure for NGC 4522. The model successfully reproduces the large-scale gas distribution and the velocity field. By assuming a Gaussian distribution of relativistic electrons, they obtained the distribution of polarized radio continuum emission, which repro-

Send offprint requests to: B. Vollmer, e-mail: bvollmer@astro.u-strasbg.fr

⋆ Based on IRAM 30m HERA observations

[1] We use a distance of 17 Mpc for the Virgo cluster.

duces the VLA observations of polarized radio continuum emission at 6 cm. The observed maximum of the polarized radio continuum emission is successfully reproduced. The eastern ridge of polarized radio continuum emission is therefore due to ram pressure compression of the interstellar medium (ISM) and its magnetic field. The dynamical model and the analysis of the stellar populations of the outer gas-free disk using optical spectra and UV photometry (Crowl & Kenney 2006) indicate that the ram pressure maximum occurred only $\sim$ 50–100 Myr ago. This scenario has one important caveat: the large projected distance of NGC 4522 (1 Mpc) to the center of the Virgo cluster (M87). Assuming a static smooth ICM and standard values for the ICM density and the galaxy velocity, the ram pressure at that location seems to be too low by an order of magnitude to produce the observed truncation of the gas disk. A natural explanation for the enhanced ram pressure efficiency is that the intracluster medium is not static but moving due to the infall of the M49 group of galaxies from behind (Kenney et al. 2004, Vollmer et al. 2004, Vollmer et al. 2006). In this case the galaxy has just passed the region of highest intracluster medium velocity.

While we know from the Hα observations (Kenney et al. 2004, Kenney & Koopmann 1999) that stars are forming in the extraplanar gas, we do not know the distribution of molecular gas in these regions. How does the complex multiphase interstellar medium respond to ram pressure stripping? Can we model the molecular gas content during the interaction using simplified recipes? Can dense molecular gas decouple from the ram pressure wind as suggested for NGC 4438 (Vollmer et al. 2005)? In this article we present IRAM 30m ^{12}CO(1–0) and ^{12}CO(2–1) HERA observations of NGC 4522 to investigate the fate of the stripped gas.

We present our CO observations in Sec. 2 followed by the observational results in Sec. 3. The detection of ram pressure wind decoupled molecular clouds is reported in Sec. 4. In Sec. 5 we compare our CO observations to existing HI and Hα emission distributions (Kenney et al. 2004) and to the dynamical model of Vollmer et al. (2006). The molecular fraction and star formation efficiencies are discussed in Sec. 6 and we give our conclusions in Sec. 7.

2. Observations

The observations of the CO(1–0) and CO(2–1) lines, with rest frequencies of 115.271204 and 230.53799 GHz respectively, were carried out at the 30 meter millimeter-wave telescope on Pico Veleta (Spain) run by the Institut de RadioAstronomie Millimétrique (IRAM). The CO(2–1) observations used the HERA multi-beam array, with 3 $\times$ 3 dual-polarization receivers, and the WILMA autocorrelator backend with 2MHz spectral resolution. The CO(1–0) observations used the single-pixel "AB" receivers and the 1MHz filterbanks as backends. The spectral resolution is 2.6 km s^{-1} in both cases. The HERA observations were made in February and March 2006 and the CO(1–0) in November 2006. In both cases, a nutating secondary ("wobbler") was used with a throw of 180–200 arcseconds in order to be clear of any emission from the galaxy. The positions observed in each line are indicated in Figs. 1 and 2 as triangles for CO(2–1) and circles for CO(1–0).

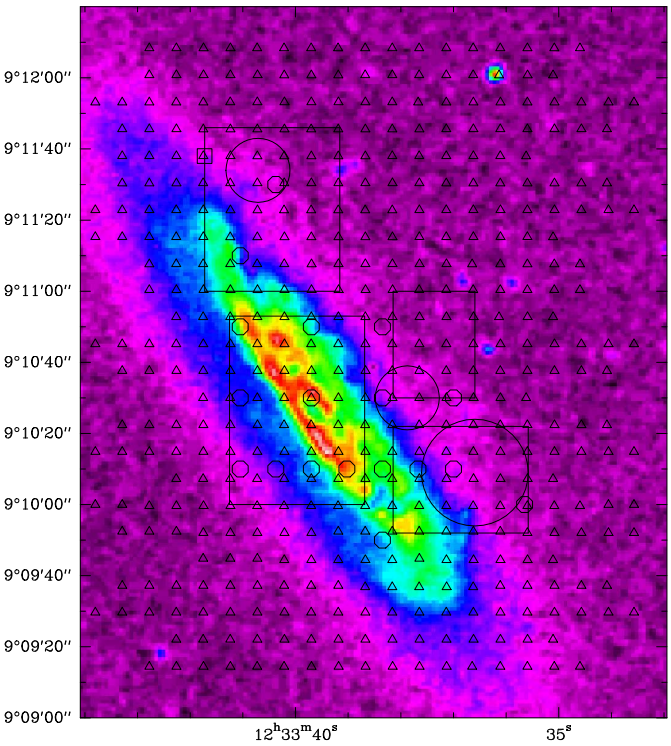

Fig. 1. IRAM 30m pointings on a DSS B band image. Triangles: ^{12}CO(2-1) HERA observations. Small circles: ^{12}CO(1-0) observations. Large circles: Binned HERA pointings (see Fig. 7). The large boxes correspond to Fig. 3 to Fig. 6.

Data reduction was straightforward, eliminating any obviously bad channels and excluding the spectra taken under particularly poor conditions (system temperature over 1000 K). Spectra were then summed position by position. System temperatures of the final spectra ranged from 200 to 500 K on the Ta* scale. All spectra are presented on the main beam temperature scale, assuming telescope main-beam and forward efficiencies of $\eta_{\rm mb} = 0.54$ and $\eta_{\rm for} = 0.90$ for HERA and $\eta_{\rm mb} = 0.74$ and $\eta_{\rm for} = 0.95$ for the CO(1–0) line. The spectra near map edges with noise levels greater than 28 mK (T_{mb} scale) are left out of Fig. 2. At the assumed distance of NGC 4522, 17 Mpc, the CO(2–1) and CO (1–0) beams correspond to 0.9 and 1.7 kpc respectively. In order to convert CO integrated intensities into molecular gas masses, we have assumed a $N({\rm H_2})/I_{\rm CO(2-1)}$ ratio of 2×10^{20} H$_2$ mol cm^{-2} per K kms^{-1}. Our conclusions, however, do not depend strongly on the $N({\rm H_2})/I_{\rm CO}$ ratio within reasonable variations.

3. Disk and extraplanar molecular gas

3.1. CO spectra

Fig. 3-6 show the ^{12}CO(2–1) HERA spectra (resolution of 11″) together with the HI spectra of Kenney et al. (2004)

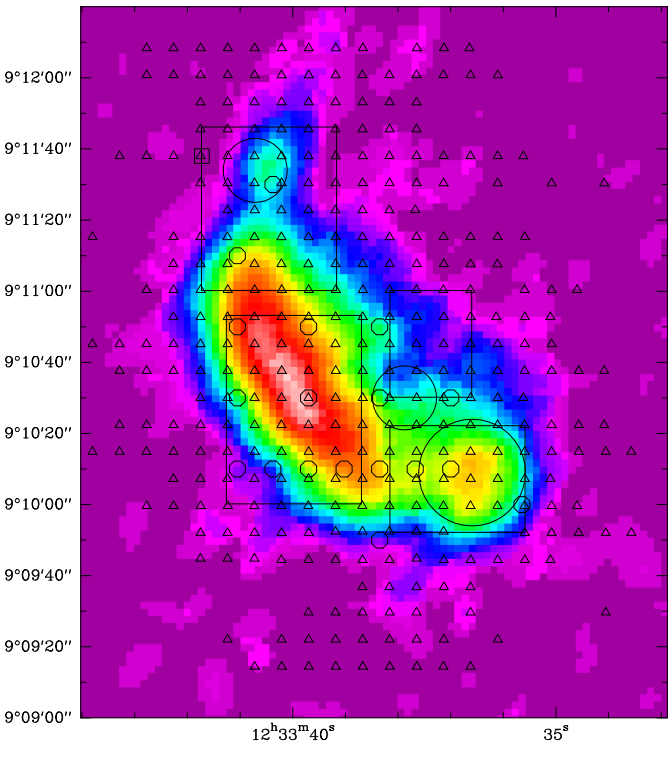

Fig. 2. ^{12}CO(2-1) HERA pointings (see Fig. 1) with low noise levels on the HI emission distribution (from Kenney et al. 2004). The large boxes correspond to Fig. 3 to Fig. 6.

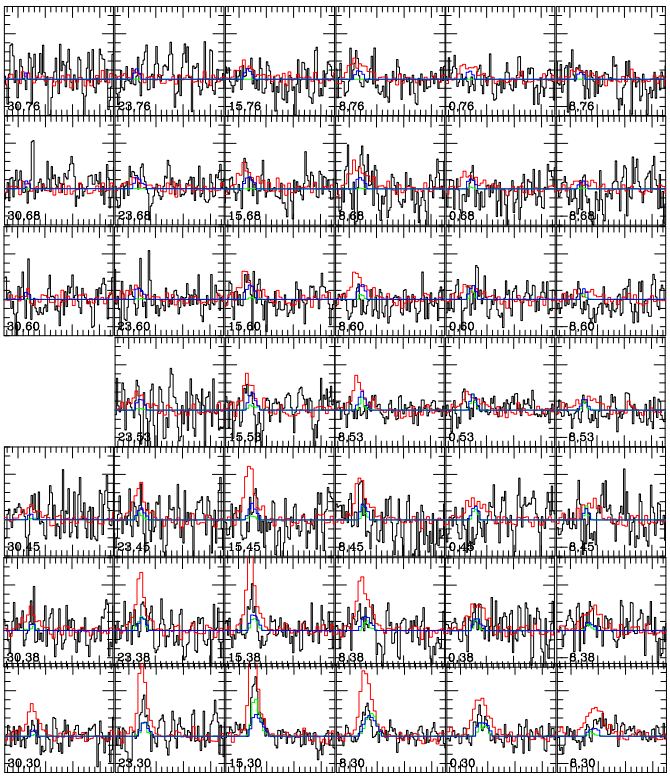

Fig. 3. IRAM 30m HERA ^{12}CO(2-1) spectra of the northeastern box of Fig. 1 (black lines). HI spectra from Kenney et al. (2004) (red lines). CO (green lines) and HI (blue lines) spectra from the dynamical model of Vollmer et al. (2006). The velocity scale is from 2150 to 2550 km s^{-1} and the main-beam temperature scale from -40 mK to 80 mK (T_{mb} scale).

(resolution of 20″) and the model HI and CO emission convolved to the observational resolutions (see Sect. 5). We observe that the HI emission is more extended than the CO emission. Where detected, the velocity of the CO lines are close to the HI velocities. In general, CO linewidths are comparable to the HI linewidths in the galactic disk (Fig. 4), but smaller in the extraplanar regions (Fig. 3, 6). A double-line profile is observed in the CO and HI line west of the galaxy center at offsets $(-23, 0)$, $(-23, 8)$ (Fig. 5). This kind of line-profile has also been observed in NGC 4438 (Vollmer et al. 2005) another Virgo spiral galaxy which undergoes ram pressure stripping together with a tidal interaction. In the southwestern part of the extraplanar gas the HI profiles show a blueshifted wing (Fig. 6), corresponding to the most strongly pushed gas. Whereas the CO peak in this region is aligned with the HI peak, the blueshifted wing is absent in CO. This might be partly due to the smaller S/N ratio of the CO data compared to the HI data. Even if there is H_2 associated with the blueshifted wing, we can conclude that the molecular fraction in this extraplanar gas is lower in the blueshifted wing than in the main line.

Fig. 7 shows ^{12}CO(2–1) HERA spectra of selected regions (large circles in Fig. 1, 2). To obtain a better S/N ratio, the HERA spectra within each region were averaged. These selected regions show the following characteristics:

– CO emission is present in the northwestern extraplanar gas at offset $(15″, 64″)$. The line is redshifted by $\sim$ 20 km s^{-1} with respect to the HI line (Fig. 7 left panel).
– The double profile observed in the HI line at offset $(-27″, 0)$ is also present in the CO line. The CO and HI peak amplitudes and their separation are the same (Fig. 7 middle panel).
– In the southwestern extraplanar gas at offset $(-46″, -21″)$ the blueshifted wing of the HI line profile has no counterpart in the CO data (Fig. 7 right panel). The CO linewidth is significantly smaller than the linewidth of the main HI line. This confirms the low molecular fraction of the blueshifted diffuse atomic gas. This blueshifted component corresponds to low surface density atomic gas discussed in Kenney et al. (2004; see their Fig. 10). The lower molecular fraction of this gas confirms the claim of Vollmer et al. (2006) that this gas has low densities making it more vulnerable to ram pressure stripping.

The ^{12}CO(1–0) spectra (resolution: 21″) are shown together with the convolved ^{12}CO(2–1) HERA spectra in Fig. 8. For all but offset $(20″, 0)$, the CO(1–0) line closely follows the CO(2–1) line with a line ratio of 0.7−0.9. Thus, the density and temperature of the molecular gas in the western extraplanar regions is probably not significantly different from those of the molecular gas in the galactic disk. At the eastern edge we observe a lower CO(2–1)/CO(1–0) ratio ($\sim$ 0.5). Given the sharpness of the gas

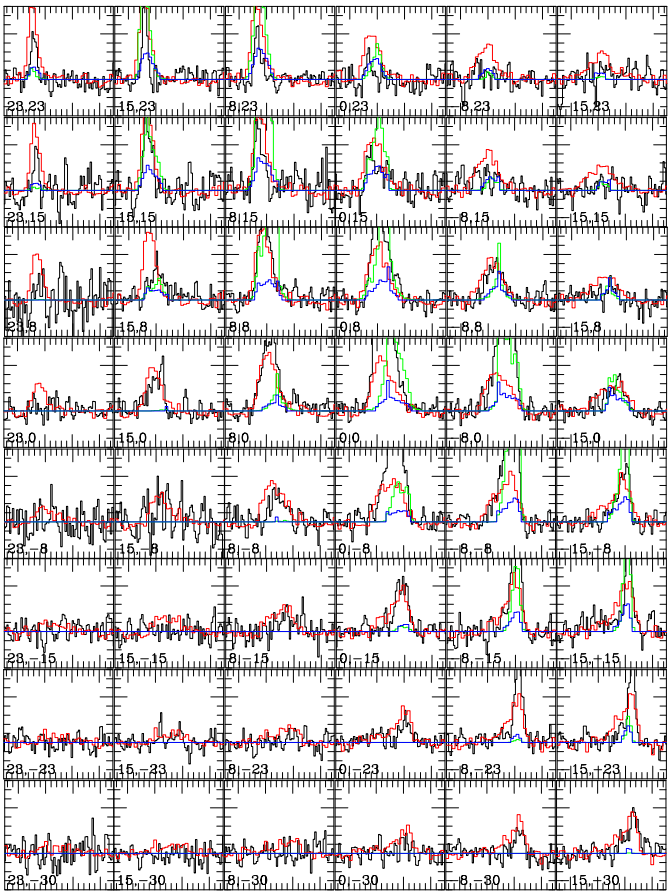

Fig. 4. IRAM 30m HERA ^{12}CO(2-1) spectra of the southeastern box of Fig. 1 (black lines). HI spectra from Kenney et al. (2004) (red lines). CO (green lines) and HI (blue lines) spectra from the dynamical model of Vollmer et al. (2006). The velocity scale is from 2150 to 2550 km s^{-1} and the main-beam temperature scale from -40 mK to 80 mK (T_{mb} scale).

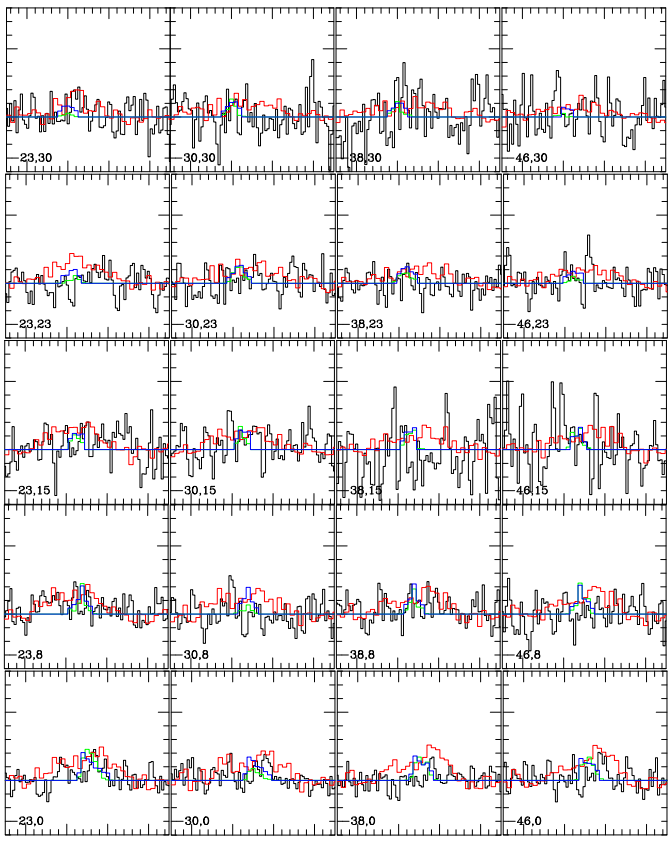

Fig. 5. IRAM 30m HERA ^{12}CO(2-1) spectra of the northwestern box of Fig. 1 (black lines). HI spectra from Kenney et al. (2004) (red lines). CO (green lines) and HI (blue lines) spectra from the dynamical model of Vollmer et al. (2006). The velocity scale is from 2150 to 2550 km s^{-1} and the main-beam temperature scale from -40 mK to 80 mK (T_{mb} scale).

distribution at the eastern edge and the pointing uncertainty of the telescope at 115 GHz, this small line ratio could be due to an offset of the CO(1–0) pointing to the west, i.e. closer to the major axis, with respect to the CO(2–1) pointing.

4. Wind-decoupled molecular gas

In another Virgo spiral galaxy, NGC 4438, Vollmer et al. (2005) found CO emission not associated with any HI emission. NGC 4438 underwent a tidal interaction $\sim$ 100 Myr ago (Combes et al. 1988) and now undergoes severe ram pressure stripping (Vollmer et al. 2005). A narrow CO line was detected in the northern tidal arm of NGC 4438, with apparently no associated HI. Since the velocity of the CO line corresponds to that of the stellar component (determined using a dynamical model of the tidal interaction), Vollmer et al. (2005) claimed that these molecular clouds were too dense to be affected by ram pressure, i.e. that they decoupled from the ram pressure wind.

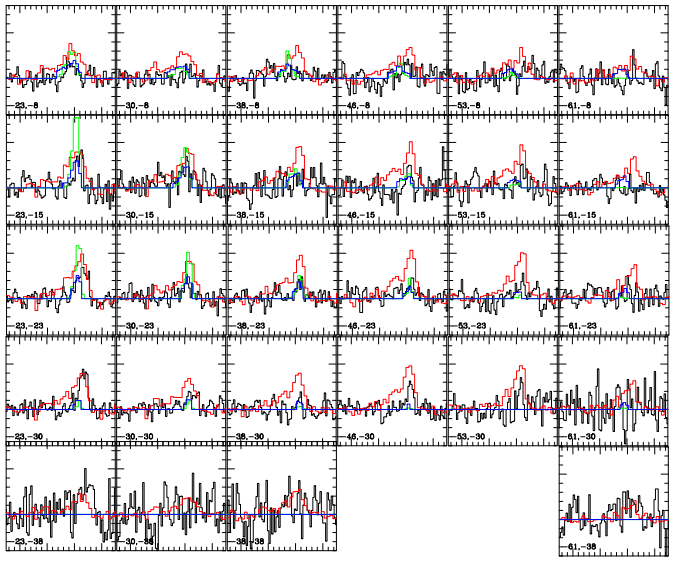

Fig. 6. IRAM 30m HERA ^{12}CO(2-1) spectra of the southwestern box of Fig. 1 (black lines). HI spectra from Kenney et al. (2004) (red lines). CO (green lines) and HI (blue lines) spectra from the dynamical model of Vollmer et al. (2006). The velocity scale is from 2150 to 2550 km s^{-1} and the main-beam temperature scale from -40 mK to 80 mK (T_{mb} scale).

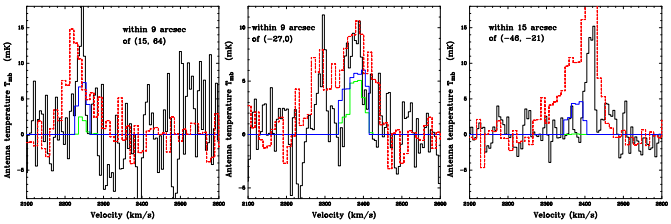

Fig. 7. Binned IRAM 30m HERA ^{12}CO(2-1) spectra (see large circles on Fig. 1). HI spectra from Kenney et al. (2004) (red lines). CO (green lines) and HI (blue lines) spectra from the dynamical model of Vollmer et al. (2006).

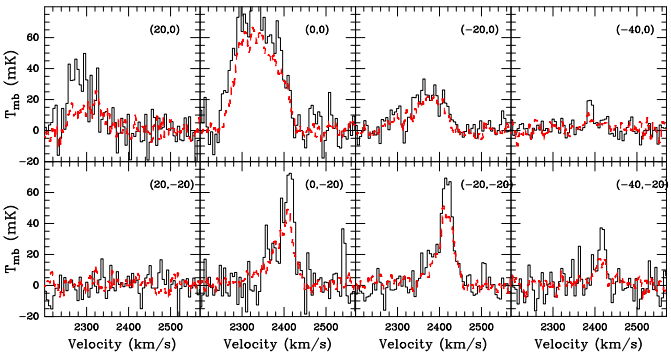

Fig. 8. Black: ^{12}CO(1–0) spectra (see small circles on Fig. 1). Red: convolved ^{12}CO(2–1) HERA spectra.

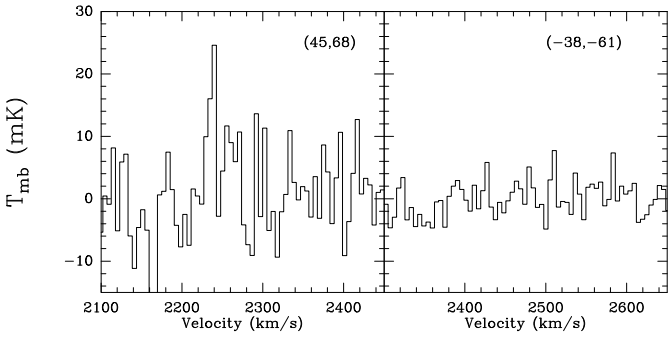

Fig. 9. Average ^{12}CO(2-1) spectra of the northeastern $(45, 68)$ and the southwestern $(-38, -61)$ ends of the galactic disk, where the atomic hydrogen has been removed by ram pressure. No HI emission is detected nor does the model predict any gas. The spectra are averaged over a region of $20''$.

Based on these findings we searched for CO lines in regions devoid of any HI emission (i) in the ram pressure stripped outer galactic disk (Fig. 9) and (ii) between the northern galactic disk and the extraplanar HI emission (Fig. 10). We only detect one CO line in the northern part of the galactic disk. The most prominent CO line is detected at the position $(30, 68)$; see the little box in Figs. 1 and 2), i.e. between the stellar disk and the stripped extraplanar atomic gas. The radial velocity of the CO lines is ~ 2250 km s^{-1}, close to the velocity of the stellar component. The HI line of the stripped extraplanar HI (Fig. 3) is blueshifted by ~ 30 km s^{-1}. We observe a clear absence of a CO line in the gas-free southwestern part of the disk

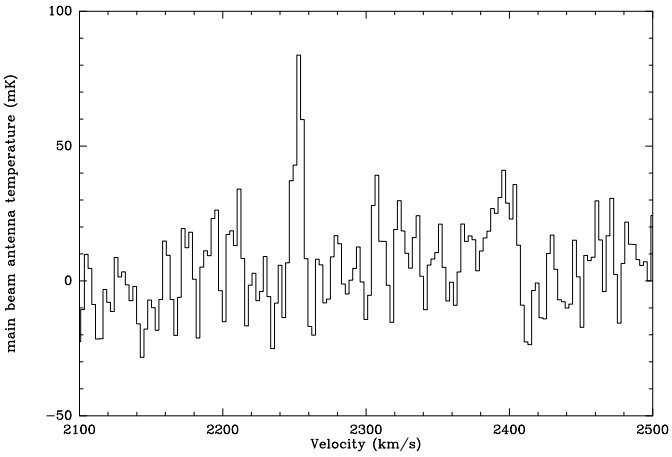

Fig. 10. Single ^{12}CO(2-1) HERA spectrum in the northeast that is located outside the HI distribution. The position is marked with an additional box in Fig. 2.

(Fig. 9 right panel), for which an explanation is proposed in Sect. 6.1.

5. Comparison with the dynamical model

In this section we will compare the molecular gas and Hα distribution to the dynamical model of Vollmer et al. (2006).

5.1. Molecular gas

In order to estimate the H_2 column density distribution, via a zero moment (integrated intensity) map of the CO(2–1) emission, we proceed as below. For the positions where the S/N of the HI is higher than 2.5σ, the linewidths of the HI spectra of these positions are determined and the CO spectra integrated over the HI velocity range. This leads to the CO emission distribution map of Fig. 11 (top panel).

To compare the HI and the CO emission distributions with the dynamical model of Vollmer et al. (2006), we assume that the molecular fraction of the gas depends on the local gas density. In a first simple approach we assume that the gas is bimodal, i.e. entirely molecular at densities > 0.03 M$_\odot$pc^{-3} $= 1$ cm^{-3} and entirely atomic at lower gas densities. The resulting model gas distribution maps were convolved to the observational resolutions (middle panel of Fig. 11). In a second approach we assume that the molecular fraction depends linearly on the square root of the gas density $f_{\rm mol} = \sqrt{\rho/(0.5\ {\rm M}_\odot{\rm pc}^{-3})}$. Moreover, the molecular fraction cannot exceed unity. In Sec. 6.2 we will give a motivation for this dependency. The resulting model CO emission distribution is shown in the lower panel of Fig. 11.

The comparison between the observed and the simulated CO emission distribution shows the following similarities:

– The galactic disk is the most prominent feature. There is more molecular gas of higher surface densities in the

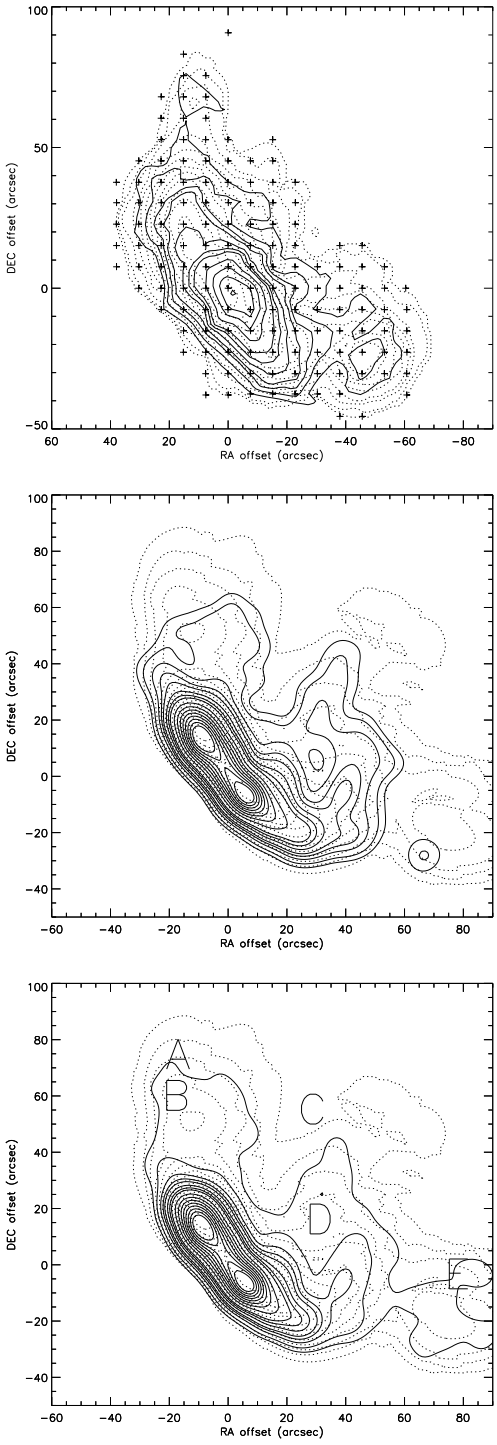

Fig. 11. Top panel: ^{12}CO(2-1) emission distribution (solid line) on the HI emission distribution (dotted line). The plus signs show the IRAM HERA pointings which were used to construct the CO moment 0 map. Middle panel: model CO distribution (solid line) on the model HI emission distribution (dotted line). The gas is assumed to be entirely molecular for gas densities $\rho > 0.03$ M$_\odot$pc^{-3}. Lower panel: model CO distribution (solid line) on the model HI emission distribution (dotted line). The molecular gas fraction is calculated using $f_{\rm mol} = \sqrt{\rho/(0.5\ {\rm M}_\odot{\rm pc}^{-3})}$. The letters refer to the regions shown in the deprojection in Fig. 14.

outer part of the gas disk in the southwest than in the northeast.
– There is CO emission in the extraplanar regions.
– The model using a molecular fraction proportional to the square root of the gas density better reproduces the CO morphology of the extraplanar regions: the northern and southwestern CO emission regions are centered on the peaks of the HI emission and there is a spatially separated CO arm between the southwestern and the disk CO emission.

On the other hand, we observe the following disagreement between the model and our observations:

– The model CO emission distribution shows a central hole. This is due to the initial conditions which had an initial gas hole for computational reasons.
– The northern part of the observed CO disk shows emission of lower surface brightness. The HI emission (Kenney et al. 2004) shows the opposite trend: high column density gas is found to the north.
– The model CO emission to the west of the galaxy center is more extended than it is observed. This is also the case for the HI emission (see Sect. 6).

We thus conclude that the model reproduces qualitatively our CO observations. The model using a density-dependent molecular fraction reproduces the observations better than a bimodal molecular fraction.

The direct comparison between the HI and CO model and observed spectra (Fig. 3 to Fig. 7) shows good agreement for high intensities, i.e. high gas densities. However, the observed CO and HI double lines and blueshifted wings of the HI lines in the western extraplanar regions are not reproduced by the model. This is due to the constant column density of the model gas in the regions affected by ram pressure (see Sect. 6).

5.2. Star formation

In typical spiral galaxies the star formation rate follows more closely the molecular gas distribution than the atomic gas distribution (Wong & Blitz 2002). The HI surface density saturates at a value of ~ 10 M$_\odot$pc^{-2} or even declines for high star formation rates per unit surface. In an unperturbed galactic disk the ISM is confined in the gravitational potential of the disk. The ISM is turbulent and this turbulence is most probably maintained by the energy input from SN explosions (see, e.g. MacLow & Klessen 2004 or Vollmer & Beckert 2003). Without a constant energy supply, turbulence is damped within a few Myr (Stone et al. 1998, MacLow 1999). Since the extraplanar gas of NGC 4522 is no longer confined to the potential of the galactic disk, it represents an ideal laboratory to test if the gravitational potential plays a role for the correlation between star formation rate and the available molecular/atomic gas mass.

To do so, we first present the Hα emission distribution overlaid onto the CO emission distribution (Fig. 12).

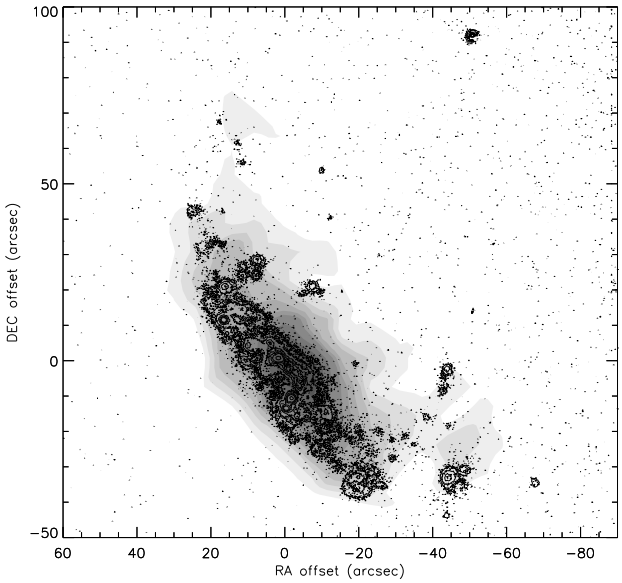

Fig. 12. Hα emission distribution (Kenney et al. 2004; contours) on the ^{12}CO(2-1) emission distribution (greyscale).

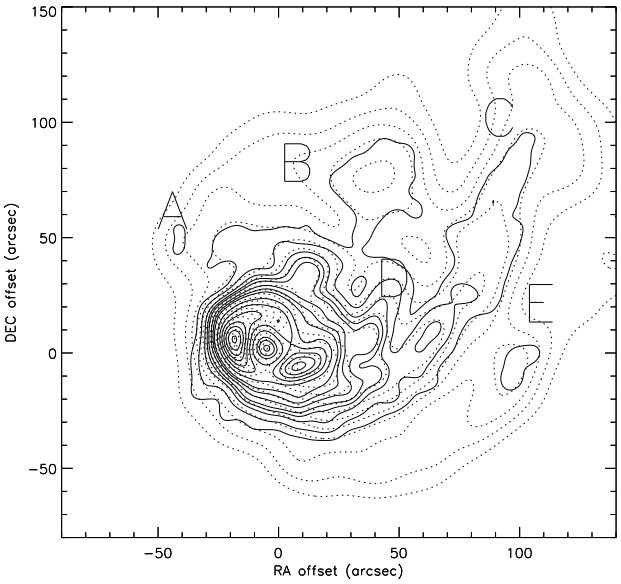

Fig. 14. Deprojected model CO distribution (solid line) on the deprojected HI distribution (dotted line). The letters correspond to the characteristic regions of Fig. 11. The galaxy is moving towards the lower left corner and rotates clockwise.

There is no major site of massive star formation without associated CO emission. At the edges and outside the galactic disk star formation does not coincide with the maxima of CO emission. A high column density of molecular gas is thus not sufficient to form massive stars. In other words, on kpc scales the star formation rate does not directly depend on the molecular gas surface density. A number of HII regions are detected at the outer edges of the CO emission distribution, at offsets $(20'', 45'')$, $(-10'', 20'')$, $(-45'', 0)$, $(-45'', -30'')$.

In the model we assume that the star formation rate is proportional to the number of collisions between the gas clouds. Numerically, the star formation rate thus depends on the local number density of the clouds, their cross section, and their local 3D velocity dispersion. Since the model clouds have a constant surface density (Vollmer et al. 2006), their cross sections vary with the cloud mass in the following way: $\pi r_{\rm cl}^2 = M_{\rm cl}/\Sigma$, where $r_{\rm cl}$ is the radius, $M_{\rm cl}$ the cloud mass and Σ the gas surface density. The cloud mass distribution is a power law with an index of -1.5. For an isolated unperturbed spiral galaxy this prescription leads to a Schmidt law of the form $\dot{\Sigma}_* \propto \Sigma^{1.7}$, where $\dot{\Sigma}_*$ is the star formation rate per area. For the construction of a star formation distribution map we store all cloud–cloud collisions during 20 Myr before the present state of the galaxy. This is twice the timescale for Hα emission, chosen to give more collisions and thus better statistics. The distribution was then convolved to 0.6 times the resolution of the CO(2–1) map. This model star formation distribution is presented in Fig. 13 together with the Hα emission distribution. We note the following points for comparison between the model and observations:

– As in the observations, our model has two prominent HII regions at the outer edges of the galactic disk, the most prominent being the southwestern HII region. These regions are separated by a local minimum from the rest of the galactic disk.
– We observe extraplanar model star formation regions close to the disk at the edges and in the middle of the galactic disk (see Sect. 6).
– There is isolated star formation over the whole extraplanar HI emission. In the model the small patches are due to multiple collisions of a single massive cloud.

We thus conclude that the model star formation distribution qualitatively reproduces the observed Hα emission distribution.

6. Discussion

6.1. Deprojecting the model

The model gives us the unique opportunity to deproject the gas distribution. One has to keep in mind that the extraplanar gas is no longer located within the galactic disk, but is a fully 3D feature. In Fig. 14, we present a deprojected face-on view of the model gas distribution of Fig. 11 (lower panel). The corresponding regions are labeled with capital letters. Region A is the tip of a spiral arm close to the main gas disk. Region B is a large overdensity within the stripped gas. Region C represents the tip of the most prominent gas (spiral) arm which is mainly made of stripped material. Region D is a secondary gas arm and region E is an overdensity in the windward, low-density side of the prominent gas (spiral) arm. As stated above, the gas outside the main gas disk ($R < 30''$) has a fully 3D structure. As can be seen in the lower panel of Fig. 11, the upper edge of the deprojected gas distribution

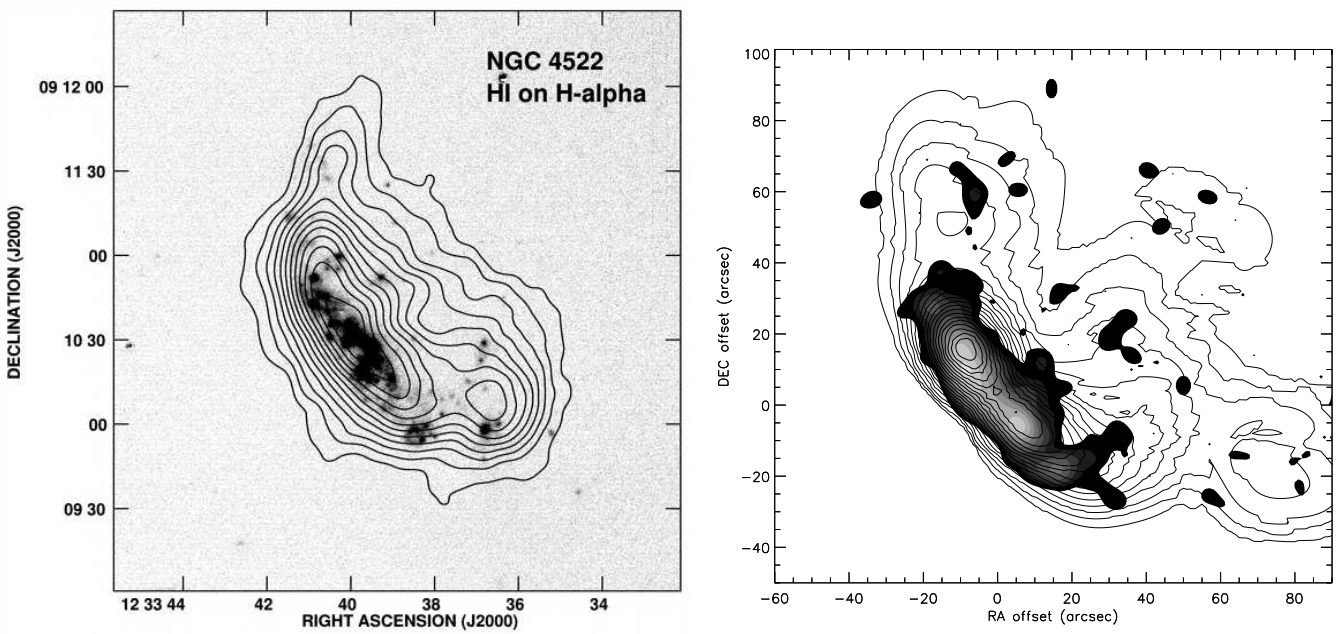

Fig. 13. Left panel: HI emission distribution on Hα emission distribution (Kenney et al. 2004). Right panel: model HI distribution (Vollmer et al. 2006; contours) on the model massive star formation distribution (greyscale). Darker regions correspond to less massive star formation.

becomes the northeastern edge of the model distribution in the observed projection. The prominent gas (spiral) arm (D, C) runs in the observed projection vertically from the southwestern edge of the galactic gas disk to the end of the gas distribution at $(40, 40)$ (Fig. 14). The southwestern extraplanar HI emission region is made of relatively diffuse gas from the low-density side of the prominent gas (spiral) arm. This low-density side has one overdensity (E) where star formation can proceed. This is consistent with the observed HI and Hα emission distribution, but we do not claim that this is the necessary configuration. Most interestingly, we can identify the upbending arm (south of D, C on the lower panel of Fig. 11) with a chain of observed HII regions (between $(12h33m38s, 09d10m00s)$ and $(12h33m37s, 09d10m30s)$ on the left panel of Fig. 13 and the corresponding molecular arm on Fig. 12. We think that this is a robust feature. As already stated in Sect. 5.1 the outer part of the upbending arm (DEC offset $0''$ to $40''$ in the lower panel of Fig. 11) is not present in the observations. In deprojection this part of the arm is located between DEC offsets of $20''$ and $80''$ (Fig. 14). Due to its low total gas surface density Σ with respect to the inner part (DEC offset $-20''$ to $0''$) it is more vulnerable to ram pressure stripping or evaporation (the acceleration a due to ram pressure p is $a = p/\Sigma$). This is consistent with the blueshift and large linewidth of the extraplanar low column density HI which is stripped more efficiently than the high column density gas (Fig. 9 of Vollmer et al. 2006). Moreover, the CO and HI spectra of the southern extraplanar HI region (Fig. 6) show that CO is only associated with high column density HI at the highest velocities. Our numerical model cannot reproduce the more efficient stripping of low column density gas, because it uses a constant column density for the atomic gas phase (see Vollmer et al. 2001 and Fig. 9 of Vollmer et al. 2006). We therefore suggest that the outer part of the stripped gas arm has been stripped more efficienctly and now has a column density too low to be detected in the HI observations. On the other hand, very dense gas can decouple from the ram pressure wind (see Sect. 4) as it is found in CO observations of NGC 4438 (Fig. 4 of Vollmer et al. 2005).

We conclude that the formation of molecular clouds and star formation mainly depend on the large-scale overdensity of the gas more than on dynamical criteria or the overall pressure (see Sect. 6.3).

Wind-decoupled molecular gas is only found in the northern part of the galactic disk (Sec. 4). With the help of the deprojection (Fig. 14), this can be understood. High density gas is stripped from the left border of the gas disk. Since the ram pressure wind is rather face-on, the gas clouds are pushed to larger heights above the galactic plane. At the same time, rotation makes clouds move towards positions A and B, i.e. the northern part of the disk where the wind-decoupled molecular clouds are found. This finding suggests that dense giant molecular clouds can decouple from the ram pressure wind at early stages of the stripping of dense gas from the galactic disk, as seems to be the case for NGC 4438 as well.

6.2. Molecular fraction

As seen in Sec. 5.1 and Fig. 11, a molecular fraction which is proportional to the square root of the total gas density reproduces the observed CO emission distribution better than a simple bimodal molecular gas fraction assum-

ing a gas density cutoff. Vollmer & Beckert (2003) approximated the molecular fraction by the ratio between the turbulent crossing time scale $t_{\rm turb} = r_{\rm cl}/v_{\rm turb}$ and the timescale for molecule formation $t_{\rm mol} = \alpha/\rho_{\rm cl}$, where $v_{\rm turb}$ is the turbulent velocity dispersion within the cloud, $\rho_{\rm cl} = \rho/\Phi_{\rm V}$ the cloud density, ρ the total large-scale gas density, $\Phi_{\rm V}$ the volume filling factor, and α the constant of molecule formation $\alpha \sim 3 \times 10^7$ yr $\rm M_\odot pc^{-3}$:

$$f_{\rm mol} = \frac{t_{\rm turb}}{t_{\rm mol}} = \frac{r_{\rm cl}\,\rho}{v_{\rm turb}\alpha\,\Phi_{\rm V}} \ . \quad (1)$$

The volume filling factor $\Phi_{\rm V}$ is defined by the condition that the gas clouds are self-gravitating, i.e. the turbulent cloud crossing time $t_{\rm turb}$ equals the free fall time $t_{\rm ff}$ of the clouds:

$$\frac{r_{\rm cl}}{v_{\rm turb}} = \sqrt{\frac{3\,\pi\,\Phi_{\rm V}}{32\,G\,\rho}} \ , \quad (2)$$

where G is the gravitation constant. Inserting Eq. 2 into Eq. 1 leads to

$$f_{\rm mol} = \sqrt{\frac{3\,\pi}{32\,G}}\alpha^{-1}\Phi_{\rm V}^{-\frac{1}{2}}\rho^{\frac{1}{2}} \ . \quad (3)$$

Thus, the molecular fraction depends on the square root of the cloud density $\rho_{\rm cl} = \Phi_{\rm V}^{-1}\rho$. For the dependence used in Sec. 5.1 we assume a constant volume filling factor (see Vollmer & Beckert 2003). A density of 0.5 $\rm M_\odot pc^{-3}$ implies a volume filling factor of $\Phi_{\rm V} = 0.03$. This is higher than the volume filling factors given in Vollmer & Beckert (2003). Eq. 1 is a crude approximation which may overestimate the molecular fraction by a factor of 5-10, probably because f_{mol} is substantially overestimated by t_{turb}/t_{mol}. However, we think that its dependence on the physical parameters of the gas are valid. Eq. 3 will be used together with a similar expression for the star formation efficiency in the next section. The observed molecular gas fraction decreases from 50 % within the galactic disk to 35 % in the extraplanar region (Table 1).

6.3. The efficiency of extraplanar star formation

Does the star formation efficiency (SFE) change once the gas has left the confining gravitational potential of the galactic disk? The role of large-scale processes in provoking star formation is subject to debate, with many "recipes" providing reasonably similar fits to observations – e.g. the "Toomre" criterion (Kennicutt 1989), a pressure-based criterion (Blitz & Rosolowsky 2006), or a basic Schmidt (1959) law. The problem is not so much predicting the behavior in spiral disks but understanding what governs large-scale star formation in general in order to be able to understand other environments, typically those at intermediate and high redshifts. In classical dwarf galaxies, it is difficult to study the SFE because the low metallicity makes the measure of the H_2 mass uncertain. In Tidal Dwarf Galaxies, morphologically similar but with higher metallicities, Braine et al (2001) found that, curiously, the SFE was not identifiably different from spiral galaxies typically 100 times more massive. In the post-collision Taffy galaxies or UGC 813/816 system, on the other hand, the SFE in the bridge gas is much lower than within spiral disks (Braine et al. 2003, 2004).

Table 1. Derived masses, molecular fractions, and star formation rates/timescales.

	galactic disk	extrapl.	total	frac.extrapl.
$M_{\rm HI}$ (10^8 $\rm M_\odot$)	2.5	1.5	4	0.4
$M_{\rm H_2}$ (10^8 $\rm M_\odot$)	2.2	0.8	3	0.25
$M_{\rm H_2}/M_{\rm HI}$	0.88	0.53	0.75	
SFR ($\rm M_\odot yr^{-1}$)	0.1	0.015		~ 0.14
$t_{\rm H_2}^{\rm SFR}$(Gyr)	2.2	5.3		
$t_{\rm tot}^{\rm SFR}$(Gyr)	4.7	15.3		

The SFE can be defined with respect to the molecular gas mass available or with respect to the total gas mass available, either $\rm SFE^{-1} = t_{H_2}^{SFR} = M(H_2)/\dot{M}_{SFR}$ or $\rm SFE^{-1} = t_{tot}^{SFR} = M(H_2 + HI)/\dot{M}_{SFR}$. The observed gas masses, molecular fractions and star formation rates and timescales are presented in Table 1. Whereas close to half of the HI is found beyond the galactic disk, this ratio decreases to 1/4 for the molecular gas and to 1/7 for the Hα emission. The averaged star formation timescale based on the molecular or total gas mass increases from 2.2 or 4.7 Gyr within the galactic disk to 5.3 or 15.3 Gyr respectively within the extraplanar region. The star formation efficiency thus decreases by a factor of ~ 3 between the disk and the extraplanar region.

In the framework of the model of Vollmer & Beckert (2003) the local star formation rate is given by

$$\dot{\rho}_* = \Phi_{\rm V}\frac{\rho}{t_{\rm ff}^{\rm cl}} \ , \quad (4)$$

where $\Phi_{\rm V}$ is the probability of finding a self-gravitating cloud, i.e. the volume filling factor of self-gravitating clouds. Inserting the expression for the free fall time of Eq. 2 into Eq. 4 yields the following expression for the star formation timescale which corresponds to the inverse of the star formation efficiency:

$$t_* = \frac{\rho}{\dot{\rho}_*} = \sqrt{\frac{3\,\pi}{32\,G}}\Phi_{\rm V}^{-\frac{1}{2}}\rho^{-\frac{1}{2}} \ . \quad (5)$$

Thus, the star formation timescale depends on the inverse of the square root of the total large-scale density and the volume filling factor.

From Table 1 we obtain:

$$\frac{f_{\rm mol}^{\rm disk}}{f_{\rm mol}^{\rm ext}} = 1.3 \ , \ \text{and} \ \ \frac{t_*^{\rm ext}}{t_*^{\rm disk}} = 3.3 \ , \quad (6)$$

leading to

$$\frac{\Phi_{\rm V}^{\rm disk}}{\Phi_{\rm V}^{\rm ext}} = 2.5 \ , \ \text{and} \ \ \frac{\rho_{\rm disk}}{\rho_{\rm ext}} = 4.3 \ . \quad (7)$$

We therefore suggest that the observed decrease of the star formation efficiency by a factor of 3 in the extraplanar region, together with a lower molecular fraction,

is due to a higher volume filling factor of self-gravitating clouds in the galactic disk of NGC 4522. These clouds are about twice as dense as their counterparts in the extraplanar regions. The overall density in the extraplanar region is about 4 times lower than that of the galactic disk, presumably because the extraplanar gas is no longer confined by the gravitational potential of the disk. This is supported by the lower CO(2–1)/(1–0) line ratio in the extraplanar gas (Fig. 8). However, the gas is still confined by the hot intracluster medium and partially compressed by ram pressure. The mixture of ram-pressure and rotation create zones where the atomic gas is dense enough to be gravitationally bound, become molecular, and form stars.

We conclude that the stripped ISM still forms molecules and stars in a way not distinguishable from disk star formation (Eqs. 1 and 4) as long as the overall gas density is high enough to form bound clouds. The ultimate fate of the stripped gas is probably ionization and evaporation, without star formation for the low-density gas, and after a generation of stars, which then disperse the remaining dense gas, for the initially denser gas.

As the simulations show (Fig. 14) part of the gas is stripped in relatively dense arms whose mean density is about 4 times lower than that of the galactic gas disk. Since these gas arm are only confined by the hot intracluster medium, they might ultimately disperse giving rise to a large low surface density tail as observed in NGC 4388 (Oosterloo & van Gorkom 2005).

6.4. Comparison with radio continuum observations

Recently, Murphy et al. (2008a, 2008b) compared Spitzer 24 μm emission with 20 cm radio continuum maps. The radio-FIR correlation is used to predict the radio emission from the Spitzer 24 μm emission. They found a radio deficient region at the eastern outer edge of NGC 4522's disk where ram pressure is pushing the interstellar medium. Since the 24 μm dust emission is associated with molecular gas, we compare in Fig. 15 the 6 cm radio continuum emission from Vollmer et al. (2004) with the CO emission distribution. The extraplanar 6 cm radio continuum emission extends farther to the west than the CO emission. The radio emission of the northeastern disk extends in the region where we found CO emission without associated HI emission (Fig. 9). The northern extraplanar CO and HI emission does not show associated radio continuum emission. We convolved the 6 cm radio continuum and CO maps to a resolution $20'' \times 20''$ and computed a ratio map which is shown in the right panel of Fig. 9. As expected, the 6 cm/CO ratio is highest in the extraplanar region. The smallest 6 cm/CO ratios are found at the extremities of the disk. We observe a maximum of the 6 cm/CO at the eastern edge of the galactic disk where Murphy et al. (2008a/b) detect a radio deficient region. Since we do not expect the 24 μm emission to be proportional to the CO emission, the interpretation of the result is difficult. In addition, we think that our data are not sensitive enough to draw a firm conclusion on the 6 cm/CO ratio map.

7. Conclusions

We present IRAM 30m ^{12}CO(2–1) HERA and ^{12}CO(1–0) observations of the ram pressure stripped Virgo spiral galaxy NGC 4522. We directly compare the CO spectra to the HI data cube of Kenney et al. (2004). In a second step a CO emission distribution map is produced in the regions where HI is detected. The CO emission distribution is compared to Hα observations of Kenney et al. (2004) and to the model distribution of molecular gas derived from dynamical simulations of Vollmer et al. (2006). A map of the distribution of star formation based on the numerical cloud–cloud collisions is produced which is then compared to the Hα emission distribution. The 3D model snapshot allows us to deproject the observed features and understand their origin. From this work we conclude that

1. CO emission is associated with the extraplanar atomic gas. The morphology of the molecular gas closely follows but is less extended than the HI morphology.
2. In the northern part of the galactic disk we find CO emission without an HI counterpart. We interpret this detection as wind-decoupled molecular clouds as observed in NGC 4438 (Vollmer et al. 2005).
3. In the extraplanar region CO emission is always associated with sites of massive star formation as probed by Hα emission. At the resolution of our observations, there is no correlation between the CO and Hα peaks.
4. A model using a molecular fraction proportional to the square root of the gas density qualitatively reproduces our CO observations.
5. The model star formation distribution, which is numerically based on cloud–cloud collisions, qualitatively reproduces the observed Hα emission distribution.
6. The deprojection of the model extraplanar gas shows that a significant part of the gas is stripped in the form of relatively dense arms.
7. The formation of molecular clouds, and subsequent star formation, occurs at peaks in the large-scale volume density of the gas, with no clear difference with respect to the disk despite the very different conditions (i.e. stellar density dominates in the disk but is negligible in the extraplanar material).
8. In the disk gas, the molecular and atomic fractions are about equal whereas in the extraplanar gas, there is twice as much HI as H_2, assuming a standard $N(H_2)/I_{CO}$ conversion ratio.
9. The star formation efficiency of the extraplanar gas is about 3 times lower than that of the galactic disk.
10. Using the analytical framework of Vollmer & Beckert (2003) we find that the overall total gas density and volume filling factor of self-gravitating clouds are factors of 4 and 2.5 lower respectively compared to the galactic disk.

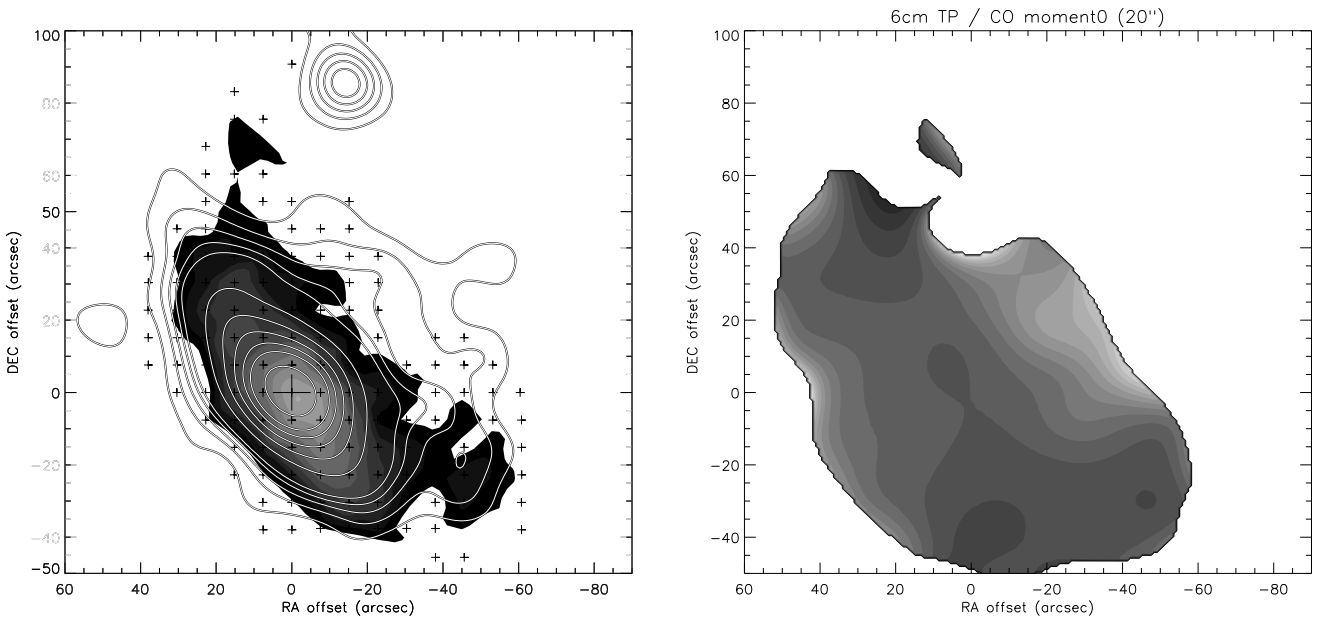

Fig. 15. Left panel: Contours of the 6 cm radio continuum emission from Vollmer et al. (2004) on the CO emission distribution (greyscale). The contour levels are $(2, 4, 6, 8, 10, 20, 30, 40, 50, 60, 80, 100) \times 20$ μJy/beam. The resolution is $15'' \times 15''$. Right panel: Ratio between the 6 cm and CO emission. Brighter regions have higher CO/6 cm ratios.

In the early phases of ram pressure stripping ($\sim$ 50 Myr after peak ram pressure; Vollmer et al. 2006) a significant part of the stripped gas is in the form of relatively dense arms. At the same time some very dense molecular clouds, representing a tiny fraction of the stripped gas, can decouple from the ram pressure wind. Molecules and stars form within the stripped dense gas according to the same laws as in the galactic disk, i.e. they mainly depend on the overall total gas density. Star formation proceeds where the local large-scale gas density is highest. Given the complex 3D morphology this does not necessarily correspond to the peaks of the surface density. In the absence of a confining gravitational potential these stripped gas arms will most probably disperse, i.e. their density will decrease and star formation will cease.

Acknowledgements. Based on IRAM observations. IRAM is supported by INSU/CNRS (France), MPG (Germany), and IGN (Spain). We made use of a DSS image. The Digitized Sky Survey was produced at the Space Telescope Science Institute under U.S. Government grant NAG W-2166. The images of these surveys are based on photographic data obtained using the Oschin Schmidt Telescope on Palomar Mountain and the UK Schmidt Telescope. The plates were processed into the present compressed digital form with the permission of these institutions.

References

Blitz, L. & Rosolowsky, E., 2006, ApJ 650, 933
Braine, J., Duc, P.-A., Lisenfeld, U., Charmandaris, V., Vallejo, O., Leon, S. & Brinks, E., 2001, A&A 378, 51
Braine, J., Davoust, E., Zhu, M., Lisenfeld, U, Motch, C. & Seaquist, E., 2003, A&A 408, L13
Braine, J, Lisenfeld, U, Duc, P.-A, Brinks, E, Charmandaris, V. & Leon, S., 2004, A&A 418, 419
Combes, F., Dupraz, C., Casoli, F., Pagani, L. 1988, A&A, 203, L9
Crowl, H.H. & Kenney, J.D.P. 2006, ApJ, 649, L75
Helou, G., Hoffman, G., & Salpeter, E.E. 1984, ApJS, 55, 433
Kenney J.P.D. & Koopmann R.A. 1999, AJ, 117, 181
Kenney J.P.D., van Gorkom J., & Vollmer B. 2004, AJ, 127, 3361
Kennicutt, R. C., Jr., 1989, ApJ, 685, 344
MacLow, M.-M. 1999, ApJ, 524, 169
MacLow, M.-M. & Klessen, R.S. 2004, RvMP, 76, 125
Murphy, E., Kenney, J., Helou, G., Chung, A., & Howell, J. 2008a ApJ submitted
Murphy E.J., Kenney J.D.P., Helou G., et al. 2008b, eprint arXiv:0802.2281
Oosterloo, T. & van Gorkom, J.H. 2005, A&A, 437, L19
Schmidt, M. 1959, ApJ 129, 243
Stone, J.M., Ostriker, E.C., & Gammie, C.F. 1998, ApJ, 508, L99
Vollmer B. & Beckert T. 2003, A&A, 404, 21
Vollmer B., Beck R., Kenney J.P.D., & van Gorkom J.H. 2004, AJ, 127, 3375
Vollmer B., Braine, J., Combes, F., Sofue, Y. 2005, A&A, 441, 473
Vollmer B., Soida, M., Otmianowska-Mazur, K. et al. 2006, A&A, 453, 883
Wong, T. & Blitz, J. 2002, ApJ, 569, 157

Chapter 6

Conclusions

In this thesis we investigated the influence of ram pressure stripping on the star formation history of clusters spiral galaxies.

Different observations of nearby cluster (Giovanelli & Haynes 1983, Binggeli et al. 1985 and Schindler et al. 1999) showed that a large fraction of cluster galaxies are HI deficient. The most probable origin for this lack of gas in cluster galaxies is an hydrodynamical processes that involves the gas of the galaxy and the medium in which the galaxy moves, i.e. the intracluster medium. A galaxy that is moving inside the potential well of a cluster undergoes a pressure exerted by the intracluster medium. If this pressure is larger than the restoring force due to the galactic potential, the galaxy loses gas from the outer disk.

The stripping of the gas produce in spiral galaxies spectacular plumes of extraplanar gas extending at distance in the order of 50-100 kpc from the disk (e.g. Oosterloo & van Gorkom (2005)).

The ram pressure stripping has not been completely understood yet, since observations found HI deficient galaxies at a distance where the ram pressure should not be efficient (Solanes et al., 2001). Applying the Gunn & Gott (1972) criterion we know that ram pressure stripping becomes efficient when the galaxy passes near the cluster center, at less that one virial radius, and for a short timescale, i.e. a few 10 Myrs.

Despite this short timescale, ram pressure stripping is able to remove up to 90% of ISM from the disk of a spiral galaxy (Gavazzi 1989, Gavazzi 1987). Once the gas has left the disk, mostly from the outer region, star formation stops. Appropriate optical spectra and photometry should recover a signature of this dramatic event, determining in this way a stripping age, i.e. the time elapsed since the star formation truncation. This age can be considered as a clock that gives the time at which the galaxy passed the cluster center.

As a first example we take NGC 4388, an edge-on Seyfert 2 galaxy at projected

distance of 1.3° from the Virgo cluster center. From Hα (Yoshida et al., 2002) line and 21-cm line observations (Oosterloo & van Gorkom 2005, Vollmer & Huchtmeier 2003) and Hα (Yoshida et al., 2002) there are clear evidences of relatively recent ram pressure stripping.

The main goal of the thesis was to investigate, through the optical spectroscopy and the photometry, the star formation history of NGC 4388. To obtain this information we performed spectroscopic observations at the European Southern Observatory (ESO) Very Large Telescope. Using the FOcal Reducer and low dispersion Spectrograph 2 (FORS2), we pointed the slit at two different regions: an inner region at 1.5 kpc from the center of the disk, and an outer region at 4.5 kpc, in a gas-free region of the disk. From archive images we extract also for the same positions the photometry of 12 bands, from the UV to the Infra Red.

The determination of the star formation history from the data set is an inverse problem that we address using a non parametric method. The estimation of the best fit model through the minimization of the usual χ^2 function is complex. Ocvirk et al. (2006a) showed that the inverse problem associated to the spectral analysis is ill-posed, i.e. small variations in the initial condition can give huge variations in the solutions. For this reason we regularize the problem using a proper penalty function. The unknowns of our problem are the star formation history, the metallicity evolution and the spectral broadening function. In addition we use a non parametric extinction correction for the spectra and an extinction law from the literature for the photometry. In this thesis we extended the method of Ocvirk et al. (2006a) to deal with photometry.

The total best fit model is estimated by minimizing a $Q_\mu(x)$ function depending on all the unknowns of the problem. The Q-function includes the usual χ^2 best-fit estimator and a penalty function. It smoothes the solutions by assuming large values when the star formation and the metallicity evolution are very irregular functions of time or the spectral broadening function is too chaotic. An adjustable parameter controls the weight of the different penalizations in the final estimation. We calibrated the weight coefficient associated to the non parametric estimation of the continuum and the spectral broadening function. The critical coefficients that affect the final solution are the penalty functions of the star formation and the metallicity, μ_x and μ_Z.

We performed a campaign of inversions, to investigate the effects of the different parameters on the final results. This campaign involved spectral, photometric, and a combined analysis. The spectral inversion has been calibrated

to match our VLT observations at intermediate resolution $R \sim 800$. In Ocvirk et al. (2006a) the method has been tested on high resolution spectra ($R \sim 10000$).

We built mock spectra and photometry from two semi-analytical models of Boissier & Prantzos (2000). We performed a campaign of inversions in the $\mu_x - \mu_Z$ plane, in ranges between $10^{-1} - 10^4$.

As for the spectroscopy, the inversion problem associated with the photometric analysis is ill-posed and needs regularization. We defined a new function that includes both spectral and photometric functions. We introduced a parameter that determines the relative weight of the photometric and spectroscopic constraints. We investigated the possibility to use a unique penalization for the analysis of combined spectroscopic and photometric data by performing a mock campaign.

We performed Monte Carlo simulations adding a gaussian noise to the mock spectrum and to the mock photometry. The results are stable, once that minimization has converged. The uncertainties for the young stellar ages ($\leq$ 10 Myr) can be large due to the uncertainties of stellar models (see Fig. 3.3).

From this campaign we conclude that:

- it is possible to use the same penalization weight for the inversion of the spectroscopic, photometric and combined data. For the same μ_x and μ_Z the spectral and photometric inversions give different answers. The photometry is systematically less constrained. This is particularly evident when we investigated the weight coefficient μ_Z, that penalizes the metallicity evolution. For $\mu_Z = 10^2$ the spectral analysis is able to reproduce the basic trend of the metallicity evolution. The photometry is less constrained and obliges us to impose a constant metallicity ($\mu_Z = 10^4$);

- analyzing the shape of the recovered solution, we can identify for each weight coefficient three different regimes. For low values of the weight coefficient, the penalization under-smoothes the solution, allowing large irregularities in the profile easily and artifacts. For high values of the penalty, the solution is over-smoothed, imposing a constant solution independently of the other parameters of the problem. Between this two regimes, there is a narrow 'transition region', in which there is a mixing between artificial and realistic features. This problem was more evident when we investigated an input model with a truncation in the star formation (see Fig. 3.27 as example);

- the star formation history recovered with $10^{-1} \leq \mu_x \leq 10^4$ for the spectral inversion is always in agreement with the model. The limit case $\mu_x = 10^{-1}$

shows irregularities and error bars larger than the other cases, fixing in this way the lower limit of our investigation;

- for spectral analysis the smooth metallicity evolution for lookback times $t < 1$ Gyr is reproduced only for $\mu_Z \geq 10^{-1}$. For $\mu_Z \geq 10^3$ the metallicity is flat independently of the values of μ_x. The basic trend of the metallicity is reproduced for an appropriate set $[\mu_x, \mu_Z] = [10^2, 10^2]$. For $\mu_Z \geq 10^4$ the metallicity is flat and can be considered as a time-bin averaged metallicity. This time-bin averaging produces a underestimation of the average metallicity at lookback times $t < 1$ Gyr. Comparing the results for different semi-analytical models we determine the underestimation to be $0.005 \leq \Delta Z \leq 0.008$;

- when using different exponentially decreasing star formation histories as initial guesses the non parametric method is able to recover flat and peaked star formation histories. The initial guess for the star formation history is less critical than that for the metallicity evolution. The initial guess for the metallicity evolution should be higher than the expected time-bin averaged metallicity;

- the star formation history is less constrained by the photometry. Therefore the photometric analysis needs a higher penalization than the spectral analysis;

- the metallicity evolution is not constrained by the evolution. Therefore we have to assume a constant metallicity ($\mu_Z = 10^4$).

- when combining the spectral and the photometric analysis the results are a balance between the separate analysis. The star formation history is smooth for $\mu_x = 10^1$, as in the spectral analysis. The metallicity is instead less constrained and requires high penalizations. For $\mu_Z = 10^4$ and $\mu_x = 10^1$ we find acceptable solutions;

- to model a spiral galaxy that undergoes ram pressure stripping we truncated the star formation of the semi-analytical models at a lookback time of $t = 130$ Myr. The results show that for high penalization ($\mu_x = 10^2$) of the star formation history the stripping age is underestimated by up to 80 Myr. In particular:

    - for the spectral analysis the star formation history is smooth before the truncation for all the penalization μ_x, μ_Z. For $\mu_x \leq 10^1$ the recovered star formation history presents some residuals at lookback times $t \leq 100$ Myr.

Only for one case $[\mu_x, \mu_Z] = [10^{-1}, 10^4]$, the stripping age is exactly reproduced. For all the other cases we can have an underestimation of one time bin, i.e. 50 Myr for $\mu_x = 10^1$, or two time bins, i.e. 80 Myr for $\mu_x = 10^2$. As for the continuous star formation history, the spectral analysis reproduces the basic trend of the metallicity for $\mu_Z = 10^2$;

- the photometric analysis showed that for $\mu_x = 10^{-1}$ the recovered star formation is irregular at lookback times $t < 300$ Myr. For $\mu_x \geq 10^1$ the solutions are smooth. As for the photometric analysis of an isolated disk, the metallicity is less constrained and requires high penalization $\mu_Z = 10^4$;
- the combined analysis showed that for $\mu_x \leq 10^{-1}$ the recovered star formation histories before the truncation are irregular, and for $\mu_x \geq 10^1$ they are smooth. The metallicity requires $\mu_Z = 10^2$ to reproduce its basic trend, as in the spectral analysis. The stripping age is underestimated by at least 50 Myr in all the cases;

A second part of the thesis applied the tested method to our observations of NGC 4388. We performed a campaign of inversions to explore the effects of different penalization weights on the solutions. The main results are:

- both for the inner and the outer region spectra we find gaussian-like spectral broadening functions. The peak and FWHM of the velocity distribution are consistent with the Hα velocity field (Veilleux et al. 1999);
- for the inner spectrum the recovered star formation history is flat;
- the FORS resolution is too low to derive a meaningful metallicity evolution. We keep the metallicity solution constant and consider it as a time-bin averaged value, rather than a realistic evolutionary track;
- we performed a non parametric inversion of the outer region of NGC 4388 using the spectral libraries of Bruzual & Charlot (2003) and Vazdekis et al. (2007), that uses the stellar library MILES (Sánchez-Blázquez et al. (2006), Cenarro et al. (2007)). We recovered a drop in the star fromation history for both spectral basis at lookback time $t \sim 300$ Myr. In this way we showed that the results of the method are independent of the chosen spectral basis;
- we performed three inversions using a flat star formation, an exponentially decreasing star formation rate with $\tau = 5$ Gyr and an increasing star foromation rate with $\tau = 5$ Gyr as intial guesses. We verify that for reasonable

initial guesses, i.e. a flat star formation history and exponentially decreasing laws, the recovered star formation shows a drop at a lookback time of $t \simeq$ 300 Myr;

- for the photometric analysis we use in the minimization procedure extinction laws of Calzetti (2001) and Cardelli et al. (1989). The different shapes of the two laws only affect the curvature of the star formation truncation (Fig. 4.18);
- we performed a campaign of inversions exploring the penalties μ_x, μ_Z. The main results of this campaign showed that for $\mu_x \geq 10^4$ the star formation solution is flat. For $\mu_x \leq 10^4$ the recovered star formation history shows a drop that can occur at lookback time $t = 250$ Myr. The metallicity is irregular and needs $\mu_Z \geq 10^2$.

As a conclusion, the non parametric method:

- indicates a constant star formation history in the inner region and a recent drop of the star formation history in the outer region;
- recovers a solar metallicity with a small radial gradient;
- provides constraints on the long term underlying stellar population;
- cannot provide precise stripping ages, because of the limited amount of information the data, obliging us to penalize.

For the last reason we introduce a parametric method that refines the precision of the determination of the stripping age under the assumption that the ram pressure stripping timescale is small ($t < 50$ Myr). Based on the non parametric results we assume a flat star formation history before the stripping event, a constant metallicity evolution and a known spectral broadening function. We approximate the effect of gas stripping by cutting the star formation at different lookback times $0 \leq t \leq 1$ Gyr. We verified the stability of the results with 500 Monte Carlo simulations. The obtained set of spectra is compared to the observed spectrum of the outer disk. From this comparison we conclude:

- the stripping age does not significantly depend on the choice of the metallicity evolution as long as the time-bin averaged metallicity is preserved;
- the chosen extinction law for the photometric analysis does not influence the recovered stripping age. We use two different exinction laws (Calzetti 2001, Cardelli et al. 1989) and we apply them to the set of spectra created from a flat

star formation history with solar metallicity. The method recovers the same stripping age for both extinction laws.

We investigate how the stripping age changes with respect to the star formation history and the chosen metallicity. We created mock spectra using different star formation histories, before the cut, and different metallicities. The main results from this campaign are:

- at fixed star formation history a decreasing metallicity leads to an increasing stripping age,
- at fixed metallicity a flatter star formation history leads to an increasing stripping age.

The non parametric inversion recovers a flat star formation history with solar metallicity. The parametric method leads to a stripping age for NGC 4388 occurred $\sim 190 \pm 30$ Myr. Revised dynamical models are in good agreement with our results (Fig. 6.1).

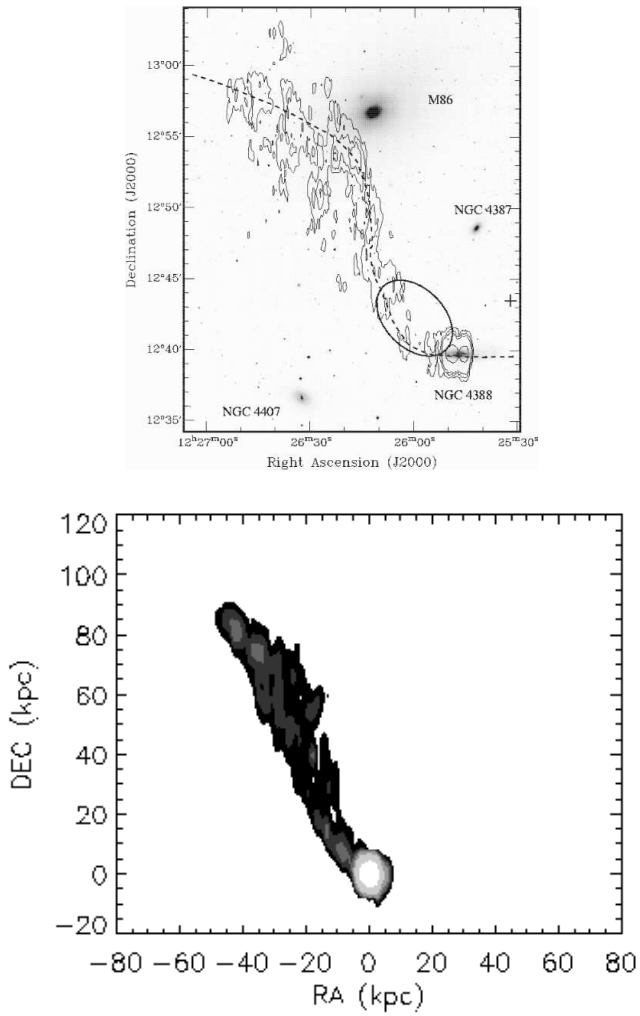

Figure 6.1: Upper panel: integrated HI emission line from Oosterloo & van Gorkom (2005) observations with Westerbork Synthesis Radio Telescope (WSRT). The ellipse indicates the region where Yoshida et al. (2002) detected ionized gas. Lower panel: revised dynamical model (Vollmer, in preparation).

Appendix A

The error spectrum associated with FORS data

The distribution of errors in the final FORS spectra is dominated by photon noise. The corresponding electrons collected in the CCD fulfill Poisson distribution:

$$\sigma_e(CCD) = \sqrt{x_e}, \tag{A.1}$$

where x_e is the number of electrons count. The final spectrum from the subtraction of a sky spectrum from a galaxy spectrum, therefore:

$$\sigma_e^2 = \sigma_e^2(SKY) + \sigma_e^2(OBJ), \tag{A.2}$$

in which $\sigma_e^2(SKY)$ is the noise in the sky background and $\sigma_e^2(OBJ)$ is the noise in the observed object. If u_e and v_e are respectively the number of counts in the sky background and in the object we have:

$$\sigma_e^2(SKY) = \sqrt{u_e}, \qquad \sigma_e^2(OBJ) = \sqrt{v_e + u_e}. \tag{A.3}$$

To have the noise in Physical Unit (PU = erg/cm^2/sec/Å) we convert σ_e in σ_{PU}. We use the gain value of the CCD ($g = 1.43e^-/ADU$) and the sensitivity function (hereafter $C(\lambda)$) of the instrument:

$$\sigma_{ADU} = \frac{\sigma_e}{g}, \qquad \sigma_{PU} = \sigma_{ADU} \cdot C(\lambda), \tag{A.4}$$

$$\sigma_{ADU} = \frac{\sqrt{v_e + 2u_e}}{g}, \qquad \sigma_{PU} = \frac{C(\lambda)}{g}\sqrt{v_e + 2u_e}. \tag{A.5}$$

Now if:

$$v_e = g \cdot v_{ADU} = \frac{g}{C(\lambda)} \cdot v_{PU}, \tag{A.6}$$

we can write:

$$\sigma_{PU} = \frac{C(\lambda)}{g}\sqrt{\frac{g}{C(\lambda)}(v_{PU} + 2u_{PU})} = \sqrt{\frac{C(\lambda)}{g}(v_e + 2u_e)}. \qquad \text{(A.7)}$$

In this expression, we have not take into account that $C(\lambda)$ is derived from the observations of spectro-photometric standard stars, i.e. it is itself subject to errors. The reason is that spectrophotometric calibrations

Appendix B

The calculation of the Q function and its derivative in practice

The solution of Eq. 2.23 and Eq. 2.19 is found by minimizing the Q-function:

$$Q(\mathbf{x}) = \chi^2(\mathbf{y} \mid \mathbf{x}) + \mu P(\mathbf{x}), \tag{B.1}$$

in which:

- $\chi^2(\mathbf{y} \mid \mathbf{x}) = [\mathbf{y} - \mathbf{s}(\mathbf{x})]^\top \cdot \mathbf{W} \cdot [\mathbf{y} - \mathbf{s}(\mathbf{x})]$ is the usual χ^2 estimator.
- $P(\mathbf{x})$ is the penalty function.

To find the minimum of the Q-function we use the *OPTIMPACK* package (Thiebaut, 2002) implemented for `Yorick` language (http://www.maumae.net/yorick/doc/index.html). This method uses the limited memory variable method (VMLM-B) and need an analytical form of the Q-function and its gradient.

In the next sections we analyze in detail each term both of Q and $\frac{\partial Q}{\partial}$.

B.1 χ^2 gradient

This term represents the usual χ^2 estimator, in which $\mathbf{s}(\mathbf{x})$ is the model spectrum associated to a defined $\mathbf{x}$. Depending on the equation considered (2.23 or 2.19), we have different solution. We follow precisely the implementation of Ocvirk et al. (2006a).

B.1.1 Without LOSVD

$$\mathbf{s}(\mathbf{x}) = diag(\mathbf{f}_{\text{ext}}) \cdot \mathbf{B} \cdot \mathbf{x}. \tag{B.2}$$

To minimize this function we need to write explicitly the gradients. For the sake of simplicity, we define a vector of the residuals:

$$\mathbf{r} = \mathbf{y} - diag(\mathbf{f}_{\text{ext}}) \cdot \mathbf{B} \cdot \mathbf{x}. \tag{B.3}$$

The gradient of χ^2 is:

$$\frac{\partial \chi^2}{\partial \mathbf{x}} = -2\mathbf{B}^\top \cdot diag(\mathbf{f}_{\text{ext}}) \cdot \mathbf{W} \cdot \mathbf{r}, \tag{B.4}$$

$$\frac{\partial \chi^2}{\partial \mathbf{Z}} = -2\mathbf{x}^\top \cdot \frac{\partial \mathbf{B}^\top}{\partial \mathbf{Z}} \cdot diag(\mathbf{f}_{\text{ext}}) \cdot \mathbf{W} \cdot \mathbf{r}, \tag{B.5}$$

$$\frac{\partial \chi^2}{\partial E} = -2\mathbf{x}^\top \cdot \mathbf{B}^\top \cdot diag\left(\frac{\partial \mathbf{f}_{\text{ext}}}{\partial E}\right) \cdot \mathbf{W} \cdot \mathbf{r}. \tag{B.6}$$

B.1.2 With LOSVD

If we consider the LOSVD the model spectrum is given by:

$$\mathbf{s} = \mathcal{F}^{-1} \cdot diag(\mathcal{F} \cdot \mathbf{K}) \cdot \mathcal{F} \cdot \mathbf{g}, \tag{B.7}$$

in which $\mathbf{K}$ is a spectra obtained from Eq. B.2 and $\mathcal{F}$ is the fast Fourier transform as defined in Press (2002).

We define a vector residual:

$$\mathbf{r} = \mathbf{y} - \mathcal{F}^{-1} \cdot diag(\mathcal{F} \cdot \mathbf{K}) \cdot \mathcal{F} \cdot \mathbf{g}. \tag{B.8}$$

The total gradient is:

$$\frac{\partial \chi^2}{\partial \mathbf{g}} = -2\mathcal{F}^* \cdot diag(\mathcal{F} \cdot diag(\mathbf{f}_{\text{ext}}(E)) \cdot \mathbf{B} \cdot \mathbf{x})^* \cdot \mathcal{F} \cdot \mathbf{W} \cdot \mathbf{r}, \tag{B.9}$$

$$\frac{\partial \chi^2}{\partial \mathbf{x}} = \left(\frac{\partial \chi^2}{\partial \mathbf{K}}\right)^\top \cdot diag(\mathbf{f}_{\text{ext}}) \cdot B, \tag{B.10}$$

$$\frac{\partial \chi^2}{\partial \mathbf{Z}} = \left(\frac{\partial \chi^2}{\partial \mathbf{K}}\right)^\top \cdot diag(\mathbf{x}) \cdot \frac{\partial \mathbf{B}}{\partial \mathbf{Z}} \cdot diag(\mathbf{f}_{\text{ext}}), \tag{B.11}$$

$$\frac{\partial \chi^2}{\partial E} = \left(\frac{\partial \chi^2}{\partial \mathbf{K}}\right)^\top \cdot diag\left(\frac{\partial \mathbf{f}_{\text{ext}})}{\partial E}\right) \cdot \mathbf{B} \cdot \mathbf{x}, \tag{B.12}$$

in which:

$$\frac{\partial \chi^2}{\partial \mathbf{K}} = -2\mathcal{F}^* \cdot diag(\mathcal{F} \cdot \mathbf{g})^* \cdot \mathcal{F} \cdot \mathbf{W} \cdot \mathbf{r}. \tag{B.13}$$

Appendix C

Non Parametric Estimation of the Continuum

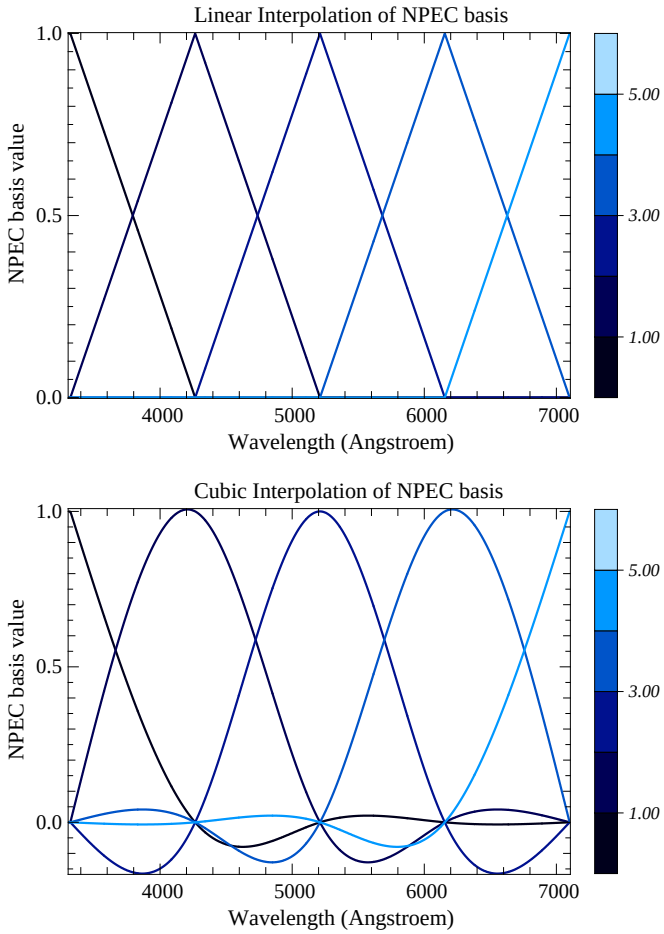

Figure C.1: Top panel: NPEC basis $f_j(\lambda)$. Bottom panel : NPEC basis obtained through a cubic spline interpolation of the vector $f_j(\lambda)$.

As in Ocvirk et al. (2006a) We define a set of λ_n anchor points equally spaced in the wavelength domain of the spectra. We create a function **E** defined in the

λ_n points. We build the extinction law by linear interpolation of the $E_n(\lambda_n)$ points according to the basis (left panel of fig. C.1):

$$f_j(\lambda) = \begin{cases} \frac{\lambda-\alpha_{j-1}}{\alpha_j-\alpha_{j-1}} & \text{for} \quad \alpha_{j-1} \leq \lambda \leq \alpha_j, \\ \frac{\alpha_{j+1}-\lambda}{\alpha_{j+1}-\alpha_j} & \text{for} \quad \alpha_j \leq \lambda \leq \alpha_{j+1}, \\ 0 & \text{otherwise.} \end{cases}$$

The extinction law is developed along this basis:

$$f_{\text{ext}}(\lambda) = \sum_{j=1}^{n} E_j f_j(\lambda), \tag{C.1}$$

or in matrix form:

$$\mathbf{f}_{\text{ext}}(\mathbf{E}) = \mathbf{R} \cdot \mathbf{E}, \tag{C.2}$$

where matrix $\mathbf{R} = R_{kj} = f_j(\lambda_k)$ samples each basis element f_j in the wavelength domain considered. The values in **E** completely define what we have called the NPEC correction curve. It may account for extinction, but also for flux calibration errors.

The basis $f_j(\lambda)$ is a sequence of triangles (see left panel of Fig. C.1). The linear combination of this basis provide a broken line. For this reason we preferred to smooth the basis using a cubic interpolation along the wavelength range (right panel of Fig. C.1). In this way we are been able to reproduce extinction laws with continuous derivatives.

Appendix D

Extinction laws

D.1 Cardelli et al. (1989)

The Cardelli et al. (1989) law is :

$$f_{\text{ext}}(\lambda, A_V, R_V) = e^{-\tau(\lambda, A_V, R_V)}, \tag{D.1}$$

where:

$$\tau(\lambda, A_V, R_V) = A_{\text{avg}} \cdot A_V \cdot ln(10) \cdot 0.4. \tag{D.2}$$

In Eq. D.2 we have:

- $A(\lambda)$ = Absolute extinction at any wavelength.
- A_V = Absolute extinction at a reference wavelength chosen for V filter (in Cardelli et al. (1989) is $\lambda_V = 5494$ Å).
- $A_{\text{avg}} = \langle A(\lambda)/A_V \rangle$ is the mean extinction law. It can be written as:

$$A_{\text{avg}} = a(x) + b(x)/R_V, \tag{D.3}$$

  in which:

  - $R_V \equiv A_V/E(B-V)$ is a parameter that is 3.1 in the diffuse interstellar medium and 5 in some dense clouds. Its value can vary with the abundances of interstellar molecules.
  - $a(x), b(x)$ are derived from a least square analysis of observations and a polynomial fitting in $x = 1/\lambda$. The coefficient depends on the wavelength.

In photometric minimization we need an analytical expression of the derivative Eq. D.1:

$$\frac{d}{dA_V} e^{-\tau(\lambda,A_V,R_V)} = -e^{-\tau(\lambda,A_V,R_V)} \cdot \left(a(x) + b(x)/R_V\right) \cdot ln(10) \cdot 0.4. \qquad \text{(D.4)}$$

D.2 Calzetti (2001)

The Calzetti law is more complex because of the distinction between gas and stars. The law is been calibrated for local starburst galaxies. The intrinsic flux density $f_i(\lambda)$ is recovered from the observed flux density $f_o(\lambda)$ using this relation:

$$f_i(\lambda) = f_o(\lambda)\, 10^{0.4E(B-V)_{\rm gas}k^e(\lambda)}, \qquad \text{(D.5)}$$

in which $E(B-V)_{\rm gas}$ is the color excess of the gas component, i.e. the difference between light absorption in B minus the light absorption in V band (emitted from the gas). The factor $k^e(\lambda)$ represents the obscuration curve for the stellar continuum (Calzetti et al., 2000) :

$$k^e(\lambda = 1.17(-1.857 + 1.040/\lambda) + 1.78, \qquad \text{(D.6)}$$

for for 0.12 μm $\leq \lambda \leq$ 2.2 μm, or:

$$k^e(\lambda) = 1.17(-2.156 + 1.509/\lambda - 0.198/\lambda^2 + 0.011/\lambda^3) + 1.78, \qquad \text{(D.7)}$$

for 0.12 μm $\leq \lambda \leq$ 0.63 μm.

The stellar continuum has a different reddening with respect to the ionized gas (Calzetti et al. 1994, Fanelli et al. 1988, Mas-Hesse et al. 1989). The relation between the gas and stars component is:

$$E(B-V)_{\rm star} = 0.44E(B-V)_{\rm gas}. \qquad \text{(D.8)}$$

The extinction law is then:

$$f_{\rm ext}(\lambda, E(B-V)) = 10^{0.4E(B-V)_{\rm gas}k^e(\lambda)}, \qquad \text{(D.9)}$$

The gradient of Eq. D.9 explicitly written is:

$$\frac{\partial f_{\text{ext}}}{\partial E(B-V)} = -0.4 \cdot k^{e}(\lambda) \cdot f_{\text{ext}}(\lambda, E(B-V)) \cdot log(10). \qquad \text{(D.10)}$$

Appendix E

Campaign of non parametric spectral inversion of the SAM2 model

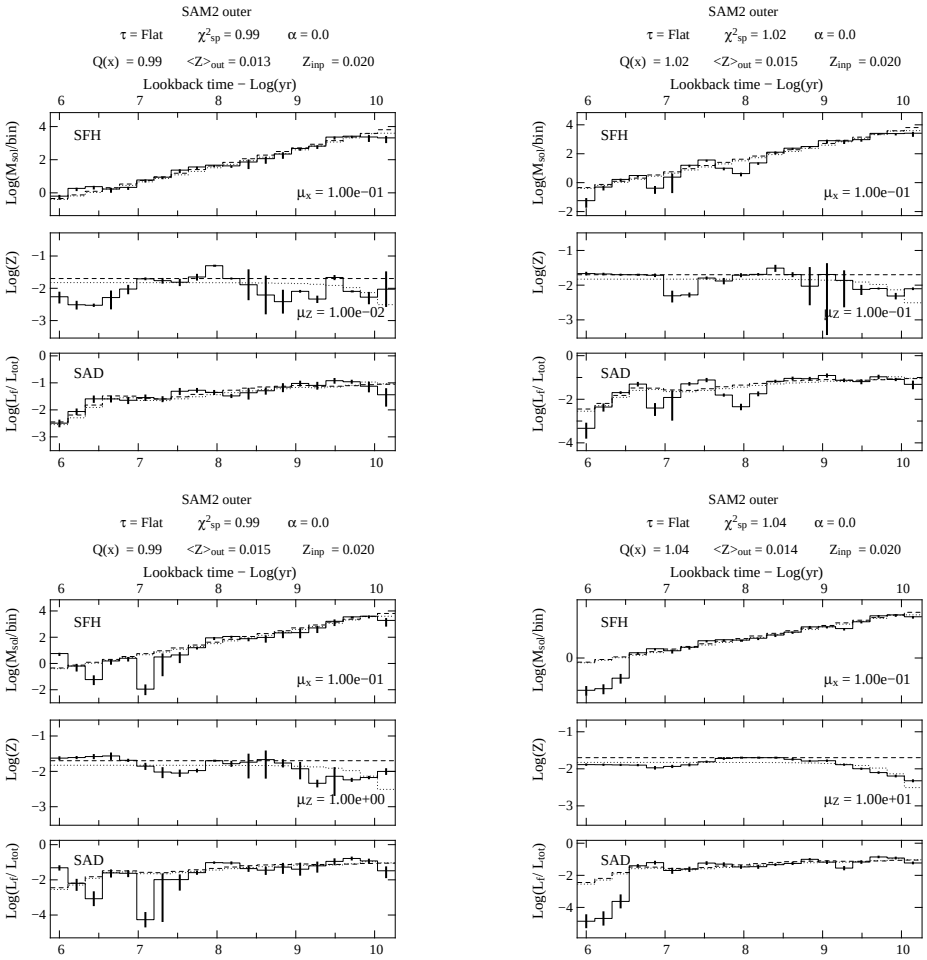

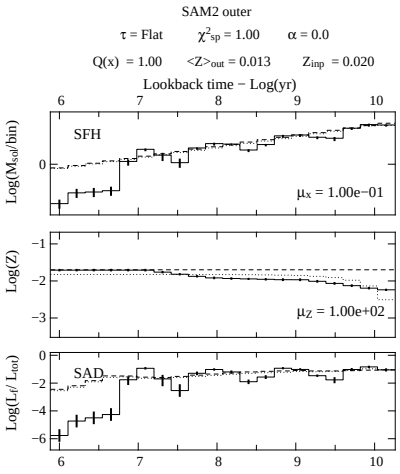
SAM2 outer
τ = Flat χ²sp = 1.00 α = 0.0
Q(x) = 1.00 <Z>out = 0.013 Zinp = 0.020
Lookback time − Log(yr)
SFH
μx = 1.00e−01
Log(Z)
μZ = 1.00e+02
SAD

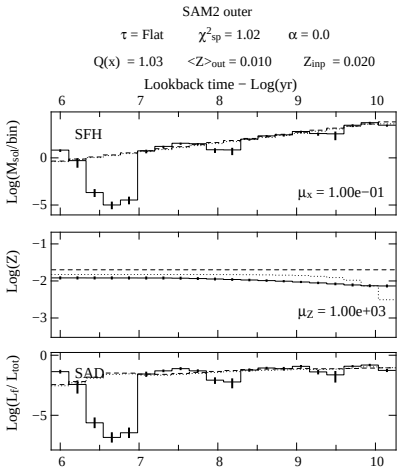
SAM2 outer
τ = Flat χ²sp = 1.02 α = 0.0
Q(x) = 1.03 <Z>out = 0.010 Zinp = 0.020
Lookback time − Log(yr)
SFH
μx = 1.00e−01
Log(Z)
μZ = 1.00e+03
SAD

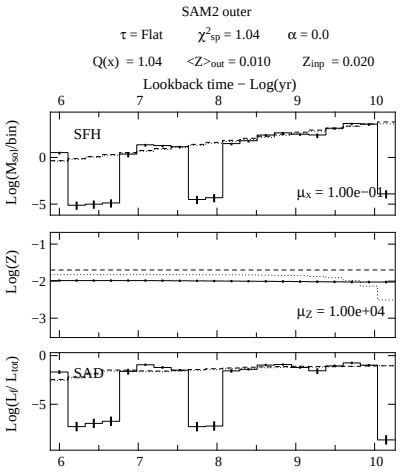
SAM2 outer
τ = Flat χ²sp = 1.04 α = 0.0
Q(x) = 1.04 <Z>out = 0.010 Zinp = 0.020
Lookback time − Log(yr)
SFH
μx = 1.00e−04
Log(Z)
μZ = 1.00e+04
SAD

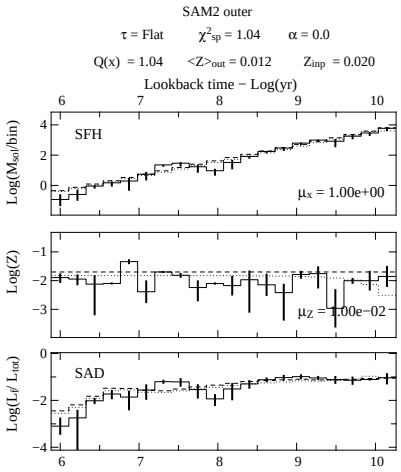
SAM2 outer
τ = Flat χ²sp = 1.04 α = 0.0
Q(x) = 1.04 <Z>out = 0.012 Zinp = 0.020
Lookback time − Log(yr)
SFH
μx = 1.00e+00
Log(Z)
μZ = 1.00e−02
SAD

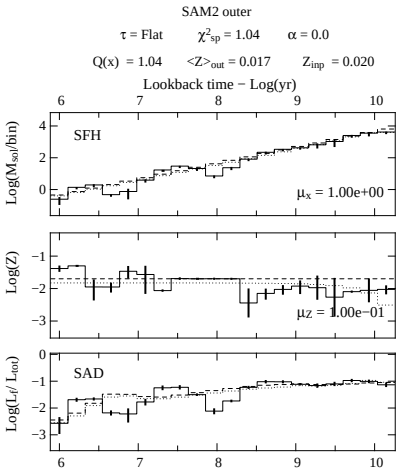
SAM2 outer
τ = Flat χ²sp = 1.04 α = 0.0
Q(x) = 1.04 <Z>out = 0.017 Zinp = 0.020
Lookback time − Log(yr)
SFH
μx = 1.00e+00
Log(Z)
μZ = 1.00e−01
SAD

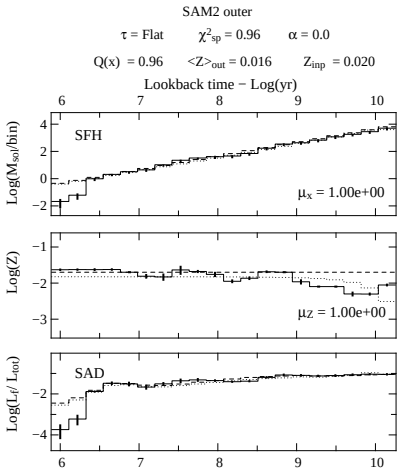
SAM2 outer
τ = Flat χ²sp = 0.96 α = 0.0
Q(x) = 0.96 <Z>out = 0.016 Zinp = 0.020
Lookback time − Log(yr)
SFH
μx = 1.00e+00
Log(Z)
μZ = 1.00e+00
SAD

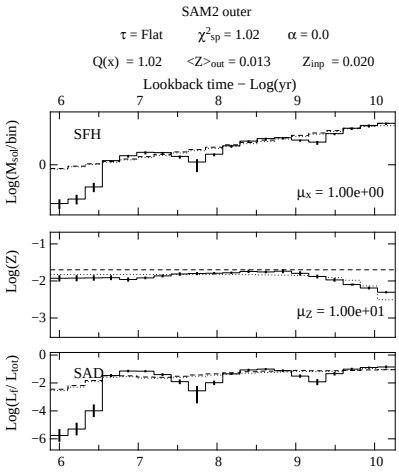
SAM2 outer
τ = Flat χ²sp = 1.02 α = 0.0
Q(x) = 1.02 <Z>out = 0.013 Zinp = 0.020
Lookback time − Log(yr)
SFH
μx = 1.00e+00
Log(Z)
μZ = 1.00e+01
SAD
Log(Mstf/bin)
Log(Lif/ Ltot)

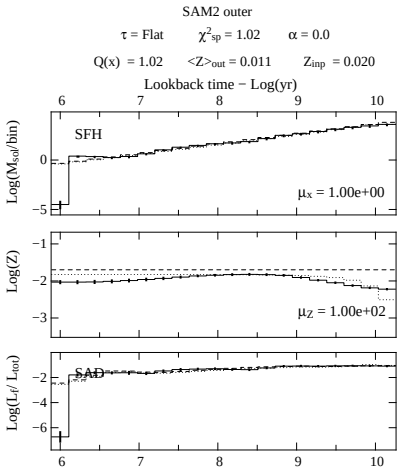
SAM2 outer
τ = Flat χ²sp = 1.02 α = 0.0
Q(x) = 1.02 <Z>out = 0.011 Zinp = 0.020
Lookback time − Log(yr)
SFH
μx = 1.00e+00
Log(Z)
μZ = 1.00e+02
SAD
Log(Mstf/bin)
Log(Lif/ Ltot)

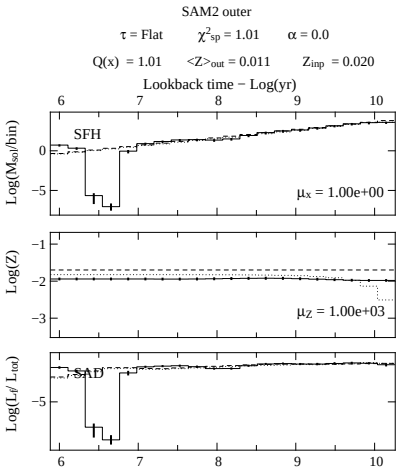
SAM2 outer
τ = Flat χ²sp = 1.01 α = 0.0
Q(x) = 1.01 <Z>out = 0.011 Zinp = 0.020
Lookback time − Log(yr)
SFH
μx = 1.00e+00
Log(Z)
μZ = 1.00e+03
SAD
Log(Mstf/bin)
Log(Lif/ Ltot)

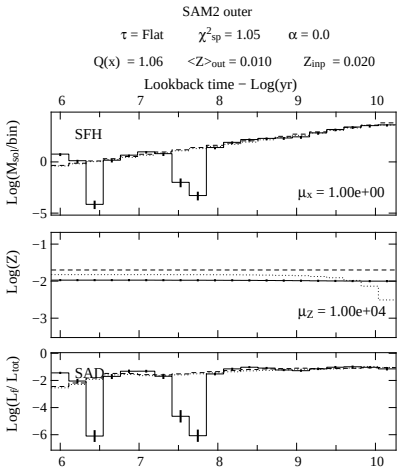
SAM2 outer
τ = Flat χ²sp = 1.05 α = 0.0
Q(x) = 1.06 <Z>out = 0.010 Zinp = 0.020
Lookback time − Log(yr)
SFH
μx = 1.00e+00
Log(Z)
μZ = 1.00e+04
SAD
Log(Mstf/bin)
Log(Lif/ Ltot)

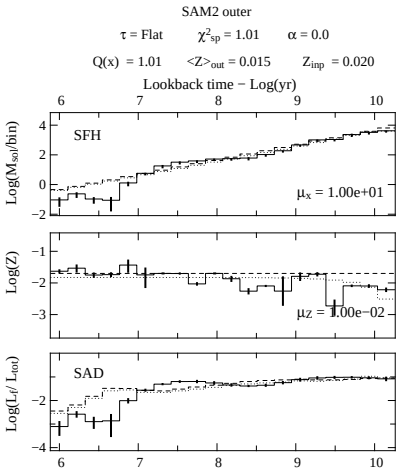
SAM2 outer
τ = Flat χ²sp = 1.01 α = 0.0
Q(x) = 1.01 <Z>out = 0.015 Zinp = 0.020
Lookback time − Log(yr)
SFH
μx = 1.00e+01
Log(Z)
μZ = 1.00e−02
SAD
Log(Mstf/bin)
Log(Lif/ Ltot)

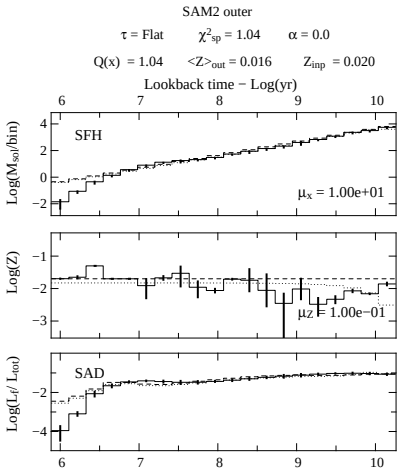
SAM2 outer
τ = Flat χ²sp = 1.04 α = 0.0
Q(x) = 1.04 <Z>out = 0.016 Zinp = 0.020
Lookback time − Log(yr)
SFH
μx = 1.00e+01
Log(Z)
μZ = 1.00e−01
SAD
Log(Mstf/bin)
Log(Lif/ Ltot)

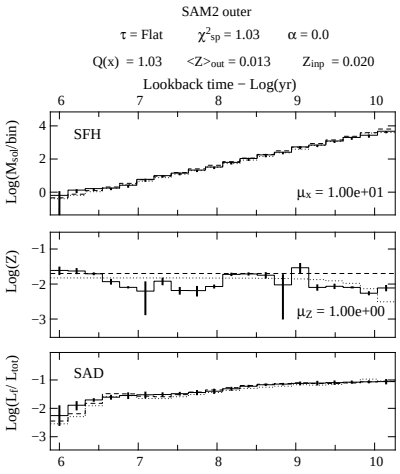
SAM2 outer
τ = Flat χ²sp = 1.03 α = 0.0
Q(x) = 1.03 <Z>out = 0.013 Zinp = 0.020
Lookback time − Log(yr)
SFH
μx = 1.00e+01
Log(Z)
μZ = 1.00e+00
SAD
Log(Mstf/bin)
Log(Lif/ Ltot)

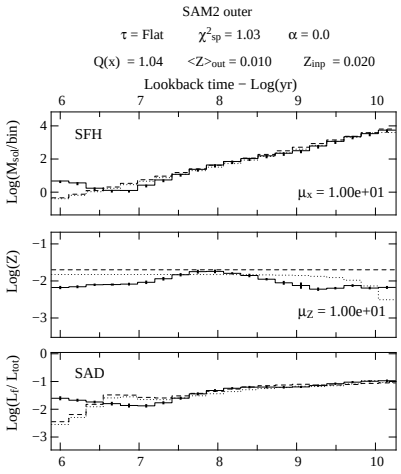
SAM2 outer
τ = Flat χ²sp = 1.03 α = 0.0
Q(x) = 1.04 <Z>out = 0.010 Zinp = 0.020
Lookback time − Log(yr)
SFH
μx = 1.00e+01
Log(Z)
μZ = 1.00e+01
SAD
Log(Mstf/bin)
Log(Lif/ Ltot)

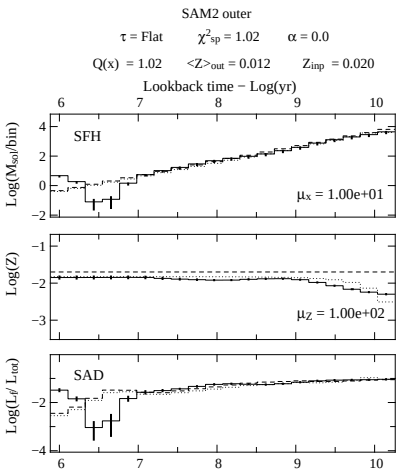
SAM2 outer
τ = Flat χ²sp = 1.02 α = 0.0
Q(x) = 1.02 <Z>out = 0.012 Zinp = 0.020
Lookback time − Log(yr)
SFH
μx = 1.00e+01
Log(Z)
μZ = 1.00e+02
SAD
Log(Mstf/bin)
Log(Lif/ Ltot)

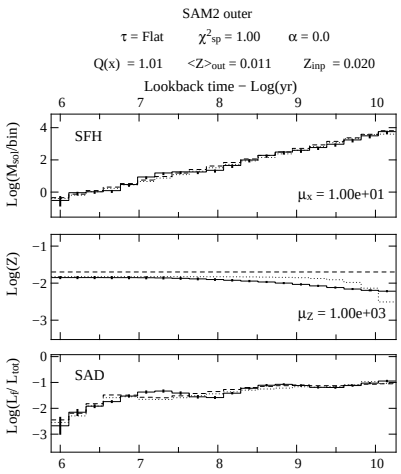
SAM2 outer
τ = Flat χ²sp = 1.00 α = 0.0
Q(x) = 1.01 <Z>out = 0.011 Zinp = 0.020
Lookback time − Log(yr)
SFH
μx = 1.00e+01
Log(Z)
μZ = 1.00e+03
SAD
Log(Mstf/bin)
Log(Lif/ Ltot)

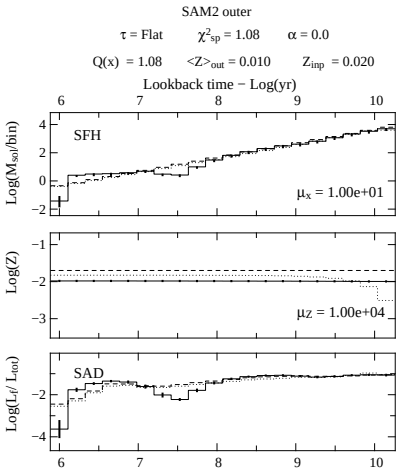
SAM2 outer
τ = Flat χ²sp = 1.08 α = 0.0
Q(x) = 1.08 <Z>out = 0.010 Zinp = 0.020
Lookback time − Log(yr)
SFH
μx = 1.00e+01
Log(Z)
μZ = 1.00e+04
SAD
Log(Mstf/bin)
Log(Lif/ Ltot)

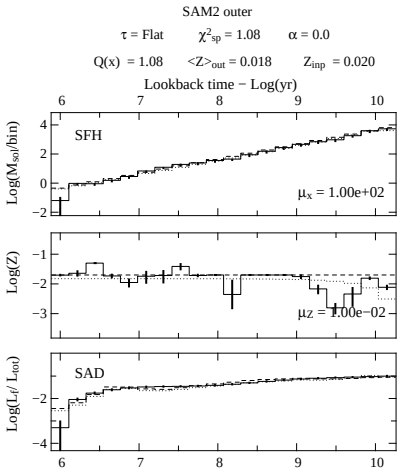
SAM2 outer
τ = Flat χ²sp = 1.08 α = 0.0
Q(x) = 1.08 <Z>out = 0.018 Zinp = 0.020
Lookback time − Log(yr)
SFH
μx = 1.00e+02
Log(Z)
μZ = 1.00e−02
SAD
Log(Mstf/bin)
Log(Lif/ Ltot)

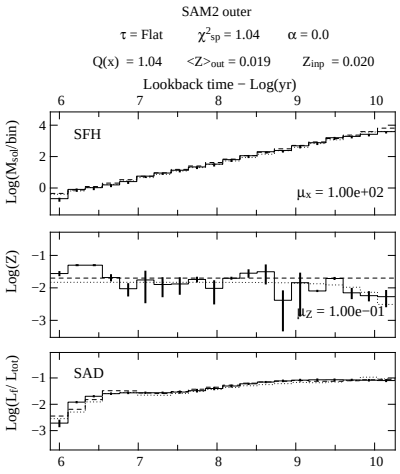
SAM2 outer
τ = Flat χ²sp = 1.04 α = 0.0
Q(x) = 1.04 <Z>out = 0.019 Zinp = 0.020
Lookback time − Log(yr)
SFH
μx = 1.00e+02
Log(Z)
μZ = 1.00e−01
SAD
Log(Mstr/bin)
Log(Lif/ Ltot)

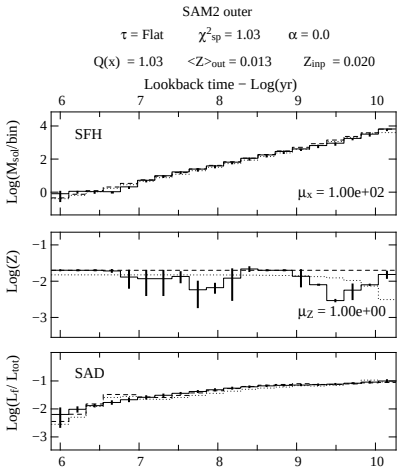
SAM2 outer
τ = Flat χ²sp = 1.03 α = 0.0
Q(x) = 1.03 <Z>out = 0.013 Zinp = 0.020
Lookback time − Log(yr)
SFH
μx = 1.00e+02
Log(Z)
μZ = 1.00e+00
SAD
Log(Mstr/bin)
Log(Lif/ Ltot)

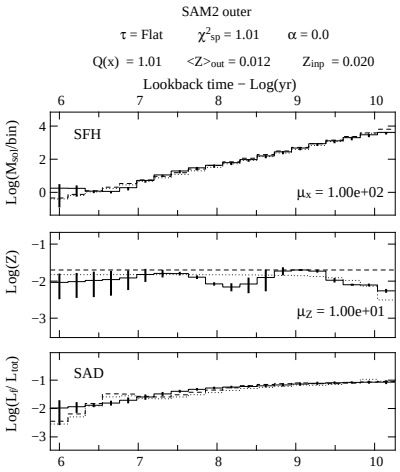
SAM2 outer
τ = Flat χ²sp = 1.01 α = 0.0
Q(x) = 1.01 <Z>out = 0.012 Zinp = 0.020
Lookback time − Log(yr)
SFH
μx = 1.00e+02
Log(Z)
μZ = 1.00e+01
SAD
Log(Mstr/bin)
Log(Lif/ Ltot)

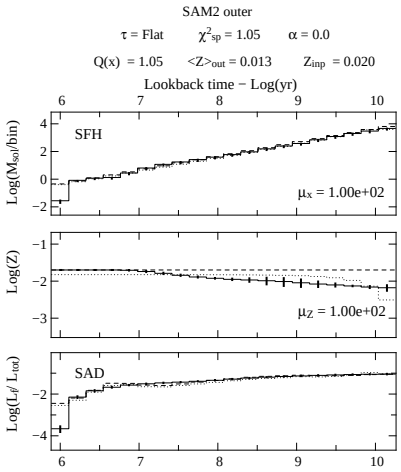
SAM2 outer
τ = Flat χ²sp = 1.05 α = 0.0
Q(x) = 1.05 <Z>out = 0.013 Zinp = 0.020
Lookback time − Log(yr)
SFH
μx = 1.00e+02
Log(Z)
μZ = 1.00e+02
SAD
Log(Mstr/bin)
Log(Lif/ Ltot)

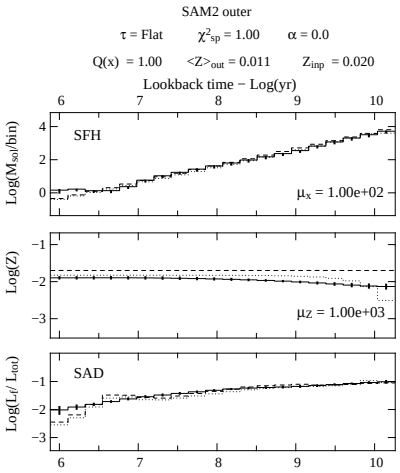
SAM2 outer
τ = Flat χ²sp = 1.00 α = 0.0
Q(x) = 1.00 <Z>out = 0.011 Zinp = 0.020
Lookback time − Log(yr)
SFH
μx = 1.00e+02
Log(Z)
μZ = 1.00e+03
SAD
Log(Mstr/bin)
Log(Lif/ Ltot)

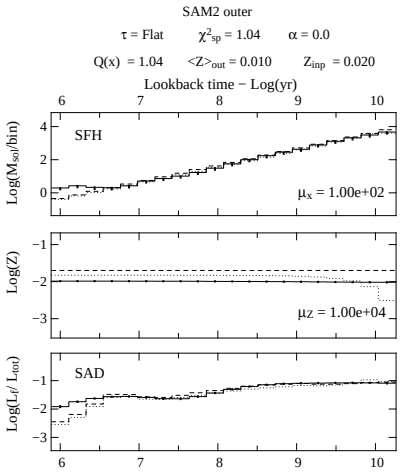
SAM2 outer
τ = Flat χ²sp = 1.04 α = 0.0
Q(x) = 1.04 <Z>out = 0.010 Zinp = 0.020
Lookback time − Log(yr)
SFH
μx = 1.00e+02
Log(Z)
μZ = 1.00e+04
SAD
Log(Mstr/bin)
Log(Lif/ Ltot)

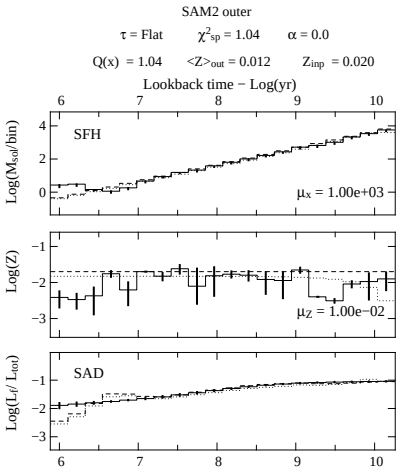
SAM2 outer
τ = Flat χ²sp = 1.04 α = 0.0
Q(x) = 1.04 <Z>out = 0.012 Zinp = 0.020
Lookback time − Log(yr)
SFH
μx = 1.00e+03
Log(Z)
μZ = 1.00e−02
SAD
Log(Mstl/bin)
Log(Lif/ Ltot)

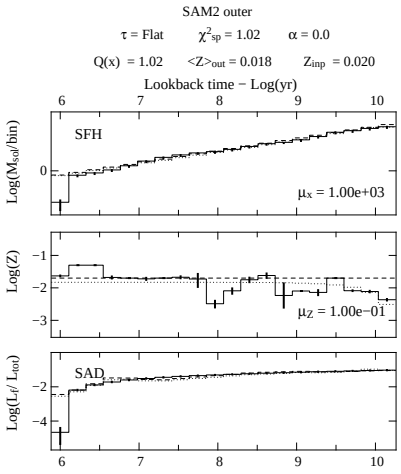
SAM2 outer
τ = Flat χ²sp = 1.02 α = 0.0
Q(x) = 1.02 <Z>out = 0.018 Zinp = 0.020
Lookback time − Log(yr)
SFH
μx = 1.00e+03
Log(Z)
μZ = 1.00e−01
SAD
Log(Mstl/bin)
Log(Lif/ Ltot)

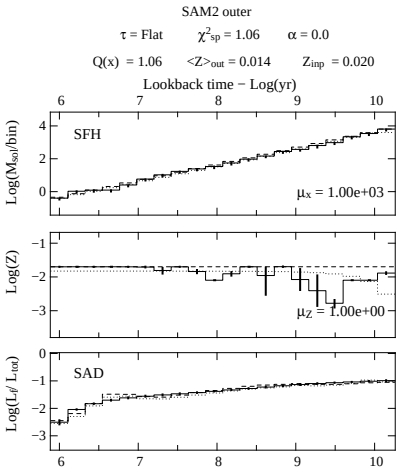
SAM2 outer
τ = Flat χ²sp = 1.06 α = 0.0
Q(x) = 1.06 <Z>out = 0.014 Zinp = 0.020
Lookback time − Log(yr)
SFH
μx = 1.00e+03
Log(Z)
μZ = 1.00e+00
SAD
Log(Mstl/bin)
Log(Lif/ Ltot)

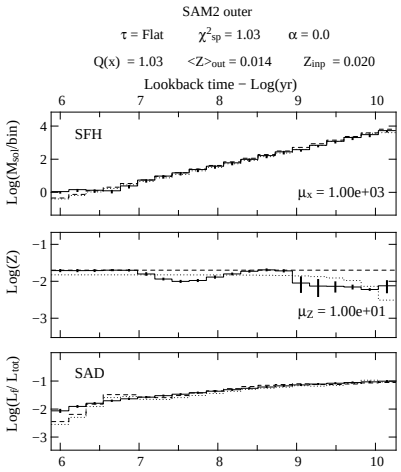
SAM2 outer
τ = Flat χ²sp = 1.03 α = 0.0
Q(x) = 1.03 <Z>out = 0.014 Zinp = 0.020
Lookback time − Log(yr)
SFH
μx = 1.00e+03
Log(Z)
μZ = 1.00e+01
SAD
Log(Mstl/bin)
Log(Lif/ Ltot)

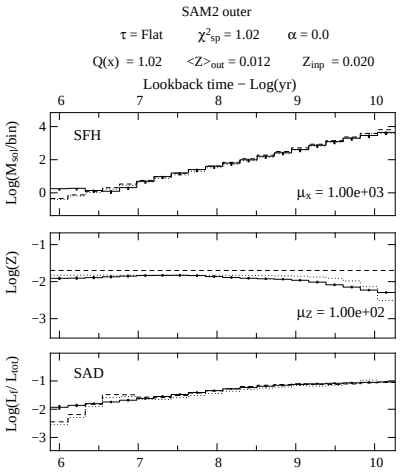
SAM2 outer
τ = Flat χ²sp = 1.02 α = 0.0
Q(x) = 1.02 <Z>out = 0.012 Zinp = 0.020
Lookback time − Log(yr)
SFH
μx = 1.00e+03
Log(Z)
μZ = 1.00e+02
SAD
Log(Mstl/bin)
Log(Lif/ Ltot)

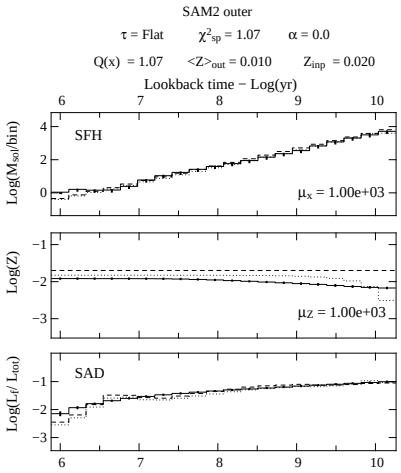
SAM2 outer
τ = Flat χ²sp = 1.07 α = 0.0
Q(x) = 1.07 <Z>out = 0.010 Zinp = 0.020
Lookback time − Log(yr)
SFH
μx = 1.00e+03
Log(Z)
μZ = 1.00e+03
SAD
Log(Mstl/bin)
Log(Lif/ Ltot)

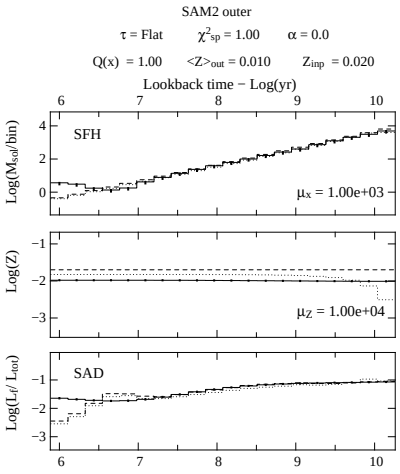
SAM2 outer
τ = Flat χ²sp = 1.00 α = 0.0
Q(x) = 1.00 <Z>out = 0.010 Zinp = 0.020
Lookback time − Log(yr)
SFH
μx = 1.00e+03
Log(Z)
μZ = 1.00e+04
SAD
Log(Mstr/bin)
Log(Lif/ Ltot)

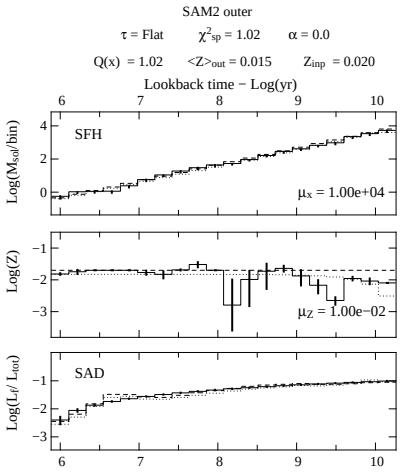
SAM2 outer
τ = Flat χ²sp = 1.02 α = 0.0
Q(x) = 1.02 <Z>out = 0.015 Zinp = 0.020
Lookback time − Log(yr)
SFH
μx = 1.00e+04
Log(Z)
μZ = 1.00e−02
SAD
Log(Mstr/bin)
Log(Lif/ Ltot)

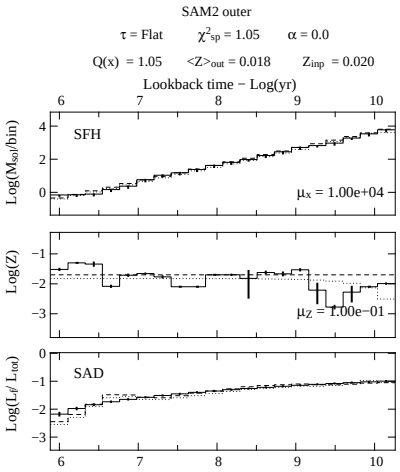
SAM2 outer
τ = Flat χ²sp = 1.05 α = 0.0
Q(x) = 1.05 <Z>out = 0.018 Zinp = 0.020
Lookback time − Log(yr)
SFH
μx = 1.00e+04
Log(Z)
μZ = 1.00e−01
SAD
Log(Mstr/bin)
Log(Lif/ Ltot)

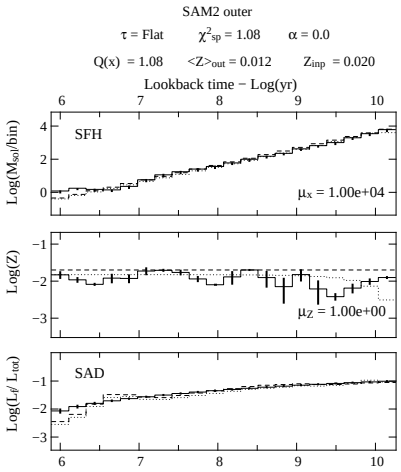
SAM2 outer
τ = Flat χ²sp = 1.08 α = 0.0
Q(x) = 1.08 <Z>out = 0.012 Zinp = 0.020
Lookback time − Log(yr)
SFH
μx = 1.00e+04
Log(Z)
μZ = 1.00e+00
SAD
Log(Mstr/bin)
Log(Lif/ Ltot)

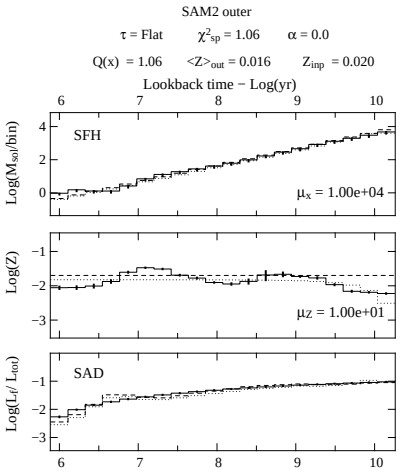
SAM2 outer
τ = Flat χ²sp = 1.06 α = 0.0
Q(x) = 1.06 <Z>out = 0.016 Zinp = 0.020
Lookback time − Log(yr)
SFH
μx = 1.00e+04
Log(Z)
μZ = 1.00e+01
SAD
Log(Mstr/bin)
Log(Lif/ Ltot)

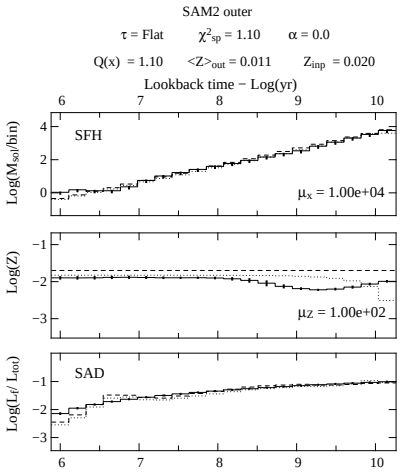
SAM2 outer
τ = Flat χ²sp = 1.10 α = 0.0
Q(x) = 1.10 <Z>out = 0.011 Zinp = 0.020
Lookback time − Log(yr)
SFH
μx = 1.00e+04
Log(Z)
μZ = 1.00e+02
SAD
Log(Mstr/bin)
Log(Lif/ Ltot)

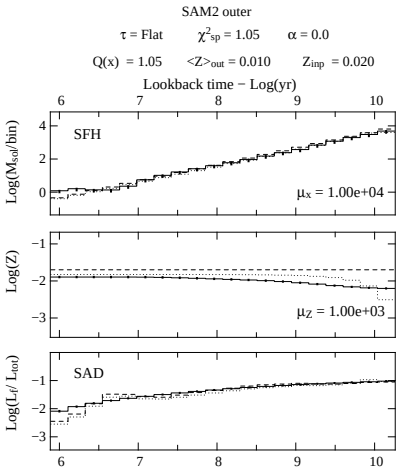
SAM2 outer
τ = Flat
χ²sp = 1.05
α = 0.0
Q(x) = 1.05
<Z>out = 0.010
Zinp = 0.020
Lookback time − Log(yr)
SFH
μx = 1.00e+04
Log(Z)
μZ = 1.00e+03
SAD
Log(Mstot/bin)
Log(Lμ/ Ltot)

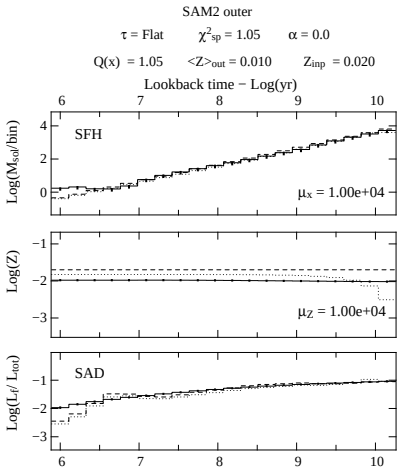
SAM2 outer
τ = Flat
χ²sp = 1.05
α = 0.0
Q(x) = 1.05
<Z>out = 0.010
Zinp = 0.020
Lookback time − Log(yr)
SFH
μx = 1.00e+04
Log(Z)
μZ = 1.00e+04
SAD
Log(Mstot/bin)
Log(Lμ/ Ltot)

Bibliography

Abadi, M. G., Moore, B., & Bower, R. G. 1999, MNRAS, 308, 947

Acreman, D. M., Stevens, I. R., Ponman, T. J., & Sakelliou, I. 2003, MNRAS, 341, 1333

Adelman-McCarthy, J. K., et al. 2008, ApJS, 175, 297

Alongi, M., Bertelli, G., Bressan, A., Chiosi, C., Fagotto, F., Greggio, L., & Nasi, E. 1993, A&AS, 97, 851

Appenzeller, I., et al. 1998, The Messenger, 94, 1

Barnes, J. E. 1998, Saas-Fee Advanced Course 26: Galaxies: Interactions and Induced Star Formation, 275

Bakos, G. Á., Sahu, K. C., & Németh, P. 2002, ApJS, 141, 187

Bekki, K., Couch, W. J., & Shioya, Y. 2002, ApJ, 577, 651

Binggeli, B., Sandage, A., & Tammann, G. A. 1985, AJ, 90, 1681

Boissier, S., & Prantzos, N. 2000, MNRAS, 312, 398

Bonnarel, F., et al. 2000, A&AS, 143, 33

Boselli, A., & Gavazzi, G. 2006, PASP, 118, 517

Bressan, A., Fagotto, F., Bertelli, G., & Chiosi, C. 1993, A&AS, 100, 647

Bruzual, G., & Charlot, S. 2003, MNRAS, 344, 1000

Calzetti, D. 2001, PASP, 113, 1449

Calzetti, D., Armus, L., Bohlin, R. C., Kinney, A. L., Koornneef, J., & Storchi-Bergmann, T. 2000, ApJ, 533, 682

Calzetti, D., Kinney, A. L., & Storchi-Bergmann, T. 1994, ApJ, 429, 582

Capak, P., Abraham, R. G., Ellis, R. S., Mobasher, B., Scoville, N., Sheth, K., & Koekemoer, A. 2007, ApJS, 172, 284

Cardelli, J. A., Clayton, G. C., & Mathis, J. S. 1989, ApJ, 345, 245

Cayatte, V., van Gorkom, J. H., Balkowski, C., & Kotanyi, C. 1990, AJ, 100, 604

Cenarro, A. J., et al. 2007, MNRAS, 374, 664

Chamaraux, P., Balkowski, C., & Gerard, E. 1980, A&A, 83, 38

Chung, A., van Gorkom, J. H., Kenney, J. D. P., & Vollmer, B. 2007, ApJ, 659, L115

Cid Fernandes, R., Mateus, A., Sodré, L., Stasińska, G., & Gomes, J. M. 2005, MNRAS, 358, 363

Craig, I. J. D., & Brown, J. C. 1986, Research supported by SERC. Bristol, England and Boston, MA, Adam Hilger, Ltd., 1986, 159 p.,

Crowl, H. H., & Kenney, J. D. P. 2008, AJ, 136, 1623

Dahlem, M. 1997, PASP, 109, 1298

Dressler, A. 1980, ApJ, 236, 351

Dressler, A. 1986, ApJ, 301, 35

Dye, S. 2008, MNRAS, 389, 1293

Faber, S. M. 1973, ApJ, 179, 731

Fagotto, F., Bressan, A., Bertelli, G., & Chiosi, C. 1994, A&AS, 105, 29

Fagotto, F., Bressan, A., Bertelli, G., & Chiosi, C. 1994, A&AS, 104, 365

Fanelli, M. N., O'Connell, R. W., & Thuan, T. X. 1988, ApJ, 334, 665

Gavazzi, G., Boselli, A., Pedotti, P., Gallazzi, A., & Carrasco, L. 2002, A&A, 396, 449

Gavazzi, G. 1989, ApJ, 346, 59

Gavazzi, G. 1987, ApJ, 320, 96

Gil de Paz, A., et al. 2007, ApJS, 173, 185

Giovanelli, R., & Haynes, M. P. 1983, AJ, 88, 881

Girardi, L., Bressan, A., Chiosi, C., Bertelli, G., & Nasi, E. 1996, A&AS, 117, 113

Gómez, P. L., et al. 2003, ApJ, 584, 210

Gunn, J. E., & Gott, J. R. I. 1972, ApJ, 176, 1

Hamuy, M., Walker, A. R., Suntzeff, N. B., Gigoux, P., Heathcote, S. R., & Phillips, M. M. 1992, Pasp, 104, 533

Hubble, E. P. 1936, Realm of the Nebulae, by E.P. Hubble. New Haven: Yale University Press, 1936. ISBN 9780300025002,

Hubble, E. P. 1927, The Observatory, 50, 276

Hubble, E. P. 1926, ApJ, 64, 321

Hubble, E. 1926, Contributions from the Mount Wilson Observatory / Carnegie Institution of Washington, 324, 1

Iwasawa, K., Wilson, A. S., Fabian, A. C., & Young, A. J. 2003, MNRAS, 345, 369

Kenney, J. D. P., Crowl, H., van Gorkom, J., & Vollmer, B. 2004, Recycling Intergalactic and Interstellar Matter, 217, 370

Koleva, M., Prugniel, P., Ocvirk, P., Le Borgne, D., Chilingarian, I., & Soubiran, C. 2007, IAU Symposium, 241, 183

Le Borgne, J.-F., et al. 2003, A&A, 402, 433

MacArthur, L. A., González, J. J., & Courteau, S. 2009, MNRAS, 395, 28

Mamon, G. A., Sanchis, T., Salvador-Solé, E., & Solanes, J. M. 2004, A&A, 414, 445

Mas-Hesse, J. M., Arnault, P., & Kunth, D. 1989, Ap&SS, 157, 131

Mateu, J., Magris, G., & Bruzual, G. 2001, Galaxy Disks and Disk Galaxies, 230, 323

Merritt, D. 1997, AJ, 114, 228

Mihalas, D., & Routly, P. M. 1968, A Series of Books in Astronomy and Astrophysics, San Francisco: W.H. Freeman and Company, —c1968,

Mo, H. J., Mao, S., & White, S. D. M. 1998, MNRAS, 295, 319

Morrissey, P., et al. 2007, ApJS, 173, 682

Moultaka, J., & Pelat, D. 2000, MNRAS, 314, 409

Moultaka, J., Boisson, C., Joly, M., & Pelat, D. 2004, A&A, 420, 459

Nulsen, P. E. J. 1982, MNRAS, 198, 1007

Ocvirk, P., Pichon, C., Lançon, A., & Thiébaut, E. 2006, MNRAS, 365, 46

Ocvirk, P., Pichon, C., Lançon, A., & Thiébaut, E. 2006, MNRAS, 365, 74

Oke, J. B. 1990, AJ, 99, 1621

Oosterloo, T., & van Gorkom, J. 2005, A&A, 437, L19

Perryman, M. A. C., et al. 1997, A&A, 323, L49

Postman, M., & Geller, M. J. 1984, ApJ, 281, 95

Press, W. H. 2002, Numerical recipes in C++ : the art of scientific computing by William H. Press. xxviii, 1,002 p. : ill. ; 26 cm. Includes bibliographical references and index. ISBN : 0521750334,

Pichon, C., Siebert, A., & Bienaymé, O. 2002, MNRAS, 329, 181

Pichon, C., & Thiebaut, E. 1998, MNRAS, 301, 419

Pilyugin, L. S. 2000, A&A, 362, 325

Quilis, V., Moore, B., & Bower, R. 2000, Science, 288, 1617

Reichardt, C., Jimenez, R., & Heavens, A. F. 2001, MNRAS, 327, 849

Kochanek, C. S., & Rybicki, G. B. 1996, MNRAS, 280, 1257

Roediger, E., & Hensler, G. 2005, A&A, 433, 875

Roediger, E., & Brüggen, M. 2006, MNRAS, 369, 567

Sabatini, S., Davies, J., Scaramella, R., Smith, R., Baes, M., Linder, S. M., Roberts, S., & Testa, V. 2003, MNRAS, 341, 981

Sánchez-Blázquez, P., et al. 2006, MNRAS, 371, 703

Saha, P., & Williams, T. B. 1994, AJ, 107, 1295

Schindler, S., Binggeli, B., Bohringer, H. 1999, A&A, 343, 420

Schulz, S., & Struck, C. 2001, MNRAS, 328, 185

Skrutskie, M. F., et al. 2006, AJ, 131, 1163

Solanes, J. M., Manrique, A., García-Gómez, C., González-Casado, G., Giovanelli, R., & Haynes, M. P. 2001, ApJ, 548, 97

Stevens, I. R., Acreman, D. M., & Ponman, T. J. 1999, MNRAS, 310, 663

Thiebaut, E. 2002, Proc. SPIE, 4847, 174

Thiébaut, E. 2005, NATO ASIB Proc. 198: Optics in astrophysics, 397

Titterington, D. M. 1985, A&A, 144, 381

Tody, D. 1993, Astronomical Data Analysis Software and Systems II, 52, 173

Vazdekis, A., et al. 2007, IAU Symposium, 241, 133

Veilleux, S., Bland-Hawthorn, J., Cecil, G., Tully, R. B., & Miller, S. T. 1999, ApJ, 520, 111

Veilleux, S., Bland-Hawthorn, J., & Cecil, G. 1999, AJ, 118, 2108

Vergely, J.-L., Lançon, A., & Mouhcine 2002, A&A, 394, 807

Vollmer, B., Cayatte, V., Balkowski, C., & Duschl, W. J. 2001, ApJ, 561, 708

Vollmer, B., & Huchtmeier, W. 2003, A&A, 406, 427

Vollmer, B., Braine, J., Pappalardo, C., & Hily-Blant, P. 2008, A&A, 491, 455

Wahba, G. 1990, CBMS-NSF Regional Conference Series in Applied Mathematics, Based on a series of 10 lectures at Ohio State University at Columbus, March 23-27, 1987, Philadelphia: Society for Industrial and Applied Mathematics, 1990,

Warmels, R. H. 1988, A&AS, 72, 57

Whitmore, B. C., Gilmore, D. M., & Jones, C. 1993, ApJ, 407, 489

Worthey, G. 1994, ApJS, 95, 107

Yasuda, N., Fukugita, M., & Okamura, S. 1997, ApJS, 108, 417

Yoshida, M., et al. 2002, ApJ, 567, 118